Enzymatic degradation of the cornea to develop an experimental model for keratoconus: Biomechanical and optical characterisation

Thesis submitted in accordance with the requirements of the University of Liverpool for the degree of Doctor of Philosophy

by

Ahmed Mohammed Ali Kazaili

January

2020

Acknowledgement

First and foremost, I thank my wonderful parents, Rajeha Ziara and Mohammed Kazaili. Your love and support have seen me through many years at university and even primary and high schools where you have supported me emotionally and financially through them all. To both, thank you for being so strong for me, thank you for forgiving me as a terrible son who had not been there for you when you needed the most.

For the work presented in this thesis, I would like to express my sincere gratitude to my primary supervisor Dr Riaz Akhtar for the continuous academic support of my PhD study and research for his patience, motivation, enthusiasm, and immense knowledge. His guidance helped me in all the time of the research and writing of this thesis. I could not have imagined having a better advisor and mentor for my PhD study.

Besides my supervisor, I would like to thank my second supervisor Professor Ahmed Elsheikh for his support and constructive feedback on my work. Special thanks go to Dr Brendan Geraghty, Dr Samuel Lawman, Dr Ya Hua Chim, Dr Zhuo Chang, Dr Zhuola and Dr George Fleming not only for their academic support, insightful comments, encouragement and most importantly their friendship. I am thankful for Professor Yaochun Shen, Dr Jill Madine, Dr Raechelle D'Sa, Dr Shao-Hsuan Chang, Dr Hannah Davies Mr Derek Neary and Mr. Dave Atkinson who provided me some laboratory support and otherwise.

I would like to express my acknowledgement to my colleagues at the University of Liverpool, past and present, for their support, encouragement and being amazing friends. Those are Dr Benjamin John Peek, Phakakorn Panpho, Michael Ward, Ashkan Eliasy, Liang Guo, Liuying Li and Dr Rui Chen.

I also acknowledge the higher committee of education development - Iraq for sponsoring this PhD programme.

Words cannot express how grateful I am for my family. Special thanks to my beloved wife, Fatemeh Rostaminiya, who has translated some papers to English, supported me through the ups and downs and motivated me to keep going at the hardest of times of this PhD. To my beloved

daughters, Maya Kazaili and Tara Kazaili, I would like to express my thanks for being such good girls, your laughs and kisses always cheer me up and keep me going.

Finally, I thank those much more external to my PhD, my sisters (specially Zena Kazaili), brothers (specially Barik Kazaili), mother-in-law (Tiaba Koshbakashthabit) and friends (Hayder Al-Hindi, Husam Al-Yasiry, Donia Khalaf, Dr Rafah Althufary, Dr Thora Al-Yasiry, Salah Al-Sultani, Ahmed Al-Yaseen, Mahir Al-Hajaj, and Hussain Al-Nori) from home and close by, who supported in different ways.

Enzymatic degradation of the cornea to develop an experimental model for keratoconus: Biomechanical and optical characterisation

Author: Ahmed Kazaili

Abstract

The cornea is the transparent front part of the eye that covers the iris, pupil, and anterior chamber. It is composed of five layers, in which the stroma is the thickest layer (approximately 90% of corneal thickness) that consists mainly of laminated collagen fibrils associated with proteoglycans. The cornea acts as the eye's outermost lens that is accounted for approximately two-thirds of the eye's total optical power. Like other lenses, the cornea's geometrical characteristics, such as the curvature, are important to maintain its functions for clear and stable vision. These geometrical characteristics are highly affected by the biomechanical properties of the cornea. For example, in keratoconus, the cornea is characterised by a progressive and localised thinning in corneal thickness, which is associated with a reduction in stiffness and other biomechanical properties. These alterations happen at the collagenous network, which is mainly responsible for the biomechanical features of the cornea, and are mostly attributed to genetic factors and abnormal enzymatic activity. Histological and biochemical studies suggested the role of amylase and collagenase activities in degradation of collagenous network and progression of keratoconus. However, the role of amylase and collagenase on biomechanical and optical properties have not been investigated.

In this study, *in vitro* enzymatic degradation of porcine corneas was conducted with varying concentrations of α-amylase and collagenase (crude and purified) enzymes for different incubation periods. Several techniques, including atomic force microscopy, nanoindentation and optical coherence tomography, were utilised to assess the effect of the enzymes on biomechanical of corneal tissue at macroscale, microscale and nanoscale levels. Corneal transparency and absorption following enzymatic incubation were also measured using spectrophotometry.

The biomechanical techniques that were utilised indicated that amylase and collagenase decrease corneal stiffness and thickness following incubation the corneas with amylase and collagenase. Further reduction in biomechanical properties and thickness of the corneas was found with increased enzymes concentrations and incubation periods. Corneal transparency was increased

following incubation with the enzymes. The results suggest depletion of proteoglycans by amylase and digestion of collagen fibrils by collagenase. These results were used to propose an animal biomechanical model for keratoconus.

Layout of this thesis

This thesis consists of eight chapters:

- Chapter 1 introduces a general background to highlight the research motivation, aims and objective of this thesis.

- Chapter 2 provides an overview of corneal structure, and its biomechanical properties. The techniques are used in this thesis are explained in this chapter. Human keratoconus and its aetiology factors are presented. Biomechanical properties are also discussed in Chapter 2.

- Chapter 3 assesses corneal viscoelastic properties under physiological pressures using oscillatory nanoindentation.

- Chapter 4 introduces line-field optical coherence tomography as a tool for *in vitro* characterisation of corneal biomechanics under physiological pressures. Geometrical properties of porcine corneas are measured in this chapter.

- Chapter 5 presents an *in vitro* assessment of corneal transparency of inflated porcine corneas. Visible light transmission through central, paracentral, peripheral corneal regions are measured.

- Chapter 6 examines the viscoelastic, geometrical and optical properties of inflated porcine corneas following enzymatic treatment with varying concentrations of amylase and collagenase (crude and purified) for different incubation periods.

- Chapter 7 demonstrates the utility of the atomic force microscopy (AFM) with Peak Force Quantitative Nanomechanical Mapping (PF-QNM) as a tool for characterising the nanomechanical and morphological properties of corneal sections following incubation with amylase and collagenase.

- Chapter 8 summarises the overall outcomes and concludes the primary key findings. Future works are suggested in this chapter.

Geometrical details of the corneal holder that was used for oscillatory nanoindentation is shown in Appendix I. The mean values of the viscoelastic properties of the enzymatic treated corneas are tabulated in Appendix II. Biomechanical properties following snap-washing of the corneas with inhibitors are presented in Appendix III. In Appendix IV, biomechanical properties and CCT of porcine corneas following incubation with tissue culture are measured. The procedure for Peak Force QNM Calibration of AFM in air is explained in Appendix V. In Appendix VI, biomechanical properties following corneal cross-linking of enzymatic treated corneas are measured.

List of peer-reviews publications

Kazaili, A., Lawman, S., Geraghty, B., Eliasy, A., Zheng, Y., Shen, Y, Akhtar, R., 2019. Line-Field Optical Coherence Tomography as a tool for *In vitro* characterization of corneal biomechanics under physiological pressures. Scientific Reports, Nature 9(1), p.6321.

Kazaili, A., Geraghty, B, Akhtar, R., 2019. Microscale assessment of corneal viscoelastic properties under physiological pressures. Journal of the Mechanical Behavior of Biomedical Materials 100, p.103375.

Kazaili, A, Akhtar, R., 2018. Ultrastructural and nanomechanical changes of the cornea following enzymatic degradation. Journal for Modeling in Ophthalmology 2(2), 24-29.

Conference presentations

Ahmed Kazaili and Riaz Akhtar, 2017, 'Ultrastructural and nanomechanical changes of the cornea following enzymatic degradation'. Poster presentation, The Italian Chapter of the European Society of Biomechanics (ESB-ITA), Roma, Italy. On September 28th - 29th 2017.

Ahmed Kazaili and Riaz Akhtar, 2016, 'Quantification of nanomechanical properties of porcine corneas. Poster presented at Annual Scanning Probe Microscopy (SPM) conference meeting. Cambridge, UK. On 13th and 14th December 2016.

Ahmed Kazaili and Riaz Akhtar, 2017, Nano-Structure and Mechanical properties mapping in cornea following proteoglycans depletion'. Poster presented at British Society for Matrix Biology (BSMB) Matrix Proteoglycans - active participants in cell-ECM communication. Oxford, UK. On 3rd - 4th April 2017

Ahmed Kazaili and Riaz Akhtar, 2019, 'Micromechanical properties of the cornea under physiological pressure', Oral presentation presented by Akhtar, R in BioMedEng19 conference, Imperial College, London, UK. On 5th and 6th September 2019.

Ahmed Kazaili and Riaz Akhtar, 2018, 'Micromechanical properties of the cornea following enzymatic treatment. Poster presentation in the 8th world congress of biomechanics, Dublin, Ireland. On 8th to 12th July 2018.

Co-author contribution

In this thesis, Chapters three and four have been published in peer-reviewed scientific journals and the work produced involved collaboration with other researchers. This thesis consists of a general background, followed by one review chapter (Chapter Two) and three chapters (chapters three - five) in which developed testing methods of the corneas are presented. Chapter three and four are presented largely in published form as they appear in respective journals, although few amendments have been included within the main text where appropriate. In addition, two chapters (Chapter Six and Seven) include enzymatic treatment of the corneas. Summary discussion and conclusions follow these chapters.

Authors contributing to specific chapters in this thesis include: Mr Ahmed Kazaili (AK), Dr Riaz Akhtar (RA), Dr Brendan Geraghty (BG), Prof Yaochun Shen (YS), Dr Samuel Lawman (SL), Dr.Yalin Zheng (YZ) and Mr Ashkan Eliasy (AE).

The nature of each co-author's contribution to published work will now be discussed explicitly in more detail. Chapter three was published online in August 2019 in the Journal of the Mechanical Behaviour of Biomedical Materials (Kazaili *et al*, 2019) in collaboration with two co-authors. AK conceived and planned the experiments, conducted all the experimental work, analysed the data, and edited and wrote the manuscript. BG built a MATLAB code for mapping corneal elastic properties, verified the analytical method and edited the manuscript. RA supervised all the work, conceived and planned the experiments, analysed the data and assisted in editing and writing the manuscript.

Chapter four was published in Scientific Reports, in April 2019 (Kazaili *et al*, 2019). AK conceived and planned the experiments, conducted all the experimental work, analysed the data, and edited and wrote the manuscript. SL and YZ developed the OCT system, verified and analysed the data and assisted in editing the manuscript. BG verified the analytical method and edited the manuscript. YS developed the OCT system and assisted in editing the manuscript. AE built a Matlab code for detecting the corneal boundaries. RA supervised all the work, conceived and planned the experiments, analysed the data and assisted in editing and writing the manuscript.

List of contents

List of figures

List of tables

List of abbreviations

Abbreviation	Description
μ_a	Absorption coefficient
B	Base of the parabola
CCT	Central corneal thickness
CCD	Charge-coupled device camera
σ	Circumferential stress
CH	Corneal hysteresis
CT	Corneal thickness
E	Elastic modulus
ECM	Extracellular matrix
FACIT	Fibril-associated collagens with interrupted triple helices
GAG	Glycosaminoglycan
H	Height of a parabola
IOP	Intraocular pressure
I	Light intensity
LF-OCT	Line field optical coherence tomography
tan(δ)	Loss factor
OCE	Optical coherence elastography
OCT	Optical coherence tomography
l	Optical path length
PF-QNM	Peak Force quantitative nanomechanical mapping

%T	Percentage light transmission
PBS	Phosphate buffer saline solution
ν	Poisson's ratio
P	Pressure
p	Probability value for statistical significance
G"	Shear loss modulus
G'	Shear storage modulus
SLRP	Small leucine-rich protein
S	Stiffness
ε	Strain
E_t	Tangent elastic modulus
t	Time
TC	Tissue culture
V	Volume
E_r	Reduced elastic modulus
E_i	Elastic modulus of the indenter

Chapter 1

General introduction

This chapter introduces the general background and the motivation of this thesis. The aims and objectives of the thesis are presented.

1.1. Motivation

The cornea plays an important role in the ocular system acting as the transparent structural barrier of the internal delicate contents of the eye, and also providing the main refractive power of the eye. Its transparency and geometrical features, such as corneal thickness and curvature, are affected by its ultrastructure (Meek and Knupp, 2015). Corneal diseases are serious conditions that can cause clouding, scarring, distortion and eventually blindness. There are many types of corneal disease. The three major types are keratoconus, Fuchs' endothelial dystrophy and bullous keratopathy. Keratoconus is a non-inflammatory and painful corneal disease, in which the normally dome-shaped cornea progressively thins leading to a localised cone-like bulge to develop that eventually impairs clear vision. The estimated prevalence of keratoconus in the general population is 54 per 100,000 individuals worldwide and effecting both genders. The majority of keratoconic patients aged from 10 to 40 years, where keratoconus is defined as a relevant age disease (Romero-Jiménez *et al*, 2010).

Keratoconus is a localised deterioration in the tissue, happens at the ultrastructural level where the collagenous structure of the stroma partially loses its strength to resist the intraocular pressure (IOP) that causes irregularity in corneal curvature, which causes vision impairment (Bao *et al*, 2017; Vellara and Patel, 2015). Many factors have been reported that induce keratoconus progression, including environmental, genetic, biomechanical and biochemical factors (Barbara *et al*, 2019; Gomes *et al*, 2015; Sugar and Macsai, 2012). Biochemical factors include the upregulation of degradation enzymes that lead to biomechanical deterioration of the ultrastructure of the stroma (Vellara and Patel, 2015). Immunohistochemical studies found that collagenase activity was increased in keratoconic corneas (Collier *et al*, 2000; Mackiewicz *et al*, 2006; Seppälä *et al*, 2006), which is attributed to an imbalance between the digestive enzymes and their inhibitors (Sherwin *et al*, 2017). Other immunohistochemical studies found that α-amylase was increased in the tear fluid in patients with early stages of keratoconus. However, the role of amylase and collagenase on viscoelastic and optical properties of the cornea has not been studied.

Early detection of keratoconus helps manage its progression. A widely used technique to stop keratoconus progression is corneal cross-linking (CXL), which utilises ultraviolet light and Riboflavin. Nowadays, CXL procedures are widely utilised in hospitals to stop the progression of keratoconus (Barbara *et al*, 2019), which limits the availability of the samples for further biomechanical research.

Hence, this thesis is motivated by the need to investigate the effect of amylase and collagenase (crude and purified) on viscoelastic, geometrical and optical properties of the corneas. In addition, it motivated to show how theses enzymes effect the ultrastructure of corneal stroma. This study will help provide better understanding for the role of amylase and collagenase in the corneal tissue. Besides, this study serves as an empirical model of keratoconus.

1.2. Aim and objectives

The main goal of this thesis is to investigate porcine corneas as a model of human corneas for geometrical, optical and biomechanical properties at different scales following enzymatic treatment with varying concentrations of amylase and collagenase (crude and purified) for different incubation periods. This study also aims to propose porcine enzymatic degraded corneas as a biomechanical model of keratoconus at different progression stages. Theses aims will be achieved through the following objectives:

- The first objective of this study is to assess localised microscale viscoelastic properties of inflated porcine corneas using a novel oscillatory nanoindentation.

- The second objective is to develop a method for characterising geometrical and macroscale biomechanical properties of porcine corneas. This method employs inflation testing and line-field optical coherence tomography (LF-OCT) to measures the volumetric deformations, central corneal thickness of inflated corneas.

- The third objective is to build a spectrophotometric method to examine corneal transparency by measuring light transmission through porcine cornea under physiological pressures.

- The fourth objective is to treat corneas with varying concentrations of amylase and collagenase (crude and purified) for different incubation periods, then utilising the above methods to assess transparency, thickness, and biomechanical properties of the corneas.

- The fifth objective is to investigate ultrastructural topography and nanomechanical properties of corneal sections following incubation with varying concentrations of amylase and collagenase (crude and purified) using atomic force microscopy.

- The sixth objective is to propose an empirical model from enzymatic treated porcine corneas that match the biomechanical and thickness of human keratoconus at different progression stages.

1.3. References

Bao, F.J., Geraghty, B., Wang, Q.M., Elsheikh, A., 2017. Role of corneal biomechanics in the diagnosis and management of keratoconus. In: Alió J. (eds) Keratoconus (pp. 141-150). Springer, Cham, pp. 141-150. USA.

Barbara, R., Turnbull, A.M., Malem, A., Anderson, D.F., Hossain, P., Konstantopoulos, A, Barbara, A., 2019. Epidemiology of keratoconus. In: Barbara, A. (eds) Controversies in the Management of Keratoconus (pp. 1-16). Springer, Cham. USA.

Collier, S., Madigan, M., Penfold, P., 2000. Expression of membrane-type 1 matrix metalloproteinase (MT1-MMP) and MMP-2 in normal and keratoconus corneas. Current Eye Research 21, 662-668.

Gomes, J., Tan, D., Rapuano, C., Belin, M., Ambrósio, R., Guell, J., Malecaze, F., Nishida, K., Sangwan, V., 2015. Global Consensus on Keratoconus and Ectatic Diseases. Cornea 34, 359-369.

Legkikh, L., Koledintsev, M., Semenova, A., Okuyama, K., 2017. Biochemical investigations of lacrima in early diagnosis of keratoconus. (Abstract) Sangubashi Eye Clinic, Japan. [available on: www.sangubashi.com/English/report/syanhai.htm] (accessed on: 12th January 2020).

Mackiewicz, Z., Määttä, M., Stenman, M., Konttinen, L., Tervo, T., Konttinen, Y., 2006. Collagenolytic proteinases in keratoconus. Cornea 25, 603-610.

Meek, K.M., Knupp, C., 2015. Corneal structure and transparency. Progress in Retinal and Eye Research 49, 1-16.

Quintarelli, G., Dellovo, M.C., Balduini, C., Castellani, A.A., 1969. The effects of alpha amylase on collagen-proteoglycans and collagen-glycoprotein complexes in connective tissue matrices. Histochemie 18, 373-375.

Romero-Jiménez, M., Santodomingo-Rubido, J., Wolffsohn, J., 2010. Keratoconus: A review. Contact Lens and Anterior Eye 33(4), 157-166.

Seppälä, H., Määttä, M., Rautia, M., Mackiewicz, Z., Tuisku, I., Tervo, T., Konttinen, Y., 2006. EMMPRIN and MMP-1 in Keratoconus. Cornea 25, 325-330.

Sherwin, T., Ismail, S., Loh, I. P., McGhee, J., 2017. Histopathology (from Keratoconus Pathology to Pathogenesis). In: Alió J. (eds) Keratoconus. Essentials in Ophthalmology. Springer, Cham. USA.

Spoerl, E., Teral, N., Raiskup, F., Pillunat, L., 2012. Amylase reduces the biomechanical stiffness of the cornea. Investigative Ophthalmology & Visual Science 53(14), 1531-1531.

Sugar, J., Macsai, M.S., 2012. What causes keratoconus? Cornea 31, 716-719.

Vellara, H., Patel, D., 2015. Biomechanical properties of the keratoconic cornea: a review. Clinical and Experimental Optometry 98, 31-38.

Wollensak, G., Spörl, E., Mazzotta, C., Kalinski, T, Sel, S., 2011. Interlamellar cohesion after corneal crosslinking using riboflavin and ultraviolet A light. British Journal of Ophthalmology 95, 876-880.

Chapter 2

Literature review

The literature review provides comprehensive background information on all of the involved topics within this thesis. Section 2.1 briefly introduces the eye and its key components. Section 2.2 presents the cornea and its layers, in which the structure of each layer is explained. In Section 2.3, the structure and function of the limbus are briefly described. Section 2.4 overviews the ultrastructure of the corneal stroma including the structural and geometrical representation of the collagen fibril. Section 2.5 highlights the importance of corneal transparency and the theories behind this essential characteristic. In section 2.6, corneal hydration and stromal swelling is explained in terms of moving, pumping, and distribution of water in the cornea. The importance of corneal shape and the factors affecting its shape are summarised in section 2.7. In section 2.8, the basic concepts of imaging techniques of the cornea are overviewed, with a focus on optical coherence tomography. Section 2.9 focuses on the characteristics and clinical features of the keratoconus, explains many factors that progress the keratoconus including the enzymatic unbalance in corneal tissue. In subsections of section 2.9, *in vivo* and *ex vivo* biomechanical characteristics and measurement techniques of keratoconus are presented. Finally, section 2.10 introduces porcine corneas as model for human corneal biomechanics/studies, in which the morphological, structural, and biomechanical features are presented and compared with the human cornea.

2.1. The eye

The eye is the most complex natural optical system of the body that is projecting visual information from the surroundings into the brain. Incoming light enters the eye through the cornea and the crystalline lens to the back where a matrix of photoreceptors situated in the retina. These photoreceptors, rods and cones convert the incident light, image, into electrical signals. Optical nerve transfers these electrical signals to the brain for further processing of the visual information.

The eye ball structure has very precise optical and geometrical features. Together, the cornea and the lens generate the total refractive power of the eye which is approximately 63 Dioptres (D) in human eyes (Sharp and Philips, 1997). The cornea provides the largest part of the total refractive power which is about 40 - 45 D, while the lens contributes with a dioptric power between 14 D to 37 D depending on its capability to reshape in order to accommodate the light on the retina (Iribarren *et al*, 2012). The amount of light reaching the retina is controlled by a variable, circular and chromatic diaphragm called the iris, which is situated between the cornea and the lens. The iris forms an aperture called the pupil that changes in size to maintain the amount of light. The iris contracts to make a small opening upon increased illumination for obtaining the best image and vision quality (Navarro, 2009). Like any optical apparatus, the optical features of the eye can be affected by its dimensions. The typical human eye is a slightly asymmetrical sphere with an approximate axial (sagittal) diameter of 24 to 25 mm and a horizontal (transverse) diameter of 24 mm. The volume of a typical human eye is about 6.5 ml (Kolb, 2007). Different animals have divergent eye globe dimensions at normal intraocular pressure (IOP). For example, the anteroposterior length of young adult porcine eyes is 23.9±0.08 mm (Sanchez *et al*, 2011), whereas it is 24±0.5 mm in adult sheep (Mohammadi *et al*, 2011).

From a structural prospective, the eyeball can be divided into an anterior and posterior segment. Figure 2.1 shows a schematic-sagittal section of the human eye. The anterior segment contains the anterior chamber, which is the area between the cornea and the iris, and posterior chamber, which is a narrow space between the iris and the suspensory ligaments of the lens. Both chambers are filled with a watery fluid called the aqueous humour, which is produced by the ciliary body. The aqueous humour flows from the posterior chamber through the pupil to the anterior chamber and provides nutrients to the surrounding structures. The posterior segment is a large cavity that is filled with the vitreous humour. The vitreous humour is a gel-like fluid and is more viscous than aqueous humour (Ng and Oliver, 2018).

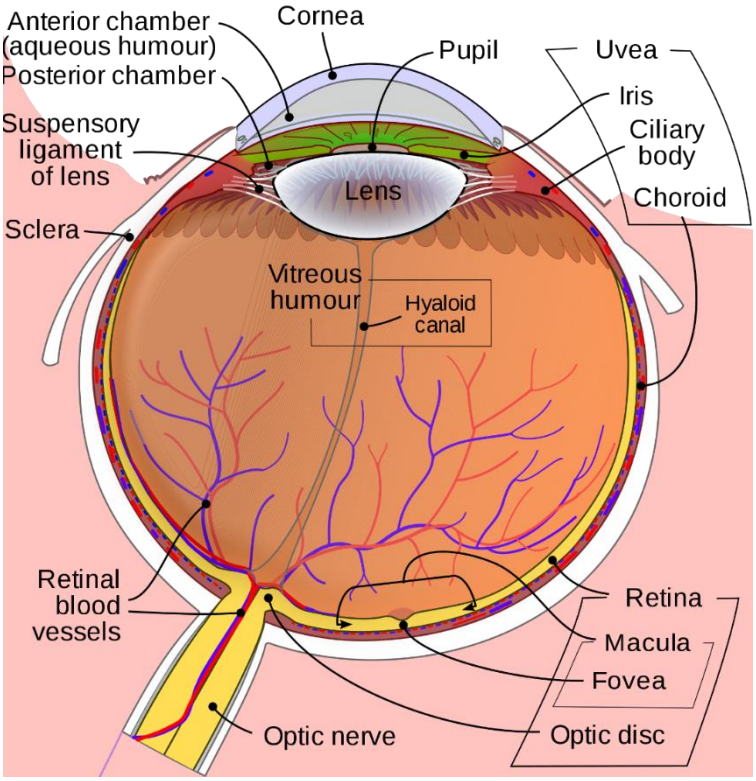

Figure 2.1: A schematic-sagittal section of the human eye (Ng and Oliver, 2018).

2.2. The cornea

The cornea is the transparent shell of the eye ball that consists of highly organised collagen fibrils. The cornea's transparent nature and its biomechanical behaviour make it very important to the ocular structure and visual system. The cornea is neither neurobiologically sophisticated, like the retina, nor has the ability of the lens for dynamic reshaping. However, the eye would not be able to achieve its necessary function without the cornea's transparency and geometrical features. The complexity of corneal structure and its essential function for the visual system has drawn many scientists to investigate its pathological, physiological, band biomechanical properties.

The cornea is an avascular connective tissue that acts as the primary infectious and structural barrier of the internal delicate contents of the eye. The cornea transmits about 90% of the visible light and even up to 98% at the near infrared region (Meek and Knupp, 2015). Interestingly, the central cornea (pre-pupillary) is more transparent than the peripheral cornea (Doutch *et al*, 2007), which is attributed to changes in its ultrastructural details (Doutch *et al*, 2008).

Geometrical features of the cornea play an important role for obtaining clear vision, since the cornea provides the main refractive power of the eye. In order for the cornea to carry out this

function properly, it has to maintain a very precise aspherical shape. In human corneas, it measures 10.5±0.5 mm in the vertical meridian and 11.5±0.5 mm in the horizontal meridian. The *in vivo* central corneal thickness (CCT) of human corneas is 530±32 μm and increases gradually up to 670±27 μm in the peripheral cornea. Therefore, the average value of the radius of curvature in human corneas is 7.8±0.2 mm for the anterior surface, while it is 6.5±0.2 mm for the posterior surface. The centre of the cornea shows steeper corneal curvature than the flatter peripheral region which makes it an aspheric structure (DelMonte and Kim, 2011; Hayes *et al*, 2007; Ng and Oliver, 2018). Geometrical features of the cornea vary among mammals, for instance, porcine corneas are slightly thicker (almost twice) and bigger in size than human corneas (Sanchez *et al*, 2011).

In many mammals, including humans and pigs, the cornea is periodically irrigated by the tear fluid, which helps maintaining smooth contact and reduces friction forces between the cornea and the eyelid. In addition, the tear fluid protects the cornea against pathogens, flushes contaminants out of the cornea surface, nurtures corneal epithelial cells, and modifies the refractive index such that the optical properties of the cornea are enhanced (Rantamäki *et al*, 2011). Internally, the posterior surface of the cornea touches the aqueous humour, which also provides nutrients to the cornea. The regulated flow of the aqueous humour inflates the eye globe and maintains the intraocular pressure (IOP) that are essential factors for the structural and optical integrity of the eye. The appropriate chemical environment provided by the aqueous humour makes the anterior segment of the eye an optical-clear medium that allows good visual function (Stamper *et al*, 2009). Figure 2.2 shows a schematic diagram of human cornea, which shows the cornea consists of five layers that are explained in the next paragraphs.

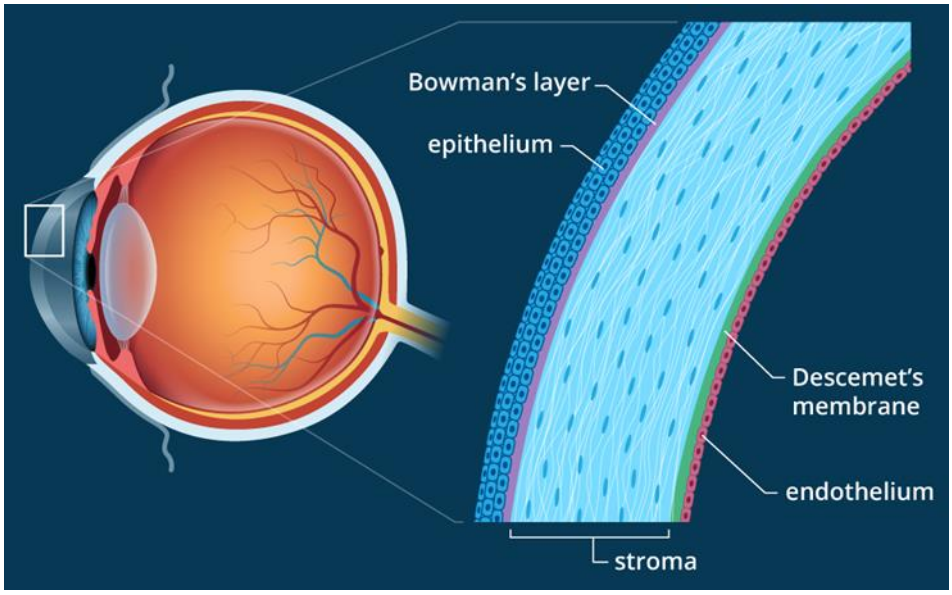

Figure 2.2: A schematic diagram of human eye (left) and cornea (right). The light blue ellipses (dots) in the stroma layer represent keratocytes (Heiting, 2017).

2.2.1. Epithelium

The corneal epithelium is the first cellular that consists of 6 layers of combined cells, stratified, non-keratinised squamous epithelium. *In vivo* adult human corneas, have a thickness in the centre ranging from 48 μm to 59 μm, about 10% of the total corneal thickness, which increases gradually toward the limbus by 30% (Ehlers *et al*, 2010; Feng and Simpson, 2008). The thickness of this layer is different in mammals; for example, the thickness of the epithelium in the apex of porcine corneas was found to be 65.28±14.31 μm, which comprises approximately 6.8% of corneal thickness at 15 mmHg (Kazaili *et al*, 2019). The main function of the epithelium is protecting the cornea, controlling the flow of fluids from the tears toward the deeper layers, and preventing organisms including bacteria from entering the corneal stroma. In addition, the epithelium is an integrated part of the tear film-cornea interface that plays an essential role in the refractive power of the eye (DelMonte and Kim, 2011). The epithelium layer sticks to Bowman's membrane posteriorly by means of anchoring fibril complexes containing type VII collagen fibrils (Bergmanson, 2001). It was found that the epithelium has negligible contribution to the total corneal stiffness (Elsheikh *et al*, 2008), hence its stiffness was mostly ignored in predictive numerical simulations and modelling programs.

2.2.2. Bowman's membrane

The Bowman's layer is an acellular layer which is 17.7±1.6 μm thick in human corneas, which is secreted by the epithelium and terminates at the limbus (Tao *et al*, 2011). Ultrastructurally, it consists of fine and randomly orientated collagen type I (primarily) and III and V fibrils. The collagen fibril diameter in the Bowman's layer is 25±5 μm (Hayashi *et al*, 2002). The functional role of Bowman's layer is not completely investigated (Jirsova, 2017). However, it has been suggested that it protects the underlying corneal stroma for traumatic injury, facilitates rapid stromal wound healing and partially supports the cornea maintain its shape (Wilson and Hong, 2000). Bowman's layer gets thinner with age due to natural collagen degradation and will not regenerate in case of disruption. Therefore, stromal collagen starts penetrating Bowman's membrane to increase its strength and maintain the overall shape of the cornea (DelMonte and Kim, 2011; Jirsova, 2017). Interestingly, Bowman's membrane is not present in corneas of all species. For instance, it is absent in porcine corneas, some carnivores, and most non-primates (Merindano *et al*, 2002; Svaldenienė *et al*, 2003).

2.2.3. Stroma

The stroma is the thickest layer of the cornea, which is about 90% of the whole corneal thickness. Therefore, the biomechanical properties of the cornea are mostly attributed to this layer. Corneal stroma is similar with other collagenous (connective) tissues in its composition, composed of relatively few cells and extracellular matrix (ECM). However, it differs from other collagenous tissues in its remarkable transparency for visible light due to precise organisation of fibres and other ECM. In human corneas, the stroma consists of around 200 to 250 lamellae, which are arranged in parallel to the surface of the cornea. The thickness of each lamella is about 2 μm, and it is mainly formed by many collagen fibrils (mostly type I, but also type III, V, VI) that range from 31 to 35 nm in diameter. Collagen fibrils are embedded in a ground substance composed mainly of proteoglycans, glycoproteins, soluble proteins, inorganic salts, and keratocytes. Collagen fibrils within a lamella run in parallel to each other and to the surface of the cornea. Although, they subtend fairly large angles with those in adjacent lamellae; Figure 2.3 demonstrates collagen fibrils orientation within stromal lamellae. As shown in Figure 2.3, collagen fibrils can be seen at all angles within the plane of the cornea (Ambekar *et al*, 2011; Meek and Boote, 2009).

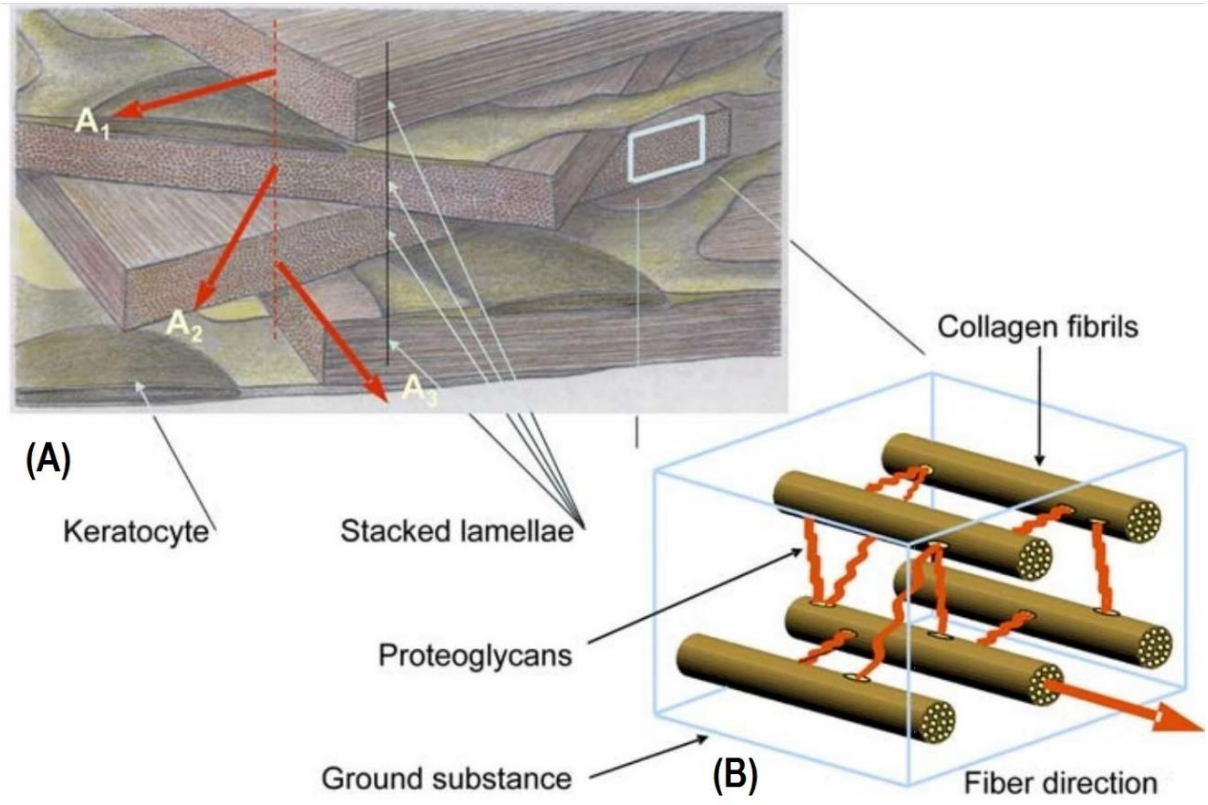

Figure 2.3: Schematic representation of the lamellar structure within corneal stroma. (A): Stacked lamellae run at an angle to each other. Plan A1, A2, and A3 show the direction of the lamellae. It shows the bundles of fibrils are run in parallel. Keratocytes randomly distributed between lamellae. (B): The orientation of collagen within a lamella of human corneal stroma. Proteoglycans link the collagen fibrils. Adapted from (Eliasy *et al*, 2018).

The peripheral region of corneal stroma is slightly thicker than the central stroma of human corneas. In addition, the collagen fibrils in the central stroma are organised in orthogonal orientation, and may change gradually in the peripheral stroma to be in circumferential orientation in the limbus annuls, see Figure 2.4. It was reported that corneal collagen arrangement varies with different species, for example, corneal collagen arrangement is circumferential in porcine corneas (Hayes *et al*, 2007). Moreover, the organisation of the lamella seems to change based on the depth within the stroma, where the lamellae of posterior layers are more organised than anterior layers (Boote *et al*, 2006; Meek and Boote, 2004). This distinct structural organisation of collagen fibres provides adequate mechanical strength to the cornea for the sake of maintaining the shape, optically reduces forward light scatter and contributes subsequently to the transparency of the cornea (DelMonte and Kim, 2011; Meek, 2009; Meek and Knupp, 2015). Since the stroma provide the main biomechanical support for the cornea, collagen fibrils and other ECM components such as hepatocytes and proteoglycans will be briefly explained in upcoming sections.

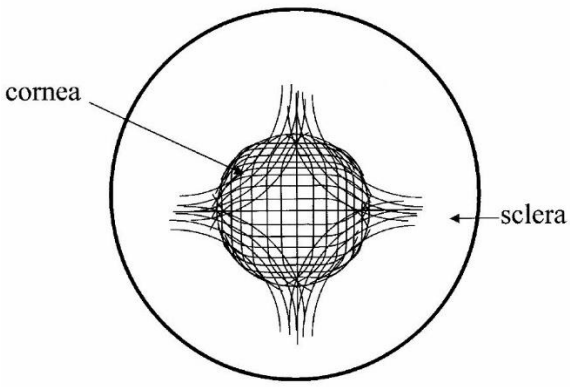

Figure 2.4: Schematic representation simplifies the arrangement of human corneal and limbal lamellae. The central lamellae are predominantly in the inferior-superior and nasal-temporal directions and curve near the limbus to form an annulus. They increase in number as the cornea thickens away from the central region. Many of these lamellae may have their origins in a set of anchoring lamellae that curve in and out of the peripheral cornea, Adapted from (Aghamohammadzadeh *et al*, 2004).

2.2.4. Descemet's membrane

Descemet's membrane is an acellular layer of 9±1 μm thick in adult human corneas, which is secreted by the endothelium. The main function of the Descemet's membrane is to obstruct the aqueous humour from diffusing into the stroma. It structurally consists of distinct anterior and posterior zone. The anterior zone appears banded in a microscopic cross-section view and looks like a hexagonal grid in microscopic-tangential sections. This highly organised collagenous structure is mostly composed of collagen type VIII, which is believed that it provides structural support for the Decement's membrane against the IOP (Cholkar *et al*, 2013; DelMonte and Kim, 2011; Jirsova, 2017). The posterior zone gradually increases its thickness with age up to 7 μm in

human corneas, appears less organised than the anterior zone. The posterior zone is mostly composed of collagen type IV fibrils (Jirsova, 2017), which are 13±5 nm thick and weaker than stromal collagen type I fibrils (Fratzl, 2008). Other constituents are present throughout the Descemet's membrane such as fibronectin, thrombospondin and laminin as well as collagen types V, VI, XVIII. The Descemet's membrane does not regenerate in case of rupture. In addition, it gets folded in case of stromal swelling (Jirsova, 2017; Joyce, 2003).

2.2.5. Endothelium

The endothelium is the posterior layer of the cornea, which is made up of a monolayer of cells that act as the border between the stroma and the contents of the anterior chamber. The cells are arranged in an irregular honeycomb mosaic shape when seen from the posterior side (Beuerman and Pedroza, 1996). The thickness of the endothelium is approximately 5.5±0.5 μm in adult human corneas. In adulthood, these cells get flatten and become tightly adherent to each other (DelMonte and Kim, 2011; Jirsova, 2017; Joyce, 2003).

Transparency is an essential feature for the cornea, which acts as the main lens of the eye. This optical function of the cornea is obtained as a result of the uniformity of the cornea and the spatial arrangement of the collagen fibrils within the corneal stroma. Endothelial cells primarily act as gates to maintain corneal transparency by controlling stromal hydration (78% water). In the stroma, the water binds with proteoglycans producing a pressure gradient between the anterior chamber and the stroma across the endothelium. The other function of the endothelium is to allow the nutrients passing from the aqueous humour of the cornea. In addition, the endothelium removes excess water from the stroma, this will counteract the tendency of the cornea to swell by pumping out the excess stromal fluid via the active transport of ions (Na+ and K+) from the stroma to the aqueous humour (DelMonte and Kim, 2011; Jirsova, 2017; Joyce, 2003).

2.3. Overview of the structure and function of the limbus

The limbus is the border zone between the cornea and the sclera. In human eyes, it is 1.5mm wide in the horizontal axis and 2mm wide in the vertical axis. Figure 2.5 shows a schematic drawing of a cross-section of the limbal area. The structure of the limbal epithelium is almost similar to the structure of the corneal epithelium but the first has a larger number of cell layers (Buskirk, 1989; Remington, 2011). A study conducted by Aghamohammadzadeh *et al* (2004) showed that collagen fibrils below the limbal epithelium run in a tangential or circular orientation in human eyes, and are of a larger diameter than those found in the corneal stroma.

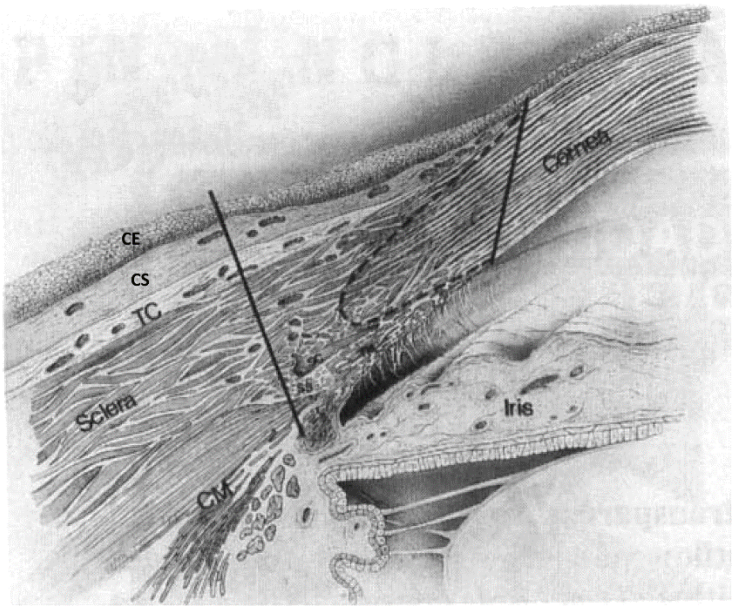

Figure 2.5: A schematic drawing of a cross-section of the limbus. The area between the two sloid lines represents the limbus from a pathological perspective. The area between the right solid line and the dotted line represents the limbus from a histological perspective. TC, Tenon's Capsule; CE, epithelial conjunctiva; CS, scleral conjunctiva; CM, CM, ciliary muscle. Adapted from (Buskirk, 1989).

2.4. Ultrastructure of the corneal stroma

The ultrastructural constituents of the cornea stroma are the collagen fibre and the other ECM components, such as proteoglycans. Collagen fibres are composed of a bundle of many smaller collagen fibrils, which run together in the same fibre. Many oriented collagen fibres will form a lamella, which was explained in a previous section. Collagen fibres supply the cornea with the strength are required to resist IOP and maintain precise corneal shape for optimal light refraction. The non-fibrillar extracellular components are primarily composed of proteoglycans, which contribute in maintaining the hydration, transparency of the cornea and supporting collagenous ultrastructure of the stroma (Meek, 2009).

2.4.1. Collagen

Collagen is a protein is the most abundant structural protein in mammals. It exists in abundance in many tissues such as tendons, ligaments, bones, skin, teeth, cornea, sclera, blood vessels, cartridges, and fascia. Many other organs and tissues, where the collagen is not the most abundant protein, depend mostly on collagen for their structural integrity (Meek, 2008; Rodríguez *et al*, 2018). Therefore, collagen plays a key role in the body, and any malfunction in the collagen leads to a variety of disorders. These malfunctions may be caused by genetic mutation, deficiency or excessive enzymatic activity, variations in the collagen-associated molecules that are necessary to generate a healthy and functional collagen (Blank and Boskey, 2008). An example of these

disorders is keratoconus, which is a non-inflammatory eye disease where the normally round dome-shaped of the cornea progressively thins causing a cone-like bulge to develop that eventually impairs clear vision. This disease will be briefly outlined in sections 2.9.

In human body, there are 29 distinct collagen types have been characterised to three different groups, each type is specific for the function required and the location (Jirsova, 2017). The fibril forming collagen group such as collagen types I, II, III, V and XI that are known to form collagen fibres. There is a non-fibril (or network) forming collagen group such as collagen types IV, VI and VII. The third group is denoted as fibril-associated collagens with interrupted triple helices (FACIT) such as IX and XX types. All these groups share the same triple-helix structure that consists of three polypeptides of amino acid sequences rich in either proline or hydroxyproline and with glycine at every third residue (Gelse *et al*, 2003; Michelacci, 2003; Rodríguez *et al*, 2018).

In the human cornea, collagen makes up about 71% of the entire dry mass in the cornea. There are different types of collagen in mammalian corneas. Collagen type I is the dominant collagen type in the cornea, which is mostly seen in the stroma and gives the cornea tensile strength. Collagen type V mostly interacts with (surrounds) collagen type I and acts to maintain the diameter of collagen fibril. Collagen type III exists in low proportion in the stroma but increases during wound healing, with age and many pathological conditions. The non-fibrillar collagen type VI is fairly presented in high proportion in the stroma, and creates corneal microfilamentar structures by binding to collagen fibrils. This microfilamentar structures may contribute to stabilisation and maintenance of a constant distance between collagen fibrils (Jirsova, 2017; Meek, 2009, 2008). Figure 2.6 summarises some of collagen types and their locations within the human cornea.

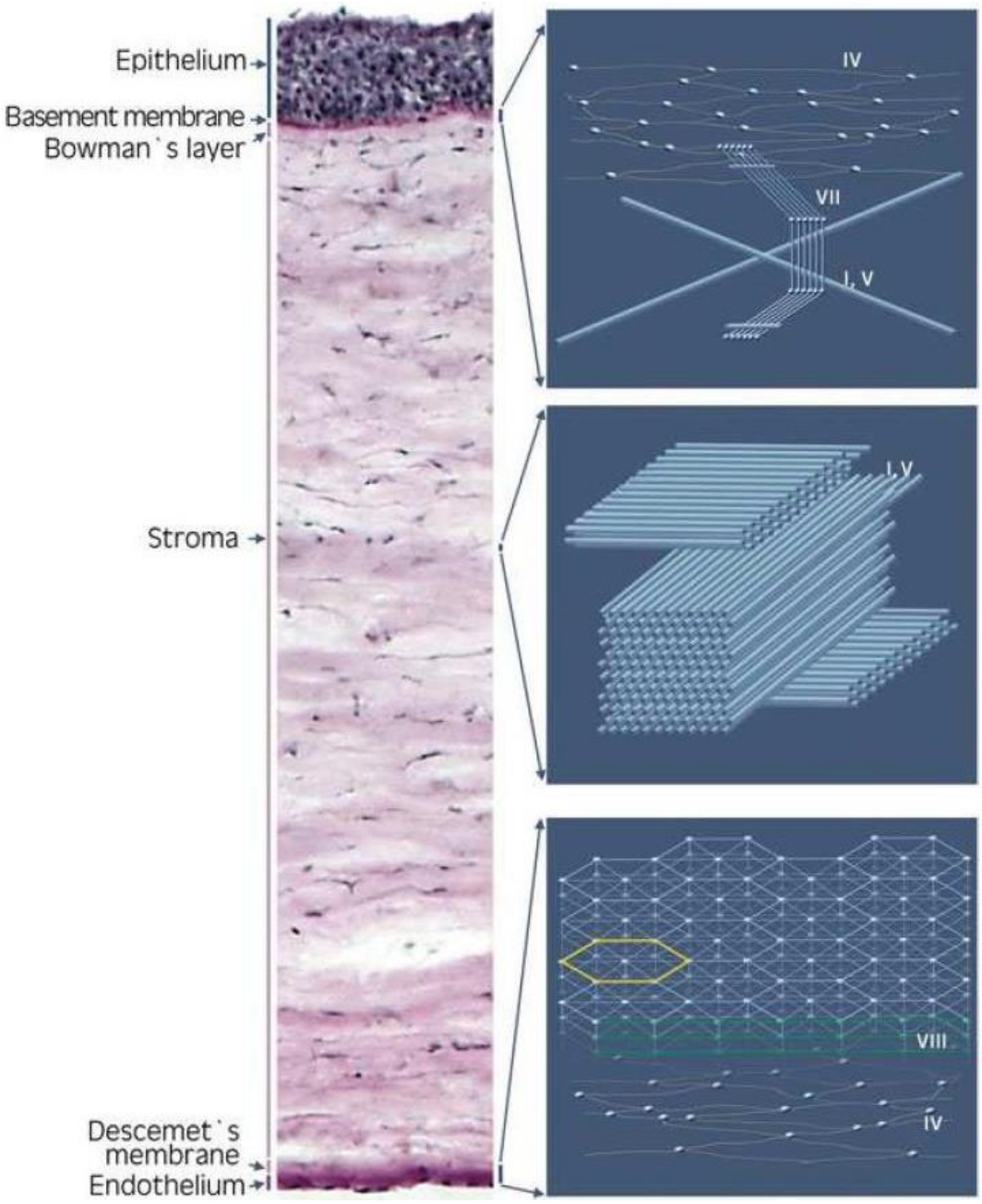

Figure 2.6: Cross-sectional anatomical image of the human cornea: Microscopic image of the human cornea (left) and the corresponding acellular structures of the ECM, schematic diagram (right). The connections between the basement membrane of the epithelium and the underlying Bowman's layer, the lamellar arrangement of the stroma, and the structure of Descemet membrane are shown. The collagen present in particular layers is indicated by Roman numerals (Jirsova, 2017).

In the corneal stroma, collagen fibril is biosynthesised in the rough endoplasmic reticulum of keratocytes, in which three alpha chains are synthesised and assembled in helical strand as longer precursors called procollagen. For instance, procollagen type I is a heterotrimer that is packaged into secretory vesicles in the Golgi apparatus of the keratocytes before being secreted into the extracellular space. The mature procollagen molecules assemble into parallel arrays to establish microfibrils (Massoudi *et al*, 2016; Michelacci, 2003). These microfibrils subsequently align together

to form striated collagen fibrils. It has been estimated that there are approximately 50 aligned microfibrils within each collagen fibril type I in the cornea (Holmes and Kadler, 2005).

The triple-helical collagenous molecules assemble together in a specific staggered arrangement in the collagen fibrils. This arrangement gives rise to a striking banding pattern of 66±1nm length, which is known as the D-period. Figure 2.7 demonstrates structural and geometrical representation of collagen fibril including the axial D-periodic of collagen fibrils. The diameter of hydrated collagen molecules is approximately 1.6 nm and is in 300 nm length approximately. It was proposed that a collagen filament is composed of five molecules, which are staggered to form one D-period. Each five-molecule arrangement is referred to as a microfibrils, which is estimated to be 2-5 nm in diameter. This reasonable geometrical arrangement can reflect the striking pattern of collagen fibril banding (Meek and Fullwood, 2001; Meek, 2008; Sherman *et al*, 2015; Smith, 1968).

Collagen fibrils, which provide the main tensile strength to the cornea, are connected by internal and external linkers. The internal molecular linkers include hydrogen bonds, which are situated between the three chains, and electrostatic interactions between the helices. The external linkers include proteoglycans and other ECM components in the stroma (Gelse *et al*, 2003; Rodríguez *et al*, 2018). Proteoglycans will be explained in the next section.

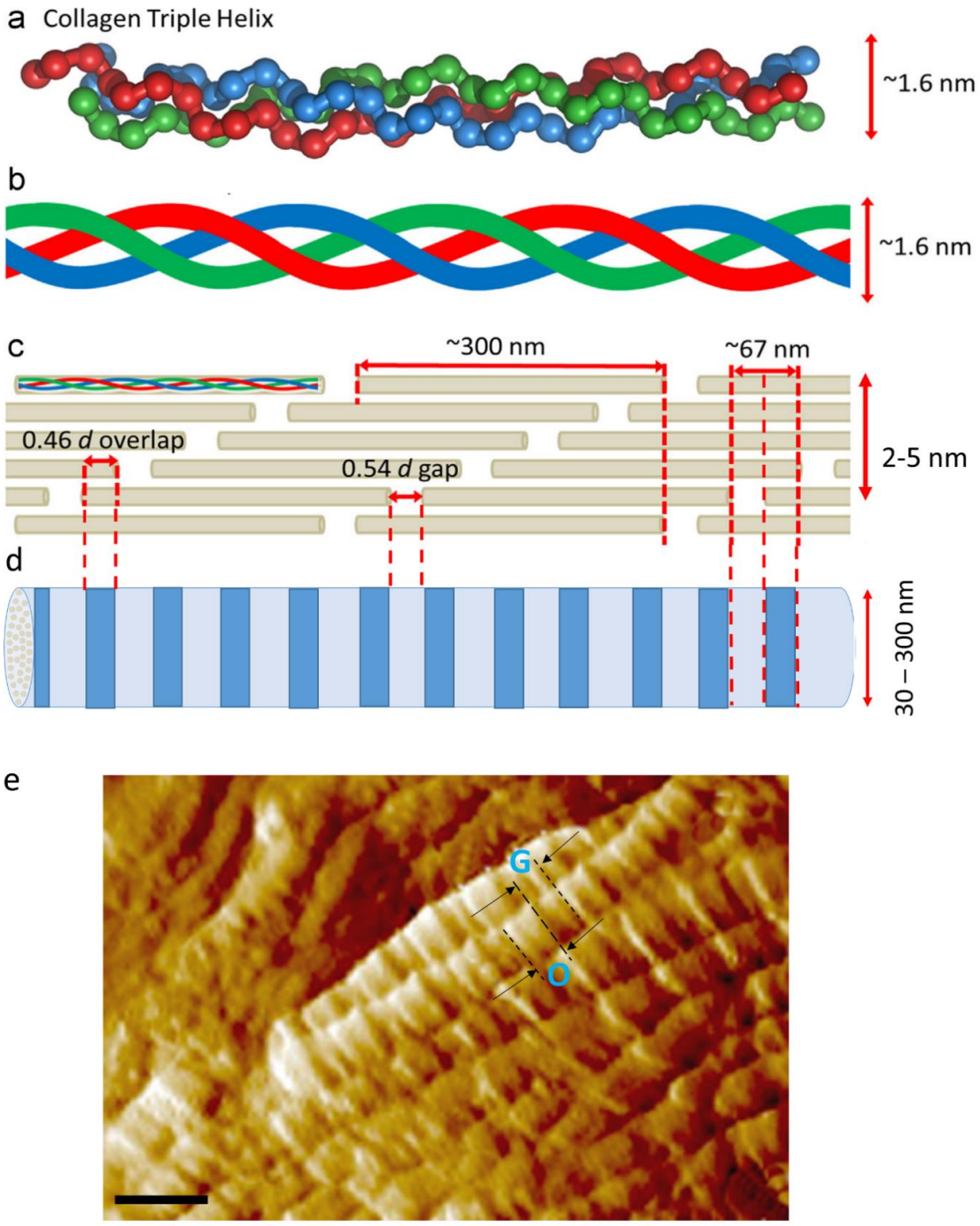

Figure 2.7: Structural and geometrical representation of a collagen fibril. (a) Collagen triple helix formation of three helical procollagen chains (Red, Green, and Blue). (b) Schematic of triple helix, which has diameter of about 1.6 nm. (c) Schematic of five collagen molecules arrangement. The helices are arranged in a staggered manner, leading to an overlap (0.46 d) and a gap (0.54 d) region. The overlap region has more triple helices across the section, and the gap region has less. Images a, b and c are adapted from (Sherman *et al*, 2015). (d) Schematic of collagen fibril showing the banding, in which each gap and overlap has a periodicity that is the cause of the visible banding in collagen fibrils. The side view, cross-section, show the collagen fibrils is composed of many parallel microfibrils, about 50 microfibrils. (e) Topographical image obtained by atomic force microscopy (AFM) shows hydrated collagen fibrils of a corneal stroma of an adult pig. This image was acquired by the author. The D-period of the fibrils is approximately 67 nm, and the diameter is approximately 46 nm. The black scale bar is 100 nm. The gap and overlap are denoted by "G" and "O" respectively.

2.4.2. Proteoglycans

The extracellular matrix (ECM) of the cornea is a complex composite of many protein families and other molecules. This complex acts for defining structural integrity and various physiological functions of the cornea. The main function of the ECM is to provide the cornea with the necessary mechanical and biochemical properties to refract and transmit light to the other components of the eye. The orientation and spacing of the collagen fibrils in the corneal stroma are regulated by their non-covalent binding to another dominant component of the ECM, the proteoglycans (Meek and Fullwood, 2001). The stromal ECM comprises of structural proteins (collagen fibrils), proteoglycans, growth factors, and matricellular proteins (non-fibular collagen fibrils). The ECM components are mainly secreted by mesenchymal cells called keratocytes, which are embedded in the collagenous matrix of the stroma (Figure 2.3) and renewed very slowly under physiological conditions. These cells abundantly secrete collagen type I and proteoglycans, which are responsible for transparency and strength of the cornea (Massoudi *et al*, 2016; Michelacci, 2003).

Proteoglycans are molecules that interact with collagen fibrils and play an important role in controlling the size and arrangement of collagen fibrils, which allows for the dynamic control of collagen fibril architecture in the cornea (Parfitt *et al*, 2010). They are tiny, interstitial, and consist of glycosaminoglycans (GAGs) attached to a small leucine-rich protein core, Figure 2.8. GAGs are unbranched chain of polysaccharides made up of repeats of sulphated disaccharide units. In corneas, there are three types of GAG chains, chondroitin sulphate/dermatan sulphate, heparin sulfate (HS) and keratan sulphate (KS), the latter being predominantly found in the corneal stroma of adult mammals (Hassell and Birk, 2010; Ho *et al*, 2014; Massoudi *et al*, 2016; Quantock *et al*, 2010). Consequently, proteoglycans are classified according to their GAG chain composition into chondroitin/dermatan sulfate, keratan sulfate and heparan sulfate macromolecules. The latter is a minor component in the cornea and is primarily synthesised by the epithelial cells (Massoudi *et al*, 2016; Tanihara *et al*, 2002).

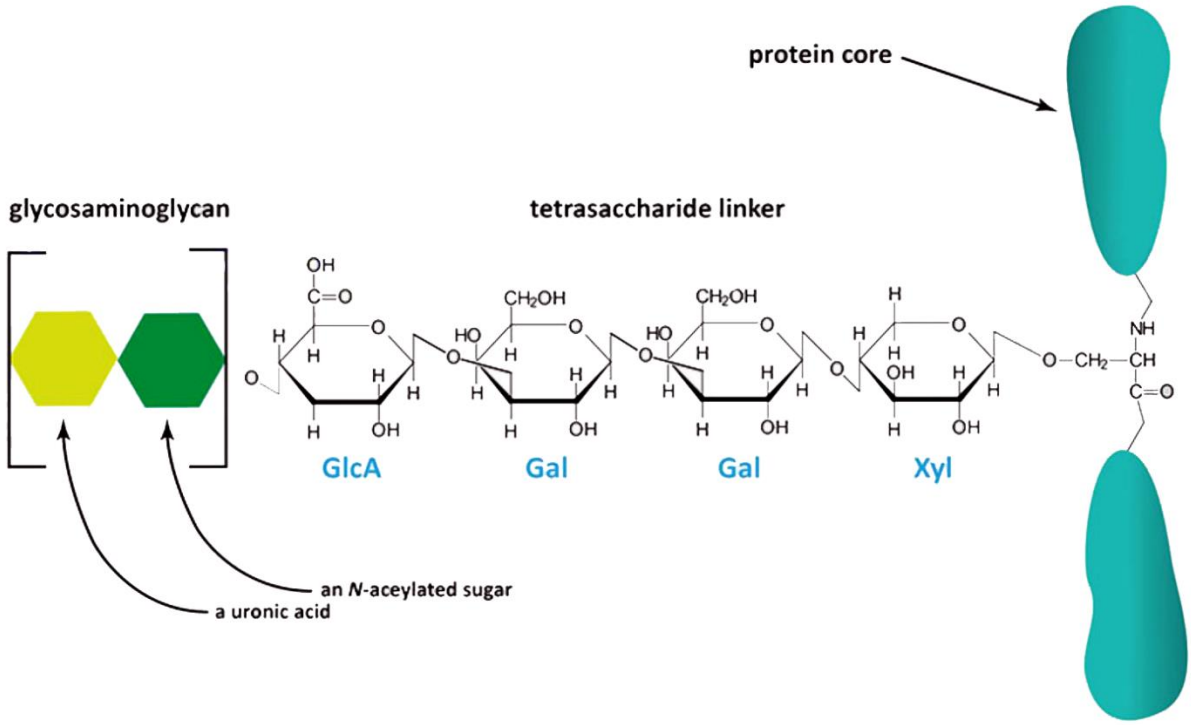

Figure 2.8: Structure of the GAG linkage to protein in proteoglycans. The majority of GAGs linked to protein to form a proteoglycan are attached via a tetrasaccharide (sugar) linker that consist of GlcA-Gal-Gal-Xyl-Ser residue in the protein core. This is true for most, but not all, heparin, heparan sulfate, chondroitin sulfate, and dermatan sulfate polymers that attached to proteins in proteoglycans.

Four of the small leucine-rich protein proteoglycans (SLRP) are predominantly found in the corneal stroma; decorin, lumican, keratocan and mimecan. Any genetic defection of SLRPs causes disruption of collagen fibre organisation and then impairs vision. For example, defection in keratoconus is associated with cornea plana, which is a congenital, bilateral and asymmetrical defect, in which corneal curvature decreases and that leads to a decrease in the refractive index.

Proteoglycans interact with collagen fibrils at specific sites. Keratan sulphate proteoglycans interact with collagen fibrils at the overlap regions, while dermatan sulphate proteoglycans interact with collagen fibrils at the gap regions (Meek *et al*, 1986; Scott and Haigh, 1985). Keratan sulphate proteoglycanases are responsible for the regulation of both collagen fibril diameter and inter-fibrillar spacing, therefore, they play an important role in maintaining corneal transparency (Michelacci, 2003; Parfitt *et al*, 2010). Experimental evidence for this was reported in a study that showed that the level of keratan sulfate increased in chick corneas during the development process of corneal (Cornuet *et al*, 1994). Another study stated that keratan sulphate (accompanied by changes in chondroitin sulphate and dermatan sulphate) in opaque corneal scar tissue is absent (Sawaguchi *et al*, 1991), and highlighted the importance of keratan sulphate proteoglycans in the maintenance of corneal transparency of in mice bred with a lumican null mutation. It is also worth

stating that dermatan sulfate proteoglycans participate with keratan sulfate in controlling of inter-fibrillar spacing and provide the adhesion properties between lamellae of corneal stroma (Michelacci, 2003).

2.5. Corneal transparency

Corneal transparency is an essential property of the ocular system and clear vision. Over the decades, various theories for corneal transparency have been proposed; one of the most basic theories, which was proposed by Leber in 1903, made efforts to elucidate the minimal light scatter in the cornea in terms of a uniform refractive index of all of the corneal components. Afterwards, other studies refuted this theory and asserted that corneal collagen fibrils have a higher refractive index than the surrounding matrix (Leonard and Meek, 1997; McCally and Farrell, 1982) and its value varies from anterior surface of the cornea toward the posterior surface (Meek *et al*, 2003; Patel *et al*, 1995).

Many theoretical and experimental studies were employed to understand and explain corneal transparency and light transmission through the cornea. It was proposed that corneal transparency may be due to the presence of very thin fibres organised in a regular arrangement. Later in 1957, this theory was numerically proven and helped in calculation of the scattered light from individual fibril (Maurice, 1957). This calculation was based on the assumption that fibrils are organised in a lattice arrangement across the stroma and this arrangement acts as diffraction grating. Maurice (1957) claimed that destructive interference occurs in all directions due to the regular arrangement of the very thin collagen fibrils in the cornea. This regular and uni-formal arrangement results in a destructive interference of the light scattered by individual fibril as long as the collagen fibrils spacing is less than the wavelength of visible light. In that way, the cornea would be transparent and passes the light to the posterior parts of the eye.

Later on, the lattice theory of transparency was assessed by Goldman and Benedek (1967) to elucidate the transparency of the dogfish cornea. They reported that the theory failed to explain the transparency of the dogfish cornea because the cornea consists of thick Bowman's layer that occupied 15% of CCT and comprises of non-parallel fibres but with no lattice arrangement. According to lattice theory, the cornea will scatter the light more at the central zone than the peripheral zone, and that contradicts the nature of the dogfish cornea. The researchers concluded that a lattice arrangement of collagen fibrils was not the main role for corneal transparency and that the transparency of Bowman's layer was because of the uniformity of collagen fibrils diameters

and the spacing between the fibrils that measures approximately half the wavelength of visible light. In 1969, Hart and Farrell mathematically demonstrated that corneal transparency is not largely dependent on regularity and uniformity of collagen fibrils spacing as had originally been thought. They suggested instead that only a short-range order of collagen fibrils was essential for corneal transparency.

Collagen fibril diameter is another important element that play an important role in corneal transparency, in addition to uniformity of collagen fibrils spacing. In corneas, collagen fibril diameters are less than the wavelength of visible light (Boote *et al*, 2003). It was found that during the early stages of development that the sclera and cornea are translucent tissues and showing constituently similar collagen fibril diameters. Subsequently in development, the diameter of scleral collagen fibrils increases making the tissue opaque. Whereas, the cornea keeps its transparency after the development, and that is attributed to the uniform diameter of collagen fibrils that are smaller than the wavelength of visible light (Farrell *et al*, 1973). However, it was found that collagen fibril diameter is mainly constant across the central 6 mm of human stroma, and it is slightly increasing in the peripheral region toward the limbus and sclera (Boote *et al*, 2011). That could explain why Doutch *et al* (2007) reported that central cornea is more transparent than the peripheral region. It also was found the cornea appears partially or totally opaque because collagen fibrils diameters become larger and highly irregular in size than those in the healthy cornea. For example, the congenital disease scleracornea, in which the cornea looks like sclera, has larger collagen fibril diameters than in the healthy corneas (Kenyon, 1975).

One of abnormal factors that influence corneal transparency is tissue swelling. Meek and his colleagues (2003) used the direct summation of transmitted fields with electron micrographs and X-ray diffraction as a method for explaining the effect of corneal swollen on its transparency. They showed that the normal order of fibrillar arrangement of the cornea was affected when the tissue becomes swollen. This disordered fibrillar arrangement causes the formation of lakes or small water-filled gaps in the tissue that increase light scattering and decrease corneal transparency. It worth to mention that their measurements were dependent on corneal thickness. It is well known that the thickness of a material is important parameter in calculation of its transparency, which is translated from Beer-Lambert law. On this basis, minimal scattering for the transmitted light may take place at Bowman's layer since it is a very thin layer in human corneas (17.7 ± 1.6 μm thick), and contains disordered collagen fibrils that are very small in diameter, and scatter light independently of one another (Freund *et al*, 1995).

The cellular components of the cornea, keratocytes, and their organisation contribute partially in its overall transparency. These very thin (approximately 0.6 μm) and flat fibroblast cells are embedded in high density between the anterior lamellae of the corneal stroma, and low density in the posterior stroma. The visible light can pass through these cells because their cytoplasm is transparent (Jester, 2008). Though, the nuclei in these cells are not transparent for visible light, regardless their size, and are responsible for the small amount of scattering existent in the healthy cornea (Jester, 2008; Møller-Pedersen, 2004; Møller-Pedersen *et al*, 1998). It has been suggested that the development of corneal haze (decreased in the corneal transparency) following phototherapeutic keratoplasty is mostly occurred because of an increased cellular backscatter from the keratocytes existent in the corneal stroma (Møller-Pedersen, 2004; Møller-Pedersen *et al*, 1998).

There are some other factors which also play a minor role in the transparency of the cornea such as absence of any blood vessels in the cornea and the smoothness of epithelium layer. In healthy cornea, the blood vessels arise from the ciliary arteries, then subsequently divide and terminate in the pericorneal plexus of the limbus. In abnormal cases like injuries and neovascularisation of the central cornea, blood vessels may be temporarily elongated to the cornea and that attenuates the transmitted light and decreases the visual acuity (Jirsova, 2017). The smoothness of epithelium layer is maintained by the tear film that coats its surface. The tear film also helps remove any small particles or dust and maintains a stable refractive index of the air-epithelium interface.

2.6. Corneal hydration and stromal swelling

Tissue hydration can be defined as the process of combining a substance chemically with water molecules. It can be calculated by dividing the weight of water to the dry weight of the tissue. Corneal hydration is an important factor in the development and improvement of ophthalmic technologies. Corneal hydration at the normal physiological condition is approximately 3.2 (Hodson *et al*, 1991). Increased hydration in the cornea causes corneal swelling and this affects its transparency and biomechanical characteristics. Dehydration of the cornea also affects its mechanical properties and then subsequently decreases optical quality (Meek and Knupp, 2015). Thus, the corneal hydration is a factor that needs to be considered in *ex vivo* measurements by a means of variety of fluids such as Optisol, which is a corneal storage medium, and Phosphate Buffer Saline solution (PBS) (Dias and Ziebarth, 2015; Hatami-Marbini and Etebu, 2013).

The stroma is the main layer that is affected by hydration. Stromal swelling is associated with many corneal disorders, and often occurs due to structural defects in the Descemet's membrane and the

endothelium such as Fuchs' corneal dystrophy. Fuchs' corneal dystrophy is a disease that usually affects both eyes in adult corneas and causes a gradual impairment in vision due to corneal swelling, stromal oedema, in which the endothelium undergoes degenerative changes (Eghrari and Gottsch, 2014). In the normal physiological condition, the stromal hydration is mainly regulated by the barrier function of the epithelium and endothelium, the endothelial water pumping mechanism and the swelling pressure exerted by GAGs. The endothelium prevents the excessive flow of fluid into the stroma from the aqueous humour, and regulates water quantity by a pumping mechanism that balances the swelling pressure of the stroma. Whilst, the outermost layer, epithelium, acts only as a barrier against the excessive flow of fluid into the stroma from the tear fluid. The active pumping mechanism involves transporting of hydrogencarbonate ions ($HCO3^-$) out of the stroma toward the aqueous humour. This active transport generates an osmotic gradient that passively moves water from the stroma to the aqueous humour (Hodson, 1997; Meek and Knupp, 2015). If any physiological malfunction takes place in the mechanism of the endothelium layer, the cornea swells due to the movement of water into the stroma and thus decreases corneal transparency (Clark, 2004; Koudouna *et al*, 2018; Meek and Knupp, 2015).

The cornea tends to imbibe water *in vitro* conditions and gradually swells because not only the epithelium and endothelium surrender for being barriers but also the existence of poly-anionic proteoglycans in the stromal ECM (Aakre and Doughty, 1997). These negative charge proteoglycans attract and bind ions; thus, water molecules are prompted to move into the cornea, which causes swelling (Klyce and Beuerman, 1988; Meek and Knupp, 2015). It was claimed that the cornea expands only in the direction of its thickness with a linear relationship between corneal thickness and corneal hydration (Hedbys, 1962; Hedbys and Mishima, 1966). They demonstrated that the structure of the corneal stroma, which is composed of parallel lamellae to the plane of the cornea, is the reason why the cornea swells in one direction. However, Meek and Knupp (2015) illustrated that water in swollen corneas (hydration$\leq$1) is distributed both within and between the collagen fibrils. They also added, if the hydration is become more than 1, collagen fibrils themselves swell very little and the rest of the water spreads into the interfibrillar spaces.

The distribution of water across the cornea is mainly depends on two factors; firstly, the changes in proteoglycans composition and concentration throughout the thickness of the tissue. It was found that the anterior stroma is more restricted to swelling than the posterior stroma (Meek and Boote, 2004; Müller *et al*, 2001). That is mainly attributed to the higher ratio of keratan sulphate to dermatan sulphate in the posterior stroma, where it was found the keratan sulphate proteoglycans

have a larger water absorptive capacity than dermatan sulphate proteoglycans. This difference causes for the positive gradient of water between the endothelium and epithelium toward the stroma (Castoro *et al*, 1988). Secondly, the structural differences of the anterior and posterior stroma, explained in next sections, contribute to the distribution of water across the cornea. It was reported that the interwoven structure of lamellae in the anterior stroma limits the ability of the anterior stroma to swell, while the posterior stroma is not interwoven and highly oriented. Therefore, the posterior stroma swells more than the anterior stroma (Meek and Boote, 2004; Müller *et al*, 2001).

2.7. Corneal shape maintenance

The biomechanical properties of the cornea play a very important role in its shape and corneal characteristics including transparency that is still not totally understood. The healthy cornea normally maintains its geometrical properties for clear vision. Once these properties get affected, changes in the optical features of the cornea will occur and consequently impairs the vision (Meek, 2009). It has been experimentally proven that the epithelium (Elsheikh *et al*, 2008) and the endothelium (Joyce, 2003) have a minor contribution on the whole stiffness of the cornea. However, these two layers have major contribution on corneal hydration, as explained earlier. Decrement's membrane is a relatively strong layer itself (Thomasy *et al*, 2014), but its mechanical influence on corneal stiffness can be neglected due to its structural organisation that means it does not come under tension until the stroma is intensely extended (Jue and Maurice, 1986). Therefore, it widely agreed that biomechanical properties of the cornea are mainly determined by the stromal layer that can be influenced by many factors related to the lamellae structure and proteoglycans components (Maurice, 1999; Meek, 2009). Some of these factors are summarised in the following sub-sections.

2.7.1. Lamination of the lamellae

Interlacing and cross-angle distribution of collagen lamellae in the anterior and posterior stroma plays a role in maintaining the shape of the cornea. It was found that lamellae in human corneal stroma interweave in angles with adjacent lamellae. Interweaving of lamellae is high within the anterior stroma and it is absent in the posterior stroma (Meek, 2009; Radner *et al*, 1998). However, some mammalian corneas exhibit a different lamellar organisation of collagen bundles, in which the orthogonal or the interwoven organisation is lost and replaced with a random lamellar pattern of collagen bundles. It was suggested therefore, these structural changes be responsible for a more uniform distribution of stresses and strains within the stroma and thus facilitate the self-stabilising

stromal structure, which maintain corneal shape (Boote *et al*, 2005; Koudouna *et al*, 2018; Winkler *et al*, 2015). Winkler *et al*, (2015) compared the collagenous structure of corneas in vertebrates by utilising a second-harmonic-generation (SHG) nonlinear optical high-resolution microscope (HRMac) to three-dimensionally (3-D) reconstruct the collagen organisation at submicron resolution. They found that corneal collagen in all non-mammalian vertebrates was organised either into sheets or ribbons extending from limbus to limbus that were oriented nearly orthogonal to their neighbours. Importantly, they also found mammalian corneas showed a different fibril structural organisation, in particular fibre bundles in human corneas often traversed many planes, especially in the anterior cornea, which was markedly more interwoven than in posterior cornea that appeared more aligned, Figure 2.9. Another study also found that structural differences in terms of collagen fibrils orientation are highly isotropic within anterior stroma while it is a more orthotropic microstructure in the posterior stroma (Benoit *et al*, 2016).

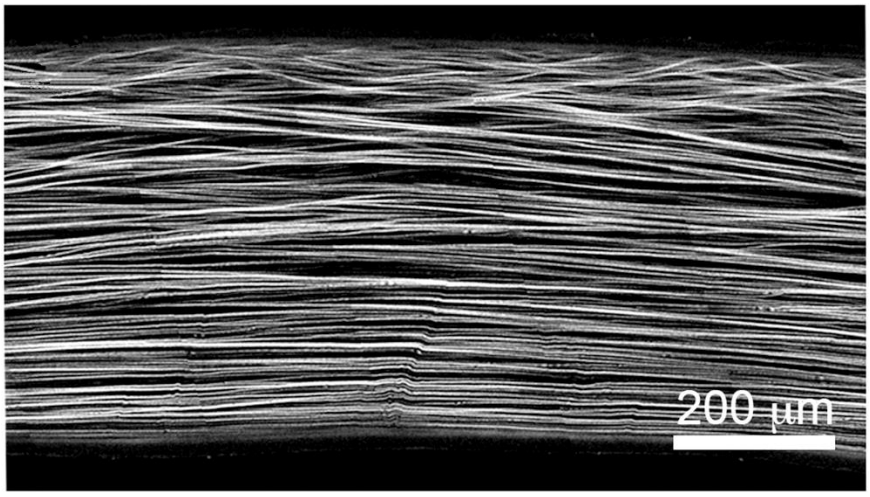

Figure 2.9: A Cross-sectional HRMac view in the human cornea showing the interweaving of collagen bundles. The bundles in the anterior cornea (top of the image) seems highly interconnected and transverse fibres than in the posterior stroma (bottom of the image). Adapted from (Winkler *et al*, 2015).

2.7.2. Lamellar cohesive strength

The anterior stroma is more resistant to tear (cohesive strength) than the posterior and the middle stroma. That could be attributed to the significant interweaving of stromal lamellae in the anterior cornea, which is absent in the posterior stroma and the middle stroma (Maurice and Monroe, 1990; Müller *et al*, 2001; Smolek, 1993). In human corneas, the cohesive strength increases with age, and differs in the horizontal meridian than the vertical meridian. The cohesive strength is greater in the peripheral cornea than at central cornea, and is lower in the inferior-peripheral cornea than in other corneal quadrants (Randleman *et al*, 2008; Wollensak *et al*, 2011). It was suggested therefore, these regional differences in cohesive strength provide a biomechanical equilibrium of the cornea and thus maintain corneal shape (Gatzioufas and Seitz, 2014).

2.7.3. Collagen fibril orientation

Collagen fibril orientation and distribution at different depths are populated equally in both directions at the central cornea, and this can support corneal elasticity along both meridians in order to withstand IOP. Meek *et al* (1987) used synchrotron X-ray diffraction to study the unique organisation of collagen fibrils in the bovine corneal stroma and found that the collagen fibrils in the stroma arrange in two preferred orientations: medial-lateral and inferior-superior. They found that arrangement of collagen fibrils was more obvious in the posterior than in the anterior stroma (Meek *et al*, 1987). In terms of the collagen fibril density, studies found that the density increases from the centre towards the periphery in human corneas (Boote *et al*, 2003; Newton and Meek, 1998). The organisation of collagen fibrils in human corneas was investigated and mapped by the use of the synchrotron x-ray scattering method (Aghamohammadzadeh *et al*, 2004; Boote *et al*, 2005). Another informative study investigated the organisation of collagen fibrils in the corneas of primates and other mammals, revealed that a predominantly circumferential arrangement of collagen fibrils was seen in corneas of rabbits, mice and pigs (Hayes *et al*, 2007). These studies supported the previous findings revealed by Meek *et al* and suggested that the detailed ultrastructural information including collagen fibrils orientation provide an important understanding for corneal shape and mechanical properties.

2.7.4. Swelling pressure

The osmotic effect, which is generated due to the Gibbs-Donnan effect, creates swelling pressure. The Gibbs-Donnan effect describes the unequal distribution of permeant charged ions on either side of the Descement's membrane (a semipermeable membrane), which occurs in the presence of impermeant charged ions. The swelling pressure is produced in the stroma from the mutual repulsion of stromal ECM fixed charges at physiologic hydration that result from the presence of collagen, salts and proteoglycans. Particularly, GAGs are able to absorb large amounts of water and thus contribute to regulate the hydration state of the cornea. They provide a swelling pressure of 50 mmHg, in human corneas, which counteracts against the pump function of the endothelium. Therefore, the swelling pressure can be defined as the equilibrium pressure required to prevent the corneal stroma from swelling, when immersed in an aqueous medium (Hedbys and Mishima, 1962). Since the tendency of the cornea to swell is quantified by its swelling pressure, maintaining the shape, thickness and transparency of the cornea is mainly achieved by balancing the IOP with swelling pressure (Hodson, 1997; Meek and Knupp, 2015).

The swelling pressure of the stroma is usually reported as functions of corneal thickness and hydration. Hatami-Marbini *et al* (2013) studied swelling pressure–thickness, swelling pressure–hydration and hydration–thickness relations of porcine corneas immersed in a saline solution. They found that an average swelling pressure of 52±13 mmHg in porcine corneas, which is very similar to swelling pressure in human corneas. They also found that the swelling pressure-thickness relation experimentally follows a hyperbolic Gibbs-Donnan equation, showed the swelling pressure–hydration can be represented by a negative power equation. In addition, in their analysis the thickness–hydration behaviour of the porcine cornea was represented by an exponential equation, and the behaviour was greatly similar to that of the human cornea.

2.7.5. Internal pressure

The IOP applies a tension on the layers of the cornea. This tension is not totally equal in all directions due to aspherical design of the eye, difference in the curvature between the cornea and the sclera, and unequal thickness of the layers of the eye. Therefore, IOP is a very important factor in maintaining corneal shape, as well as its contribution in balancing the swelling pressure and therefore the transparency. In terms of corneal shape at the macro-level, Asejczyk-Widlicka and Pierscionek (2008) utilised digital cameras to measure the corneal and scleral curvatures of porcine eyes in response to five consecutive incremental 100 ml saline intravitreal injections that were used to change the IOP. They found that IOP increase slightly affects corneal curvature, and the elastic modulus of the cornea is independent on IOP. In terms of organisation of the lamellae with IOP, Benoit *et al* (2016) combined nonlinear optical microscopy and mechanical testing to investigate the microstructure of a human corneal stroma in response to increased IOP. The study found that the stroma microstructure appeared to be modified by increased IOP, in which the lamellae gradually slid and slightly rotated relative to each other towards balancing the proportions of lamellae oriented along the two preferential orientations.

2.8. Overview of anterior segment imaging techniques

Assessment of anterior segment structures is an essential step for diagnosing and treating a wide variety of ocular diseases. Imaging of the anterior segment has ordinarily been performed with slit lamp biomicroscopy, which allows for detailed anterior and posterior segment assessment of the eye at the micro and macro-level. A number of imaging techniques that can image corneal topography and tomography will be summarised in this section; ultrasound pachymeter and optical coherence tomography (OCT) imaging techniques have been used in the work presented in thesis.

2.8.1. Slit lamp biomicroscopy

The most common instrument utilised in eye examinations to assess the cornea is the slit lamp biomicroscopy, which has been used since beginning of the 20th century. It consists of two arms, the observational arm and the illumination arm, which can rotate independently around a common axis. The observational arm consists of an adjustable magnification microscope which allows the direct visualization of the cornea. Currently, the observational arm is a joystick-controlled, and includes a high-resolution digital camera for saving patients' ocular images. The other, the illumination arm is equipped with a light source, in which the incident light is centred on the focal plane of the microscope. The incident light beam can be tilted, broadened, dimmed or filtered to a specific wavelength for obtaining high quality images of the eye. One of the applications of this routine device in eye care consulting is to view Fleischer rings in keratoconus, which are pigmented rings in the peripheral cornea that resulting from iron deposition of basal epithelial cells (Martin, 2018).

2.8.2. Scheimpflug camera

A further development in the geometry of the slit lamp biomicroscopy has been carried out to utilise cameras in Scheimpflug's principle that aims to improve the depth of focus. In a slit-lamp camera system, the object and image plane, charge-coupled device camera chip (CCD camera), are parallel to the lens plane, which makes the plane of focus parallel to the assembly. If this alignment is altered, it will be in focus only along a line where it intersects the plane of focus, and that is what is called Scheimpflug's principle. Figure 2.10 shows a brief explanation of Scheimpflug's principle. In a Scheimpflug camera the slit beam, lens, and camera sensor intersect in a line where a controlled depth tomographical image of the eye appears in focus. Topographical images with localised thickness of the cornea can also be obtained by the Scheimpflug camera, which makes such a device very helpful for ophthalmologists and optometrists to diagnose certain corneal diseases including keratoconus (Faria-Correia and de Oftalmologia, 2016). However, the obtained topographical and tomographical images are affected by two kinds of distortion. Firstly, geometrical distortions take place due to the tilt in the image plane, CCD camera chip, in which the image appears in trapezoidal dimensions instead of real rectangular dimensions. Secondly, optical distortion arises as posterior optical surfaces are viewed through preceding refractive surfaces (Rosales and Marcos, 2009). Numerous efforts have been made to correct these distortions by improving correction algorithms and enhancing the design of the device (Li *et al*, 2015; Sun *et al*, 2018).

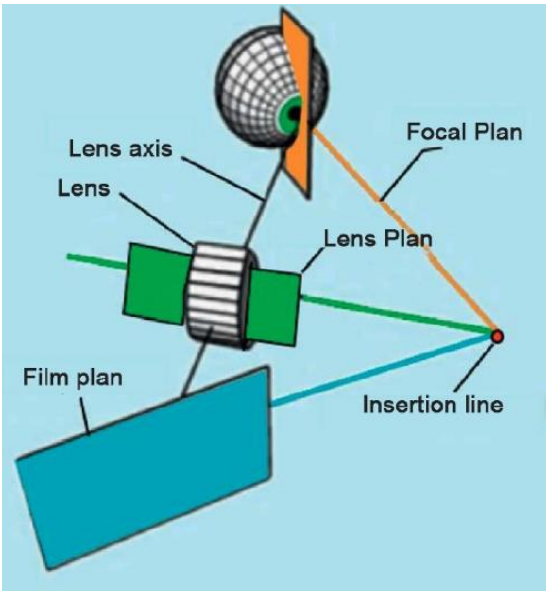

Figure 2.10: Scheme of the Scheimpflug principle. The film plane, the lens plane and the focal plane - are arranged in a non-parallel way and meet at a point. Adapted from (Faria-Correia and Ambrósio Jr, 2016).

Scheimpflug camera was utilised as dynamic scanning instrument for many applications including measuring mechanical properties of the cornea *in vivo* and *ex vivo* conditions. For example, Hon and Lam (2013) determined the intra-examiner repeatability and intersession reproducibility of corneal deformation of adult humans (Hon and Lam, 2013). Lombardo *et al* (2014) analysed the viscoelastic properties of inflated human corneas in *ex vivo* conditions (Lombardo *et al*, 2014). However, these studies would provide more qualitative results if a sophisticated device, such as the optical coherence tomography (OCT), was used for dynamic screening of the corneal deformation.

2.8.3. Optical coherence tomography

Tomographic techniques generate a set of sliced images, cross-sections, of objects and are very important in medicine due to the crucial advantage of non-invasive scanning into the living body. Since the beginning of OCT in the 1990s, it has become an essential *in vivo*, non-invasive, high resolution, imaging instrument in ophthalmology especially in the assessment of the retina and the anterior segment components. Anterior segment OCT help ophthalmologists in diagnosis and documentation of corneal disorders such as dystrophies and degenerations, as well as various inflammatory and non-inflammatory pathologies (Ramos *et al*, 2009).

OCT basically consists of a light source that generates near infrared light waves that are directed onto the samples and the reflected echo time delay of light are then recorded. The working

principle of OCT is based on the design of interferometry, which is composed of two arms; reference arm and sample arm. Figure 2.11 demonstrates a typical schematic diagram of an OCT. In interferometers, the light beam is separated in two arms by a beam splitter. The light in the reference arm is focused on a reference mirror, while the other focused on the sample. Typically, OCT utilises a low coherent light source and the sample is scanned in two directions for generating a two-dimensional image (2D image): in depth and laterally. The depth scan (A-scan) either is carried out by utilising a moveable reference mirror, time domain OCT (TD-OCT), or by employing a light source with wider bandwidth and analysing the interference signal, Fourier domain OCT (FD-OCT). The lateral scan is mostly performed by steering the object beam across the sample. In TD-OCT setup, the reference mirror should move for each depth scan, pixel by pixel, as a result of that image acquisition speed is relatively limited. In contrast, FD-OCT has a stationary reference mirror and employs a Fourier transformation algorithm of the spectral interferogram to measure the depth information, thereby faster acquisition and better image quality is obtained (Fercher, 2010; Hamdan *et al*, 2012).

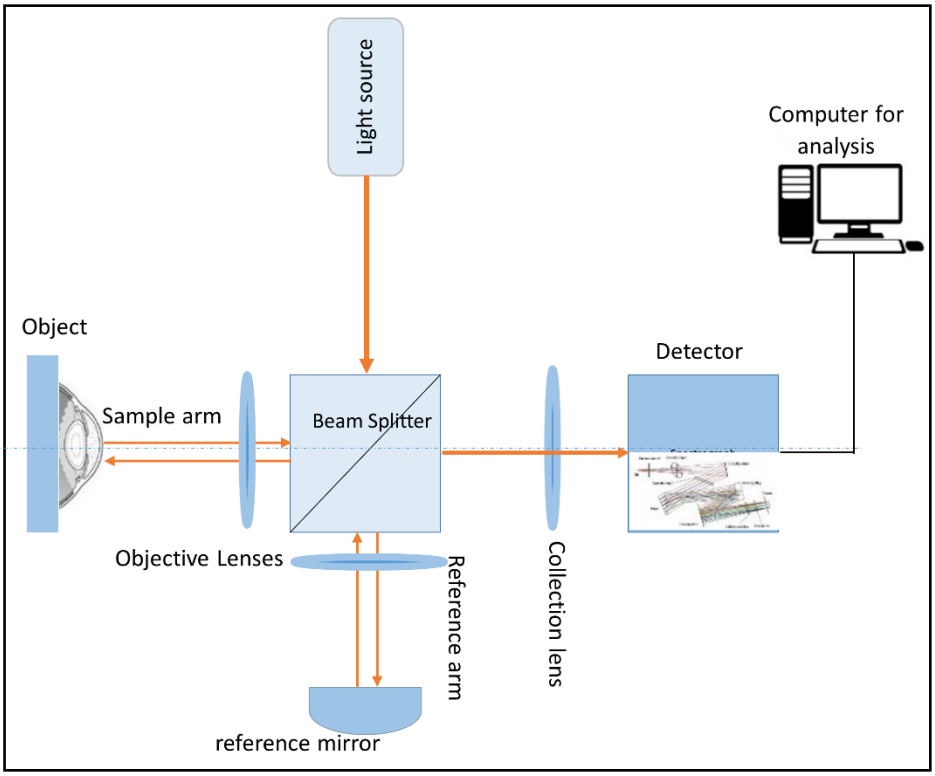

Figure 2.11: A basic setup of OCT. Reference mirror is moving in time domain OCT, and it is stationary in spectral domain OCT. Objective lenses are basically used for obtaining optimal focusing on the mirror and the sample. Collection lens focuses the beam on the detector.

There are different approaches to OCT, all developed the basic technique. The OCT variants arise from the fact that there are several methods to achieve depth ranging such as TD-OCT, Swept Source OCT (SS-OCT) and Spectral Domain OCT (SD-OCT). In addition, OCT variants come from several methods to get lateral information such as scanning point OCT (SP-OCT), line field OCT (LF-OCT) and full field OCT (FF-OCT). Moreover, OCT variants are also generated from a number of functionalities that the OCT can be built in, including, polarisation sensitivity OCT (PS-OCT), OCT angiography, and optical coherence elastography (OCE). Furthermore, OCT variants are also come from physical structure of interferometer, for example, fibre Michelson, free space Michelson, Linnik, fibre common path and Mach-Zander (Leitgeb, 2019; Gabriele *et al*, 2011). These different variants can be put together in a multitude of combinations for specific purpose. LF-OCT is among the more recent developments that is utilised for the experiments presented in this study, Chapter 4. Figure 2.12 demonstrates the relationship between the main variants of the original OCT approach.

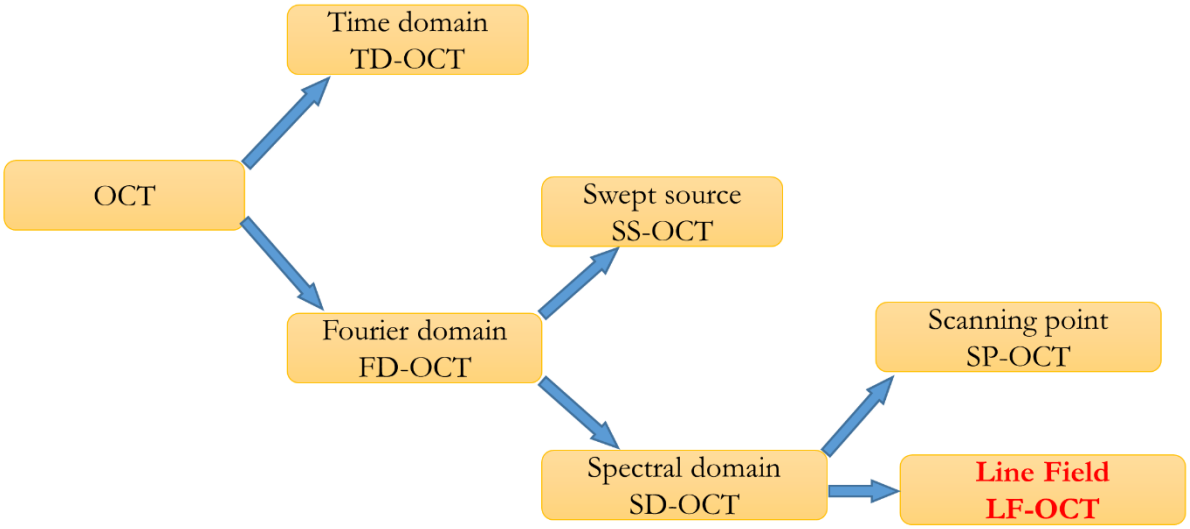

Figure 2.12: The main variants of the OCT imaging technique. LF-OCT is the recent development in SP-OCTs subgroup.

The main development in the LF-OCT approach is the ability to measures all the lateral positions in cross-sectional image simultaneously (Lawman *et al*, 2016). In most modern OCTs, each lateral position is captured at a time. The common SS-OCT implementation uses a very fast single point detector to measure the interference signal, and a limited optical bandwidth swept source. This implementation does give advantages in terms of image depth, speed and signal to noise ratio (SNR) but the optical bandwidth range limitation of swept source means low depth resolution. SP-

OCT approach uses a single channel input spectrometer such as a photodiode array or a charged couple device (CCD), which captures all the wavelengths from the broadband source that illuminate the sample at the same time. In this approach, a 2-dimension sectional image is built by scanning laterally across the sample (Leitgeb, 2019). The approach in LF-OCT depends on increased parallelisation compared to SP-OCT approach. In LF-OCT approach, a line of illumination is delivered on to the sample and the reflected light is subsequently focused on the controlled entrance of the slit of a multi-channel imaging spectrograph. Fast Fourier transformation uses the spectral information to measure the spectral interferograms of all positions at the same time. This approach allows measuring the illumination of one complete section through the sample resulting in the capture of one complete B-scan image in one acquisition, measures all the lateral positions in cross-sectional image simultaneously. This fast-parallel acquisition of spectral information makes the LF-OCT the main advantage of reducing artefacts caused by motion. The lateral resolution in LF-OCT depends intimately on the quality of the imaging device of the spectrograph. Whereas, the axial resolution depends intrinsically on the optical bandwidth of the light source. Therefore, LF-OCT offers a number of key benefits over current clinically approved instruments, including high data acquisition speeds and the simultaneous acquisition of complete 2D sectional images with high sensitivity and axial depth (Lawman *et al*, 2016).

2.8.4. Ultrasonic imaging

Ultrasonic imaging techniques in medical applications are usually known as diagnostic sonography or ultrasonography. It is widely used technique for *in vivo* imaging of internal body structures due to many advantages such as it is a cost-effective and non-invasive technique, can offer a wide penetration depth and can be companied with specialised surgical tools. However, ultrasonic image quality is relatively less than those obtained by other instruments (Silverman, 2009).

The basic concept of ultrasound imaging techniques goes as follows; a sonographer positions a probe (or a transducer) on the body and initiates scanning, where electrical pulses trigger the transducer to generate ultrasound waves that propagate in the body. The propagated ultrasound waves will be attenuated in the body, where the reflections and back-scattered acoustic waves are received by the same transducer that converts them to electrical pulses. These electrical pulses are then sent to the computer for processing and display. Scanning depth normally depends on the frequency of the acoustic waves that are generated by the transducer (Foster *et al*, 2000). In ophthalmology, ultrasound imaging is used in two modalities; A-scan and B-Scan. A-scan

ultrasound can obtain one-dimensional images that can be used for thickness estimation or knowing object distance from the surface. B-scan can acquire 2D cross-sectional images, which are useful for assessment of many ocular pathologies (Dudea, 2011). A further development on the A-scan modality was performed to produce a medical device, which is called ultrasonic pachymeter (US pachymeter), to measure the thickness of the eye's cornea. A commercial US pachymeter was utilised in this project to measure the thickness of inflated porcine corneas.

2.9. Keratoconus

Keratoconus is the most common ectatic disorder of the cornea. Ectasia refers to a group of conditions that are caused by irregularities in the cornea that lead to loss of vision. It is usually diagnosed between ages 15 and 40, and affects both genders. The estimated prevalence in the general population is 54 per 100,000 individuals worldwide. It affects all ethnicities, however, some specific ethnic groups are more at risk, such as East Asians (Godefrooij *et al*, 2017; Romero-Jiménez *et al*, 2010).

2.9.1. Characteristics of keratoconus

2.9.2. Keratoconus is usually characterised by non-inflammatory, progressive and localised stromal thinning. This corneal degradation leads to protrusion of the thinned cornea into a conical shape, in which the anterior and posterior curvature of the cornea are affected. The corneal protrusion leads to high myopic cornea with irregular astigmatism, decreasing visual quality (Rabinowitz, 1998). The degree of corneal deformation can vary greatly between patients, and mainly depends on the progression of the disease. Therefore, tracking corneal shape changing over time is the most reliable way of identifying keratoconus progression (Volatier *et al*, 2019). Corneal thinning commonly takes place in the inferior and central region of the cornea (Auffarth *et al*, 2000). However, some studies reported the occurrence of keratoconus above the horizontal meridian (Prisant *et al*, 1997; Weed *et al*, 2005). Figure 2.13 shows a sketch for keratoconic and healthy corneas. Keratoconus is usually a bilateral disease, affecting both eyes. However, the disease appears to be unilateral in a few cases, in such cases a further and periodic examination of the other eye reveals some evidence of the disease (Holland *et al*, 1997; Rabinowitz *et al*, 2003). The localised corneal changes in keratoconus may potentially lead to difficulties in accurate determination of IOP in patients because tonometric devices based upon the applanation principle are known to be affected by altered corneal parameters (Liu and Roberts, 2005). Previous studies investigating IOP in keratoconic subjects using applanation tonometric techniques found falsely low IOP values suggesting that errors are result of using applanation tonometry for measuring

corneas with altered biomechanical properties (Browning et al. 2004; Patel and McLaughlin 1999). Read and Collins (2011) used dynamic contour tonometer (DCT), which is a contact contour matching tonometer that measures IOP independently of corneal thickness and biomechanical properties, to investigate IOP measurements in patients with keratoconus. They found that the presence or severity of keratoconus was not correlated with IOP values.

Keratoconus has also been reported as a non-inflammatory disease due to absence of obvious inflammation (Krachmer *et al*, 1984). However, recent studies have found inflammatory factors such as matrix metalloproteinases (MMPs) and interleukins in the tear fluid of patients with clinical and subclinical keratoconus (Kaiserman and Sella, 2019; Galvis *et al*, 2015; Volatier *et al*, 2019). Therefore, further inflammatory factors can worsen the condition and accelerate the need for treatment, such as corneal collagen cross-linking (CXL) (Kaiserman and Sella, 2019; Volatier *et al*, 2019), which is a technique that uses UV light and a photosensitiser to strengthen chemical bonds in the cornea. The CXL technique will be briefly outlined in Section 2.9.9 of this thesis.

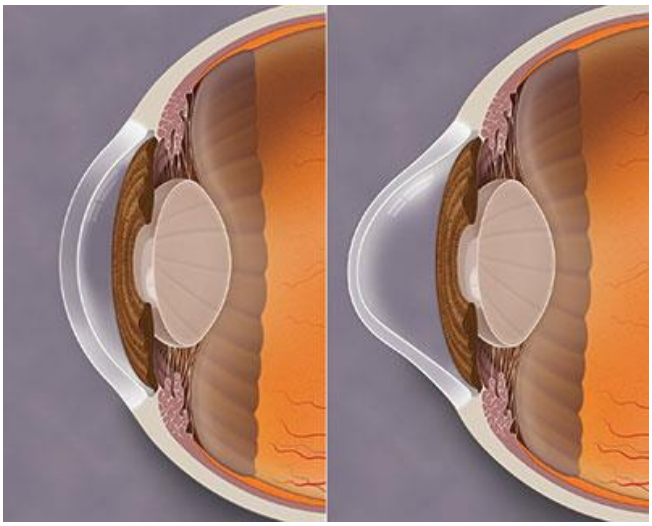

Figure 2.13: A sketch showing keratoconic (right) and healthy (left) corneas (Boyd, 2019).

2.9.3. Clinical features

Diagnosis of keratoconus can be achieved by detecting a number of clinical manifestations that can be used to distinguish keratoconus from other ectatic conditions. Patients with early stages of keratoconus normally complain about mild blurred and distorted vision, in which straight lines look bent or wavy. In addition, the sensitivity to light and glare in such patients is higher than individuals with healthy eyes. These symptoms become more severe in progressed keratoconus (Volatier *et al*, 2019). Clinical manifestations can be detected by physicians that include centrally and paracentrally corneal stroma thinning and irregular astigmatism that causes blurred vision. In addition, thin epithelium layer and proud nebulae, which is a small scar at the apex of the cone

that often causes in some loss of vision. Furthermore, break in Descemet's membrane and visible corneal nerves are also clinical signs of keratoconus (Kaiserman and Sella, 2019; Volatier *et al*, 2019),

2.9.4. Corneal topography

Corneal topography is an important clinical assessment that provides geometrical information of the cornea. The assessment provides measurements of the anterior and posterior corneal surface shapes, corneal tomography (pachymetry), and biometry of the anterior segment. These geometrical information are utilised for calculation of elevation and curvature of the cornea. Hence, topographical assessment an important tool for diagnosis of many corneal diseases including keratoconus. However, the use of this assessment will not actually ease the detection and characterisation of the very early stages of keratoconus and the ability to differentiate it from other conditions (Roberts, 2019). Corneal topographers provide morphological maps of the cornea that includes curvature (sagittal and tangential), elevation, and thickness. The curvature keratometric maps provide information about curvature at each point of the anterior and posterior corneal surfaces. Figure 2.14 demonstrate a quad map of a keratoconic cornea acquired by a commercial system "Orbscan". The elevation map provides the elevation of the corneal apex, the elevation of the minimum thickness point and the elevation of the centre of the central region maps. These measurements are obtained by comparing the reconstruction of the anterior or posterior corneal surface to the best fitted surface, typically a sphere and ellipsoid. Finally, the thickness map, which is not directly measured by the corneal topographer, offers information of the minimum thickness point and its location on the cornea (Cavas-Martínez *et al*, 2017). This map provides the clinicians with an image of corneal structure, by which clinicians can determine the progressive thinning of the cornea when the severity of keratoconus progresses (Emre *et al*, 2007).

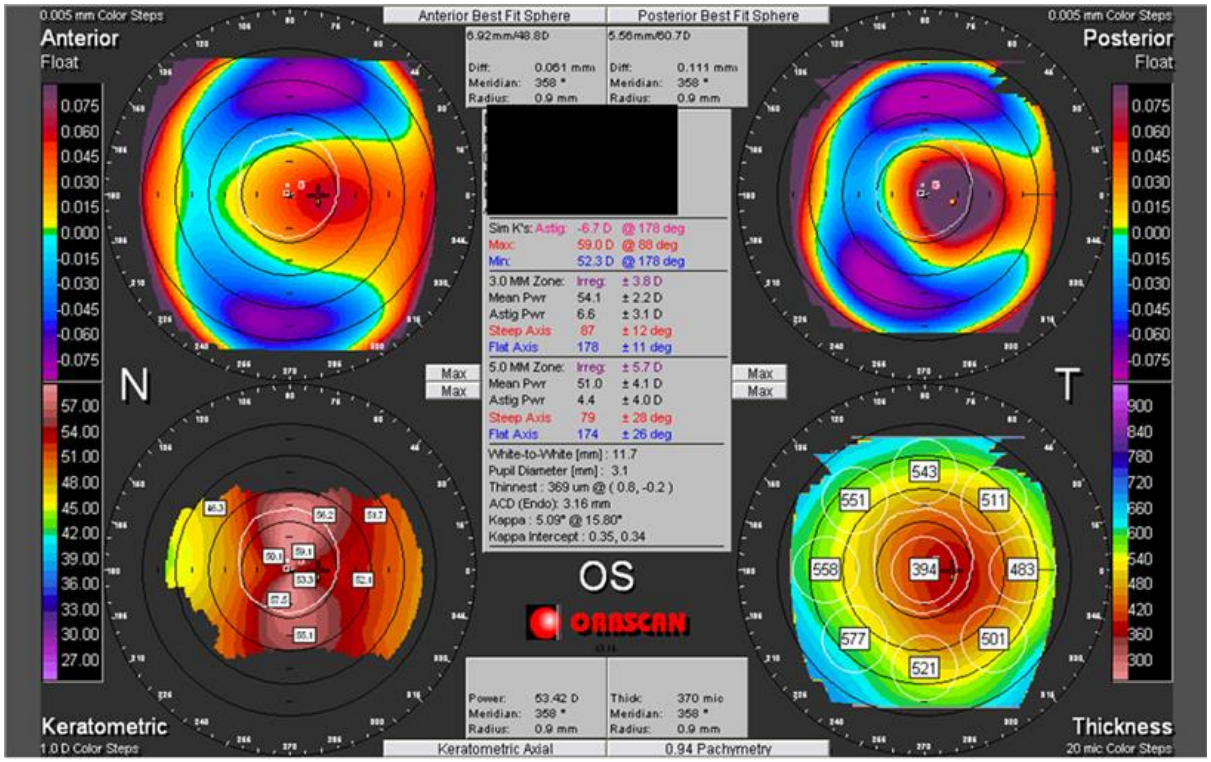

Figure 2.14: Corneal topography of keratoconic cornea. It was acquired by a commercial system "Orbscan". This case had the following clinical signs: Munson's, Vogt's striae, and Fleischer's ring. Adapted from (Prakash *et al*, 2012).

2.9.5. Classification

In the literature, classifications of keratoconus are provided based on morphology, disease evolution, ocular signs and index-based systems.

2.9.4.1. Morphology

Classification of human keratoconic corneas has classically been presented in three major patterns, as shown in Figure 2.15: nipple-like shape, oval-like shape and dome-like shape. Nipple like shape, is when the cone has a diameter less than 5 mm. These corneas can be corrected with contact lenses. Oval-like shape, is when the cone has a diameter of 5 mm that is located more commonly in the inferior temporal corneal quadrant. Correction with contact lenses is more difficult. Keratoglobus, or dome-like shape is when the cornea is large, thin and bulbous. The dome is situated throughout 75% of the cornea. In this case, correction with contact lenses is extremely challenging (Kantzou, 2018).

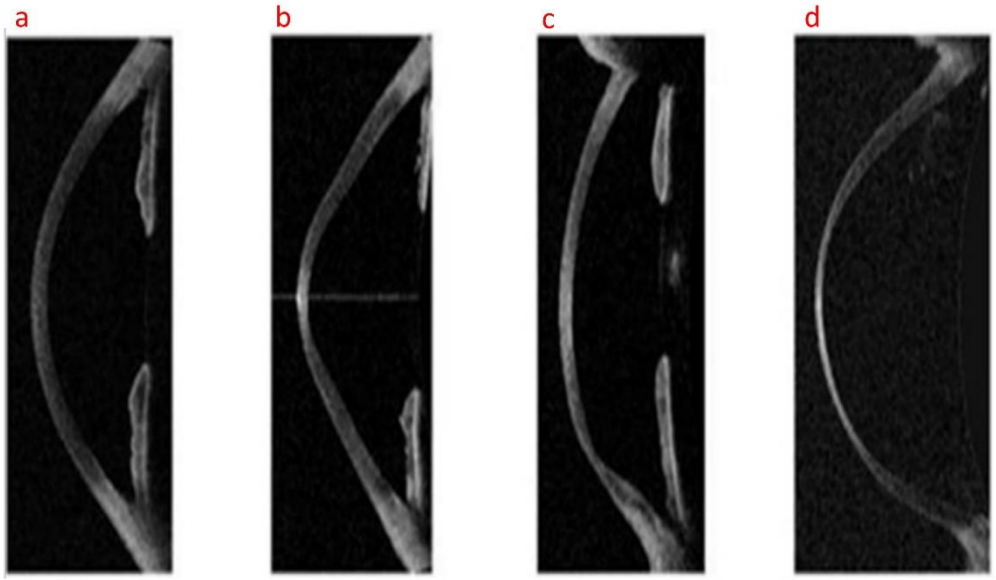

Figure 2.15: Morphological patterns of keratoconus. (a) normal, (b) nipple like shape, (c) oval like shape, and (d) Keratoglobus. Adapted from (Kantzou, 2018).

2.9.4.2. Disease evaluation

Keratoconus is also classified based on disease evolution, in which the disease is classified into four different severity stages. Fruste or subclinical stage that can be corrected with spectacles. Early stage is characterised by mild corneal thinning with no scarring. Moderate keratoconus is characterised by significant corneal thinning and appearance of some clinical features of keratoconus progression. This stage can be corrected by contact lenses and immediate treatment is needed to prevent the progression of the disease to the next severe stage "severe keratoconus stage". The last stage is characterised by severe corneal steepening and scarring, where contact lenses will not be suitable for correction and immediate treatment or surgical intervention is needed to restore the vision (Bao *et al*, 2017; Romero-Jiménez *et al*, 2010). All previous stages of keratoconus may benefit from the biomechanical corneal strengthening providing by CXL (Mazzotta *et al*, 2018) that will be presented in a following section.

2.9.4.3. Corneal thickness

The most significant parameter in keratoconic corneas is the reduction in central corneal thickness (CCT). This reduction is typically due to the thinning of the stroma, which is primarily responsible for most of the biomechanical stability of the cornea. Since the cornea is subjected to internal pressures, the thin corneal portion will bulge out and consequently changes the shape of the cornea. In keratoconus, the thinning of the corneal stroma is characterised as an asymmetrical and highly irregular topography, which is (sometimes) wrongly reported as steep astigmatism (Asimellis and Kaufman, 2019).

It has been a great focus on evaluation of corneal thickness and topography of keratoconus. One of the previous attempts for measuring the central and peripheral corneal thickness of 28 human keratoconic eyes, *in vivo* conditions, using an US pachymeter found that the average CCT for keratoconus corneas was 0.52 mm compared to 0.56 mm for healthy corneas (Gromacki and Barr, 1994). They did not detect any significant difference in peripheral corneal thickness between keratoconus and normal corneas. Although the study provided quantitative measurements, a limitation is that the US pachymeter can only measure average readings of central corneal thickness (Wheeler *et al*, 2012), but cannot identify the thinnest corneal site. Since the first commercial corneal topographer introduced, an accurate evaluation for simultaneous corneal thickness and corneal morphology can be achieved (Yaylali *et al*, 1997), which encouraged scientists to assess keratoconus. Consequently, corneal topography in 71 eyes of 38 patients with keratoconus was evaluated using the Orbscan topography system to analyse with special reference to the central point, the apex (the point with maximum reading on the anterior elevation best-fit sphere map), and the thinnest point of the cornea (TCT) (Auffarth *et al*, 2000). They found that TCT, the apical corneal thickness (ACT), and CCT were 457 μm, 483 μm, and 490 μm, respectively. They also showed that the corneal apex is not necessarily the thinnest point. A study conducted by Gherghel *et al*, (2004) measured CCT and ACT using both Orbscan II and ultrasonic pachymetry in 72 human keratoconic eyes and 71 healthy eyes (Gherghel *et al*, 2003). The study revealed that the pachymetry measurements conducted with the Orbscan II were in good agreement with those obtained using US pachymeter in normal eyes only, but the pachymetry measurements obtained by Orbscan II were significantly lower than those measured by US pachymeter in keratoconic eyes. Furthermore, the study reported ACT in keratoconic eye was 460.8±75.8 μm, regardless the value of IOP.

Corneal thickness has been measured in attempt for grading the severity and the progression of keratoconus. Avitabile and colleagues (2004) classified the stages of 60 eyes with different forms of keratoconus to stages using the Paradigm ultrasound biomicroscope. They found that TCT ranged between 0.278-0.592 mm, and concluded that the evolution of the keratoconus can be classified on the basis of corneal thickness rather than the curvature. Emre and co-workers (2007) evaluated the alteration in anterior chamber parameters, including TCT and anterior chamber volume (ACV), with the progression of keratoconus using the Oculus pentacam Scheimpflug topographer. The study included 216 eyes of 123 human patients diagnosed with keratoconus and were divided into 3 groups according to mean keratometer (K) readings: mild, moderate, and severe. They reported that TCT of control healthy corneas was 532.2±31.9 μm and that the TCT

significantly reduced in mild, moderate, and severe keratoconic corneas by 8.9%, 14.8%, and 29.7%, respectively (Emre *et al*, 2007). It was suggested that the reported values of the stages of keratoconus could be used for mathematical and biomechanical modelling of keratoconus, and thereby improve detection algorithms to provide a better understanding of the disease.

2.9.6. Histopathology

A number of histopathologic features have been found in keratoconus including thinning of the corneal stroma, breaks in Bowman's layer, and deposition of iron in the basal layers of the corneal epithelium. Figure 2.16 demonstrates microscopic images of classical histopathologic features found in keratoconic human corneas (Rabinowitz, 1998).

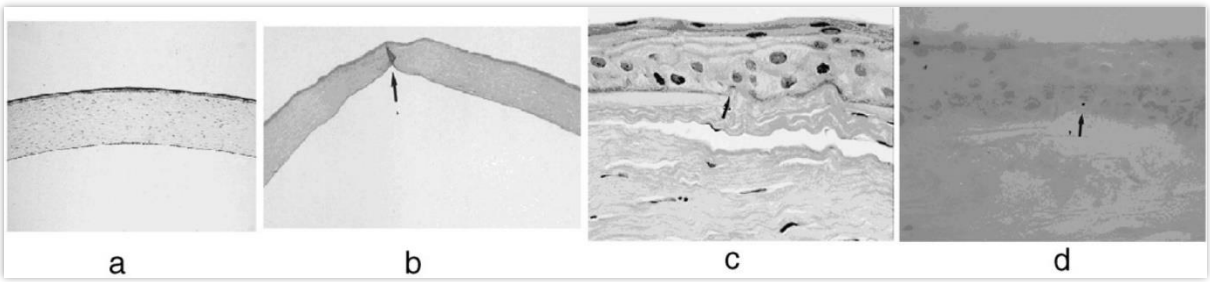

Figure 2.16: Histopathologic features noticed in human keratoconic corneas: (a) normal cornea: (b) thinning of the stroma with folding artefacts among its lamellae: (c) uniformity of the Bowman's layer: (d) iron deposition seen in basal layers of the epithelium (Rabinowitz, 1998).

Each of the layers of the cornea can get involved in the pathological process of the keratoconus, however, that depends on the stage of the disease. The epithelium may show structural changes such as elongation, compression, and degeneration of its basal cells that breaks accompanied by a reduction in growth of epithelium into Bowman's layer. In addition, the epithelium may show particles within the basement membrane and between basal epithelial cells, and accumulation of ferritin particles within and between epithelial cells most prominently in the basal cells of the epithelium in a ring form called Fleischer ring (Mathew *et al*, 2011; Rabinowitz, 1998). The ring is usually located in the midperiphery of the superficial cornea and may be slightly eccentrically located. It can be diagnosed in the early stages of keratoconus prior to the development of advanced corneal changes. The ring is often incomplete or shows sector variation in intensity of pigmentation. Physiologically, iron is needed for the completion of the citric acid cycle and production of energy in heathy corneas. Iron is also an essential component of the corneal epithelium wound healing and repopulation. Iron is present in the tear film on the surface of the cornea. Iron is transferred by two iron binding glycoproteins (transferrin and lactoferrin) that are found in many mucosal fluids, including tears (Reitz *et al*, 1998; ward *et al*, 2005). Through binding to iron, lactoferrin helps

regulate iron levels, prevent oxidative damage, and strengthen the cornea's antibacterial defences (Loh *et al*, 2009). Decreased expression of lactoferrin has been reported in both corneal epithelial cells (Chaerkady *et al*, 2013) and tear fluid (Balasubramanian *et al*, 2012) of keratoconic corneas. Transferrin has been found to be expressed at lower levels in the corneal stroma in patients with Keratoconus (Joseph *et al*, 2011). All these data indicate that the reduction in expression of iron binding proteins may contribute to deposition of iron in keratoconus that possibly participate to weaken the collagenous network of the corneal stroma (Khaled *et al*, 2017). To the best of the author's knowledge, no studies to date have examined the precise role of the iron deposition on regional biomechanical changes in the keratoconic cornea. However, clinical diagnosis of keratoconus in biomechanical studies (Fontes *et al*, 2011) has been made with Fleischer ring identification where mechanical parameters such as corneal hysteresis (CH) corneal resistance factor (CRF) are reduced in the corneas with Fleischer rings. Microscopic studies have documented that Bowman's layer may include breaks (commonly identified in the central cornea) filled by eruptions of underlying stromal collagen (Kaiserman and Sella, 2019), periodic acid Schiff-positive nodules, and Z-shaped interruptions, possibly due to separation of collagen bundles and reticular scarring (Scroggs and Proia, 1992; Rabinowitz, 1998).

Histopathologic features of keratoconus observed in the anterior stroma are compaction and loss of arrangement of fibrils in the anterior stroma, decrease in the number of collagen lamellae, normal and degenerating fibroblasts in addition to keratocytes, and fine granular and microfibrillar material associated with the keratocytes. Meek and colleagues (2005) observed modifications in collagen orientation and distribution in keratoconic corneas. Ultrastructural abnormalities in proteoglycans have also been found in keratoconic corneas, such as generally fewer number of proteoglycans in keratoconic eyes than in normal eyes (Fullwood *et al*, 1990), proteoglycans with fewer than normal keratan sulphate side chains, and increased mount of dermatan sulphate (Funderburgh *et al*, 1989; Sawaguchi *et al*, 1991). Descemet's membrane and the endothelium are rarely affected by the disease. However, the Descemet's membrane can be affected by breaks seen in acute hydrops, in which elongation of endothelial cells is also occurred with their long axis toward the cone (Mathew *et al*, 2011; Rabinowitz, 1998).

2.9.7. Aetiology and pathogenesis of keratoconus

Intensive research activities over the last decades have taken place into the aetiology and pathogenesis of keratoconus. This work has led to several hypotheses being proposed into the genetic and biochemical mechanisms. The association of other diseases to keratoconus has also been investigated. However, the cause(s) and possible mechanisms for its development still not

fully understood. Generally, there is an acceptance that the aetiology of keratoconus is in a relative combination of environmental and genetic factors, as well as biomechanical and biochemical disorders (Barbara *et al*, 2019; Gomes *et al*, 2015; Sugar and Macsai, 2012).

Previous studies suggested a possible genetic origin of keratoconus, such as the inheritance from relatives or at least one close relative affected by the disease (Owens and Gamble, 2003), bilateralism of the disease (Gomes *et al*, 2015), its association with other genetic disorders (Nowak and Gajecka, 2011; Wheeler *et al*, 2012), the trend for a higher genetic concordance rate in monozygotic twins compared to dizygotic twins (Rabinowitz, 1998). Some other studies linked keratoconus to genetic mutations (Galvis *et al*, 2015). Due to variations, contradictions of previous studies in the suggested genetic/epigenetic factors of keratoconus and association of keratoconus with many ocular or systematic disorders, the proposed genetic factors are likely at fault and can be associated to particular ethnic groups at times. Therefore, suggestions have been made to conduct large-scale genomic studies in South Asia where the disease is most prevalent and for the inclusion of particular candidate genes that have already been identified in relation to keratoconus pathogenesis (Volatier *et al*, 2019; Wheeler *et al*, 2012; Rabinowitz, 1998).

2.9.8. Biochemical factors

Many biochemical studies for keratoconus development have been conducted, which support the hypothesis that corneal thinning occurs as a result of the loss of corneal microstructural components. It has been suggested that an increase in enzymatic proteolysis would degrade the collagen and a reduction in stromal cell population would delay replacement of lost ECM. In other words, an increased level of proteases and other catabolic enzymes, or decreased levels of proteinase inhibitors such as α2-macroglobulin and α1-antiprotease may cause an excessive degradation of the corneal stroma commonly observed in keratoconus (Romero-Jiménez *et al*, 2010).

The cells of the various layers of the cornea secrete an abundance of molecules that influence the milieu in which the cells are housed. In keratoconic corneas, the levels of these secreted molecules are changed and this could produce an altered proteolytic or inflammatory cascade in response to localised trauma (Sherwin *et al*, 2017). MMPs and the lysyl oxidases are a large group of secreted molecules of degradative enzymes, which are both associated with ECM degradation and oxidative stress (Kenney and Brown, 2003; Sawaguchi *et al*, 1989). MMPs are tightly regulated, being secreted as inactive zymogens, which require proteolytic cleavage of a pro-peptide for activation, and they

are inhibited by their specific inhibitors, the tissue inhibitors of metalloproteinases (Sethi *et al*, 2000). Nakamura *et al* (2005) used histopathological and immunohistochemical methods to compare between eight keratoconic and seven normal human corneas. They found that immunostaining of α1-proteinase inhibitor and α2- macroglobulin was lower in keratoconic samples, which in turn increase the activity of digestion enzymes such as collagenase.

The collagenases (MMP-1 and MMP-13) and gelatinases (MMP-2) are members of the MMP family of endopeptidases, which have a zinc atom at their active site. Some studies have addressed collagenase implication in the pathology of keratoconic corneas, which is secreted by corneal epithelial cells and stromal cells in response to repeated micro-traumas (eye rubbing, UV, contact lenses, allergy) in genetically susceptible individuals (Balasubramanian *et al*, 2012, 2010; Collier *et al*, 2000; Collier, 2001; Kaiserman and Sella, 2019; Kao *et al*, 1982; Lema and Durán, 2005; Lema *et al*, 2008; Mackiewicz *et al*, 2006; Pannebaker *et al*, 2010). Higher concentrations of collagenase and other degradation enzymes were found in tear fluid of patient with keratoconus (Lema *et al*, 2008; Pannebaker *et al*, 2010). Other studies also found collagenase and other proteinases in corneal tissue (Collier *et al*, 2000; Mackiewicz *et al*, 2006; Seppälä *et al*, 2006). They used immunohistochemical method to investigate histopathological changes and expression differences in biochemical factors including MMP-1 and MMP-13 in human keratoconic corneas. They found that MMP-1 expression in keratoconic corneas was slightly increased in epithelial cells and also appeared locally in a scattered manner in the stroma, concluded that collagenase MMP-1 is upregulated in keratoconus, and suggested that collagenase might not be the only tissue destructive enzyme in keratoconic corneas. That supports the hypothesis that ECM degradation occurs in the keratoconic corneal tissue due to an imbalance between MMP and their inhibitors (Sherwin *et al*, 2017). In this project, crude and purified collagenase are used to degrade the ECM of porcine corneas, which will be presented in Chapter 6 and 7.

Other biochemical substances such as the Interleukin-1(IL-1), pro-inflammatory cytokine, was also found in keratocytes from eyes with KC have four times as many IL-1 receptors than keratocytes from normal eyes do (Galvis *et al*, 2015; Pannebaker *et al*, 2010). Furthermore, cathepsins are proteases that were originally identified in the lysosome, where they participate in housekeeping tasks such as degradation of phagocytosed photoreceptors. The most likely mechanism by which Cathepsins contribute to ocular pathologies is via degradation of the ECM, and/or regulation of angiogenesis (Kaiserman and Sella, 2019; Regmi *et al*, 2017).

Various studies have treated corneas with a variety of enzymes *in vitro*, in order to investigate the change in mechanical response of the cornea. One such example involved treating porcine corneas with α-amylase, a technique which has proven to significantly decrease the mechanical interlamellar cohesive force, by approximately 31% (Wollensak *et al*, 2011). The reduction in interlamellar cohesive force is predominantly attributed to the loss of proteoglycans, which are digested selectively by α-amylase. The digestion of proteoglycans, following α-amylase treatment, was also investigated during an earlier study (Quintarelli *et al*, 1969), in which α-amylase was found to release acid GAGs from various collagenous tissues, thus suggesting that the enzymes act on the protein moiety of the core protein-polysaccharide linkage. This in turn means that changes in corneal optical, and biomechanical, properties could potentially take place due to the presence, activity and association of these enzymes in tear fluid and the cornea (Haeringen *et al*, 1975; van Haeringen and Glasius, 1976), particularly in patients with early stages of keratoconus (Legkikh *et al*, 2018). That suggests to conduct further studies using sophisticated mechanical, optical and immunohistological testing techniques in order to investigate the presence of α-amylase, in keratoconus, and the effect on the type of proteoglycans which are primarily targeted.

2.9.9. Biomechanical factors

The changes in collagen orientation and lower number of stromal lamellae in keratoconic compared with normal corneas (Meek *et al*, 2005) has been suggested as an indication for corneal rigidity reduction and thinning, eventually leading to keratoconus development (Wheeler *et al*, 2012). Moreover, oxidative damage has been described as a co-factor in keratoconus progression, which can be increased by ultraviolet radiation, atopy and mechanical trauma; the latter could occur as a result of chronic eye rubbing and contact lens wear (Kenney and Brown, 2003). It has found that patients with keratoconus rub their eyes much more frequently than those have normal eyes (Barbara *et al*, 2019; Rogers and Attenborough, 2014). However, conflicting results have been reported in the literature with regards to whether, or not atopy is associated with keratoconus progression. Hard contact lens wear has also been associated with keratoconus progression (Kaiserman and Sella, 2019; Romero-Jiménez *et al* 2010).

2.9.10. Management and treatment of keratoconus

Keratoconic corneas management and treatment methods mainly depends on the severity of the disease. Usually, early stages of keratoconus, Fruste or subclinical stage, can be managed with spectacles. The vision in mild to moderate keratoconic eye can be corrected with contact lenses. Severe stages of keratoconus can be treated with keratoplasty or combination of corneal surgical

treatment and contact lenses. Surgical treatments may mainly include corneal cross-linking (CXL) procedures, intra-corneal rings segments, laser procedures (e.g. phototherapeutic keratoctomy, photorefractive keratectomy, lasik), and intraocular implants (Romero-Jiménez *et al*, 2010). Nowadays, CXL procedures are widely utilised in hospitals to stop the progression of keratoconus (Barbara *et al*, 2019).

CXL is a treatment for patients with keratoconus which can prevent their condition getting worse. The CXL treatment utilises ultraviolet light (UV) of 370 nm and vitamin B2 (0.1% riboflavin) drops to create cross-linking photochemical reaction that induce covalent bonds between collagen molecules and also between proteoglycans and collagen that consequently stiffen the cornea (Randleman *et al*, 2015). The standard CXL protocol involves removing the epithelium and applying riboflavin 0.1% eye drops in 20% dextran T-500 every 5 minutes for 30 minutes before exposure of the central 9.0 mm region of the cornea. Afterward, UV with a fluence of 3 mW/cm2 is applied for 30 minutes that combined with application of riboflavin eye drops every 5 min throughout the period of irradiation. There are other accelerated protocols that deliver approximately the same total amount of UV light energy in shorter time than the standard protocol (Aldahlawi *et al*, 2015). After treatment, patients may still need to wear spectacles or contact lenses and may need to be re-examined for up to five years to confirm that the corneal shape has stabilised (Randleman *et al*, 2015). The CXL treatment successful rate is more than 90% of cases, where it reduced the availability of the keratoconus models for *ex vivo* and *in vitro* researches.

2.9.11. Biomechanical characteristics of human keratoconic corneas

The cornea is a viscoelastic tissue that is associated with elasticity, stress relaxation, creep and hysteresis (Dupps and Wilson, 2006). Studies have proved that some of these properties are altered in keratoconus (Bao *et al*, 2017; Vellara and Patel, 2015). Fundamentally, the Young's modulus (E), or elasticity of a material, is defined as the ratio of applied stress (amount of applied force per unit cross-sectional area) to the resultant strain (percentage change in the length of the specimen, or proportional deformation). Ideally, the ratio between stress (σ) and strain (ε) in purely elastic materials is constant for all levels of stress/strain. While, the ratio between stress and strain in viscoelastic materials, such as cornea, changes at different levels of stress/strain, as shown in Figure 12.17 (Vellara and Patel, 2015).

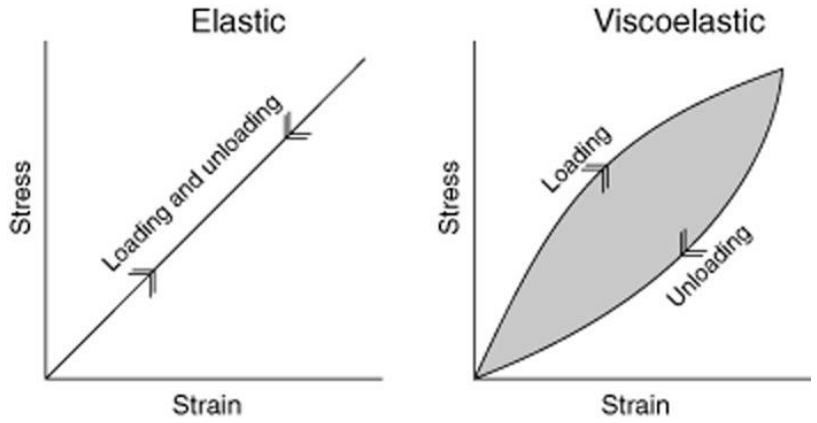

Figure 2.17: Typical stress-strain graphs for elastic and viscoelastic materials. The grey area between the loading and unloading curves is hysteresis, which shows the amount of energy lost (Vellara and Patel, 2015).

The geometrical alterations of keratoconic corneas are simply the consequence of biomechanical deteriorations in corneal structure. Therefore, it has been suggested that corneal biomechanical tests should be included as an additional assessment for keratoconus evaluation and diagnosis (Ortiz *et al*, 2007; Shah *et al*, 2007). However, *in vivo* evaluation of corneal biomechanical properties is challenging due to many limitations including the need of applying external forces on the ocular tissue (Piñero *et al*, 2012). Biomechanical properties of *ex vivo* Keratoconic corneas have been also investigated in varying of methods and conditions for obtaining better understanding and more effective treatment approaches of the disease. In the next sub-topics, *in vivo* and *ex vivo* biomechanical characteristics of keratoconus with varying approaches will be presented.

2.9.10.1. *In vivo* biomechanical characteristics of keratoconus

To date, Ocular Response Analyzer (ORA) and CorVis ST dynamic Scheimpflug analyser (CST) are the only approved clinical devices for characterising the viscoelasticity of the cornea in *in vivo* condition, which basically consist of a corneal biomechanics analyser and air tonometer (Hong *et al*, 2013; Luce, 2005). However, there are new non-commercial methods that can measure distinctive biomechanical features and differentiate normal and keratoconic corneas. These *in vivo* methods include OCE (Ford *et al*, 2011), ultrasonic spectroscopy (He and Liu, 2009) with a controlled external force generator, and Brillouin microscopy (Scarcelli *et al*, 2015).

The working principle of ORA is based on analysing corneal reaction to the applied external force, which is known as the force - displacement relationship. Simply, an air jet force is delivered to the cornea that causes movement of its surface (inward applanation). Subsequently, the cornea returns to its normal curvature under the decreasing force of the air pulse (outward applanation). Corneal displacement is monitored by electro-optical collimation detector system for calculating corneal

hysteresis (CH) and the corneal resistance factor (CRF) (Luce, 2005). The ORA measures corneal hysteresis that is measured from the difference between the air pulse pressures at the inward and outward applanation and represents the viscoelastic nature of the cornea, or its 'viscous-damping' capacity. Figure 2.18 shows a typical ORA measurement signal. The CRF is calculated using a proprietary algorithm for offering a measurement largely related to the elastic properties of the cornea, in which the algorithm uses the relationship between both inward and outward applanation and CCT (Goebels *et al*, 2012; Kaushik and Pandav, 2012; Luce, 2005). However, the exact physical meaning of these two parameters, CH and CRF, is not well understood. In addition, there is no study proves whether these parameters are directly related to the standard mechanical properties used for describing the elasticity of the cornea (Young's modulus) (Piñero *et al*, 2012).

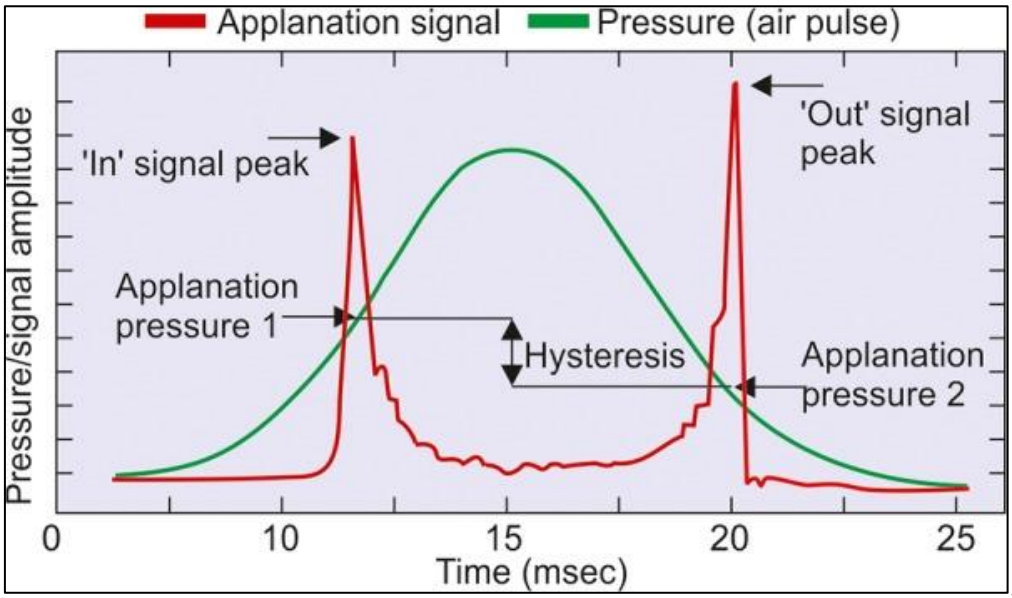

Figure 2.18: Ocular response analyser signal diagram. The green line represents the pressure changes of the air pules. The red line represents the applanation signal, response of the cornea in milliseconds after the first applanation. (CH=P1-P2) (Kaushik and Pandav, 2012).

Many studies conducted by ORA, have demonstrated that CH and CRF are significantly lower in keratoconic corneas than in normal corneas (Ortiz *et al*, 2007; Shah *et al*, 2007; Touboul *et al*, 2011). Ortiz and his colleagues (2007) used ORA to compare 21 keratoconic corneas with 165 normal human eyes, found the mean value of CH was 7.7±1.3 mmHg and CRF was 6.2±1.9 mmHg in keratoconic corneas, while CH was 10.8±1.5 mmHg and CRF was 11.0±1.6 mmHg in normal corneas. Shah *et al* (2007) used ORA and pachymeter to compare CH and CCT of 207 normal with 93 keratoconic human eyes. Their results are summarised in Table 2.1. The study found that CH is significantly lower in keratoconic eyes than in normal eyes, showed that CH is changing with the severity of keratoconus.

Table 2.1: Hysteresis and CCT of keratoconic eyes according to grading by disease severity (Shah *et al*, 2007).

Cornea's condition	Hysteresis (mmHg)	Hysteresis range (mmHg)	CCT (µm)	CCT range (µm)
Normal cornea (n= 207)	10.7±2.0	6.1-17.6	545.0±36.4	471-650
Mild keratoconus (n= 33)	10.3±2.1	4.7-15.3	523.1±44.1	442-611
Moderate keratoconus (n=19)	9.7±2.4	5.0-16.7	487.0±52.4	417-599
Severe keratoconus (n=41)	9.0±2.1	5.9-13.7	470.2±53.9	341-607

CCT: central corneal thickness; n: number of samples

The CorVis ST dynamic Scheimpflug analyser (Oculus, Wetzlar, Germany) is another commercial approved tool for assessing corneal biomechanical properties *in vivo* that indents the cornea using air puff tonometer. The response of the cornea, cross-section of an 8 mm-wide-cornea and deformation, is captured by a high-speed Scheimpflug camera during the indentation (Ambrósio Jr *et al*, 2013). The analyses of the captured data provide the parameters shown in Figure 2.19, which are of great importance for many ocular diseases including keratoconus. However, the use of Scheimpflug camera for dynamic imaging of the cornea creates some image distortion that should be corrected using highly complex algorithms (Li *et al*, 2015).

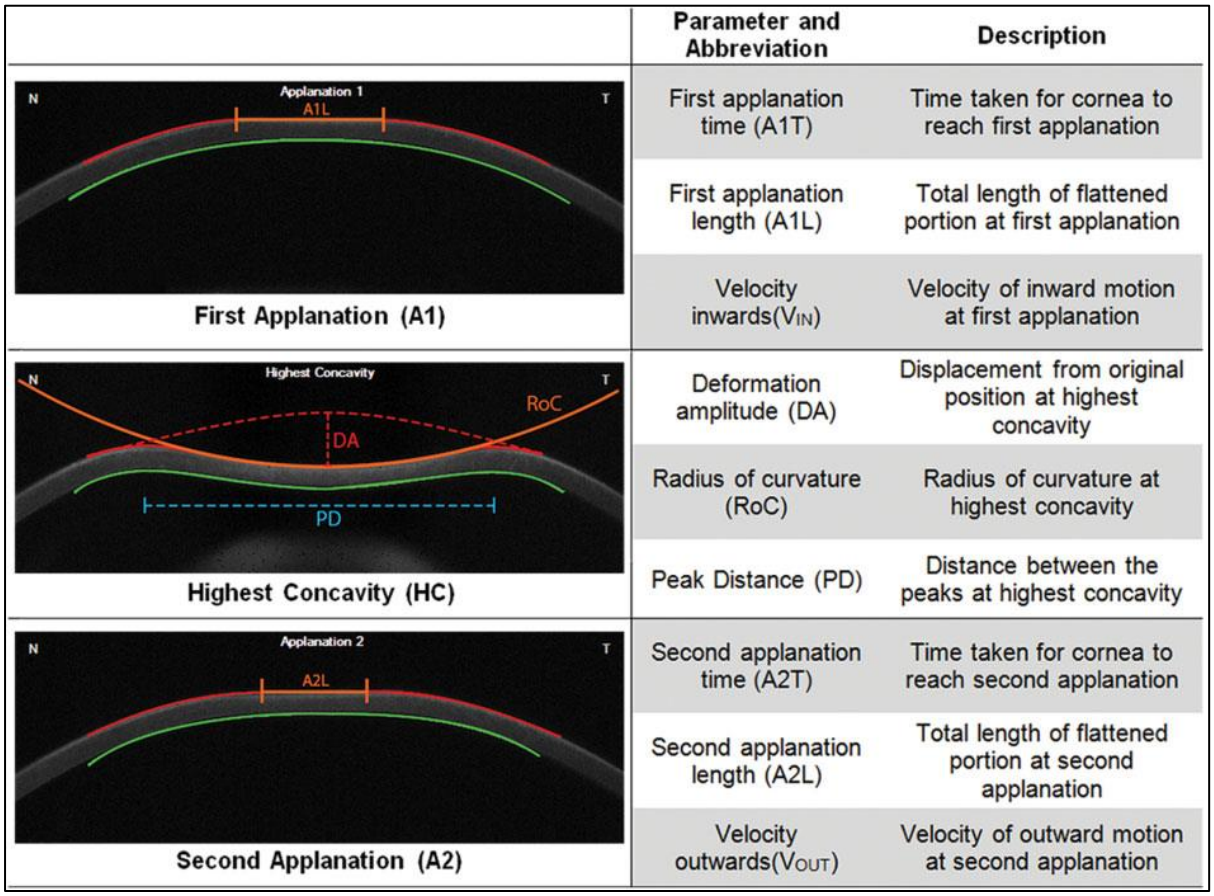

Figure 2.19: CorVis ST parameter abbreviations and descriptions. Images analysed from the CorVis ST output of a normal cornea (Ambrósio Jr *et al*, 2013).

Studies conducted by CST demonstrated that a greater deformation amplitude (DA) and higher velocity of inward (Vin) and outwards (Vout) motion in keratoconus compared to healthy corneas (Ali *et al*, 2014; Ambrósio Jr *et al*, 2013; Herber *et al*, 2019; Tian *et al*, 2014). Ali *et al*, (2014) utilised CST to investigate potential differences between healthy and keratoconic corneas with comparable IOP and central corneal thickness. They found keratoconus is associated with greater DA than in healthy eyes, and concluded that DA may be a useful adjunct in keratoconus assessment and monitoring, but cannot solely discriminate between healthy and keratoconic corneas. The study suggested conducting farther studies to examine the sensitivity and a specificity in differentiating mild keratoconic from healthy corneas. A recent study investigated corneal biomechanical parameters in 60 healthy and 60 keratoconic eyes using ORA and CST, in which participants were matched by age, IOP and severity of keratoconus (Herber *et al*, 2019). The study found that most of the obtained parameters were able to discriminate healthy eyes from different keratoconus stages, and concluded that ORA and CST allowed for decent differentiation between healthy and keratoconic corneas at different severity grades due to high sensitivity and specificity values for keratoconus detection.

There are a number of non-commercial approaches that can measure biomechanical properties of the cornea *in vivo*, including OCE. Significant advances in the field of OCE as a non-invasive tool for obtaining biomechanical properties of the cornea with employing non-contact indentation force delivered by air puff tonometer (Han *et al*, 2017; Larin and Sampson, 2017; Wang and Larin, 2015). A very recent development presented OCE as a non-invasive tool for *in vivo* qualitative/quantitative measurements of normal, keratoconic, and post cross-linked keratoconic human cornea (Ford *et al*, 2019). The study showed that OCE could differentiate between healthy eyes and keratoconic samples; however, further development was needed to reduce OCE sensitivity for noise and increase diagnosis sensitivity.

2.9.10.2. *Ex vivo* biomechanical characteristics of keratoconus

The assumption that there are biomechanical differences between keratoconus, healthy corneas and treated corneas has encouraged intensive investigations in this field. In early *ex vivo* studies, strip extensometery (tensile testing) was utilised to measure classical mechanical properties, such as Young's modulus, of corneal samples. Inflated corneas are tested in static and dynamic approaches at controlled IOP. In more recent study, elasticity was assessed using sound waves. These testing strategies will be explained in the following sections.

2.9.10.2.1. Strip extensometery

In tensile test, strip extensometery, is the most common method in engineering to measure the macroscopic mechanical properties within a typical setting. In these experiments, enucleated corneas are normally eviscerated and small strips (typically) of pre-defined dimensions are fixed within clamps. Then, a pre-defined force is applied and the corresponding displacement is determined. For elastic testing, a gradually increasing axial force is applied and stress-strain diagram is calculated to derive Young's modulus (Elsheikh and Anderson, 2005). Strip extensometery is also used to measure viscoelastic behaviour that arises from the time-dependent nature of biomechanical responses in biological soft tissues, in particular these properties are hysteresis, stress-relaxation relationship, and creep. Stress relaxation is defined as a change in load applied to the material under a constant strain, in which permanent deformation revealed only when unloaded. Creep is the change in the strain of the material under a constant applied force (Dupps and Wilson, 2006). In viscoelastic materials such as the cornea, there is a delay in the response of the material to the loaded force, as well as in the recovery of the material to the unloading of the force. This time-dependent viscoelastic property is known as hysteresis, which represents the area between loading and unloading curves of the stress-strain graph and may arise from the force dissipated due to internal friction (Elsheikh *et al*, 2008b). Another complex biomechanical characteristic can be shown in the cornea is hyperelasticity, which is a nonlinear stress increase with a linear strain increase, and anisotropy, which is directionally dependent response to applied loads (Eliasy *et al*, 2018).

In earlier study conducted by Andreassen *et al* (1980), a significant reduction of Young's modulus in keratoconic corneas was found compared to normal corneas. Andreassen and colleagues used tensile testing on normal and keratoconic corneal strips that were stretched at a constant speed while recording load and deformation. Although the method provided the important differentiation between normal and keratoconic corneas, possible criticises for a such method could be arise from removing the cornea out of its physiological environment, which leads to involvement of many factors that likely affect the measurement of *ex vivo* mechanical properties of the cornea. These factors include disruption of corneal anatomy, age, corneal hydration and dehydration, tissue degradation and freshness, temperature and non-physiological stresses. Since it is unclear how *ex vivo* tensile testing measurements are related to true biomechanical properties *in vivo*, inflation test was developed to fulfil the need of testing corneas in a condition similar to the *in vivo* physiological condition (Elsheikh and Anderson, 2005).

2.9.10.2.2. Inflation testing

Inflation test was introduced because it can preserve corneal structure, which makes the cornea more closely in representation of *in vivo* biomechanical properties. In addition, it can permit for studying the response of the cornea to varying IOP (Elsheikh and Anderson, 2005). Corneal button (only-cornea model) (Elsheikh and Anderson, 2005) and whole-eye model (Whitford *et al*, 2016) inflation setups were proposed, where either the displacement of mercury droplets (Hjortdal, 1996), graphite flakes (Boyce *et al*, 2008), the corneal apex (Elsheikh and Anderson, 2005), curvature changes (Kling *et al*, 2010), or all corneal geometrical changes (Kazaili *et al*, 2019) were recorded. A special holder for both models is required for obtaining the measurement, in which corneal response to IOP increase or external force is recorded for obtaining biomechanical properties. The pressure-apex axial displacement (Elsheikh and Anderson, 2005) or pressure-volume change relationships (Kazaili *et al*, 2019) are monitored, then the apparent stiffness of the corneas is calculated, which is known as static deformation. Another setup, where a controller for the velocity of the applied force is used, called dynamic deformation, the time-dependent deformation of the inflated cornea in response to a localised external force is utilised for elastic behaviour calculation. Examples of localised external forces include controlled air-puff pulses, acoustic waves, or surface indenters (Larin and Sampson, 2017; Wang and Larin, 2015).

Static deformation of the corneas can be recorded by utilising different tools such as OCT (Kazaili *et al*, 2019; Wang *et al*, 2018), high resolution cameras (Whitford *et al*, 2016) , Scheimpflug imaging (Kling *et al*, 2010) and laser micrometres (Boschetti *et al*, 2012; Bryant and McDonnell, 1996; Elsheikh and Anderson, 2005). Dynamic deformation of the corneas can be monitored using high speed cameras (Ambrósio Jr *et al*, 2013) or spectral domain OCT (Singh *et al*, 2015; Wang and Larin, 2015).

Inflation experiments on human whole globes with keratoconus have not been performed because they are rarely available for experimental studies, to the best of author's knowledge. Moreover, the donor age at post mortem acquisition is sufficiently past the age of progression due to stabilisation secondary to natural age-related stiffening. Furthermore, recent medical procedures of reducing corneal transplants for keratoconus patients with the development of CXL approaches has further limited the availability of corneal samples (Vellara and Patel, 2015). Therefore, suggestions have been made for modelling keratoconus.

2.9.10.2.3. Scanning acoustic microscopy

The scanning acoustic microscopy (SAM) is a novel tool that utilises focused sound waves to investigate, measure, or image an object in non-distractive manner. SAM can be utilised to analyse the microstructural properties of materials, providing both quantitative and qualitative characterisation of the tissue (Akhtar *et al*, 2008; Briggs and Kolosov, 2010). SAM can provide information about sample thickness, attenuation, density, stiffness and roughness. This tool can measure the speed of sound, which is directly proportional to the square root of the stiffness in the samples (Akhtar *et al*, 2009; Beshtawi *et al*, 2013). Therefore, it has been used to assess the biomechanical changes of collagen cross-linking on keratoconic corneas *in vitro* (Beshtawi *et al*, 2015). Beshtawi and colleagues found a higher speed of sound (higher stiffness) in cross-linked keratoconic corneal tissue when compared with their controls, and proved the effectiveness of CXL treatment on the first third of the keratoconic corneas. Table 2.2 summarises some studies outcomes along with the method utilised for testing human keratoconic corneas *ex vivo*.

Table 2.2: Studies of *ex vivo* mechanical properties on human keratoconic corneas.

Reference	No. KC	No. NC	Method	Results	Relevant outcomes
(Andreassen *et al*, 1980)	6	7	Uniaxial extensometer	2nd order curve, NC mean stress (N/mm2) = from 0-13.5; strain (%) = from 0-0.37. KC mean stress (N/mm2) = from 0-7.2; strain (%) = from 0-0.47.	The mechanical strength of the cornea is reduced in KC.
(Nash *et al*, 1982)	6	8	Uniaxial extensometer	2nd order curve, The slope of the resultant straight line from stress-strain curves of NC (gm/mm^2) = 59.1±3.4; The slope of the resultant straight line from stress-strain curves of KC (gm/mm^2) = 45.3±3.8;	There is a significant difference in the stiffening parameter between KC and NC.
(Scarcelli *et al*, 2014)	10	8	Confocal Brillouin microscope	The mean Brillouin shift in the anterior 200 lm at the cone of KC = 7.99±0.10 GHz and for NC = 8.17±0.06 GHz	The mechanical loss is primarily concentrated within the area of the keratoconic cone. Outside the cone, the Brillouin shift was similar of that of healthy corneas.

(Beshtawi *et al*, 2015) and (Beshtawi *et al*, 2013)	6	---	SAM	The speed of sound in NC = 1672.5±36.9 ms^{-1} The speed of sound in KC = 1492.8±5.14 ms^{-1} The speed of sound in CXL = 1551.4±7.5 ms^{-1}	NC were 10% stiffer than KC CXL treatment on KC increased the stiffness by 4%.

KC: Keratoconus; NC: normal corneas; CXL: cross-linked corneas, SAM: scanning acoustic microscope.

2.9.10.2.4. Micromechanical testing with nanoindentation

Indentation of material is a depth-sensing technique that is utilised to measure local mechanical properties, such as hardness and reduced elastic modulus of materials. The technique can be performed on different scales, depending on the size of the indenter probe, and typically records the load and surface deformation, and allows the elucidation of structure-biomechanics relationships in the material. Indentation has been successfully used in testing many biological tissues such as arteries (Akhtar *et al*, 2009; Chim *et al*, 2019), dentine (Angker and Swain, 2006), and corneas (Eberwein *et al*, 2014). However, it has not been used to characterise micromechanical properties of inflated corneas or keratoconic corneas.

Indentation (microscale and nanoscale) techniques involved measuring the deformation (depth-sensing) of materials to the very small forces, microscale and nanoscale forces. Figure 2.20 demonstrates the schematic of indentation process that can be represented by a force - displacement curve as shown in Figure 2.21. The mechanical properties then can be directly calculated from the load - displacement curve using analysis that is often based on a work by (Doerner *et al*, 1986) and (Oliver and Pharr, 1992). Their analyses were in turn based upon relationships initially developed by Sneddon (Sneddon, 1965) for the penetration of a flat elastic half space by varying indenters with particular axisymmetric shapes (e.g., conical end, a circular flat punch end, a paraboloid of revolution). These elasticity-based analyses are usually applied to the unloading portion of the indentation measurement (curve), presuming the unloading behaviour of the indented material is characterised by elastic recovery only (Oliver and Pharr, 2004). Other analytical models are also used to fit the indentation data to calculate elastic modulus, including the Hertz model (Johnson, 1982), the Johnson-Kendall-Roberts (JKR) adhesion model (Johnson *et al*, 1971) and The Derjaguin-Muller-Toporov (DMT) model (Dokukin & Sokolov, 2012). Eberwein and colleagues used an indenter with a spherical end of 0.5 mm radius to calculate Young's modulus of human corneas by fitting the loading data to the Hertzian contact model (Eberwein *et al*, 2014). Generally, the relationships between penetration depth (h) and force (F) during unloading can be represented by Equation 2.1 (Van Landingham, 2003).

$$F = \alpha(h - h_f)^m \quad \ldots (2.1)$$

where α is a parameter that contains the geometric constants, the sample elastic modulus (E), the sample Poisson's ratio (ν), the indenter elastic modulus (E_i), the indenter Poisson's ratio (ν_i). "h_f" refers to the final unloading depth. "m" represents a power law exponent that is related to the geometry of the indenter that equals 1 in case of circular flat punch ended tip. An appropriate fit to the unloading data, a derivative dF/dh, applied at the maximum loading point (h_{max}, F_{max}) should yield information about the state of contact at that point. This derivative is termed the contact stiffness (S) and is given mathematically by Equation 2.2 that can obtain the reduced elastic modulus (E_r). The elastic modulus of the sample (E) then can be calculated from Equation 2.3 (Van Landingham, 2003).

$$S = 2aE_r = \frac{2}{\sqrt{\pi}} E_r \sqrt{A} \quad \ldots (2.2)$$

$$\frac{1}{E_r} = \frac{1 - \nu^2}{E} + \frac{1 - \nu_i^2}{E_i} \quad \ldots (2.3)$$

where "a" is the cross section of the stiff indenter and "A" is the projected area of tip-sample contact. The E_r is the reduced elastic modulus that accounts for elastic deformation of both the stiff indenter (E_i) and the sample (E).

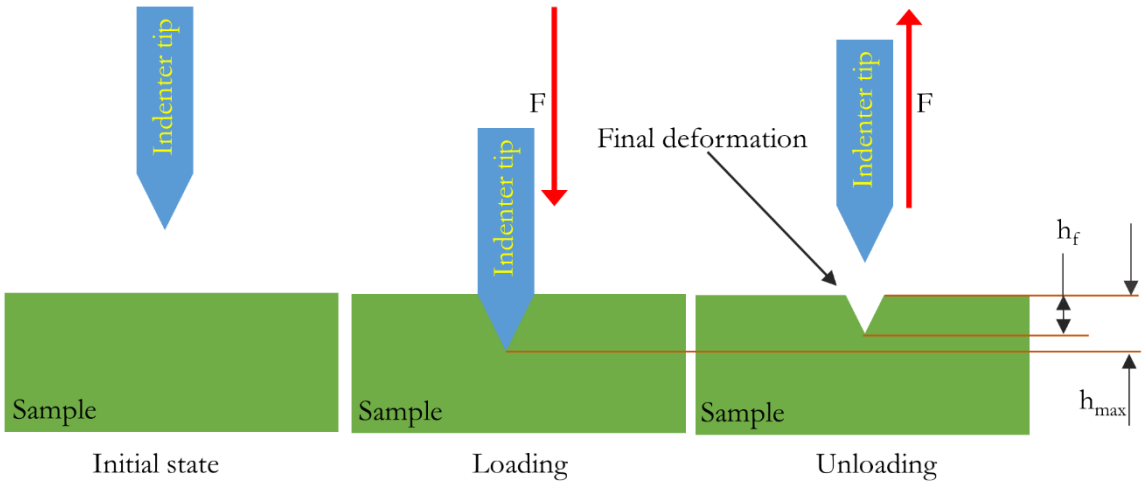

Figure 2.20: A schematic diagram showing the working principles of the nanoindentation. The loading force (F) is applied on the sample. the "h_f" refers for the final unloading depth. The "h_{max}" represents the maximum indentation depth. The final deformation is the residual impression after the indentation process. The indenter tip is typically much stiffer than the sample.

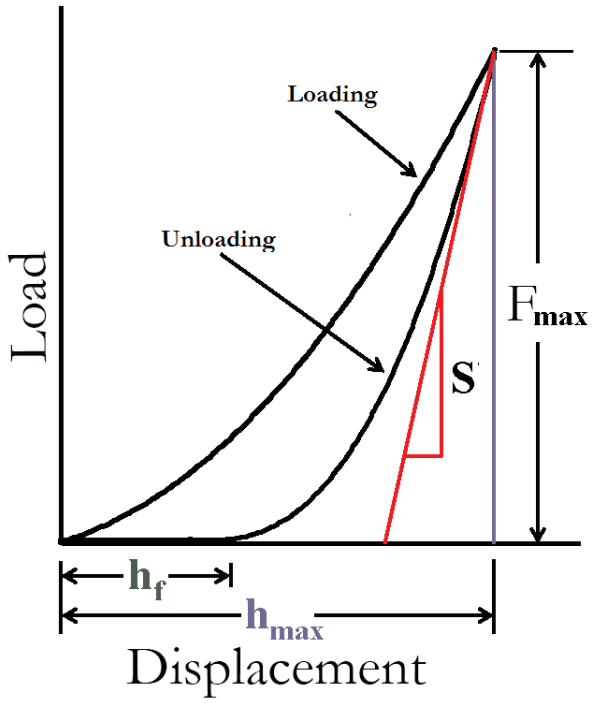

Figure 2.21: A typical nanoindentation force - displacement curve. The red linear line represents the fitting of the unloading portion of the curve. "h_{max}" is the maximum indentation and "h_f" refers to the final depth. Adapted from (Van Landingham, 2003).

Nanoindentation has been utilised to measure the biomechanical properties of biological tissues at the micron-length scale that can reflect the histological features within the samples (Akhtar *et al*, 2009). Tips of different shapes and sizes are used depending on the tested material. Initially, the technique was developed to characterise stiffness of calcified tissues (Rho *et al*, 1999). It then used to assess stiffness of engineering materials (Bembey *et al*, 2006). However, a challenge of penetration the samples was associated with testing of soft materials, such as arteries (Akhtar *et al*, 2009) and hydrogels (Akhtar *et al*, 2016). This challenge was overcome by utilising a larger radius tip with either flat or rounded ends (tip radius more than 100 μm) (Ebenstein and Pruitt, 2004).

The continuous control and monitoring throughout the nanoindentation experiment, dynamic mechanical analysis (DMA) technique, was further developed through applying oscillatory force (stress) on the samples and recording the resulting displacement (oscillatory strain) (Hayes *et al*, 2004). Typically, the oscillatory stress in traditional DMA technique is applied on the sample, either as torsion, compression or tension, where the samples should be relatively thick. In oscillatory nanoindentation with DMA, soft samples, including tissues, are indented with a flat-ended cylindrical punch, the response can be expressed in terms of storage shear modulus (G′) and the loss shear modulus (G″) as shown in Equation 2.4 and 2.5. G′ measures the sample's ability to store energy elastically, while G″ characterises the sample's ability to dissipate energy as heat. The

complex shear modulus (G*) then can be determined that has real and imaginary components to represent the viscoelastic properties, Equation 2.6. Rotating vectors analysis of DMA mechanics reveals that G′ and G″ are concisely related through the loss factor, which is the tangent of the phase angle, δ, by which the strain lags the stress, Equation (2.7). tan(δ) provides a measure of damping in the material. For material with tan(δ) > 1, the material exhibits more damping than a material with tan (δ) ≤ 1, where G″ is greater than G′. That means the energy dissipating, where viscous component of the complex modulus prevails as the defining factor of the material's characteristics. In practice, G′, G″, and tan(δ) are measured by DMA as a function of frequency and temperature (Akhtar *et al*, 2018, 2016). Further details on calculation of elastic modulus from oscillatory nanoindentation is found in Chapter 3.

$$G' = \frac{S(1-v)}{2D} \quad \ldots (2.4)$$

$$G'' = \frac{Cw(1-v)}{2D} \quad \ldots (2.5)$$

$$G^* = G' + iG'' \quad \ldots (2.6)$$

$$\tan(\delta) = G''/G' \quad \ldots (2.7)$$

where "D" is the punch diameter. "C*w*" refers to the contact damping that is obtained by subtracting the instrument damping (Ci*w*) from the total measured damping (Cs*w*). "*i* " is the imaginary constant.

The advantages of the oscillatory nanoindentation over the traditional DMA is can test samples with varying ranges of diminutions. Unlike, in the traditional DMA, the samples need to be relatively thick. The moving mass of the oscillatory nanoindenter tip is much smaller than the moving mass of a traditional DMA instrument, which means that the oscillatory nanoindenter can be made to oscillate at much higher frequencies, then it will be useful for testing different materials at frequencies far way from their natural frequency. Finally, sample preparation for oscillatory nanoindentation testing is generally easier than for traditional DMA (Hay, 2015; Hayes *et al*, 2004).

2.9.10.2.5. Atomic force microscopy

AFM was firstly designed by Binnig *et al* (1986) and considered as a high-resolution microscope for biological tissue imaging in comparison with other techniques such as Scanning Electron Microscope (SEM) and Transmission Electron Microscopy (TEM) because it allows measurements of biological samples in conditions approximately similar to their native conditions (Alessandrini and Facci, 2005; Binnig *et al*, 1986). The principle of the AFM is sensing the topography of the sample by using a very sharp tip that is mounted on a cantilever. Figure 2.22 shows a schematic representation of AFM. The sample is placed on a piezoelectric drive stage. As the tip approaches the sample surface, attractive force between the surface and the tip cause the cantilever to slightly deflect towards the surface. This deflection is detected using the laser beam and photodetector system. A laser beam is positioned on the reflecting surface of the free end of the cantilever. The reflected laser beam is aimed by a mirror on a highly sensitive photodetector to records movements of the cantilever. These movements represent cantilever deflections as the tip senses the sample surface (Binnig *et al*, 1986; Jalili and Laxminarayana, 2004).

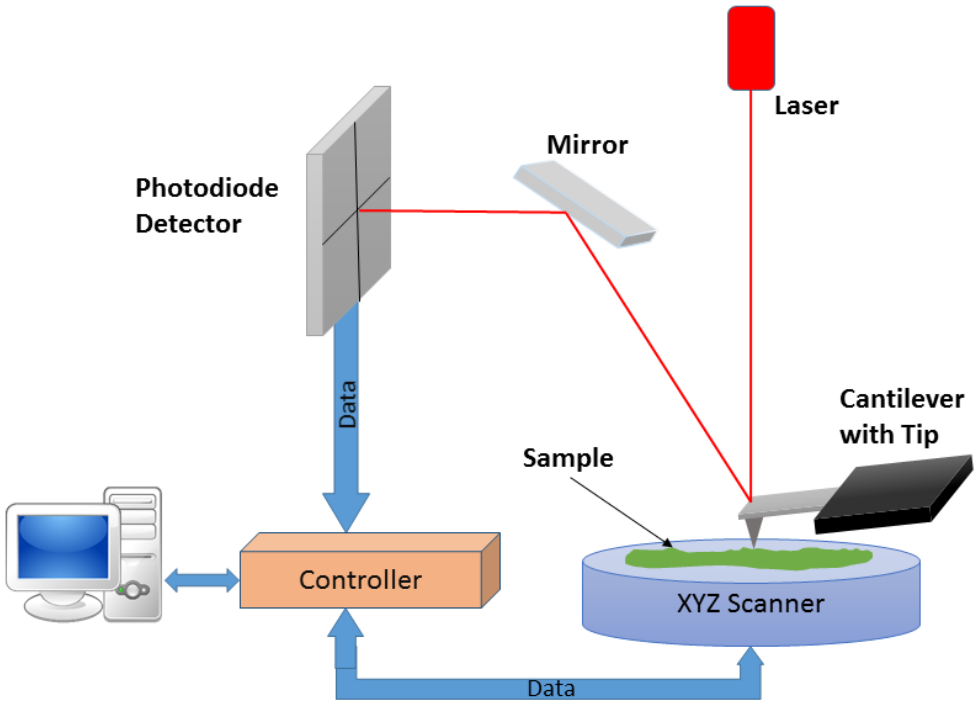

Figure 2.22: A schematic illustration of the AFM. The cantilever and the tip are typically made of silicon with reflecting coating at the free end of the cantilever. The dimensions of the tip and the cantilever normally are known.

Technically, AFM has three operational modes: non-contact mode, contact mode and tapping mode. In contact mode, the tip is continuously dragging onto the sample, which could cause destructive changes of the sample surface. Whereas in the non-contact mode, the tip is oscillating above the sample surface, which prevents damage to soft tissues but does not usually provide high-

resolution images of biological samples, therefore other imaging modes are preferred (Jalili and Laxminarayana, 2004). The developed tapping mode is normally used that is combination of both the non-contact and contact modes (Haugstad, 2012). In this mode, the cantilever tip oscillates near or at its natural resonance frequency while it lightly impacts or contacts the sample surface for a short time. The advantage of this mode is that soft tissue samples such as corneal tissue can be scanned efficiently with minimal destruction (Salapaka and Cleveland, 1998).

The developments of the AFM modes make it possible to observe the different stiffness of a composite material (soft tissues) and visually distinguish between hard and soft regions (Jalili and Laxminarayana, 2004). The principle of measuring the mechanical properties is approximately similar to the one proposed earlier in nanoindentation tests (previous section). The interaction between the tip and the sample is monitored and the displacement of the cantilever with the applied force at each pixel is collected to generate a force - displacement curve. The mechanical properties, such as elastic modulus, of the sample then can be calculated after applying fitting models (mentioned earlier in previous section) on the curves.

With the new developments of the AFM, biomechanical properties such as elastic modulus and adhesion of the samples cannot only be measured, but can also be visualised. Initially, force volume (FV) mode was used to measure elastic properties. FV mode is a trusted technique utilised extensively in mechanical investigations of biological samples. Where this mode can show how the samples respond to mechanical stimuli or exert forces on their environments by obtaining Force-Distance Measurements in a 2-dimensional array. Force variations and topography of samples are obtained, along with individual force curves at any point. Further development on AFM mechanical measurements included Peak Force Quantitative Nanomechanical (PF-QNM) mode that was also used in biomechanical research. Both modes produce a force-displacement curve in each pixel of the image. This mechanical data then is collected at each pixel and directly linked to the sample morphology to generate an image that can be presented as a mechanical property map (Pittenger *et al*, 2010; Young *et al*, 2011)

The main difference between FV and PF-QNM modes is in working principles of measuring mechanical properties with the effect of sample surface adhesion. In FV mode, the Z scanner (for measuring deformation) stops when a predefined force is reached that is used as a trigger to stop the Z actuator. Whereas, PF-QNM mode takes the peak force as a feedback parameter during each driving cycle to control the Z scanner. The driving frequency in FV mode is triangular wave, which

makes the probe approaches and retracts at a constant rate. However, the QNM is driven by a sine wave that makes the cantilever controlled by a process of deceleration to avoid the possibility of overshooting before reaching a predefined peak force. This advantage decreases the possibility of sample surface damage. The FV mode is driven by a low loading rate (<250 Hz), while the PF-QNM mode is driven by a high loading rate (>250 Hz). This makes the FV mode spends more (acquisition) time to collect the measurements than the PF-QNM mode. In case of increase loading rate in the FV mode, the influence of surface adhesion affects the accuracy of the elastic modulus measurement. These differences make the PF-QNM mode more suitable for measuring elastic properties of biological tissues than the FV mode (Yang *et al*, 2019). In PF-QNM mode, samples will not be subjected to visual damage (plastic deformation) (Pittenger *et al*, 2012) and has been applied for elastic measurements of sclera (Papi *et al*, 2014), whereas plastic deformation is more common in FV mode (Grant *et al*, 2012). In this thesis, PF-QNM mode was used and further explanation is shown in Chapter 7.

Using AFM, the mechanical properties to the tissue can be correlated to ultrastructural details, which in turn can provide better understanding of various tissue diseases, including keratoconus. Fullwood *et al*, (1995) used AFM for conducting the first study to investigate the ECM of bovine cornea and sclera. They showed scleral collagen fibril in which the D-periodicity was clearly evident, and evaluated the potential ability of employing AFM as a tool to obtain nanoscale resolution of corneal and scleral tissues in a condition near to their natural status (Fullwood *et al*, 1995). Elastic properties of each layer of the normal human cornea were also investigated using AFM (Last *et al*, 2012). Lombardo *et al* (2012) measured the viscoelastic properties (hysteresis and elastic modulus) of the anterior stromal of human corneas using AFM and utilised Sneddon model for fitting force curve data (Lombardo *et al*, 2012). Papi *et al* (2014) utilised the PF-QNM mode for the investigation of regional variations in the nanomechanical properties of porcine sclera, and examined the variations in the collagen fibril diameter in the posterior, equatorial and anterior regions of the sclera. They found that collagen fibril diameter and elastic modulus increased from the posterior to the anterior region, and there was a linear correlation between collagen fibril diameter and elastic modulus. They demonstrated that the PF-QNM mode can provide high spatial resolution nanomechanical information of soft tissues.

2.10. Characterisation of porcine corneas

Animal organs are normally utilised for many advanced biomedical technologies, research and drug development applications. In addition, biomedical studies are frequently improving the reliability

and standardisation of *in vitro*/*ex vivo* animal models as a replacement for the use of living laboratory animals. Many studies have assessed the effect of various ocular products and conducted biomechanical/biochemical trials on the mammalian eye, in particular the porcine eye (Shafaie *et al*, 2016).

2.10.1. Morphology of porcine corneas

Porcine corneas are used in many studies as they are similar to human corneas in many parameters, in particular dimensions and thickness (Menduni *et al*, 2018). However, porcine corneas are slightly oval in shape, in which the horizontal corneal diameter is slightly larger than the vertical diameter. Human corneas are more circular in shape. Some studies that have reported the topography of porcine corneas are summarised in Table 2.3.

Table 2.3: Summary of some previous studies which have analysed the topography of the anterior chamber of the porcine eye.

Author/s	No. of eyes	Method	Results
(Bartholomew *et al*, 1997)	25	US biomicroscopy	Anterior chamber depth = 2.21 mm Horizontal corneal diameter = 16.61 mm vertical corneal diameter = 14.61 mm
(Asejczyk-Widlicka *et al*, 2008)	12	Time domain - OCT	Anterior chamber depth = 2.21 mm CCT: 0.96±0.05 mm
(Sanchez *et al*, 2011)	5	Portable autokeratometer Manual keratometer US pachymeter Corneal topographer	Keratometry at steepest meridian =41.2±1.7 D Keratometry at flattest meridian = 38.8±2.8 D Horizontal corneal diameter = 14.3±0.25 mm Vertical corneal diameter = 12.00±0 mm CCT by US-pachymetry =877±13.58 µm CCT by Slit-scan pachymetry =906.2±15.3 µm
(Heichel *et al*, 2016)	16	Orbscan Corneal topographer	Keratometry at steepest meridian =39.6±0.9 D Keratometry at flattest meridian =38.5±0.92 D Corneal diameter = 13.81±0.83 mm CCT pachymetry = 832.6±40.18 µm
(Menduni *et al*, 2018)	60	Medmont corneal topographer Visante OCT US pachymeter ImageJ software	Anterior chamber depth = 1.72±0.26 mm Curvature at steepest meridian = 7.8±0.32 mm Curvature at flattest meridian = 8.28±0.32 mm Horizontal diameter = 14.88±0.66 mm Vertical diameter = 12.69±0.58 mm CCT by OCT = 1009±1 µm CCT by US = 1248±144 µm

CCT: central corneal thickness; D: dioptres; OCT: optical coherence tomography; US: Ultrasound

2.10.2. Structural and ultrastructural features of porcine corneas

Porcine corneas are almost double the thickness of human corneas and only have four layers. It has been reported that Bowman layer is absent in porcine corneas (Merindano *et al*, 2002; Svaldenienė *et al*, 2003). At IOP equals 15 mmHg, the thickness of epithelium layer is 50.25±27.5 μm, the stromal thickness is 950±33.8 μm, Descemet's membrane with the endothelium has a thickness of approximately 30 μm (Kazaili *et al*, 2019). The thickness of the cornea gradually increases up to 8% at 5 mm from the centre. Like human corneal stroma, porcine corneal stroma has a large amount of collagen type I arranged in lamellae. The collagen fibril diameter is 41±9 nm. The axial D-periodicity of collagen fibril ranged from 64-70 nm, as measured by AFM (Kazaili and Akhtar, 2018). Collagen fibrils mainly run in circumferential orientation (Hayes *et al*, 2007). The water content of the porcine cornea is 71.93±0.47% (Xu *et al*, 2008).

2.10.3. Biomechanical properties of porcine corneas

This section will review literature on techniques and the measured biomechanical properties of porcine corneas. Topography and thickness distribution of corneas can be measured *in vivo* (Sanchez *et al*, 2011). However, determinations of biomechanical properties still rely on *ex vivo* experiments involving human and animal corneas. Most experiments measuring biomechanical properties of the cornea are conducted *in vitro* (Elsheikh *et al*, 2008). Animal corneas have been used as approximate models for human corneas in biomechanical property characterisation studies because of the difficulties in obtaining human donor corneas, in particularly the fresh/healthy corneas. Therefore, many studies (Asejczyk-Widlicka *et al*, 2008; Boschetti *et al*, 2012; Elsheikh *et al*, 2008b; Menduni *et al*, 2018; Wollensak and Spoerl, 2004; Zeng *et al*, 2001) have used porcine corneas in different approaches to measure biomechanical properties due to their similar anatomy compared to the human cornea (Kling and Hafezi, 2017).

Spoerl *et al* (1998) used extensometer to investigate the possibility of induction of cross-linking in porcine corneas by measuring the stress-strain behaviour. Strips of 80 porcine corneas were treated with different intrafibrillar cross-links and compared with 10 control corneas. They found that the biomechanical behaviour of the cornea can be altered by certain cross-linking agents including glutaraldehyde, Karnovsky's solution, and with riboflavin and UV-irradiation that offers the potential of a conservative treatment of keratoconus.

A study conducted by Zeng *et al* (2001) used tensile test to compare between porcine and human corneas, and found that tensile strength and stress-strain relation were very similar. The study

showed that porcine cornea relaxed much more than human cornea under the same stretch ratio, suggesting that porcine cornea can be used as a substitute model for human cornea research if tensile strength and the stress-strain relation are the only mechanical factors to be investigated. Elsheikh *et al* (2008b) made a comparison between biomechanical properties of porcine and human corneas using tensile test. They found that porcine and human corneas had almost the same form of behaviour under short and long-term loading, both showed non-linear stress-strain behaviour, and reacted to sustained loading in a similar fashion. Furthermore, the study found that human corneas were significantly stiffer and exhibited less creep than porcine corneas. These findings question the suitability of porcine corneas as models for human corneas in mechanical studies. However, corneal extensometery studies cannot show the exact response of the corneas because the orientation, diameter and density of collagen fibrils in human corneas are quite different than in porcine corneas. Therefore, *in vitro* experiments for porcine corneas, such as inflation testing, can provide fair comparison of biomechanical properties between corneas of different species. Table 2.4 summarises biomechanical properties of porcine corneas reported by different approaches.

Inflation testing can reflect the real response of the corneas to the stresses and may offer realistic viscoelastic properties. However, it is more complicated and needs special holders for fixing the cornea (Elsheikh and Anderson, 2005). Many studies inflated the corneas and measured biomechanical properties using certain approaches. Boschetti *et al* (2012) investigated the mechanical properties of 51 fresh porcine corneas using both inflation and tensile tests. A special holder was designed to hold the corneas, in which corneas were subjected to a gradually increasing posterior pressure, 0 to 40 mmHg, applied through a column of Eusol-C, corneal tissue culture, to simulate the effect of the IOP. The apex corneal displacement during loading and unloading was monitored using a laser micrometre. The study showed a non-linear behaviour of pressure-apex displacement and stress-strain relationship, see Figure 2.23. The study presented average measurements to show the main behaviour of porcine corneas, where the presented values can be affected by several variables including pressure step, uploading rate, the cornea-only (open system) or whole-eye (closed system) model, age, preservation method and hydration liquid used, the level of preloading, corneal apex displacement method, the presence of the endothelium and/or the epithelium, the level of strain at which the elastic modulus has been calculated, and finally, the type of modulus computed.

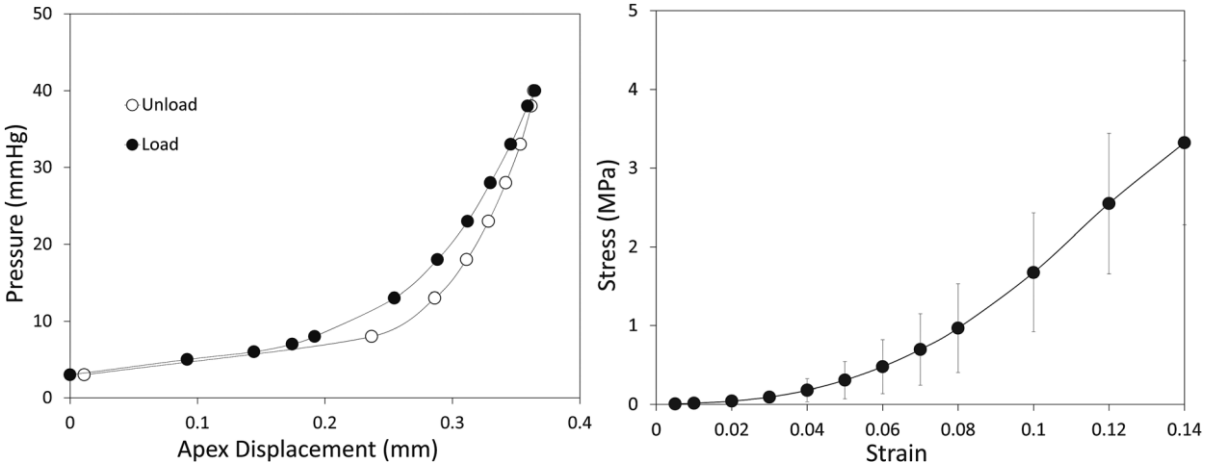

Figure 2.23: Average loading and unloading curves of apex displacement of porcine corneas from 2 - 40 mmHg, showing 25% of hysteresis (Left). Average uniaxial stress-strain curve of porcine corneal strips (Right). The figures were taken directly from (Boschetti *et al*, 2012).

Many other approaches utilised different tools for monitoring corneal apex displacement, including OCT (Kazaili *et al*, 2019; Wang *et al*, 2018), High resolution cameras (Whitford *et al*, 2016), Scheimpflug imaging (Kling *et al*, 2010) and laser micrometres (Boschetti *et al*, 2012; Bryant and McDonnell, 1996; Elsheikh and Anderson, 2005).

Table 2.4: Summary of biomechanical properties of porcine corneas reported by different approaches.

Authors	Method	Sample shape	Fluid	Aim	Measured parameters
(Kling *et al*, 2010)	Scheimpflug topographer was used to record corneal geometry and apex displacement in response to IOP change. IOP increased from 18.5 to 58.5 mm Hg and then was decreased to 18.5 mm Hg.	WE	Saline solution	corneal response to variable IOP in porcine eyes after CXL	E-control=0.69±0.3 kPa E-CXL=1.09±0.3 KPa
(Scarcelli *et al*, 2013)	Brillouin light-scattering Microscopy method was used to measure the Brillouin frequency shift within relaxed corneas	WE	dextran-based and saline-based solutions	validating noncontact Brillouin microscopy to quantify corneal mechanical properties before and after CXL	They found variation of the Brillouin elastic modulus across the cornea, from 8.2 GHz in the epithelium to 7.5 GHz near the endothelium of untreated cornea. Depth-dependent increase in Brillouin modulus of CXL corneas
(Kling and Marcos, 2013)	The Corvis ORA was used on both human and porcine corneas *in vitro*. Both corneal fixation models were used. Several factors were	WE and OC	Water	testing the influence of several factors on corneal deformation	Corneal deformation was very sensitive to IOP change.

	considered during mechanical testing. Including IOP, corneal rigidity, dehydration, presence of sclera, and *in vivo* versus *in vitro* conditions. IOP was increased from 15 to 45 mm Hg				No significant effect on CCT was detected but the degree of symmetry of CAD was changed when different fixation models were used No significant difference was found between the temporal symmetry in human whole globes *in vitro* and *in vivo*.
(Metzler *et al*, 2016)	Tensile test was used on porcine corneas. While, the CorVis ST dynamic Scheimpflug analyser was utilised for human corneas. samples were treated using human decorin core protein	CS of porcine OC for human	-	investigating changes in corneal human and porcine biomechanics after CXL	E was higher in the CXL porcine corneas than the untreated corneas at 4%, 5%, and 6% strain.
Kampmeier *et al*, 2000)	Tensile tests including stress relaxation were used.	Corneal strips	-	Investigating material properties of porcine cornea including density, Young's Modulus and heat capacity	Density =1062±5 kg/m3. The stress-strain relation for corneal strips is represented by a third order approximation E≈ 400 kPa for small strains less than 2%. heat capacity = 3.74±0.05 J/gK
(Elsheikh and Alhasso, 2009)	Tensile tests conducted in tube filled with Eusol C, tissue culture. The specimens were subjected to three different strain rates	CS (horizontal vertical And orthogonal)	Eusol C	determining corneal anisotropy and assess the assumption of corneal symmetry in eyes of the same animal	The vertical and horizontal specimens were found to have almost the same behaviour, and both were marginally stiffer than diagonal specimens
(Dupps *et al*, 2007)	Surface wave elastometer system consists of two transducers positioned on the corneal surface. Corneas were inflated at 15 mmHg.	WE	0.9% normal saline	Measuring ultrasound surface wave propagation time through corneas along a ten-position map.	Wave velocity decreases through the cornea as function of depth
(Singh *et al*, 2015)	Phase-sensitive OCT with External forced air-pulse. Corneas were inflated at 10, 15 and 20 mmHg.	OC	PBS		Phase data was converted to displacement in microscale.

					E = 2.1±0.1 kPa, 4.9±1.0 kPa, and 15.7±5.1 kPa
(Singh, Li, Han, Vantipalli, *et al*, 2016)	Phase-sensitive OCT with External forced air-pulse. Corneas were tested in loading and unloading at IOP values 15, 20, 25 and 30 mmHg.	OC	PBS	Investigating the effects of CXL on corneal E and mechanical anisotropy.	E values ranged from 14.7 kPa at 15 mmHg to 72.6 kPa at 30 mmHg (for untreated corneas); while 33.5 kPa at 15 mmHg to 228.1 kPa at 30 mmHg (for CXL corneas).
(Liu *et al*, 2017)	Single shot line-field low coherence holography with External forced air-pulse. Corneas were inflated at 10, 15 and 20 mmHg	OC	PBS	To quantify wave velocity and corneal mechanical properties	E values were 14.52±1.21, 30.94±2.46, and 55.33±5.08 kPa respectively at 10, 15, 20 mmHg IOP
(Dorronsoro *et al*, 2012)	Spectral domain OCT system with external air pulse was used to measure of several deformation parameters, such as amplitude, diameter and volume of the maximum deformation, duration and speed of the increasing deformation, and period and the recovery period Corneas were inflated at 18 mmHg. CXL technique was used on porcine corneas	WE	sodium chloride	Proposing a new *in vivo* and *in vitro* non-invasive technique to imaging of the dynamic response of human and porcine corneas to an air puff inducing a deformation	They offered a new technique that has proved very sensitive to detect differences in the deformation parameters across conditions. The technique could differentiate CXL porcine corneas from untreated corneas.

WE: whole-eye model. OC: only-cornea model. CS: corneal strips. CXL: corneal cross-linking, E: elastic modulus, PBS: phosphate buffer saline solution, IOP: intraocular pressure.

In summary, fresh enucleated porcine corneas are often utilised because of their similar anatomy to the human cornea, as well as their availability. *Ex vivo* biomechanical destructive tests are carried out using either complete (inflation tests) or strips (extensometery) corneas that have been removed from the eye. These types of tests allow for extensive testing including multiple loading patterns and measurement of various properties. These tests have enabled determination of the biomechanical characteristics of the cornea including the non-linear stress-strain response with progressive stiffening at high strains or IOPs. In addition, it was found that the cornea shows a non-linear viscoelastic response (time dependent) with varying amounts of hysteresis on different rates of loading cycles (Boyce *et al*, 2007). Moreover, some studies also showed regional variations in corneal stiffness due to differing orientation and number of collagen fibrils, in which the central cornea is stiffer than the paracentral and peripheral (Bell *et al*, 2018; Boyce *et al*, 2008; Mikula *et al*, 2016; Whitford *et al*, 2016). However, this contradicts work from a previous study that found the paracentral corneal region deformed most (Hjortdal, 1996). It has also been reported that corneal elastic modulus is a function of depth, where it is decreasing from the anterior to the posterior

stroma (Mikula *et al*, 2016; Randleman *et al*, 2008; Smolek, 1993). Finally, corneal biomechanical properties are dependent on age, with corneal stiffness increasing with the age of the patient (Cartwright *et al*, 2011; Elsheikh *et al*, 2007).

2.11. Summary

In summary, the literature review encompasses a wide range of disciplines, presents an overview of information that is relevant to this study. The author has briefly presented the cornea and its layers, and shown the contribution of each layer to the whole biomechanics of the cornea. The effects of some factors, such as corneal hydration and thickness, on the biomechanics and transparency of the corneas were briefly introduced. The ultrastructure of the stroma was described with some details of transparency theories. An overview of corneal imaging techniques was proposed with especial focus on OCT and ultrasound. Keratoconus was introduced with focusing on some factors that were related to biomechanical and geometrical changes associated with keratoconic corneas. In particular, the author has highlighted the contribution of enzymatic unbalance of amylase and collagenase and their supposed effect on keratoconus progress. The multiscale *in vitro* biomechanical testing methods have been highlighted with a special focus on AFM, inflation tests and nanoindentation. Structural and biomechanical features of porcine corneas were introduced to highlight their use as a biomechanical model. In this chapter, the author has declared the methods and the enzymes that will be utilised to present an animal model for keratoconus.

2.12. References

Aakre, B.M., Doughty, M.J., 1997. *In vitro* hydration kinetics of recent post-mortem tissue versus pre-dried corneal stromal tissue. Experimental Eye Research 65, 127-33.

Aghamohammadzadeh, H., Newton, R., Meek, K., 2004. X-ray scattering used to map the preferred collagen orientation in the human cornea and limbus. Structure 12, 249-256.

Akhtar, R., Draper, E., Adams, D., Hay, J., 2018. Oscillatory nanoindentation of highly compliant hydrogels: A critical comparative analysis with rheometry. Journal of Materials Research 33, 873-883.

Akhtar, R., Draper, E.R., Adams, D.J, Pfaff, H., 2016. Complex shear modulus of hydrogels using a dynamic nanoindentation method. In: Tekalur S., Zavattieri P., Korach C. (eds) Mechanics of Biological Systems and Materials, Volume 6 (pp. 141-145). Springer, Cham. USA.

Akhtar, R., Sherratt, M.J., Watson, R.E., Kundu, T, Derby, B., 2008. Mapping the micromechanical properties of cryo-sectioned aortic tissue with scanning acoustic microscopy. MRS Online Proceedings Library Archive 1132, Z03-Z07.

Akhtar, Schwarzer, Sherratt, M.J., Watson, R.E.B., Graham, H.K., Trafford, A.W., Mummery, P.M., Derby, 2009. Nanoindentation of histological specimens: Mapping the elastic properties of soft tissues. Journal of Materials Research 24, 638-646.

Aldahlawi, N., Hayes, S., O'Brart, D., Meek, K., 2015. Standard versus accelerated riboflavin-ultraviolet corneal collagen crosslinking: Resistance against enzymatic digestion. Journal of Cataract & Refractive Surgery 41, 1989-1996.

Alessandrini, A, Facci, P, 2005. AFM: a versatile tool in biophysics. Measurement Science and Technology 16(6), R65-R70.

Ali, N.Q., Patel, D.V., McGhee, C.N., 2014. Biomechanical responses of healthy and keratoconic corneas measured using a noncontact scheimpflug-based tonometer. Investigative Ophthalmology & Visual Science 55, 3651-9.

Ambekar, R, Toussaint, KC, Johnson, AW, 2011. The effect of keratoconus on the structural, mechanical, and optical properties of the cornea. Journal of the Mechanical Behavior of Biomedical Materials, 4(3), 223-236.

Ambrósio Jr, R., Ramos, I., Luz, A., Faria, F., Steinmueller, A., Krug, M., Belin, M., Roberts, C., 2013. Dynamic ultra-high speed Scheimpflug imaging for assessing corneal biomechanical properties. Revista Brasileira de Oftalmologia 72, 99-102.

Andreassen, T., Simonsen, A., Oxlund, H., 1980. Biomechanical properties of keratoconus and normal corneas. Experimental Eye Research 31, 435-441.

Angker, L., Swain, M.V., 2006. Nanoindentation: Application to dental hard tissue investigations. Journal of Materials Research 21, 1893-1905.

Asejczyk-Widlicka, M., Pierscionek, B., 2008. The elasticity and rigidity of the outer coats of the eye. British Journal of Ophthalmology 92, 1415-1418.

Asejczyk-Widlicka, M., Schachar, R., Pierscionek, B., 2008. Optical coherence tomography measurements of the fresh porcine eye and response of the outer coats of the eye to volume increase. SPIE 13, 024002-1 - 024002-6.

Asimellis G, Kaufman E., J., 2019. Keratoconus. In: StatPearls [webpage]. Treasure Island (FL): StatPearls. [Published on: 2019 January]. [Available: www.ncbi.nlm.nih.gov/books/NBK470435/].

Auffarth, G.U., Wang, L, Völcker, H.E., 2000. Keratoconus evaluation using the Orbscan topography system. Journal of Cataract & Refractive Surgery 26(2), 222-228.

Avitabile, T., Franco, L., Ortisi, E., Castiglione, F., Pulvirenti, M., Torrisi, B., Castiglione, F., Reibaldi, A., 2004. Keratoconus Staging. Cornea 23, 655-660.

Balasubramanian, S., Mohan, S., Pye, D., Willcox, M., 2012. Proteases, proteolysis and inflammatory molecules in the tears of people with keratoconus. Acta Ophthalmologica 90, e303-e309.

Balasubramanian, S., Pye, D., Willcox, M., 2010. Are proteinases the reason for keratoconus? Current Eye Research 35, 185-191.

Bao, F.J., Geraghty, B., Wang, Q.M., Elsheikh, A., 2017. Role of corneal biomechanics in the diagnosis and management of keratoconus. In: Alió J. (eds) Keratoconus (pp. 141-150). Springer, Cham. USA.

Barbara, R., Turnbull, A.M., Malem, A., Anderson, D.F., Hossain, P., Konstantopoulos, A, Barbara, A., 2019. Epidemiology of keratoconus. In: Barbara, A. (eds) Controversies in the Management of Keratoconus (pp. 1-16). Springer, Cham. USA.

Bartholomew, L., Pang, D., Sam, D., Cavender, J., 1997. Ultrasound biomicroscopy of globes from young adult pigs. American Journal of Veterinary Research 58, 942-948.

Bell, J.S., Hayes, S., Whitford, C., Sanchez-Weatherby, J., Shebanova, O., Vergari, C., Winlove, C.P., Terrill, N., Sorensen, T., Elsheikh, A., Meek, K.M., 2018. The hierarchical response of human corneal collagen to load. Acta Biomaterialia 65, 216-225.

Bembey, A.K., Oyen, M.L., Bushby, A.J, Boyde, A., 2006. Viscoelastic properties of bone as a function of hydration state determined by nanoindentation. Philosophical Magazine 86(33-35), 5691-5703.

Benoit, A., Latour, G., Marie-Claire, S.-K., Allain, J.-M., 2015. Simultaneous microstructural and mechanical characterization of human corneas at increasing pressure. Journal of the Mechanical Behavior of Biomedical Materials 60, 93-105.

Bergmanson, J., 2001. Light and electron microscopy. In: Efron, N. (eds.) The cornea: Its Examination in Contact Lens Practice (pp. 137-177). Butterworth-Heinemann, Oxford. UK.

Beshtawi, I., Akhtar, R., Hillarby, M., O'Donnell, C., Zhao, X., Brahma, A., Carley, F., Derby, B., Radhakrishnan, H., 2015. Biomechanical changes of collagen cross-linking on human keratoconic corneas using scanning acoustic microscopy. Current Eye Research 1-7.

Beshtawi, I.M., Akhtar, R., Hillarby, M.C., O'Donnell, C., Zhao, X., Brahma, A., Carley, F., Derby, B., Radhakrishnan, H., 2013. Biomechanical properties of human corneas following low- and high-intensity collagen cross-linking determined with scanning acoustic microscopy. Investigative Ophthalmology & Visual Science 54, 5273-80.

Beuerman, R.W., Pedroza, L., 1996. Ultrastructure of the human cornea. Microscopy Research and Technique 33(4), 320-335.

Binnig, G., Quate, C., Gerber, C., 1986. Atomic force microscope. Physical Review Letters 56, 930.

Blank, R., Boskey, A.L., 2008. Genetic collagen diseases: influence of collagen mutations on structure and mechanical behavior. In: Fratzl P. (eds) Collagen (pp. 447-474). Springer, Boston. USA.

Boote, C., Dennis, S., Huang, Y., Quantock, A., Meek, K., 2005. Lamellar orientation in human cornea in relation to mechanical properties. Journal of Structural Biology 149, 1-6.

Boote, C., Dennis, S., Newton, R., Puri, H., Meek, K., 2003. Collagen fibrils appear more closely packed in the prepupillary cornea: optical and biomechanical implications. Investigative Ophthalmology & Visual Science 44, 2941-2948.

Boote, C., Hayes, S., Abahussin, M., Meek, K., 2006. Mapping Collagen Organization in the Human Cornea: Left and Right Eyes Are Structurally Distinct. Investigative Ophthalmology & Visual Science 47, 901-908.

Boote, C., Kamma-Lorger, C.S., Hayes, S., Harris, J., Burghammer, M., Hiller, J., Terrill, N.J., Meek, K.M., 2011. Quantification of collagen organization in the peripheral human cornea at micron-scale resolution. Biophysical Journal 101, 33-42.

Boschetti, Triacca, Spinelli, Pandolfi, 2012. Mechanical Characterization of Porcine Corneas. Journal of Biomechanical Engineering 134, 031003.

Boyce, B., Grazier, M., Jones, R., Nguyen, T., 2008. Full-field deformation of bovine cornea under constrained inflation conditions. Biomaterials 29, 3896-3904.

Boyce, B.L., Jones, R.E., Nguyen, T.D., Grazier, J.M., 2007. Stress-controlled viscoelastic tensile response of bovine cornea. Journal of Biomechanics 40, 2367-2376.

Boyd, K., 2019. Keratoconus Symptoms. American Academy of Ophthalmology. [Available at: www.aao.org/eye-health/diseases/keratoconus-symptoms] (Accessed: 20th December 2019).

Browning, A.C., Bhan, A., Rotchford, A.P., Shah, S., Dua, H.S., 2004. The effect of corneal thickness on intraocular pressure measurement in patients with corneal pathology. British Journal of Ophthalmology 88(11), 1395-1399.

Bryant, M., McDonnell, P., 1996. Constitutive laws for biomechanical modelling of refractive surgery. the American Society of Mechanical Engineers 118, 473 - 481.

Buskirk, M., 1989. The anatomy of the limbus. Eye 3(2), 101-108.

Cartwright, N., Tyrer, J., Marshall, J., 2011. Age-related differences in the elasticity of the human cornea. Investigative Ophthalmology & Visual Science 52, 4324-4329.

Castoro, J.A., Bettelheim, A.A., Bettelheim, F.A., 1988. Water gradients across bovine cornea. Investigative Ophthalmology & Visual Science 29, 963-958.

Cavas-Martínez, F., Sánchez, E., Martínez, J., Cañavate, F., Fernández-Pacheco, D., 2017. Diagnostic approach of corneal topography maps. In: Alió J. (eds) Keratoconus. Essentials in Ophthalmology (pp. 87-102). Springer, Cham. USA.

Chaerkady, R., Shao, H., Scott, S.G., Pandey, A., Jun, A.S., Chakravarti, S., 2013. The keratoconus corneal proteome: loss of epithelial integrity and stromal degeneration. Journal of Proteomics 87, 122-131.

Chim, Y., Davies, H., Mason, D., Nawaytou, O., Field, M., Madine, J., Akhtar, R., 2019. Bicuspid valve aortopathy is associated with distinct patterns of matrix degradation. The Journal of Thoracic and Cardiovascular Surgery [doi.org/10.1016/j.jtcvs.2019.08.094].

Cholkar, K., Dasari, S.R., Pal, D, Mitra, A.K., 2013. Eye: Anatomy, physiology and barriers to drug delivery. In: Mitra, A. (eds) Ocular Transporters and Receptors (pp. 1-36). Woodhead publishing, Cambridge. UK.

Clark, J., 2004. Order and disorder in the transparent media of the eye. Experimental Eye Research 78, 427-432.

Collier, S., Madigan, M., Penfold, P., 2000. Expression of membrane-type 1 matrix metalloproteinase (MT1-MMP) and MMP-2 in normal and keratoconus corneas. Current Eye Research 21, 662-668.

Collier, S.A., 2001. Is the corneal degradation in keratoconus caused by matrix-metalloproteinases? Clinical & Experimental Ophthalmology 29, 340-4.

Cornuet, P.K., Blochberger, T.C., Hassell, J.R., 1994. Molecular polymorphism of lumican during corneal development. Investigative Ophthalmology & Visual Science 35, 870-7.

DelMonte, D., Kim, T., 2011. Anatomy and physiology of the cornea. Journal of Cataract & Refractive Surgery 37, 588-598.

Dias, J., Ziebarth, N., 2015. Impact of hydration media on *ex vivo* corneal elasticity measurements. Eye and Contact Lens 41, p, 281-286.

Doerner, M.F., Gardner, D.S., Nix, W.D., 1986. Plastic properties of thin films on substrates as measured by submicron indentation hardness and substrate curvature techniques. Journal of Materials Research 1, 845-851.

Dokukin, M., Sokolov, I., 2012. Quantitative mapping of the elastic modulus of soft materials with HarmoniX and PeakForce QNM AFM modes. Langmuir 28, 16060-16071.

Dorronsoro, C., Pascual, D., Pérez-Merino, P., Kling, S., Marcos, S., 2012. Dynamic OCT measurement of corneal deformation by an air puff in normal and cross-linked corneas. Biomedical Optics Express 3, 473-87.

Doutch, J., Quantock, A., Smith, V., Meek, K., 2008. Light transmission in the human cornea as a function of position across the ocular surface: theoretical and experimental aspects. Biophysical Journal 95, 5092-5099.

Doutch, J., Quantock, A.J., Meek, K.M., 2007. Changes in visible light transmission across the corneal stroma. International Society for Optics and Photonics 6535, 65350Q.

Dudea, S.M., 2011. Ultrasonography of the eye and orbit. Medical ultrasonography, 13(2), 171-174.

Dupps, W., Wilson, S., 2006. Biomechanics and wound healing in the cornea. Experimental Eye Research 83, 709-720.

Dupps, W.J., Netto, M.V., Herekar, S., Krueger, R.R., 2007. Surface wave elastometry of the cornea in porcine and human donor eyes. Journal of Refractive Surgery (Thorofare, N.J.: 1995) 23, 66-75.

Eberwein, P., Nohava, J., Schlunck, G, Swain, M., 2014. Nanoindentation derived mechanical properties of the corneoscleral rim of the human eye. Key Engineering Materials 606, 117-120.

Eghrari, A., Gottsch, J., 2014. Fuchs' corneal dystrophy. Expert Review of Ophthalmology 5, 147-159.

Ehlers, N., Heegaard, S., Hjortdal, J., Ivarsen, A., Nielsen, K., Prause, J., 2010. Morphological evaluation of normal human corneal epithelium. Acta Ophthalmologica 88, 858-861.

Eliasy, A., Dong, Z., Studer, H., Boote, C, Elsheikh, A., 2018. Material properties of the human cornea: Anisotropy. In: Robert, C., Downs, W. (eds) Biomechanics of the Eye (pp.81-90) Kugler Publications, Amsterdam, The Netherlands.

Elsheikh, A., Alhasso, D., 2009. Mechanical anisotropy of porcine cornea and correlation with stromal microstructure. Experimental Eye Research 88, 1084-1091.

Elsheikh, A., Alhasso, D., Rama, P., 2008a. Assessment of the epithelium's contribution to corneal biomechanics. Experimental Eye Research 86, 445-451.

Elsheikh, A., Alhasso, D., Rama, P., 2008b. Biomechanical properties of human and porcine corneas. Experimental Eye Research 86, 783-790.

Elsheikh, A., Anderson, K., 2005. Comparative study of corneal strip extensometry and inflation tests. Journal of the Royal Society Interface 2, 177-185.

Elsheikh, A., Wang, D., Brown, M., Rama, P., Campanelli, M., Pye, D., 2007. Assessment of corneal biomechanical properties and their variation with age. Current Eye Research 32, 11-19.

Elsheikh, A., Wang, D., Rama, P., Campanelli, M., Garway-Heath, D., 2008c. Experimental assessment of human corneal hysteresis. Current Eye Research 33, 205-213.

Emre, S., Doganay, S., Yologlu, S., 2007. Evaluation of anterior segment parameters in keratoconic eyes measured with the Pentacam system. Journal of Cataract & Refractive Surgery 33, 1708-1712.

Faria-Correia, F, Ambrósio Jr, R, 2016. Clinical applications of the Scheimpflug principle in ophthalmology. Revista Brasileira de Oftalmologia 75.

Farrell, R.A., McCally, R.L, Tatham, P.E.R., 1973. Wave-length dependencies of light scattering in normal and cold swollen rabbit corneas and their structural implications. The Journal of Physiology, 233(3), 589-612.

Feng, Y., Simpson, T., 2008. Corneal, limbal, and conjunctival epithelial thickness from optical coherence tomography. Optometry and Vision Science 85, E880-E883.

Fercher, A.F., 2010. Optical coherence tomography-development, principles, applications. Zeitschrift für Medizinische Physik, 20(4), 251-276.

Fontes, B.M., Ambrósio Jr, R., Velarde, G.C., Nosé, W., 2011. Corneal biomechanical evaluation in healthy thin corneas compared with matched keratoconus cases. Arquivos Brasileiros De Oftalmologia 74(1), 13-16.

Ford, M., Dupps, W., Rollins, A., Roy, A., Hu, Z., 2011. Method for optical coherence elastography of the cornea. Journal of Biomedical Optics 16, 016005-016005-7.

Ford, M., Seven, I., Dupps, W., DeStefano, V., 2019. *In vivo* measurements of normal, keratoconic, and post crosslinked keratoconic human cornea with optical coherence elastography (Conference Presentation). SPIE, p. 32.

Foster, F.S., Pavlin, C.J., Harasiewicz, K.A., Christopher, D.A., Turnbull, D.H., 2000. Advances in ultrasound biomicroscopy. Ultrasound in Medicine & Biology 26, 1-27.

Fratzl P., 2008. Collagen: Structure and mechanics, an introduction. In: Fratzl P. (eds) Collagen (pp. 1-13). Springer, Boston. USA.

Freund, D.E., McCally, R.L., Farrell, R.A., Cristol, S.M., L'Hernault, N.L., Edelhauser, H.F., 1995. Ultrastructure in anterior and posterior stroma of perfused human and rabbit corneas. Relation to transparency. Investigative Ophthalmology & Visual Science 36, 1508-23.

Fullwood, N.J., Hammiche, A., Pollock, H.M., Hourston, D.J., Song, M., 1996. Atomic force microscopy of the cornea and sclera. Current Eye Research 14, 529-535.

Fullwood, N.J., Meek, K.M., Malik, N.S., Tuft, S.J., 1990. A comparison of proteoglycan arrangement in normal and keratoconus human corneas. Biochemical Society Transactions 18, 961-962.

Funderburgh, J.L., Panjwani, N., Conrad, G.W., Baum, J., 1989. Altered keratan sulfate epitopes in keratoconus. Investigative Ophthalmology & Visual Science 30, 2278-81.

Gabriele, M., Wollstein, G., Ishikawa, H., Kagemann, L., Xu, J., Folio, L., Schuman, J., 2011. Optical coherence tomography: history, current status, and laboratory work. Investigative Ophthalmology & Visual Science 52, 2425-2436.

Galvis, V, Sherwin, T, Tello, A, Merayo, J, Eye, B.-R., 2015. Keratoconus: an inflammatory disorder? Eye 29(7), 843-852.

Gatzioufas, Seitz, 2014. Determination of corneal biomechanical properties *in vivo*: a review. Materials Science and Technology 31, 188-196.

Gelse, Pöschl, Aigner, 2003. Collagens—structure, function, and biosynthesis. Advanced Drug Delivery Reviews 55, 1531-1546.

Gherghel, Hosking, S., Mantry, Banerjee, Naroo, S., Shah, 2004. Corneal pachymetry in normal and keratoconic eyes Orbscan II versus ultrasound. Journal of Cataract & Refractive Surgery 30, 1272-1277.

Godefrooij, D., de Wit, A., Uiterwaal, C., Imhof, S., Wisse, R., 2017. Age-specific Incidence and Prevalence of Keratoconus: A Nationwide Registration Study. American Journal of Ophthalmology 175, 169-172.

Goebels, S., Seitz, B., Langenbucher, A., 2012. Precision of Ocular Response Analyzer. Current Eye Research 37, 689-693.

Goldman, J.N., Benedek, G.B., 1967. The relationship between morphology and transparency in the nonswelling corneal stroma of the shark. Investigative Ophthalmology & Visual Science 6, 574-600.

Gomes, J., Tan, D., Rapuano, C., Belin, M., Ambrósio, R., Guell, J., Malecaze, F., Nishida, K., Sangwan, V., 2015. Global Consensus on Keratoconus and Ectatic Diseases. Cornea 34, 359-369.

Grant, C., Phillips, M., Thomson, N., 2012. Dynamic mechanical analysis of collagen fibrils at the nanoscale. Journal of the Mechanical Behavior of Biomedical Materials 5, 165-170.

Gromacki, S.J, Barr, J.T., 1994. Central and peripheral corneal thickness in keratoconus and normal patient groups. Optometry and Vision Science 71(7), 437-441.

Hamdan, R., Gonzalez, R., Ghostine, S., Caussin, C., 2012. Optical coherence tomography: From physical principles to clinical applications. Archives of Cardiovascular Diseases 105, 529-534.

Han, Z., Li, J., Singh, M., Wu, C., Liu, C., Raghunathan, R., Aglyamov, S., Vantipalli, S., Twa, M., Larin, K., 2017. Optical coherence elastography assessment of corneal viscoelasticity with a modified Rayleigh-Lamb wave model. Journal of the Mechanical Behavior of Biomedical Materials 66, 87-94.

Hart, R.W., Farrell, R.A., 1969. Light scattering in the cornea. Journal of the Optical Society of America 59, 766.

Hassell, J., Birk, D., 2010. The molecular basis of corneal transparency. Experimental Eye Research 91, 326-335.

Hatami-Marbini, H., Etebu, E., 2013. Hydration dependent biomechanical properties of the corneal stroma. Experimental Eye Research 116, 47-54.

Haugstad, G., 2012. Atomic Force Microscopy: Understanding Basic Modes and Advanced Applications. John Wiley & Sons: USA.

Hay, Jennifer, 2015. Dynamic mechanical analysis (DMA) of polymers by oscillatory indentation. KLA-Tencor Company: USA [Available on: http://nanomechanicsinc.com/wp/wp-content/uploads/2015/10/Report-01-2015-09-031.pdf] (Accessed on 4th January 2020).

Hayashi, S., Osawa, T., Tohyama, K., 2002. Comparative observations on corneas, with special reference to bowman's layer and descemet's membrane in mammals and amphibians. Journal of Morphology 254, 247-258.

Hayes, S.A., Goruppa, A.A, Jones, F.R., 2004. Dynamic nanoindentation as a tool for the examination of polymeric materials. Journal of Materials Research 19(11), 3298-3306.

Hayes, S., Boote, C., Lewis, J., Sheppard, J., Abahussin, M., Quantock, A., Purslow, C., Votruba, M., Meek, K., 2007. Comparative study of fibrillar collagen arrangement in the corneas of primates and other mammals. The Anatomical Record: Advances in Integrative Anatomy and Evolutionary Biology 290, 1542-1550.

He, X., Liu, J., 2009. A Quantitative Ultrasonic Spectroscopy Method for Noninvasive Determination of Corneal Biomechanical Properties. Investigative Ophthalmology & Visual Science 50, 5148-5154.

Hedbys, B.O, Mishima, S., 1962. Flow of water in the corneal stroma. Experimental Eye Research 1(3), 262-275.

Hedbys, B.O., Mishima, S., 1966. The thickness-hydration relationship of the cornea. Experimental Eye Research 5, 221-8.

Heichel, J., Wilhelm, F., Kunert, K.S., Hammer, T., 2016. Topographic findings of the porcine cornea. Medical Hypothesis, Discovery and Innovation in Ophthalmology 5, 125-131.

Heiting, G., 2017. Cornea of The Eye [Webpage: All about vision], [Available on: www.allaboutvision.com/resources/cornea.htm.] (Accessed on: 20th December 2019).

Herber, R., Ramm, L., Spoerl, E., Raiskup, F., Pillunat, L., Terai, N., 2019. Assessment of corneal biomechanical parameters in healthy and keratoconic eyes using dynamic bidirectional applanation device and dynamic Scheimpflug analyzer. Journal of Cataract & Refractive Surgery 45(6), 778-788.

Hjortdal, J., 1996. Regional elastic performance of the human cornea. Journal of Biomechanics 29, 931-942.

Ho, L., Harris, A., Tanioka, H., Yagi, N., Kinoshita, S., Caterson, B., Quantock, A., Young, R., Meek, K., 2014. A comparison of glycosaminoglycan distributions, keratan sulphate sulphation patterns and collagen fibril architecture from central to peripheral regions of the bovine cornea. Matrix Biology 38, 59-68.

Hodson, S., O'Leary, D., Watkins, S., 1991. The measurement of ox corneal swelling pressure by osmometry. The Journal of Physiology 434, 399-408.

Hodson, S.A., 1997. Corneal stromal swelling. Progress in Retinal and Eye Research 16, 99-116.

Holland, D.R., Maeda, N., Hannush, S.B., Riveroll, L.H., Green, M.T., Klyce, S.D., Wilson, S.E., 1997. Unilateral keratoconus. Incidence and quantitative topographic analysis. Ophthalmology 104, 1409-13.

Holmes, D., Kadler, K., 2005. The precision of lateral size control in the assembly of corneal collagen fibrils. Journal of Molecular Biology 345, 773-784.

Hon, Y., Lam, A., 2013. Corneal deformation measurement using Scheimpflug noncontact tonometry. Optometry and Vision Science 90, e1 - e8.

Hong, J., Xu, J., Wei, A., Deng, S., Cui, X., Yu, X., Sun, X., 2013. A new tonometer—the Corvis ST tonometer: clinical comparison with noncontact and Goldmann applanation tonometers. Investigative Ophthalmology & Visual Science 54, 659-665.

Iribarren, R., Morgan, I., Nangia, V., Jonas, J., 2012. Crystalline Lens Power and Refractive Error. Investigative Ophthalmology & Visual Science 53, 543-550.

Jalili, N, Laxminarayana, K, 2004. A review of atomic force microscopy imaging systems: application to molecular metrology and biological sciences. Mechatronics 14(8), 907-945.

Jester, J., 2008. Corneal crystallins and the development of cellular transparency. Seminars in Cell & Developmental Biology 19, 82-93.

Jirsova, K., 2017. The cornea, anatomy and function. In Light and Specular Microscopy of the Cornea (pp. 1-21). Springer: USA.

Joseph, R., Srivastava, O.P., Pfister, R.R., 2011. Differential epithelial and stromal protein profiles in keratoconus and normal human corneas. Experimental Eye Research 92(4), 282-298.

Joyce, N.C., 2003. Proliferative capacity of the corneal endothelium. Progress in Retinal and Eye Research, 22(3), 359-389.

Jue, B., Maurice, D., 1986. The mechanical properties of the rabbit and human cornea. Journal of Biomechanics 19, 847-853.

Kaiserman I., Sella S., 2019. Chronic ocular inflammation and keratoconus. In: Barbara A. (eds) Controversies in the Management of Keratoconus (pp. 17-27). Springer, Cham. USA.

Kampmeier, J., Radt, B., Birngruber, R., Brinkmann, R., 2000. Thermal and biomechanical parameters of porcine cornea. Cornea 19, 355-363.

Kantzou, A., 2018. Contact lens fitting: A guide and methodology of contact lens fitting. (PhD thesis) Saera University, Spain. Juniper Publishers Incorporation [Available on: https://juniperpublishers.com/ebooks/Contact%20Lens%20Fitting%20A%20Guide%20and%20Methodology%20of%20Contact%20Lens%20Fitting.pdf]. (Accessed on: 2nd January 2020).

Kao, W.W., Vergnes, J.P., Ebert, J., Sundar-Raj, C.V., Brown, S.I., 1982. Increased collagenase and gelatinase activities in keratoconus. Biochemical and Biophysical Research Communications 107, 929-36.

Kaushik, S, Pandav, S.S., 2012. Ocular response analyzer. Journal of Current Glaucoma Practice 6(1), 17-19.

Kazaili, A., Akhtar, R.R., 2018. Ultrastructural and nanomechanical changes of the cornea following enzymatic degradation. Journal for Modeling in Ophthalmology 2(2) 24-29.

Kazaili, A., Lawman, S., Geraghty, B., Eliasy, A., Zheng, Y., Shen, Y., Akhtar, R., 2019. Line-Field Optical Coherence Tomography as a tool for *In vitro* characterization of corneal biomechanics under physiological pressures. Scientific Reports 9, 6321.

Kenney, C., Brown, D., 2003. The cascade hypothesis of keratoconus. Contact Lens and Anterior Eye 26, 139-146.

Kenyon, K., 1975. Mesenchymal dysgenesis in Peters' anomaly, sclerocornea and congenital endothelial dystrophy. Experimental Eye Research 21, 125-142.

Khaled, M.L., Helwa, I., Drewry, M., Seremwe, M., Estes, A., Liu, Y., 2017. Molecular and histopathological changes associated with keratoconus. BioMed Research International 2017.

Kling, S., Hafezi, F., 2017. Corneal biomechanics - a review. Ophthalmic & physiological optics: the journal of the British College of Ophthalmic Opticians (Optometrists) 37, 240-252.

Kling, S., Marcos, S., 2013. Contributing factors to corneal deformation in air puff measurements. Investigative Ophthalmology & Visual Science 54, 5078-85.

Kling, S., Remon, L., Pérez-Escudero, A., Merayo-Lloves, J., Marcos, S., 2010. Corneal biomechanical changes after collagen cross-Linking from porcine eye inflation experiments. Investigative Ophthalmology & Visual Science 51, 3961-3968.

Klyce, S.D., Beuerman, R.W., 1988. Structure and function of the cornea. In Kaufman, H., Barron, B., McDonald, M., Waltman, S. (eds). The Cornea (pp. 3-54). Churchill Livingstone, New York. USA.

Kolb, H., 2007. Gross anatomy of the eye. In Kolb, H., Fernandez, E., Nelson, R. (eds) Webvision: The Organization of the Retina and Visual System (pp. 1-36) University of Utah Health Sciences Center, Utah. USA. [eBook available on: https://www.ncbi.nlm.nih.gov/books/NBK11530/pdf/Bookshelf_NBK11530.pdf] (accessed on: 4th January 2020).

Koudouna, E., Winkler, M., Mikula, E., Juhasz, T., Brown, D., Jester, J., 2018. Evolution of the vertebrate corneal stroma. Progress in Retinal and Eye Research.

Krachmer, J.H., Feder, R.S., Belin, M.W., 1984. Keratoconus and related noninflammatory corneal thinning disorders. Survey of ophthalmology 28, 293-322.

Larin, K.V., Sampson, D.D., 2017. Optical coherence elastography - OCT at work in tissue biomechanics [Invited]. Biomedical Optics Express 8, 1172-1202.

Last, J., Thomasy, S., Croasdale, C., Russell, P., Murphy, C., 2012. Compliance profile of the human cornea as measured by atomic force microscopy. Micron 43, 1293-1298.

Lawman, S., Dong, Y., Williams, B., Romano, V., Kaye, S., Harding, S., Willoughby, C., Shen, Y.-C., Zheng, Y., 2016. High resolution corneal and single pulse imaging with line field spectral domain optical coherence tomography. Optics Express 24, 12395.

Legkikh, L., Koledintsev, M., Semenova, A., Okuyama, K., 2017. Biochemical investigations of lacrima in early diagnosis of keratoconus. (Abstract) Sangubashi Eye Clinic, Japan. [available on: www.sangubashi.com/English/report/syanhai.htm] (accessed on: 12th January 2020).

Leitgeb, R.A., 2019. En face optical coherence tomography: a technology review [Invited]. Biomedical Optics Express 10, 2177-2201.

Lema, I., Durán, J., 2005. Inflammatory molecules in the tears of patients with keratoconus. Ophthalmology 112, 654-659.

Lema, I., Durán, J., Ruiz, C., Díez-Feijoo, E., Acera, A., Merayo, J., 2008. Inflammatory response to contact lenses in patients with keratoconus compared with myopic subjects. Cornea 27, 758-763.

Leonard, D.W., Meek, K.M., 1997. Refractive indices of the collagen fibrils and extrafibrillar material of the corneal stroma. Biophysical Journal 72, 1382-1387.

Li, T., Tian, L., Wang, L., Hon, Y., Lam, A., Huang, Y., Wang, Y., Zheng, Y., 2015. Correction on the distortion of Scheimpflug imaging for dynamic central corneal thickness. Journal of Biomedical Optics 20, 056006-056006.

Liu, C.-H.H., Schill, A., Raghunathan, R., Wu, C., Singh, M., Han, Z., Nair, A., Larin, K.V., 2017. Ultra-fast line-field low coherence holographic elastography using spatial phase shifting. Biomedical Optics Express 8, 993-1004.

Loh, A., Hadziahmetovic, M., Dunaief, J.L., 2009. Iron homeostasis and eye disease. Biochimica et Biophysica Acta 1790(7), 637-649.

Lombardo, G., Serrao, S., Rosati, M., Lombardo, M., 2014. Analysis of the viscoelastic properties of the human cornea using scheimpflug imaging in inflation experiment of eye globes. PLoS ONE 9, e112169.

Lombardo, M., Lombardo, G., Carbone, G., De Santo, M.P., Barberi, R., Serrao, S., 2012. Biomechanics of the anterior human corneal tissue investigated with atomic force microscopy. Investigative Ophthalmology & Visual Science 53, 1050-7.

Luce, D., 2005. Determining *in vivo* biomechanical properties of the cornea with an ocular response analyzer. Journal of Cataract & Refractive Surgery 31, 156-162.

Mackiewicz, Z., Määttä, M., Stenman, M., Konttinen, L., Tervo, T., Konttinen, Y., 2006. Collagenolytic proteinases in keratoconus. Cornea 25, 603-610.

Martin, R., 2018. Cornea and anterior eye assessment with slit lamp biomicroscopy, specular microscopy, confocal microscopy, and ultrasound biomicroscopy. Indian Journal Ophthalmology 66, 195-201.

Massoudi, D., Malecaze, F., Galiacy, S., 2016. Collagens and proteoglycans of the cornea: importance in transparency and visual disorders. Cell and Tissue Research 363, 337-349.

Mathew, J., Goosey, J., Bergmanson, J., 2011. Quantified histopathology of the keratoconic cornea. Optometry and Vision Science 88, 988-997.

Maurice, 1957. The structure and transparency of the cornea. The Journal of Physiology 136, 263-286.

Maurice, D.M., 1999. Some puzzles in the microscopic structure of the stroma. Journal of Refractive Surgery 15, 692-4.

Maurice, D.M., Monroe, F., 1990. Cohesive strength of corneal lamellae. Experimental Eye Research 50, 59-63.

Mazzotta, C., Rechichi, M, Ferrise, M., 2019. Customized Corneal Cross-Linking. In Controversies in the Management of Keratoconus (pp. 117-144). Springer, Cham: USA.

McCally, R., Farrell, R., 1982. Structural implications of small-angle light scattering from cornea. Experimental Eye Research 34, 99-113.

Meek, K., 2009. Corneal collagen—its role in maintaining corneal shape and transparency. Biophysical Reviews 1, 83-93.

Meek, K., Boote, C., 2004. The organization of collagen in the corneal stroma. Experimental Eye Research 78, 503-512.

Meek, K., Dennis, S., Khan, S., 2003. Changes in the refractive index of the stroma and its extrafibrillar matrix when the cornea swells. Biophysical Journal 85, 2205-2212.

Meek, K., Tuft, S., Huang, Y., Gill, P., Hayes, S., Newton, R., Bron, A., 2005. Changes in collagen orientation and distribution in keratoconus corneas. Investigative Ophthalmology & Visual Science 46, 1948-1956.

Meek, K.M., 2008. The cornea and sclera. In: Fratzl, P. (eds) Collagen (pp. 359-396). Springer, Boston. USA.

Meek, K.M., Blamires, T., Elliott, G.F., Gyi, T.J., Nave, C., 1987. The organisation of collagen fibrils in the human corneal stroma: a synchrotron X-ray diffraction study. Current Eye Research 6, 841-6.

Meek, K.M., Boote, C., 2009. The use of X-ray scattering techniques to quantify the orientation and distribution of collagen in the corneal stroma. Progress in Retinal and Eye Research 28, 369-92.

Meek, K.M., Elliott, G.F., Nave, C., 1986. A synchrotron X-ray diffraction study of bovine cornea stained with cupromeronic blue. Collagen and Related Research 6(2), 203-18.

Meek, K.M, Fullwood, N.J., 2001. Corneal and scleral collagens—a microscopist's perspective. Micron 32(3), 261-272.

Meek, K.M., Knupp, C., 2015. Corneal structure and transparency. Progress in Retinal and Eye Research 49, 1-16.

Menduni, F., Davies, L., Madrid-Costa, Fratini, A., Wolffsohn, J., 2018. Characterisation of the porcine eyeball as an in-vitro model for dry eye. Contact Lens and Anterior Eye 41, 13-17.

Merindano , M.D., J., Canals, M., Potau, J.M., Ruano, D., 2002. A comparative study of Bowman's layer in some mammals: relationships with other constituent corneal structures. European Journal of Anatomy 6, 133-139.

Metzler, K., Roberts, C., Mahmoud, A., Agarwal, G., Liu, J., 2016. *Ex vivo* transepithelial collagen cross-linking in porcine and human corneas using human decorin core protein. Journal of Refractive Surgery 32, 410-417.

Michelacci, Y.M., 2003. Collagens and proteoglycans of the corneal extracellular matrix. Brazilian Journal of Medical and Biological Research 36(8), 1037-1046.

Mikula, E.R., Jester, J.V., Juhasz, T., 2016. Measurement of an elasticity map in the human cornea. Investigative Ophthalmology & Visual Science 57, 3282-3286.

Mohammadi, S., Mazouri, A., Jabbarvand, M., Rahman-A, N., Mohammadi, A., 2011. Sheep practice eye for ophthalmic surgery training in skills laboratory. Journal of Cataract & Refractive Surgery 37, 987-991.

Møller-Pedersen, T., 2004. Keratocyte reflectivity and corneal haze. Experimental Eye Research 78, 553-560.

Møller-Pedersen, T., Cavanagh, D., Petroll, M., Jester, J., 1998. Corneal haze development after PRK is regulated by volume of stromal tissue removal. Cornea 17, 627.

Müller, L., Pels, E., Vrensen, G., 2001. The specific architecture of the anterior stroma accounts for maintenance of corneal curvature. British Journal of Ophthalmology 85, 437.

Nakamura, Riley, Sakai, Rademaker, Yue, B., Edward, 2005. Histopathological and immunohistochemical studies of lenticules after epikeratoplasty for keratoconus. British Journal of Ophthalmology 89, 841-846.

Nash, I., Greene, P., Foster, C.S., 1982. Comparison of mechanical properties of keratoconus and normal corneas. Experimental Eye Research 35, 413-424.

Navarro, R., 2009. The optical design of the human eye: A critical review. Journal of Optometry 2, 3-18.

Newton, R.H., Meek, K.M., 1998. Circumcorneal annulus of collagen fibrils in the human limbus. Investigative Ophthalmology & Visual Science 39, 1125-34.

Ng, P.C, Oliver, J.J., 2018. Anatomy of the eye. In: Long, B., Koyfman, A. (eds) Handbook of Emergency Ophthalmology (pp. 1-12). Springer, Cham: USA.

Nowak, D., Gajecka, M., 2011. The genetics of keratoconus. Middle East African Journal of Ophthalmology 18, 2-6.

Oliver, W.C., Pharr, G.M., 1992. An improved technique for determining hardness and elastic modulus using load and displacement sensing indentation experiments. Journal of Materials Research 7, 1564-1583.

Oliver, W.C., Pharr, G.M., 2004. Measurement of hardness and elastic modulus by instrumented indentation: Advances in understanding and refinements to methodology. Journal of Materials Research 19, 3-20.

Ortiz, D., Piñero, D., Shabayek, M., Arnalich-Montiel, F., Alió, J., 2007. Corneal biomechanical properties in normal, post-laser in situ keratomileusis, and keratoconic eyes. Journal of Cataract & Refractive Surgery 33, 1371-1375.

Owens, H., Gamble, G., 2003. A profile of keratoconus in New Zealand. Cornea 22, 122-125.

Pannebaker, C., Chandler, H.L., Nichols, J.J., 2010. Tear proteomics in keratoconus. Molecular Vision 16, 1949-1957.

Papi, M., Paoletti, P.A.O.L.O., Geraghty, B.R.E.N.D.A.N, Akhtar, R., 2014. Nanoscale characterization of the biomechanical properties of collagen fibrils in the sclera. Applied Physics Letters 104(10), 103703-1-4.

Parfitt, G., Pinali, C., Young, R., Quantock, A., Knupp, C., 2010. Three-dimensional reconstruction of collagen-proteoglycan interactions in the mouse corneal stroma by electron tomography. Journal of Structural Biology 170, 392-397.

Patel, S., Marshall, J., Fitzke, F.W., 1995. Refractive index of the human corneal epithelium and stroma. Journal of Refractive Surgery 11, 100-5.

Patel, S., McLaughlin, J.M., 1999. Effects of central corneal thickness on measurement of intra-ocular pressure in keratoconus and post-keratoplasty. Ophthalmic and Physiological Optics 19(3), 236-241.

Pittenger, B, Erina, N, Su, C, 2010. Quantitative mechanical property mapping at the nanoscale with Peak Force QNM. Application Note Veeco Instruments Inc. p, 1-12. [Available on: https://www.bruker.com/fileadmin/user_upload/8-PDF-Docs/SurfaceAnalysis/AFM /ApplicationNotes/AN128-RevB0Quantitative_Mechanical_Property_Mapping_at_the_ Nanoscale_with_PeakForceQNM-AppNote.pdf] (Accessed on: 12th January 2020).

Piñero, D., Nieto, J., Lopez-Miguel, A., 2012. Characterization of corneal structure in keratoconus. Journal of Cataract & Refractive Surgery 38, 2167-2183.

Prakash, Agarwal, Mazhari, Kumar, Desai, Kumar, Jacob, 2012. A new, pachymetry-based approach for diagnostic cutoffs for normal, suspect and keratoconic cornea. Eye 26, 650.

Prisant, O., Legeais, J.M, Renard, G., 1997. Superior keratoconus. Cornea, 16(6), 693-694.

Quantock, A., Young, R., Akama, T., 2010. Structural and biochemical aspects of keratan sulphate in the cornea. Cellular and Molecular Life Sciences 67, 891-906.

Quintarelli, G., Dellovo, M.C., Balduini, C., Castellani, A.A., 1969. The effects of alpha amylase on collagen-proteoglycans and collagen-glycoprotein complexes in connective tissue matrices. Histochemie 18, 373-375.

Rabinowitz, Y., 1998. Keratoconus. Survey of Ophthalmology 42(4), 297-319.

Rabinowitz, Y., Yang, H., Rasheed, K., Li, X., 2003. Longitudinal analysis of the fellow eyes in unilateral keratoconus. Investigative Ophthalmology & Visual Science 44(13), 1311-1311.

Radner, W., Zehetmayer, M., Aufreiter, R., Mallinger, R., 1998. Interlacing and cross-angle distribution of collagen lamellae in the human cornea. Cornea 17, 537-543.

Ramos, J., Li, Y., Huang, D., 2009. Clinical and research applications of anterior segment optical coherence tomography - a review. Clinical & Experimental Ophthalmology 37, 81-89.

Randleman, J., Khandelwal, S., Hafezi, F., 2015. Corneal cross-linking. Survey of Ophthalmology 60, 509-523.

Randleman, J.B., Dawson, D.G., Grossniklaus, H.E., McCarey, B.E., Edelhauser, H.F., 2008. Depth-dependent cohesive tensile strength in human donor corneas: implications for refractive surgery. Journal of Refractive Surgery 24, S85-S89.

Rantamäki, A., Seppänen-Laakso, T., Oresic, M., Jauhiainen, M., Holopainen, J., 2011. Human Tear Fluid Lipidome: From Composition to Function. PLoS one 6 (5), e19553.

Read, S.A. Collins, M.J., 2011. Intraocular pressure in keratoconus. Acta Ophthalmologica 89(4), 358-364.

Regmi, S., Samsom, M., Heynen, M., Jay, G., Sullivan, B., Srinivasan, S., Caffery, B., Jones, L., Schmidt, T., 2017. Degradation of proteoglycan 4/lubricin by cathepsin S: Potential mechanism for diminished ocular surface lubrication in Sjögren's syndrome. Experimental Eye Research 161, 1-9.

Reitz, C., Breipohl, W., Augustin, A., Bours, J., 1998. Analysis of tear proteins by one-and two-dimensional thin-layer iosoelectric focusing, sodium dodecyl sulfate electrophoresis and lectin blotting. Detection of a new component: cystatin C. Graefe's Archive for Clinical and Experimental Ophthalmology 236(12), 894-899.

Remington, L. A., 2011. Cornea and sclera. In: Remington, L. A. (ed) Clinical Anatomy of The Visual System E-Book (pp. 10-39). Elsevier Health Sciences. USA.

Rho, J.Y., Roy, M.E., Tsui, T.Y, Pharr, G.M., 1999. Elastic properties of microstructural components of human bone tissue as measured by nanoindentation. Journal of Biomedical Materials Research 45(1), 48-54.

Roberts, C.J., 2019. Corneal topography. In: Azar, D. (ed) Refractive Surgery (3rd edition) (pp. 49-57). Elsevier, Germany.

Rodríguez, M., Barroso, L., Sánchez, M., 2018. Collagen: A review on its sources and potential cosmetic applications. Journal of Cosmetic Dermatology 17, 20-26.

Rogers, Attenborough, 2014. Bilateral superior keratoconus: two case reports. Eye 28, 1254.

Romero-Jiménez, M., Santodomingo-Rubido, J., Wolffsohn, J., 2010. Keratoconus: A review. Contact Lens and Anterior Eye 33(4), 157-166.

Rosales, P., Marcos, S., 2009. Pentacam scheimpflug quantitative imaging of the crystalline lens and intraocular lens. Journal of Refractive Surgery 25, 421-8.

Salapaka, MV, Cleveland, JP, 1998. Stability and sensitivity analysis of periodic orbits in tapping mode atomic force microscopy. In proceedings of the 37th IEEE Conference on Decision and Control (Cat. No. 98CH36171) (Vol. 2, pp. 2047-2052).

Sanchez, I., Martin, R., Ussa, F., Fernandez-Bueno, I., 2011. The parameters of the porcine eyeball. Graefe's Archive for Clinical and Experimental Ophthalmology 249(4), 475-482.

Sawaguchi, S., Yue, B., Sugar, J., Gilboy, J., 1989. Lysosomal enzyme abnormalities in keratoconus. Archives of Ophthalmology 107, 1507-1510.

Sawaguchi, S., Yue, B.Y., Chang, I., Sugar, J., Robin, J., 1991. Proteoglycan molecules in keratoconus corneas. Investigative Ophthalmology & Visual Science 32, 1846-53.

Scarcelli, G., Besner, S., Pineda, R., Kalout, P., Yun, S., 2015. *In vivo* biomechanical mapping of normal and keratoconus corneas. JAMA Ophthalmology 133, 480-482.

Scarcelli, G., Besner, S., Pineda, R., Yun, S., 2014. Biomechanical characterization of keratoconus corneas *ex vivo* with Brillouin microscopy evaluation of Brillouin microscopy for keratoconus. Investigative Ophthalmology & Visual Science 55, 4490-4495.

Scarcelli, G., Kling, S., Quijano, E., Pineda, R., Marcos, S., Yun, S., 2013. Brillouin microscopy of collagen crosslinking: noncontact depth-dependent analysis of corneal elastic modulus. Investigative Ophthalmology & Visual Science 54, 1418-1425.

Scott, Haigh, 1985. "Small"-proteoglycan: collagen interactions: Keratan sulphate proteoglycan associates with rabbit corneal collagen fibrils at the "a" and "c" bands. Bioscience Reports 5, 765-774.

Seppälä, H., Määttä, M., Rautia, M., Mackiewicz, Z., Tuisku, I., Tervo, T., Konttinen, Y., 2006. EMMPRIN and MMP-1 in keratoconus. Cornea 25, 325-330.

Sethi, C.S., Bailey, T.A., Luthert, P.J., Chong, N.H., 2000. Matrix metalloproteinase biology applied to vitreoretinal disorders. British Journal of Ophthalmology 84, 654-66.

Shafaie, S., Hutter, V., Cook, M., Brown, M., Chau, D., 2016. *In vitro* cell models for ophthalmic drug development applications. BioResearch Open Access 5, 94-108.

Shah, S., Laiquzzaman, M., Bhojwani, R., Mantry, S., Cunliffe, I., 2007. Assessment of the biomechanical properties of the cornea with the ocular response analyzer in normal and keratoconic eyes. Investigative Ophthalmology & Visual Science 48, 3026-3031.

Sharp, P.F, Philips, R., 1997. Physiological optics. In: Hendee, W., Wells, P. (eds) The Perception of Visual Information (pp. 1-32). Springer, New York, NY.

Sherman, V.R., Yang, W., Meyers, M.A., 2015. The materials science of collagen. Journal of the Mechanical Behavior of Biomedical Materials 52, 22-50.

Sherwin, T., Ismail, S., Loh, I.-P., McGhee, J., 2017. Histopathology (from Keratoconus Pathology to Pathogenesis). In: Alió J. (eds) Keratoconus. Essentials in Ophthalmology. Springer, Cham. USA.

Silverman, R., 2009. High-resolution ultrasound imaging of the eye - a review. Clinical & Experimental Ophthalmology 37, 54-67.

Singh, M., Li, J., Han, Z., Raghunathan, R., Nair, A., Wu, C., Liu, C.-H., Aglyamov, S., Twa, M., Larin, K., 2016. Assessing the effects of riboflavin/UV-A crosslinking on porcine corneal mechanical anisotropy with optical coherence elastography. Biomedical Optics Express 8, 349.

Singh, M., Wu, C., Liu, C.-H., Li, J., Schill, A., Nair, A., Larin, K., 2015. Phase-sensitive optical coherence elastography at 15 million A-Lines per second. Optics Letters 40, 2588.

Smith, J.W., 1968. Molecular pattern in native collagen. Nature 219, 157-158.

Smolek, M.K., 1993. Interlamellar cohesive strength in the vertical meridian of human eye bank corneas. Investigative Ophthalmology & Visual Science 34, 2962-2969.

Sneddon, I., 1965. The relation between load and penetration in the axisymmetric boussinesq problem for a punch of arbitrary profile. International Journal of Engineering Science 3, 47-57.

Spoerl, E., Huhle, M., Seiler, T., 1998. Induction of cross-links in corneal tissue. Experimental Eye Research 66, 97-103.

Stamper, L, Lieberman, M.F., Drake, M.V., 2009. Aqueous humor formation. In: Stamper, L, Lieberman, M.F., Drake, M.V. (eds) Becker-Shaffer's Diagnosis and Therapy of the Glaucomas (8th edition) (pp. 8-24). Elsevier Health Sciences. USA.

Sugar, J, Macsai, M.S., 2012. What causes keratoconus?. Cornea 31(6), 716-719.

Sun, C., Liu, H., Jia, M., Chen, S., 2018. Review of calibration methods for Scheimpflug camera. Journal of Sensors 2018, 1-15.

Svaldenienė, E, Babrauskienė, V, Zoot, P.-M., 2003. Structural features of the cornea: light and electron microscopy. Veterinarija ir Zootechnika. Kaunas 24(46).

Tanihara, H., Inatani, M., Koga, T., Yano, T., Kimura, A., 2002. Proteoglycans in the Eye. Cornea 21, S62-S69.

Tao, A., Wang, J., Chen, Q., Shen, M., Lu, F., Dubovy, S., Shousha, M., 2011. Topographic thickness of Bowman's layer determined by ultra-high resolution spectral domain-optical coherence tomography. Investigative Ophthalmology & Visual Science 52, 3901-3907.

Thomasy, S., Raghunathan, V., Winkler, M., Reilly, C., Sadeli, A., Russell, P., Jester, J., Murphy, C., 2014. Elastic modulus and collagen organization of the rabbit cornea: Epithelium to endothelium. Acta Biomaterialia 10, 785-791.

Tian, L., Huang, Y.-F., Wang, L.-Q., Bai, H., Wang, Q., Jiang, J.-J., Wu, Y., Gao, M., 2014. Corneal biomechanical assessment using corneal visualization scheimpflug technology in keratoconic and normal eyes. Journal of Ophthalmology 2014, 1-8.

Touboul, D., Bénard, A., Mahmoud, A., Gallois, A., Colin, J., Roberts, C., 2011. Early biomechanical keratoconus pattern measured with an ocular response analyzer: Curve analysis. Journal of Cataract & Refractive Surgery 37, 2144-2150.

Van Haeringen, N.J., Ensink, F., Glasius, E., 1975. Amylase in human tear fluid: Origin and characteristics, compared with salivary and urinary amylases. Experimental Eye Research 21, 395-403.

Van Haeringen, N.J., Glasius, E., 1976. The origin of some enzymes in tear fluid, determined by comparative investigation with two collection methods. Experimental Eye Research 22, 267-72.

Van Landingham, M.R., 2003. Review of Instrumented Indentation. Journal of Research of the National Institute of Standards and Technology, 108(4), 249-65.

Vellara, H., Patel, D., 2015. Biomechanical properties of the keratoconic cornea: a review. Clinical and Experimental Optometry 98, 31-38.

Volatier, T.L., Figueiredo, F.C., Connon, C.J., 2019. Keratoconus at a molecular level: A review. The Anatomical Record 1,1-5. [doi:10.1002/ar.24090].

Wang, L., Tian, L., Huang, Y., Huang, Y., Zheng, Y., 2018. Assessment of corneal biomechanical properties with inflation test using optical coherence tomography. Annals of Biomedical Engineering 46, 247-256.

Wang, S., Larin, K., 2015. Optical coherence elastography for tissue characterization: a review. Journal of Biophotonics 8, 279-302.

Ward, P.P., Paz, E., Conneely, O.M., 2005. Lactoferrin. Cellular and molecular life sciences 62(22), 2540.

Weed, K.H., McGhee, C.N.J., MacEwen, C.J., 2005. Atypical unilateral superior keratoconus in young males. Contact Lens and Anterior Eye 28, 177-179.

Wheeler, J., Hauser, M. A., Afshari, N. A., Allingham, R. R., & Liu, Y. 2012. The Genetics of Keratoconus: A Review. Reproductive system & sexual disorders: current research, (Suppl 6), 001. [doi:10.4172/2161-038X.S6-001].

Whitford, C., Joda, A., Jones, S., Bao, F., Rama, P., Elsheikh, A., 2016. *Ex vivo* testing of intact eye globes under inflation conditions to determine regional variation of mechanical stiffness. Eye and Vision 3, 21.

Wilson, S.E., Hong, J.W., 2000. Bowman's layer structure and function: critical or dispensable to corneal function? A hypothesis. Cornea 19, 417-20.

Winkler, M., Shoa, G., Tran, S., Xie, Y., Thomasy, S., Raghunathan, V., Murphy, C., Brown, D., Jester, J., 2015. A comparative study of vertebrate corneal structure: The evolution of a refractive lens vertebrate corneal structure. Investigative Ophthalmology & Visual Science 56, 2764-2772.

Wollensak, G., Spoerl, E., 2004. Collagen crosslinking of human and porcine sclera. Journal of Cataract & Refractive Surgery 30, 689-695.

Wollensak, G., Spörl, E., Mazzotta, C., Kalinski, T., Sel, S., 2011. Interlamellar cohesion after corneal crosslinking using riboflavin and ultraviolet A light. British Journal of Ophthalmology 95, 876-880.

Xu, Y.-G.G., Xu, Y.-S.S., Huang, C., Feng, Y., Li, Y., Wang, W., 2008. Development of a rabbit corneal equivalent using an acellular corneal matrix of a porcine substrate. Molecular Vision 14, 2180-9.

Yang, Y., Xiao, X., Peng, Y., Yang, C., Wu, S., Liu, Y., Yue, T., Pu, H., Liu, N., Jiang, H., 2019. The comparison between force volume and Peak Force quantitative nanomechanical mode of atomic force microscope in detecting cell's mechanical properties. Microscopy Research and Technique 82, 1843-1851.

Yaylali, V., Kaufman, S.C., Thompson, H.W., 1997. Corneal thickness measurements with the Orbscan Topography System and ultrasonic pachymetry. Journal of Cataract & Refractive Surgery 23, 1345-50.

Young, M., Burnett, B., Ogin, S., 2011. The use of the PeakForce™ quantitative nanomechanical mapping AFM-based method for high-resolution Young's modulus measurement of polymers. Measurement Science and Technology 22, 125703.

Zeng, Y., Yang, J., Huang, K., Lee, Z., Lee, X., 2001. A comparison of biomechanical properties between human and porcine cornea. Journal of Biomechanics 34, 533-537.

Chapter 3

Microscale assessment of corneal viscoelastic properties under physiological pressures

This chapter presents a novel method for assessment of corneal viscoelastic properties under physiological pressures. The microscale viscoelastic properties (the shear storage and shear loss modulus) and apical thickness of porcine corneas under various pressures are presented. In addition, a map showing the distribution of the elastic modulus under IOP across the surface of the cornea is shown. Finally, the results are discussed and compared with previous studies.

Abstract

The micromechanical behaviour of the cornea is important for understanding and modelling of many ocular disorders. Whereas inflation testing has been utilised to determine the bulk mechanical properties of the cornea under physiological pressures, micromechanical testing has been limited to unpressurised corneal samples. In this study the micromechanical properties of pressurised porcine corneas were determined using oscillatory nanoindentation coupled with a custom inflation method. Inflation was conducted in phosphate buffered saline (PBS) and tissue culture (TC) solutions. The shear storage modulus (G′) and shear loss modulus (G″) was determined for corneas inflated corneas with PBS and TC. Central corneal thickness (CCT) was monitored during the inflation (0-60 mmHg). Elastic modulus (E) was also calculated and quantitatively mapped for corneas. The results showed that G' at 15 mmHg was 86.18 ± 16 kPa and 88.86 + 13.54 kPa inflated by PBS and TC respectively. These values increased 3.2 times in an approximate linear relationship to 60 mmHg. G″ at 15 mmHg was 12.5 ± 2.5 kPa and 13.54 + 1.9 kPa inflated by PBS and TC respectively. G″ increased 1.9 times in an approximate linear relationship to 60 mmHg. No significant change was noticed in viscoelastic properties of corneas inflated by TC for 4 hours whereas 4 hours of hydration on PBS affected the mechanical properties. The central corneal region was found to be stiffer than in peripheral region. Mapping of elasticity revealed a symmetrical distribution of properties that varied with inflation. The current method has potential for measurement of viscoelastic properties of corneas in conditions where there have been localised changes in mechanical properties such as keratoconus.

3.1. Introduction

The cornea is the principle refractive element of the eye which has a natural curvature and is transparent. These properties of the cornea arise from it being under intraocular pressure (IOP). The structural and optical properties of the cornea can largely be attributed to the stromal layer, which represents around 90 % of the corneal thickness. The stromal layer is composed of collagen fibres which provide the cornea with mechanical properties and are also responsible for corneal transparency. Conventionally, *in vitro* experimental testing has been conducted on isolated corneal strips with uniaxial testing, requiring preconditioning to align the collagen fibres. Additionally, in such a test the corneal tissue is not under physiological pressure. The importance of considering the microstructure of the cornea under physiological pressures and how that influences the mechanical behaviour of the tissue has been highlighted in a recent study (Benoit *et al*, 2016). In that study, polarization-resolved second harmonic generation microscopy (P-SHG) was combined with inflation testing as a novel approach to capture both surface strain and the evolution of collagen fibril re-organisation with increasing pressure in human corneas. The organisation of collagen lamellae was recorded across pressures from 12 mmHg-48 mmHg. Benoit *et al* demonstrated that the stromal microstructure is modified with increased IOP. Interesting, they demonstrated that the preferential orientation of collagen lamellae differed across different regions of the cornea as the pressure increased.

Given this insight into how the stromal microstructure is altered across different regions as pressure increases, this study hypothesised that a micromechanical approach such as nanoindentation could be used to capture regional variations in the viscoelastic behaviour of the cornea with increasing pressure. Nanoindentation is powerful and established technique for measuring small volumes of material. In recent years, approaches have been developed to utilise nanoindentation for hydrated biological tissues (Labate *et al*, 2015; Last *et al*, 2012, 2010, 2009; Lombardo *et al*, 2012; Oyen, 2015). Whilst there are a number of challenges that need to be overcome when utilising commercial instruments for testing of hydrated and compliant materials such as hydrogels and biological soft tissues, research to date has mostly focussed on analytical methods or technique development for maintaining hydration whilst testing. A major gap in biomechanical testing of soft tissues is the ability to conduct micro-scale testing under physiological pressure. This is important not only because the fibrous architecture is completely different to tissue in its relaxed (unpressurised) state (Walton *et al*, 2015), but, as already demonstrated for the cornea, the mechanical response and anisotropy of the cornea is significantly altered at high physiological pressures (Benoit *et al*, 2016; Singh *et al*, 2016).

This study has utilised oscillatory nanoindentation coupled with inflation testing. The oscillatory nanoindentation method has previously been used for mechanical characterisation of hydrogels (Akhtar *et al*, 2018, 2016) canine articular cartilage (Peters *et al*, 2017) and porcine skin (Moronkeji *et al*, 2017). One of the main advantages of using this approach is the ability of probing regional locations of the cornea. Hence, when coupled with inflation testing this approach has significant advantages over macroscale inflation testing that is more widely used in the literature (Boyce *et al*, 2008; Elsheikh *et al*, 2008; Whitford *et al*, 2016).

The current study focuses on porcine corneas and demonstrate how the shear storage and loss modulus vary with increasing IOP (0-60 mmHg) across the central cornea. The inflation testing is conducted in phosphate buffered saline (PBS) and tissue culture medium (TC) to explore the role of different hydrating media. Corneal swelling and mechanical properties are also considered in terms of hydration time. Finally, the micromechanical properties are mapped across different regions of the cornea demonstrating the full potential of the current technique.

3.2. Aim

This chapter focuses on measuring viscoelastic properties of inflated porcine corneas and demonstrate how the shear storage and loss modulus vary with increasing IOP (0 to 60 mmHg) across the central cornea. The inflation testing is conducted in phosphate buffered saline (PBS) and tissue culture medium (TC) to explore the role of different hydrating media. Corneal swelling and mechanical properties are also considered in terms of hydration time. Finally, the micromechanical properties are mapped across different regions of the cornea demonstrating the full potential of the current technique.

3.3. Materials and methods

3.3.1. Sample preparation

Thirty-four fresh porcine eyes were obtained from a local abattoir shortly after slaughter. The pigs were aged between 5 and 6 months. The epithelium layer was peeled off from the corneas using a cotton-tipped applicator and tweezers. This was done to ensure consistency with results explained in later chapters. The corneas, with a 2 mm scleral ring, were subsequently dissected and placed in a specially designed artificial anterior chamber (shown in Appendix I). The corneas were split into two experimental setups as summarised in Table 3.1. The number of indents and experimental setting are explained in the following sections.

Table 3.1: Summary of the experimental setup used within the study.

	Experiment 1		Experiment 2		
Incubation solution	TC	PBS	PBS	PBS	PBS
Number of corneas (n)	8	8	6	6	6
IOP (mmHg)	0 - 60	0 - 60	0	15	60
Indented region	Central		Central to limbus		
Incubation period (hours)	0, 4		0		
No. of indents per IOP	3		49		
Acquired data	G′, G″, E, tan(δ), CCT		E		

TC: tissue culture, PBS: phosphate buffered saline, G′: shear storage modulus, G″: shear loss modulus, E: elastic modulus, tan(δ): loss factor, CCT: central corneal thickness. Experiment 1: Micromechanical characterisation under pressure, Experiment 2: Micromechanical mapping under pressure.

3.3.2. Experiment 1: Micromechanical characterisation under pressure

Sixteen corneas were divided into two groups categorised by the solution used to inflate the samples: Tissue culture solution (TC-0h group; n = 8) or phosphate buffered saline (PBS-0h group; n = 8). An elevated reservoir was filled with either TC solution (CARRY-C, ALCHIMIA, Italy) or PBS (Sigma-Aldrich, Dorset, UK). The solutions were used to apply hydraulic pressure to the posterior surface of the corneas, simulating intraocular pressures (IOP) in the range 0-60 mmHg. The pressure was controlled by the height of the reservoir and measured using a pressure sensor (ABP series, Honeywell, USA). The experimental setup is shown in Figure 3.1.

The micromechanical testing was conducted with a Nanoindenter G200 system with a dynamic contact module II head (DCM-II, KLA-Tencor company, CA, USA). A cylindrical flat punch tip with a 100 µm diameter (Synton-MDP Ltd, Nidau, Switzerland) was utilised with the DCM-II indenter head. A custom, dome-shaped corneal holder was used to hold the corneas in place. In principle, this setup enabled the viscoelastic properties of the cornea to be measured at any point on the cornea with the spatial resolution limited by the indenter tip radius (100 µm). Oscillatory nanoindentation was conducted to determine the shear storage (G') and shear loss modulus (G") using a method which has been described in detail elsewhere (Akhtar *et al*, 2018, 2016) and summarised in Chapter 2.

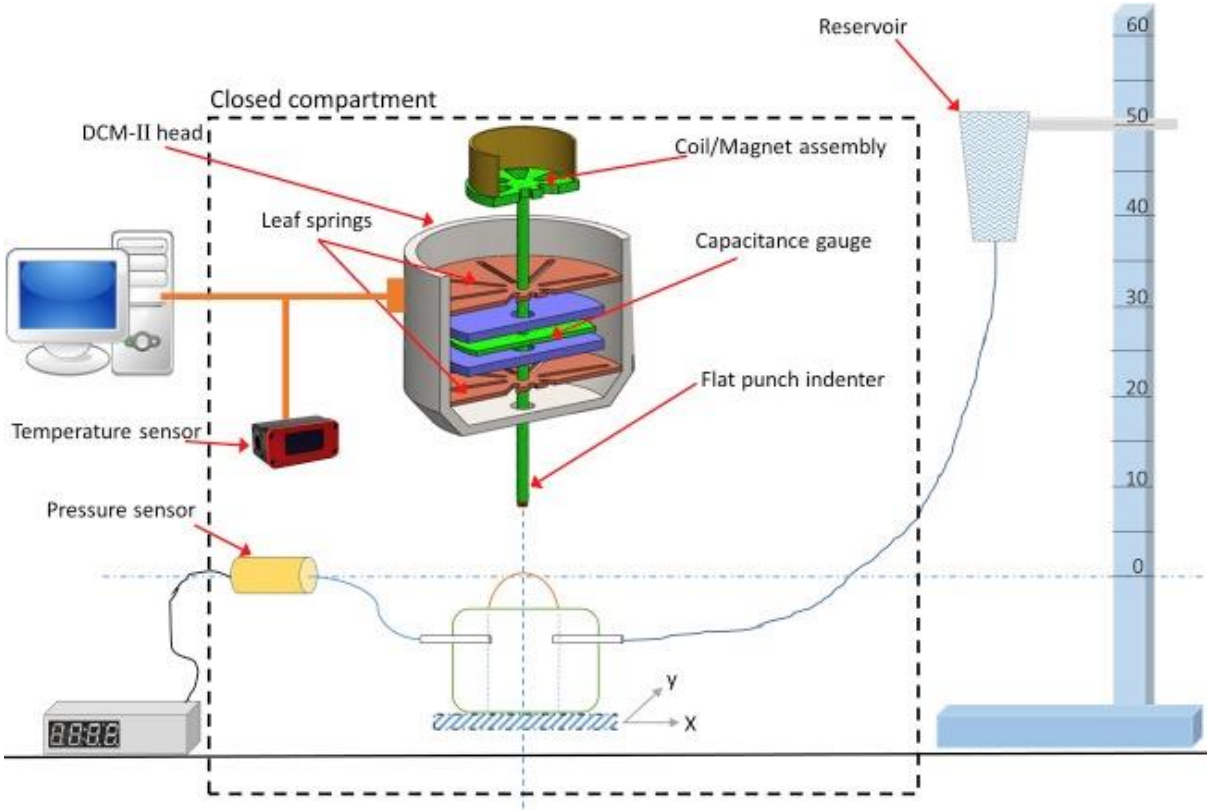

Figure 3.1: Schematic diagram which shows a sketch of DCM-II head and the experimental setup that was used to vary the IOP during the nanoindentation process. The cornea was placed at the same level as the pressure sensor and zero pressure level. The DCM-II head consists of coil/magnet assembly, capacitance gauge, leaf spring and oscillation transducer (with permission form KLA Instruments Group). The coil/magnet assembly generates controlled forces by using an electromagnetic system. The capacitance gauge is used for sensing displacement. Leaf springs are used to secure the indentation column for stability and maximum lateral stiffness. All of the testing was conducted in a closed compartment to minimise any external mechanical vibrations.

The apex of the inflated corneas was indented 3 times at each IOP level. Each indent was performed with a 700 µm distance between each indent, thus covering a total distance of 1700 µm in the peripapillary region of the cornea. The apex of the inflated corneas was defined using the built-in microscope of the nanoindenter, which was in-line with the centre point of the controlled stage, where the corneal holder was placed. In the video image generated for the inflated corneas, the apex was brighter than other points. A pre-compression of 5 µm was chosen that provided sufficient contact of the tip with the corneal apex surface, which was also used in a previous study on soft tissue (Akhtar *et al*, 2016). An oscillation amplitude of 500 nm and testing frequency of 110 Hz (the resonant frequency of the indenter head) was selected for all experiments. The indenter tip was cleaned by driving into double-sided Scotch Tape (3M) after each set of 3 indents. The testing and tip cleaning at each pressure step took approximately 12 min.

The elastic modulus was calculated using Equation 3.1.

$$E = 2\,G'(1+v) \tag{3.1}$$

where ν represents the Poisson's ratio of the cornea which was assumed to be 0.4 based on a previous study (Ford *et al*, 2011).

Central corneal thickness (CCT) was measured at 0 mmHg and then in 5 mmHg increments up to 60 mmHg by using a Pachymeter (DGH 55 Pachmate, DGH Technology Inc, USA). The accuracy of the pachymeter used was suitable because the manufacturer's specifications state that its accuracy is 5 μm. Both the mechanical measurements and the corneal thickness measurements at each IOP level were repeated after 4 hours for both groups to detect any time-dependent changes. The 4 hours timeframe was between the testing at 0 mmHg of the first experiment and the testing at 0 mmHg of the second experiment. The corneas were kept in the holder in a relaxed state immersed in the same solution that was used for inflation. By Keeping the corneas in the holder ensured the ability of indenting the same area in each experiment.

All of the experiments were carried out at room temperature (approximately 22 °C) and 45 ± 2.1% relative humidity, as determined with a humidity-temperature meter (OMEGA engineering, USA). One drop (40 μl) of PBS (Sigma-Aldrich, Dorset, UK) was applied on the external surface of the corneas at every pressure step to maintain the hydration of the tissue.

3.3.3. Experiment 2: Micromechanical mapping under pressure

Twelve corneas were used to map the elastic properties across the surface of the cornea under pressure; 15 mmHg (n = 6), and 60 mmHg (n = 6). A further 6 corneas were used under unpressurised conditions (0 mmHg). The samples were prepared using the same method as described in 2.1. The orientation of corneas (nasal-temporal and superior-inferior) were marked when the samples were fixed on the dome-shaped sampled holder. The corneas were inflated with TC media and indented in an array covering 49 indents. The same experimental settings as described earlier were used for all of the nanoindentation tests except that the pre-compression value was increased to 7 μm. This higher value was required to make better contact with corneal surface at the peripheral region. The indent matrix covered a square region of 9 × 9 mm to map the micromechanical properties of the sclera; the centre of the matrix was on the apex of the cornea. The corneal Elastic modulus was calculated from the shear storage modulus as described

earlier. A MATLAB code (Mathworks Company, Natick, Massachusetts, USA) was used to create a contour map showing the distribution of the elastic modulus under IOP across the surface of the cornea.

3.3.4. Statistical analysis

All statistical analysis was carried out using OriginPro 2016 version 9.3 (OriginLab, USA). All data are expressed as mean values and standard deviation (mean ± standard deviation). In order to determine statistical significance for the changes in shear storage and loss modulus and CCT at each IOP, paired Sample t-Tests were used. In order to determine statistical significance for changes in shear storage and loss modulus and CCT for the two incubation solution groups, unpaired Two sample t-Test was used. For nonparametric data (micromechanical mapping data), the Mann-Whitney test was used. The significance level (α) was set as 0.05 for all tests.

3.4. Results

3.4.1. Micromechanical properties under IOP

The shear storage modulus (G'), shear loss modulus (G"), loss factor (tan(δ)) and the calculated elastic modulus of the inflated porcine corneas are shown in Figure 3.2. An approximate linear relationship was observed between viscoelastic shear moduli and the applied internal pressure; as the internal pressure increases, the viscoelastic shear moduli also increases ($R2 > 0.9$). The loss factor (ratio of G"/G') was initially very high in the unpressurised cornea (>0.6) but reduced to around 0.1 as the IOP increased, Figure 3.2C. Hence, the viscous behaviour of the cornea was significantly diminished with increasing IOP. Overall, the trends in G', G" and tan(δ) were comparable across both time points and for both hydrating solutions. G′ following 4 hours of hydration in PBS deviated most from the other tests, as evident in Figure 3.2A.

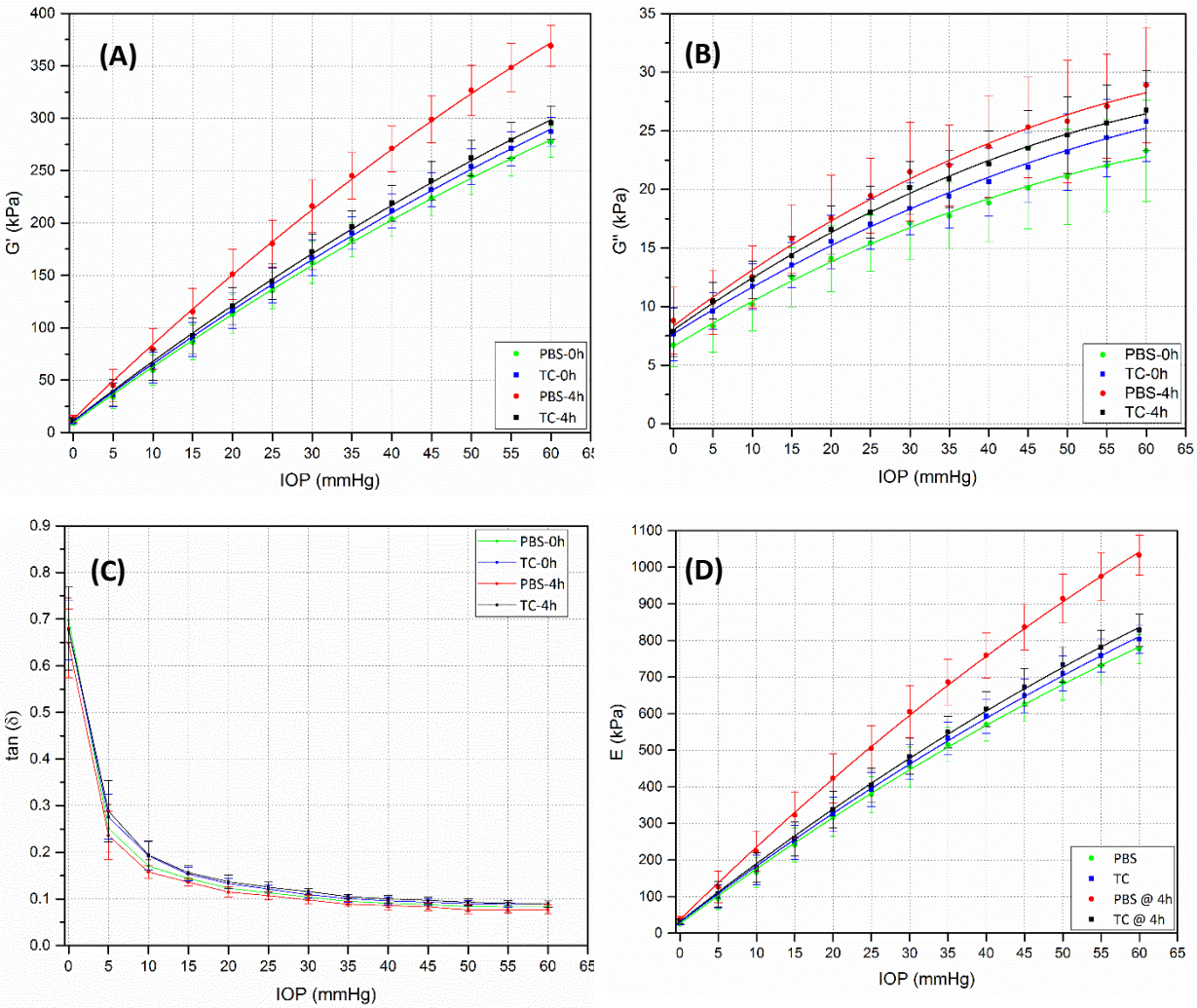

Figure 3.2: Micromechanical properties of the cornea under IOP (A) shear storage modulus (G'), (B) shear loss modulus (G''), (C) loss factor (tan(δ)), and (D) elastic modulus (E). Error bars represent standard deviation. (n = 8/group). PBS-4h refers to the same corneas that were initially inflated by PBS and then retested after 4 hours. TC-4h refers to the same corneas that were initially inflated by TC and then retested after 4 hours.

The elastic modulus of inflated porcine corneas is illustrated in Figure 3.2D. At normal physiological pressure of porcine eyes inflated with PBS, G' is 86.19 ± 16.6 kPa and E is 241.3 ± 46.5 kPa.

Statistical analysis shows that there is no significant increase in G' between PBS-group and TC-group, (PBS-0h) and (TC-0h), when they were initially tested ($p \geq 0.201$). There was no statistically significant increase in G' of corneas that were initially inflated by TC and the same corneas when retested after 4 hours ($p \geq 0.073$). In contrast, corneas inflated by PBS behaved differently; the shear storage modulus was significantly increased (33.7%) for corneas when retested after 4 hours

($p \leq 0.00013$). A significant difference in G' was seen (25%) between corneas in different groups when retested after 4 hours ($p \leq 0.000035$).

When comparing the viscous component for the corneas inflated by the solutions, it was found that G" was approximately 6% higher in TC-0h group as compared to PBS-0h group. However, this difference was not statistically significant ($p = 0.221$). Interestingly, there was no significant increase in G" of corneas initially inflated by TC (TC-0h group) and the same corneas when retested after 4 hours (TC-4h group), ($p \geq 0.409$). Unlike the corneas inflated by TC, a significant increase in G" was observed (25%) between corneas initially inflated by PBS (PBS-0h group) and the same corneas when retested after 4 hours (PBS-4h), ($p \leq 0.029$). Non-significant difference in G" was detected between corneas in different groups when retested after 4 hours (TC-4h and PBS-4h groups), ($p \geq 0.324$).

The loss factor was 5% lower between corneas of PBS-0h group and the same corneas when retested after 4 hours (PBS-4h), ($p \leq 0.0408$). On the other hand, there was no statistical difference in the loss factor between the two time points for corneas inflated by TC ($p \geq 0.1802$). The loss factor of corneas in PBS-0h group was 6% lower than that of corneas in TC-0h group but not statistically significant ($p \geq 0.183$). This difference became statistically significant when the corneas of both groups (PBS-4h and TC-4h) were retested ($p \leq 0.0391$).

3.4.2. Central corneal thickness

In all the groups, central corneal thickness (CCT) decreased as IOP increased, as shown in Figure 3.3. The extent of this change differed in each of the groups. Initially, CCT of the TC-0h group was decreasing gradually for the first three IOP values in a similar manner to the PBS-0h group. Subsequently, the difference in CCT between PBS-0h and TC-0h groups became statistically significant after 15 mmHg (about 1.6% reduction), ($p < 0.036$), which correlates to more than 37 min in the inflating solutions. The results of retesting the corneas after 4 hours showed that CCT of the PBS-4h group significantly increased (approximately 9.3%), as compared to corneas in the PBS-0h group. In comparison, CCT of the TC-4h significantly decreased (approximately 11%) than when the corneas were initially tested. The maximum difference in CCT (about 19.8%) was observed between the swollen corneas in PBS (PBS-4h group) and the contracted corneas in TC (TC-4h group), and these differences were found to be statistically significant ($p < 0.0001$). Overall, the rate of CCT decrease was found to be lowest in TC after 4 hours.

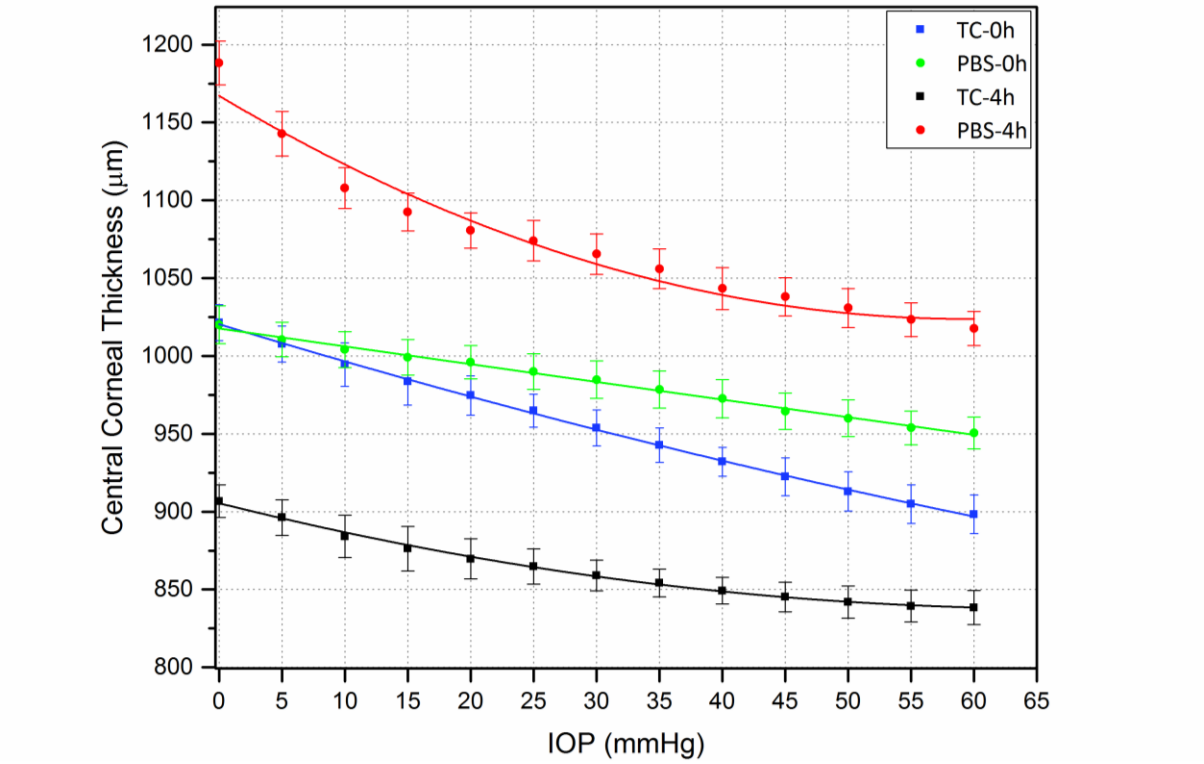

Figure 3.3: Central corneal thickness of porcine corneas. Error bars represent standard deviation. (n = 8/group). PBS-4h refers to the same corneas that were initially inflated by PBS and then retested after 4 hours. TC-4h refers to the same corneas that were initially inflated by TC and then retested after 4 hours.

3.4.3. Quantitative microscale mapping

Figure 3.4 demonstrates quantitative microscale mapping for the porcine corneas at 0, 15 and 60 mmHg. These elastic modulus maps show that corneal apex is significantly stiffer than that at para-central and peripheral regions of the corneas, $p \leq 0.05$. The inflated corneas (at 15 and 60 mmHg) exhibited an almost symmetric distribution of elastic modulus, as evident in Figure 3.4b and c. Here, the elastic modulus was decreasing circumferentially in intervals from the centre toward the furthest point, near the limbus region. In the uninflated corneas (0 mmHg) there was an unremarkable distribution of elastic modulus as evident from Figure 3.4A. Here, there was a small variation in elasticity between the centre and all of the other regions of the cornea. The elastic modulus at the centre of the uninflated corneas was 23.7 ± 5.7 kPa and decreased by 5% at the peripheral cornea. The apex corneal elastic modulus was 228.314 ± 10.7 kPa at 15 mmHg and decreased by 11.5% in the far peripheral region. A line of data from the nasal to the temporal region passing through the apex of inflated cornea at 15 mmHg can be represented by Equation 3.2, (R = 0.995).

$$E(x) = 0.065x^4 + 0.0172x^3 - 2.757x^2 - 0.2625x + 228.65 \quad (3.2)$$

where x is the location of a point on the line from the nasal to the temporal regions passing through the apex of the cornea, i.e., the point x = 0 is located at the centre of the cornea.

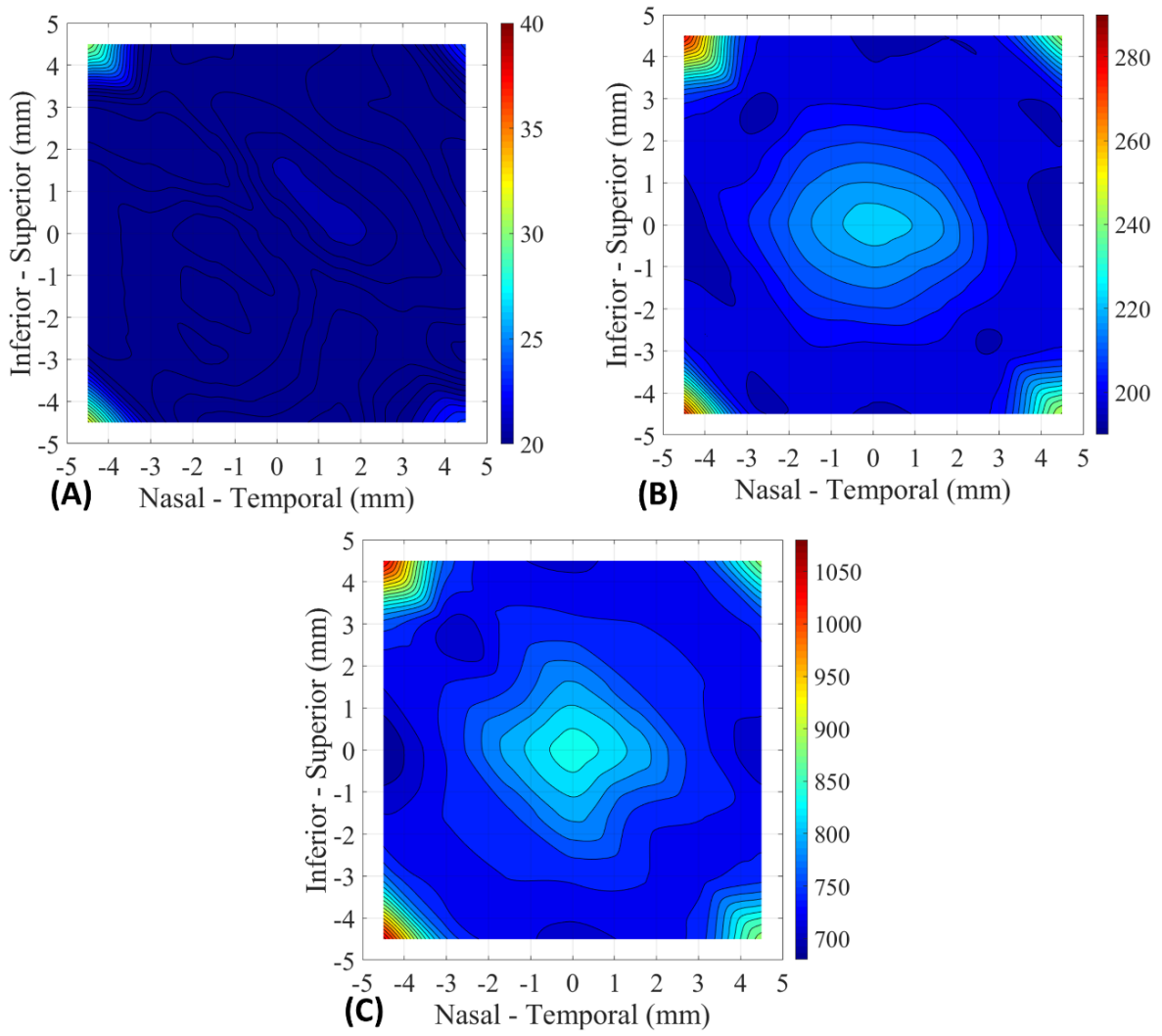

Figure 3.4: Quantitative representation of corneal elastic modulus at varying IOPs (A) Elastic modulus map at 0 mmHg and the contour interval of 1 kPa (B) Elastic modulus map at 15 mmHg and the contour interval of 5 kPa (C) Elastic modulus map at 60 mmHg and the contour interval of 18 kPa. The scale bar represents the elastic modulus values in kPa. Each map is an average of 6 corneas.

The elastic modulus at the centre was 842.94 ± 11.5 kPa at 60 mmHg and decreased by 15.5% in the peripheral region. The nasal-superior and nasal-inferior corners exhibit the highest elastic modulus values in all maps, which are located around 8.4 mm from the centre of the cornea, the

limbus. In comparison, the temporal-superior and temporal-inferior corners have slightly lower values. As an example, Figure 3.5 shows how the elastic modulus values vary from the centre of the cornea toward the nasal-superior corner at 15 mmHg.

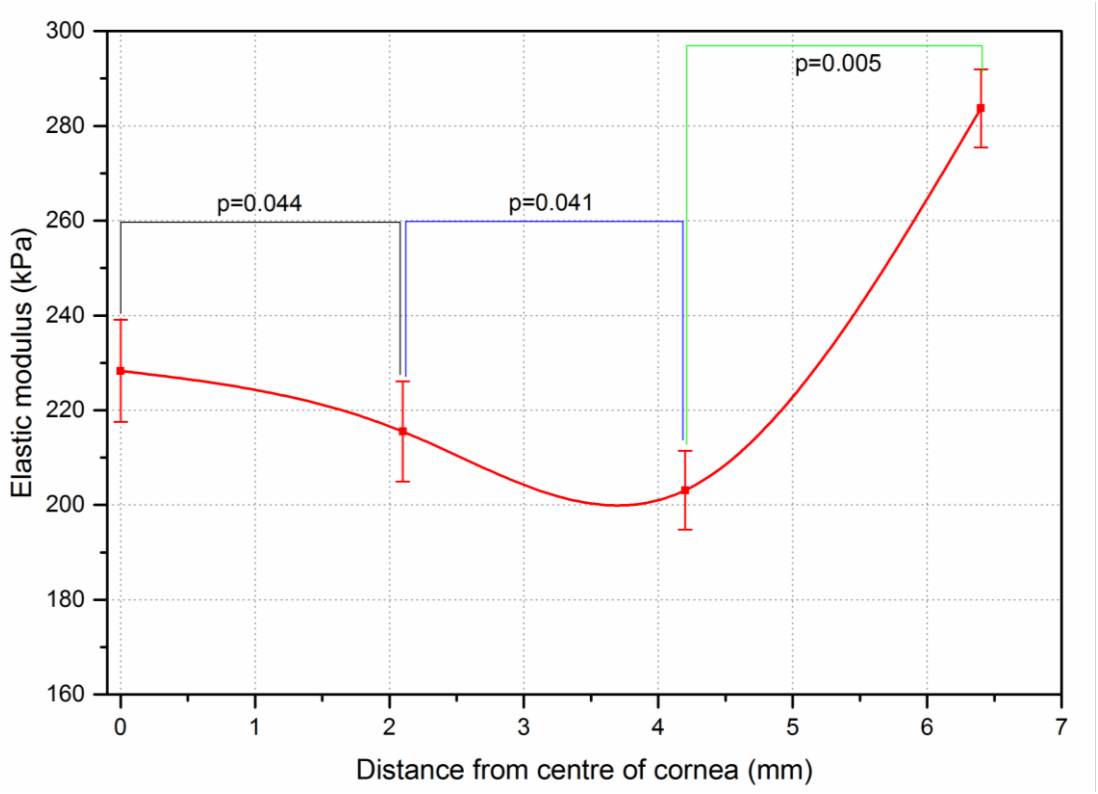

Figure 3.5: Elastic modulus values from the centre of the cornea toward the nasal-superior corner at 15 mmHg. Errors bars represent standard deviation (n=6 corneas). "p" refers to the statistical significance value that was measured using Mann-Whitney test.

3.5. Discussion

This study aimed to measure the micromechanical properties of porcine corneas under physiological pressures using oscillatory nanoindentation. In addition, the current study aimed to demonstrate the potential to map the regional quantitative microscale elastic behaviour of the corneas. The main advantage of the current novel method is the ability to probe localised regions of inflated corneas with a microscale resolution and map the viscoelastic properties at specific points in the cornea. This study also investigated the effect of using PBS and TC, as inflation solutions, on the viscoelastic properties of the corneas with hydration time and also on corneal thickness change.

The advantages of using corneal inflation over other methods has been reported previously, where the key benefit is the ability of loading the cornea in a manner similar to *in vivo* conditions

(Asejczyk-Widlicka and Pierscionek, 2008; Kling and Marcos, 2013; Whitford *et al*, 2016). Previous studies using inflation testing have enabled monitoring of bulk geometrical changes of the inflated corneas during the loading and unloading cycles, which can then be used to predict the elasticity and hysteresis from corneal deformation (Asejczyk-Widlicka and Pierscionek, 2008; Boyce *et al*, 2008; Elsheikh *et al*, 2008, 2007; Wang *et al*, 2018; Whitford *et al*, 2016). In contrast to these methods, the current method allowed the microscale viscoelastic properties of the cornea to be precisely measured at predetermined points.

3.5.1. **Nanoindentation of pressurised corneas**

There are two models for inflating the corneas that have been used in biomechanics research. Firstly, the whole-eye model; where the whole eye tissue (sclera, limbus and cornea) share in the deformation that is caused by increasing the internal pressure (Asejczyk-Widlicka and Pierscionek, 2008; Kling *et al*, 2010; Whitford *et al*, 2016). Secondly, the cornea-only model (Anderson *et al*, 2004; Elsheikh *et al*, 2007; Wang *et al*, 2018), where the cornea is cut from the eye and fixed in a special holder for monitoring the deformation. In both inflation models, there are some complexity in calculating the biomechanical properties due to contribution or exclusion of other connected tissues to the cornea (Anderson *et al*, 2004) and the need for assuming some parameters. The current method overcomes some of the issues with these methods and harnesses the high spatial resolution capabilities of nanoindentation, allowing the microscale mechanical properties of the cornea to be determined with a 100 μm indenter tip at predetermined points. Indeed, these microscale measurements with the current setup primarily reflect the mechanical behaviour of the anterior lamellae of the stroma, which was shown as having a more isotropic microstructure than the deeper lamellae (Benoit *et al*, 2016).

Although the current study is the first to provide the microscale shear modulus for corneal tissue under pressure, the author can compare the current data with other studies which have provided the shear modulus for unpressured corneas. Hatami-Marbini (2014) examined the effect of compressive strain on the viscoelastic behaviour of the porcine corneal stroma using torsional shear experiments. In that study, the average shear storage and loss moduli varied from 2 to 8 kPa, and 0.3-1.2 kPa respectively. These values are substantially lower than the current values even at 0 mmHg. A number of reasons can be cited to explain the discrepancy: firstly, the current data is collected at the micron level from the stromal layer whereas Hatami-Marbini used a bulk method (the stiffness of the whole eye); secondly, the current data is at 110 Hz (the resonant frequency of the nanoindenter) (Akhtar *et al*, 2018) whereas Hatami-Marbini's method was at 1 Hz and thirdly,

the corneas of this study were intact and clamped whilst Hatami-Marbini used 8 mm punch samples from the central region.

There are no previous studies utilising oscillatory nanoindentation to study the cornea. However, Eberwein and colleagues utilised a depth-sensing indenter with a spherical indenter of 0.5 mm radius to calculate Young's modulus of unpressurised (0 mmHg) human corneas by fitting the loading data to the Hertzian contact model. They reported that the elastic modulus of the central cornea was in the range of 19 kPa (Eberwein *et al*, 2014), which is comparable with the current results for unpressurised porcine corneas (0 mmHg). Ko and his colleagues used a 5-mm-diameter cylindrical indenter to characterise elasticity of *ex vivo* inflated porcine corneas (from 12 to 40 mmHg) (Ko *et al*, 2013). They showed a linear relationship between elastic modulus of the corneas and IOP, with an elastic modulus range from 50 to 550 kPa at IOPs from 10 to 40 mmHg. These values are approximately in the same range of elastic modulus presented in this study. Higher values, in the range 2.7-3.3 MPa, were reported for rodent corneas by Wu *et al* using quasi-static nanoindentation to investigate the stiffness change associated with elevated IOP (Wu *et al*, 2013). Another study in which AFM-based nanoindentation has been utilised to investigate the impact of hydration media on the elasticity of porcine corneas (Dias and Ziebarth, 2015). They reported that the Young's modulus of unpressurised corneas immersed in PBS was between 130 and 299 kPa (with the intact scleral rim and without the intact scleral rim respectively) (Dias and Ziebarth, 2015). These values are slightly higher than the range of elastic modulus presented in this study. The differences in elastic modulus values can be related to the type of tip used, indentation depth, analytical solution used and the time of storage in hydration solution.

3.5.2. Corneal hydration

There are many solutions for preserving corneal tissue. Every preserving solution has its specific characteristics and can influence mechanical properties of corneas differently (Kling and Marcos, 2013; Thomasy *et al*, 2014). In this study, PBS and TC were used as inflating solutions for a set period of time. Hydration time is an important factor when determining mechanical properties. Hence, following some preliminary work, the author selected to perform 3 indents at the apex per IOP which reduced the standard deviation as compared to a larger matrix of indents where the time per test was significantly increased. The statistical test did not find any significant differences in mechanical properties between the samples in PBS-0h, TC-0h and TC-4h groups. However, this was not the case for PBS-4h. Hence, the author suggests that using PBS for inflation or possibly for preservation of corneas is suitable for short periods of time e.g. 1 hour. The current

findings are consistent with the finding of Dias and Ziebarth (2015) who reported that the elastic modulus increased linearly over time in corneas were immersed in PBS and swelled up for 2 hours.

CCT decreased with increasing IOP for all groups, regardless of the initial condition. The results of CCT and the trend of changing with IOP are in agreement with other studies (Dias and Ziebarth, 2015; Kling and Marcos, 2013; Vantipalli *et al*, 2018). Corneal swelling was most pronounced in corneas inflated by PBS. The isotonic PBS solution is commonly utilised to rinse (Rihawi *et al*, 2006) or preserve corneas for a short time (Dias and Ziebarth, 2015; Elsheikh *et al*, 2008; Vantipalli *et al*, 2018). However, the effect of significant tissue swelling in PBS is well-known in collagen rich tissues (Screen *et al*, 2006). They found that prolonged preservation of tendons in PBS affects their microstructure by increase in both fibril diameter and inter-fibrillar space. Although PBS-incubation is associated with a reduction of mechanical properties in tendon fascicles, the current data which showed an increase in stiffness with PBS matched other work on the cornea, as described in the previous section (Dias and Ziebarth, 2015). The current study suggests that TC is most appropriate for preserving both the mechanical properties and minimising corneal swelling, particularly if testing is required over long periods of time.

3.5.3. Quantitative microscale mapping of corneal elasticity

The quantitative microscale mapping data showed that the porcine corneas appeared significantly stiffer in the centre than in para-central and peripheral regions. It seems that the regional thickness of the cornea is not the main factor for determining the elasticity response, although porcine corneas are thicker in peripheral region than in the centre of the cornea (Faber *et al*, 2008; Sanchez *et al*, 2011). The inflated corneas showed a nearly symmetrical distribution of elastic modulus from the centre toward the peripheral regions and that is expected according to a model in which collagen fibrils of porcine corneas run in circumferential orientation (Hayes *et al*, 2007). In addition, the distribution of elastic modulus changed to be symmetric with increased IOP (from 0 to 15 mmHg), and it was slightly modified when IOP increased from 15 to 60 mmHg. A reasonable explanation could be that the stromal microstructure is modified by increased IOP, which was shown in a previous microstructural study demonstrate that the collagen lamellae slide and slightly rotate relative to each other when IOP increases(Benoit *et al*, 2016). Regional differences in the elastic behaviour of inflated human (Hjortdal, 1996) and porcine (Boyce *et al*, 2008; Whitford *et al*, 2016) corneas was previously proposed by utilising digital image correlation (DIC) methods to permit three-dimensional deformation mapping. In another study in which optical coherence elastography was used to assess the effect of riboflavin UV-A crosslinking (CXL) on porcine

corneal mechanical anisotropy, it was shown that the central region was stiffer than the para-central region of the CXL and control corneas (Singh *et al*, 2016). The current findings are in agreement with these previous studies.

The observed increase in elastic modulus in the limbal and para-limbal region can be related to the increase in the presence of elastin fibres, thickness, density and orientation of collagen fibrils to form an annulus surrounding and reinforcing the cornea. It has been reported that the aligned collagen fibrils in the limbal annulus appears to be a common feature in many animals such as in human and pig eyes (Hayes *et al*, 2007). The limbus of human eyes was found to exhibit a high level of x-ray scattering intensity (Newton and Meek, 1998) that was suggested due to an increase in the density and the alignment of collagen fibrils (Aghamohammadzadeh *et al*, 2004).

3.6. Limitations

The main limitation of this work is that the oscillatory nanoindentation method assumes linear viscoelastic behaviour and hence is not suitable for determining the constitutive material behaviour of the cornea. However, it does have significant advantages over other quasi-static nanoindentation methods that have been used in other studies. Another limitation was that the number of indents per cornea was reduced in order to minimise testing time. Finally, there is some inaccuracy in corneal thickness values over 1100 μm, which arise due to a lack of accuracy of the pachymeter for thickness over this value. Hence, a technique such as optical coherence tomography (OCT) would be useful for thickness measurements in future work.

3.7. Conclusions

This study utilises oscillatory nanoindentation with inflation to determine localised measurements of viscoelastic properties of inflated corneas at the micron length scale. The effects of thickness changes and mechanical properties in different hydration solutions was also presented, with TC found to be more suitable than PBS when testing over long periods of time (4 hours). The current method has potential to be used to study localised differences between regions of healthy and diseased tissue. For example, corneal disorders such as keratoconus are characterised by a localised reduction in stiffness in specific regions.

3.8. References

Aghamohammadzadeh, H., Newton, R., Meek, K., 2004. X-ray scattering used to map the preferred collagen orientation in the human cornea and limbus. Structure 12, 249-256.

Akhtar, R., Draper, E., Adams, D., Hay, J., 2018. Oscillatory nanoindentation of highly compliant hydrogels: A critical comparative analysis with rheometry. Journal of Materials Research 33, 873-883.

Akhtar, R., Draper, E.R., Adams, D.J, Pfaff, H., 2016. Complex shear modulus of hydrogels using a dynamic nanoindentation method. In: Tekalur S., Zavattieri P., Korach C. (eds) Mechanics of Biological Systems and Materials, Volume 6 (pp. 141-145). Springer, Cham.USA.

Anderson, K., Elsheikh, A., Newson, T., 2004. Application of structural analysis to the mechanical behaviour of the cornea. Journal of The Royal Society Interface 1, 3-15.

Asejczyk-Widlicka, M., Pierscionek, B., 2008. The elasticity and rigidity of the outer coats of the eye. British Journal of Ophthalmology 92, 1415-1418.

Benoit, A., Latour, G., Marie-Claire, S.-K., Allain, J.-M., 2015. Simultaneous microstructural and mechanical characterization of human corneas at increasing pressure. Journal of the Mechanical Behavior of Biomedical Materials 60, 93-105.

Boyce, B., Grazier, M., Jones, R., Nguyen, T., 2008. Full-field deformation of bovine cornea under constrained inflation conditions. Biomaterials 29, 3896-3904.

Dias, J., Ziebarth, N., 2015. Impact of hydration media on *ex vivo* corneal elasticity measurements. Eye and Contact Lens 41, 281-286.

Eberwein, P., Nohava, J., Schlunck, G., Swain, M., 2014. Nanoindentation derived mechanical properties of the corneoscleral rim of the human eye. Key Engineering Materials 606, 117-120.

Elsheikh, A., Alhasso, D., Rama, P., 2008. Biomechanical properties of human and porcine corneas. Experimental Eye Research 86, 783-790.

Elsheikh, A., Wang, D., Brown, M., Rama, P., Campanelli, M., Pye, D., 2007a. Assessment of corneal biomechanical properties and their variation with age. Current Eye Research 32, 11-19.

Elsheikh, A., Wang, D., Pye, D., 2007b. Determination of the modulus of elasticity of the human cornea. Journal of Refractive Surgery 23, 808-18.

Faber, C., Scherfig, E., Prause, J., Soensen, K., 2008. Corneal thickness in pigs measured by ultrasound pachymetry *in vivo*. Scandinavian Journal of Laboratory Animal Sciences 35, 39-43.

Ford, M., Dupps, W., Rollins, A., Roy, A., Hu, Z., 2011. Method for optical coherence elastography of the cornea. Journal of Biomedical Optics 16, 016005-016005-7.

Hatami-Marbini, H., 2014. Viscoelastic shear properties of the corneal stroma. Journal of Biomechanics 47, 723-728.

Hayes, S., Boote, C., Lewis, J., Sheppard, J., Abahussin, M., Quantock, A., Purslow, C., Votruba, M., Meek, K., 2007. Comparative study of fibrillar collagen arrangement in the corneas of primates and other mammals. The Anatomical Record: Advances in Integrative Anatomy and Evolutionary Biology 290, 1542-1550.

Hjortdal, J., 1996. Regional elastic performance of the human cornea. Journal of Biomechanics 29, 931-942.

Kling, S., Marcos, S., 2013. Effect of hydration state and storage media on corneal biomechanical response from *in vitro* inflation tests. Journal of Refractive Surgery 29, 490-7.

Kling, S., Remon, L., Pérez-Escudero, A., Merayo-Lloves, J., Marcos, S., 2010. Corneal biomechanical changes after collagen cross-linking from porcine eye inflation experiments. Investigative Ophthalmology & Visual Science 51, 3961-3968.

Ko, M., Leung, L., Lam, D., Leung, C., 2013. Characterization of corneal tangent modulus *in vivo*. Acta Ophthalmologica 91, e263-e269.

Labate, C., Lombardo, M., Santo, M., Dias, J., Ziebarth, N., Lombardo, G., 2015. Multiscale investigation of the depth-dependent mechanical anisotropy of the human corneal stroma. Investigative Ophthalmology & Visual Science 56, 4053-4060.

Last, J., Liliensiek, S., Nealey, P., Murphy, C., 2009. Determining the mechanical properties of human corneal basement membranes with atomic force microscopy. Journal of Structural Biology 167, 19-24.

Last, J., Russell, P., Nealey, P., Murphy, C., 2010. The applications of atomic force microscopy to vision science. Investigative Ophthalmology & Visual Science 51, 6083-6094.

Last, J., Thomasy, S., Croasdale, C., Russell, P., Murphy, C., 2012. Compliance profile of the human cornea as measured by atomic force microscopy. Micron 43, 1293-1298.

Lombardo, M., Lombardo, G., Carbone, G., De Santo, M.P., Barberi, R., Serrao, S., 2012. Biomechanics of the anterior human corneal tissue investigated with atomic force microscopy. Investigative Ophthalmology & Visual Science 53, 1050-7.

Moronkeji, Todd, Dawidowska, Barrett, S.D., Akhtar, 2017. The role of subcutaneous tissue stiffness on microneedle performance in a representative *in vitro* model of skin. Journal of Controlled Release 265, 102-112.

Newton, R.H., Meek, K.M., 1998. Circumcorneal annulus of collagen fibrils in the human limbus. Investigative Ophthalmology & Visual Science 39, 1125-34.

Oyen, M., 2015. Nanoindentation of hydrated materials and tissues. Current Opinion in Solid State and Materials Science 19, 317-323.

Peters, A., Comerford, E., Macaulay, S., Bates, K., Akhtar, R., 2017. Micromechanical properties of canine femoral articular cartilage following multiple freeze-thaw cycles. Journal of the Mechanical Behavior of Biomedical Materials 71, 114-121.

Rihawi, Frentz, Schrage, 2006. Emergency treatment of eye burns: which rinsing solution should we choose? Graefe's Archive for Clinical and Experimental Ophthalmology 244, 845-854.

Sanchez, I., Martin, R., Ussa, F., Fernandez-Bueno, I., 2011. The parameters of the porcine eyeball. Graefe's Archive for Clinical and Experimental Ophthalmology 249(4), 475-482.

Screen, H., Chhaya, V., Greenwald, S., Bader, D., Lee, D., Shelton, J., 2006. The influence of swelling and matrix degradation on the microstructural integrity of tendon. Acta Biomaterialia 2, 505-513.

Singh, M., Li, J., Han, Z., Raghunathan, R., Nair, A., Wu, C., Liu, C.-H., Aglyamov, S., Twa, M., Larin, K., 2016. Assessing the effects of riboflavin/UV-A crosslinking on porcine corneal mechanical anisotropy with optical coherence elastography. Biomedical Optics Express 8, 349.

Thomasy, S., Raghunathan, V., Winkler, M., Reilly, C., Sadeli, A., Russell, P., Jester, J., Murphy, C., 2014. Elastic modulus and collagen organization of the rabbit cornea: Epithelium to endothelium. Acta Biomaterialia 10, 785-791.

Vantipalli, S., Li, J., Singh, M., Aglyamov, S., Larin, K., Twa, M., 2018. Effects of thickness on corneal biomechanical properties using optical coherence elastography. Optometry and Vision Science 95, 299.

Walton, L., Bradley, R., Withers, P., Newton, V., Watson, R., Austin, C., Sherratt, M., 2015. Morphological characterisation of unstained and intact tissue micro-architecture by X-ray computed micro-and nano-tomography. Scientific Reports 5, 10074.

Wang, L., Tian, L., Huang, Y., Huang, Y., Zheng, Y., 2018. Assessment of corneal biomechanical properties with inflation test using optical coherence tomography. Annals of Biomedical Engineering 46, 247-256.

Whitford, C., Joda, A., Jones, S., Bao, F., Rama, P., Elsheikh, A., 2016. *Ex vivo* testing of intact eye globes under inflation conditions to determine regional variation of mechanical stiffness. Eye and Vision 3, 21.

Wu, K., Li, S., Lo, A., Ngan, A., Wong, D., So, K., Ellis-Behnke, R., Tang, B., 2013. Micro-scale stiffness change of cornea tissues suffered from elevated intraocular pressure investigated by nanoindentation. Soft Materials 11, 244-253.

Chapter 4

Line-field optical coherence tomography as a tool for *in vitro* characterisation of corneal biomechanics under physiological pressures

This chapter focuses on optimising an accurate method that uses optical coherence tomography for measuring geometrical and biomechanical properties of porcine corneas under physiological pressures. The introduction of this chapter reviews the literature with highlighting the limitations and drawbacks, then shows why there is a need for optimising the current method. This chapter shows the effect of intraocular pressure on corneal geometry (thickness and radius) and biomechanical properties (elastic modulus and hysteresis). The chapter also presents the influence of the prolonged preservation of corneas in phosphate buffer saline solution on geometrical and biomechanical properties.

Abstract

There has been a lot of interest in accurately characterising corneal biomechanical properties under intraocular pressure (IOP) to help better understand ocular pathologies that are associated with elevated IOP. This study investigates the novel use of Line-Field Optical Coherence Tomography (LF-OCT) as an elastographic tool for accurately measuring mechanical properties of porcine corneas based on volumetric deformation following varying IOPs. A custom-built LF-OCT was used to measure geometrical and corneal surface displacement changes in porcine corneas under a range of IOPs, from 0-60 mmHg. Corneal thickness, elastic properties and hysteresis were calculated as a function of pressure. In addition, the effects of hydration were explored. This study found that the elastic modulus increased in a linear fashion with IOP. Corneal thickness was found to reduce with IOP, decreasing 14% from 0 to 60 mmHg. Prolonged hydration in phosphate buffered saline (PBS) was found to significantly increase the elastic modulus and corneal hysteresis. The present study demonstrates that LF-OCT can be used to accurately measure the elastic properties based on volumetric deformation following physiological pressures. Furthermore, the current study shows that prolonged hydration in PBS has a significant effect on the measured corneal properties.

4.1. Introduction

A comprehensive understanding of the biomechanical properties of the cornea is important for many clinical applications, for example, accuracy of intraocular pressure (IOP) measurement (Orssengo and Pye, 1999; Gunvant *et al*, 2005; Liu and Roberts, 2005), treatment of keratoconus (Bao *et al*, 2017; Kotecha, 2007), and corneal refractive surgery (Fernández *et al*, 2005; Guirao, 2005; Spoerl and Seiler, 1999). The biomechanical behaviour of the cornea is governed by its geometry and microstructure, which consists of integrated collagen type-I embedded in sub-ground matrix of proteoglycans. This structure exhibits nonlinear viscoelastic and anisotropic properties providing the biomechanical and geometrical characteristics that in turn contribute to the refractive power for satisfactory vision (Bao *et al*, 2017). Corneal microstructure and geometry are also influenced by IOP, which should be in the range of 10 - 20 mmHg to maintain the normal shape and healthy function of the entire eye globe including the cornea (Grehn and Stamper, 2009). It is for this reason that a number of studies have focussed on understanding how geometrical and biomechanical properties of the cornea are altered with elevated IOP (Elsheikh *et al*, 2015; Guarnieri, 2014; Whitford *et al*, 2016; *et al*, 2013). With a better understanding of how corneal geometry and biomechanics are correlated with IOP, there is potential to gain new insight in to the diagnosis of some ocular conditions that in turn could lead to correcting ocular disorders and restoring sight (Gatzioufas and Seitz, 2014; Kling *et al*, 2010; Kotecha, 2007; Radhakrishnan *et al*, 2012).

Studies that focus on corneal biomechanics under IOP typically utilise inflation (bulge) testing allowing corneal deformation to be assessed as a function of pressure (Boyce *et al*, 2008; Bryant and McDonnell, 1996; Elsheikh *et al*, 2008, 2007). Unlike conventional mechanical testing, inflation testing measures the biomechanical properties by expanding the entire cornea through a change in pressure whilst keeping the entire tissue intact (Anderson *et al*, 2004; Asejczyk-Widlicka and Pierscionek, 2008; Asejczyk-Widlicka *et al*, 2008; Elsheikh and Anderson, 2005; Wang *et al*, 2018; Whitford *et al*, 2015; Yu *et al*, 2013). In some studies, digital image correlation has been combined with inflation testing to provide spatially-resolved deformation mapping via of the cornea (Boyce *et al*, 2008; Whitford *et al*, 2016). Other studies have measured the apical displacement-IOP curve for inflated corneas by using laser reflectometry (Elsheikh *et al*, 2007; Boschetti *et al*, 2012; Bryant and McDonnell, 1996). In this approach, an artificial anterior chamber is used to hold the corneal samples and internal pressure is applied by using a PBS reservoir connected to the chamber. Scheimpflug imaging has also been used to capture the thickness of the cornea in inflation testing (Kling and Marcos, 2013; G. Lombardo *et al*, 2014; M. Lombardo *et al*, 2014). Although each of

these corneal inflation studies demonstrate that elastic properties are altered with IOP, there are some limitations which must be considered. For example, the effect of optical and geometrical distortions of the cameras are underestimated and hence a number of correction factors are needed. These have been explained by Li *et al* (Li *et al*, 2015) and also by Rosales and Marcos (Rosales and Marcos, 2009). In addition, the methodologies employed in these studies do not allow real-time corneal geometrical changes to be captured with varying IOP. As a result, a number of assumptions have to be made about the elastic properties of the cornea.

Elastography measurements with optical coherence tomography (OCT) is a field which has emerged over the past two decades, and is termed optical coherence elastography (OCE) (Dorronsoro *et al*, 2012; Ford *et al*, 2011; Han *et al*, 2017, 2015a, 2015b; Liu *et al*, 2017; Singh *et al*, 2016a, 2016b; Vantipalli *et al*, 2018; Wang and Larin, 2015). OCE has been developed and applied extensively to the cornea, as discussed in the comprehensive review by Larin and Sampson (Larin and Sampson, 2017). The non-invasive OCE technique employs optical coherence tomography (OCT) to detect the deformation of inflated corneas following applied external force on the cornea. These forces can be applied on the cornea in a contact (small indenter) or non-contact (e.g. air-pulse or acoustic wave) modalities. OCE techniques can also be used for biomechanical evaluation of the cornea following inflation. For example, a swept-source OCE system utilising an air-pulse has been used to test treated and untreated cross-linked porcine corneas of the same mechanical stiffness but under different IOPs (Li *et al*, 2014). This setup was successfully able to distinguish between the two groups, demonstrating the potential of such OCE-methods.

However, OCE methods for assessing viscoelastic properties quantitatively are still at a very early stage (Larin and Sampson, 2017). One approach is to utilise static deformation through OCT and thereby exerting the cornea to a similar condition as with inflation test, as described earlier (Boyce *et al*, 2008; Bryant and McDonnell, 1996; Elsheikh *et al*, 2008, 2007). Ford *et al* (Ford *et al*, 2011, 2014) demonstrated such an approach for inflation utilising OCT, although the IOP range was limited and therefore the elastic modulus and hysteresis was not calculated. A recent study by Wang *et al* (Wang *et al*, 2018) effectively utilised optical coherence tomography (OCT)-based inflation testing for measuring the non-linear elastic behaviour of porcine corneas. This study makes an important contribution to the field of inflation testing via OCT because it bridges the gap between imaging via OCT and corneal biomechanical characterisation conducted with non-OCT based approaches as highlighted earlier. Specifically, they successfully demonstrated that a spectral domain OCT could be incorporated with inflation testing where the IOP is varied at

different loading rates. They were able to observe the pressure-apex displacement relationship and calculate the apparent stiffness of the corneas using the axial deformation of the apex. Their study is more analogous to previous non-OCT studies (Boyce *et al*, 2008; Bryant and McDonnell, 1996; Elsheikh *et al*, 2008, 2007), where static deformation is captured for elasticity calculations rather than these in which dynamic deformation in response to a localised external force is monitored for elastic modulus calculation (Dorronsoro *et al*, 2012; Ford *et al*, 2011; Han *et al*, 2017, 2015a, 2015b; Liu *et al*, 2017; Singh *et al*, 2016a, 2016b; Wang and Larin, 2015). Elastic modulus values are intuitively comparable by both methods. However, corneal deformation (apex displacement) is not comparable due to the different force modalities. Although an important step forward in integrating OCT and corneal biomechanics, a limitation in the work of Wang *et al* appears to be that the change of corneal thickness and the elastic modulus values following hydration in saline solution was not considered (Wang *et al*, 2018). It is well-established that hydration has a significant effect on corneal geometry and biomechanical properties (Kling and Marcos, 2013; Vantipalli *et al*, 2018). In addition, their work did not consider the role of corneal thickness in strain calculations, given that the approach they utilised is based on the assumption of axial deformation of corneal apex only (Anderson *et al*, 2004).

4.2. Aim

This current study aims to present a new inflation method utilising Line-Field OCT (LF-OCT) to measure the corneal geometrical parameters during the loading and unloading phases of corneal inflation in real-time. The approach in the present study provides significant advantages over previous methods including a large scan size which gives sufficient resolution to accurately measure corneal apex geometrical changes including its displacement, real-time monitoring and high axial resolution. In addition, the resulting elastic properties and hysteresis are quantitatively correlated with hydration time.

4.3. Materials and methods

Eight fresh porcine eyes were obtained from a local abattoir shortly after slaughter. The pigs were aged from 5 to 6 months. The corneas, with a 2 mm scleral ring, were dissected and placed in a Barron Artificial Anterior Chamber (Katena Company, USA). An elevated reservoir of Phosphate Buffered Saline solution (PBS) (Sigma-Aldrich, Dorset, UK) was used to apply a hydraulic pressure to the posterior surface of the corneas, simulating intraocular pressures (IOP) of 0 to 60 mmHg. The pressure was controlled by the height of the reservoir and measured using an ABP series pressure sensor (Honeywell, NJ, USA). The corneas were measured at 0 mmHg and 2 mmHg, and

then in 5 mmHg increments from 5 mmHg up to 60 mmHg during the loading phase. This sequence was then inverted for the unloading phases. The testing at each pressure step took 20 seconds, and time between pressure steps was 10 seconds. The experiments were carried out at room temperature (approximately 22.5°C) and 45±2.1% relative humidity, as determined with a humidity-temperature meter (OMEGA engineering Ltd., Manchester, UK). One drop (60 μl) of PBS was applied on the external surface of the corneas (epithelium) every 4 min to maintain the hydration of the corneas. The testing was completed within 15 min after fixing the samples in the holder. The described experimental protocol was repeated every hour for four hours to detect the effects of corneal hydration on mechanical properties.

A LF-OCT system was used for this study, explained in Chapter 2 and elsewhere (Lawman *et al*, 2016, 2017a, 2017b). A schematic of the experimental setup is shown in Figure 4.1. The system was setup with a charge-coupled device (CCD) camera (iVac, Andor, UK), 2Hz frame rate, 75 mm objective and 100 mm collection achromatic lenses. The commercial Czerny-Turner spectrograph (Shamrock 303i, Andor, UK) utilised with the system provides flexibility in the axial resolution by selection of the grating on the mechanical turret. In this study, a medium-resolution mode was selected by using a 600 lines/mm grating. This gave a larger axial range than at a higher axial resolution mode to facilitate monitoring of the corneal surfaces of the swelling porcine corneas while maintaining an axial resolution of approximately 3.5 μm in the corneal tissue. The signal to noise ratio (SNR) of the system was 79 dB, with a sensitivity of 93dB and a roll off of 15dB at 1mm (Lawman *et al*, 2016). In this study, the sensitivity of the device was sufficient to distinguish the surfaces of the corneas. The group refractive index of the fresh porcine cornea at the central wavelength of 800 nm was assumed to be 1.389 based on previous studies (Lai *et al*, 2010; Tuchin, 2007; Tuchin *et al*, 2006; Yuzhakov *et al*, 2013). OCT images were analysed by using a semi-automated code written in MATLAB (Mathworks Company, Natick, Massachusetts, USA) to identify the boundaries of corneas using segmentation technique. The corneal apex thickness, radius of curvature and displacement were measured with time at each pressure level. The corneal apex thickness was calculated and averaged for a cross-sectional image of the central 3 mm of the cornea. In OCT system of the current study, the total thickness error/repeatability of approximately 2.2 μm was deemed acceptable. The adjustable microscale stage of sample arm and the flexibility of selecting the big axial depth (low-resolution mode 1200 lines/mm grating) were used to take the initial measurement of the height of the parabolic volume under the cornea (H_o) at 2 mmHg.

4.3.1. Calculation of elastic properties

The bulk elastic properties of the cornea were calculated by applying thin-walled sphere theory and Hooke's law, since the thickness of the cornea is much smaller than the radius and the properties are measured at discrete pressure steps. The collected geometrical data was used to calculate the circumferential stress (σ) at each pressure level using Equation (4.1) (Fung, 2013; Pierscionek *et al*, 2007):

$$\sigma = \frac{P.R}{2.CCT} \tag{4.1}$$

where P is the internal pressure that mimics the IOP, R is the radius of curvature and CCT is corneal apex thickness, see Figure 4.2.

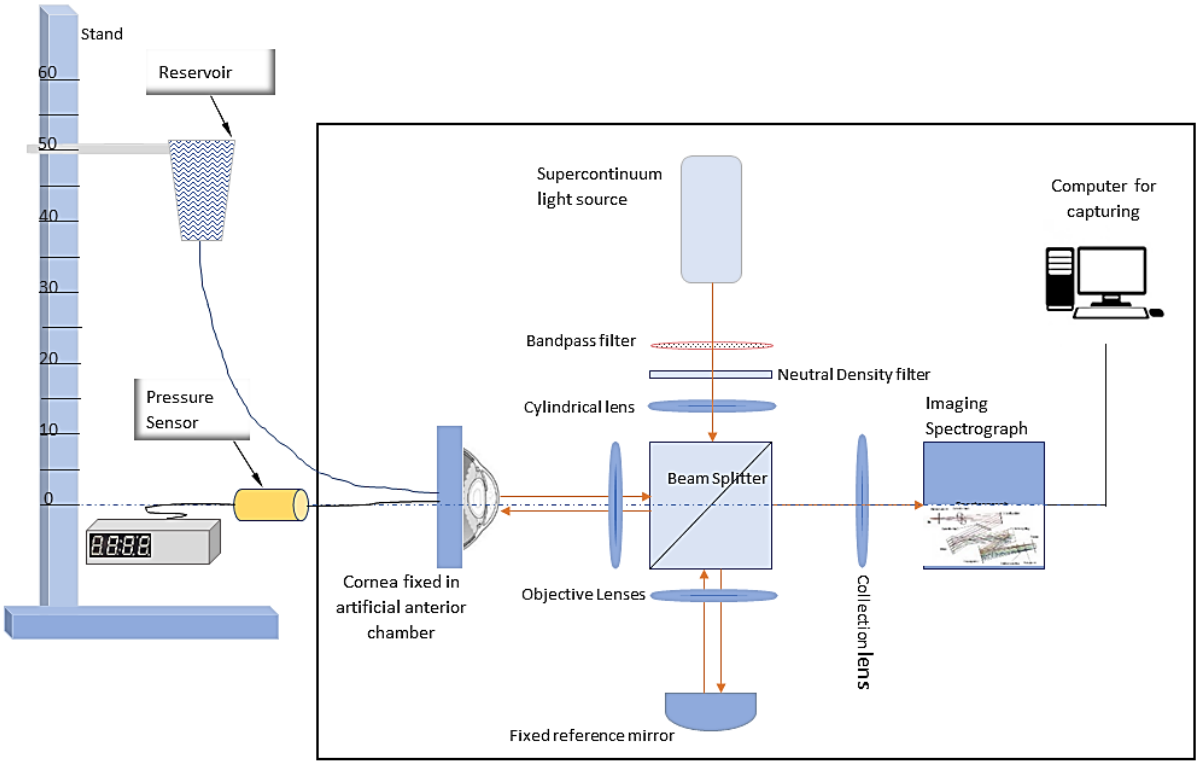

Figure 4.1: Schematic diagram for the combined corneal inflation and LF-OCT setup. The artificial anterior chamber was filled with PBS and connected to a reservoir which moved vertically up and down on a graded stand to control the pressure.

Figure 4.2 shows the model of thin-walled sphere theory and the needed assumptions. The volumetric strain (ε) was calculated from the geometrical variations of the cornea in response to IOP changes as shown Equation (4.2). The initial displacement D_o and the interior apical height

H_o were initially measured at 2 mmHg, where the cornea starts exhibiting curvature and stability of the corneal apex displacement (Whitford *et al*, 2016).

$$\varepsilon = \frac{V_o - V}{V_o} \tag{4.2}$$

where ε is the volumetric strain; V_o is the initial volume under the cornea; V is the current volume.

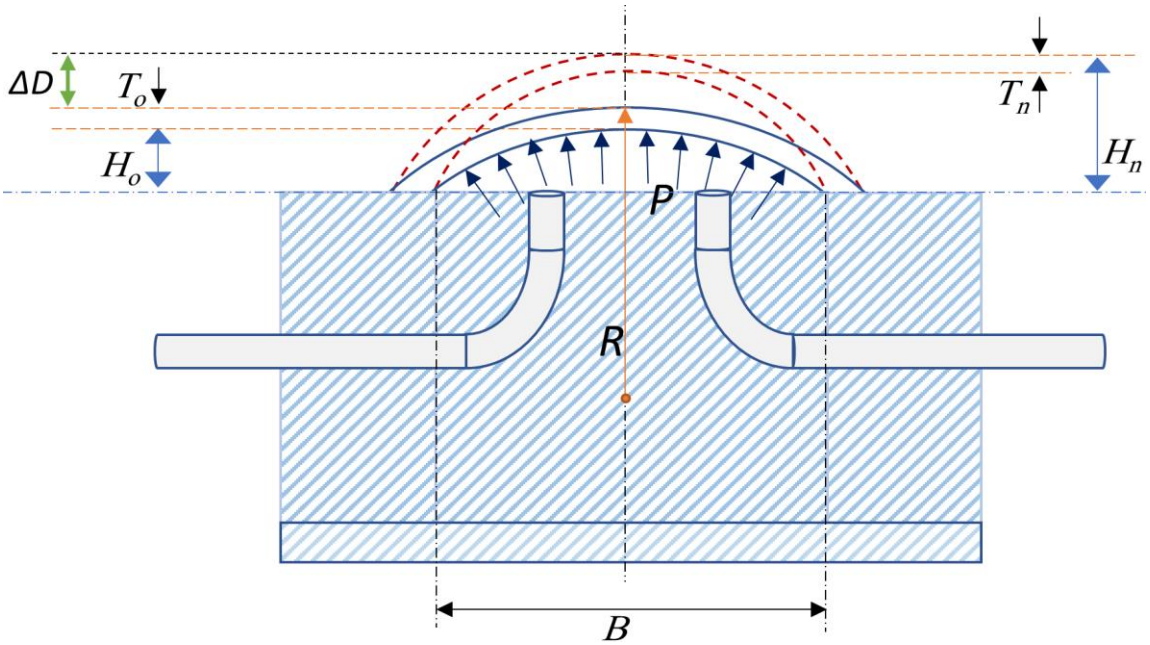

Figure 4.2: A schematic diagram shows thin-walled sphere model for representing a cornea fixed in the holder (cornea-only model). T_o and T_n: Apex corneal thickness (initial and current), H_o and H_n: The height of parabolic volume under the cornea (initial and current), B: The base of the parabolic shape (B= 12.5 mm). R: Radius of curvature of the anterior surface of the corneal apex, P: pressure that mimics intraocular pressure (IOP), $\Delta D = D\text{-}D_o$, and $V_o = (\pi/2)H_oB^2$ (initial volume). In this model, a rigid sclera was assumed. The centre of corneal curvature was assumed to be fixed in the central axes of the cornea. Dashed arcs at the top of the figure represent the deformed (inflated) cornea.

The tangent elastic modulus (E_t) was calculated by using equation (4.3) (Pierscionek *et al*, 2007):-

$$E_t = 3(1 - v)\frac{\sigma}{\varepsilon} \tag{4.3}$$

where v is Poisson's ratio for the corneas. v was assumed to 0.40 based on a study that showed that the cornea behaves as a slightly compressible body (Ford *et al*, 2011).

The stress-strain relationship was calculated for both loading and unloading phases. Corneal hysteresis was then calculated by measuring the area between the curves of the loading and unloading phases to show the cornea's ability to absorb and dissipate energy.

4.3.2. Statistical analysis

All Statistical analysis and graphs were carried out in OriginPro 2016 version 9.3 (OriginLab, MA, USA). All data are expressed as mean values and standard deviation (mean ± standard deviation). The statistical significance of corneal thickness change of the samples over time at each IOP was calculated by using Wilcoxon signed ranks test. The statistical significance of elastic modulus and hysteresis changes with hydration time was also measured by the same method. $p<0.05$ was considered as statistically significant for all tests.

4.4. Results

Figure 4.3 shows an example LF-OCT images of a cornea inflated at 15 mmHg.

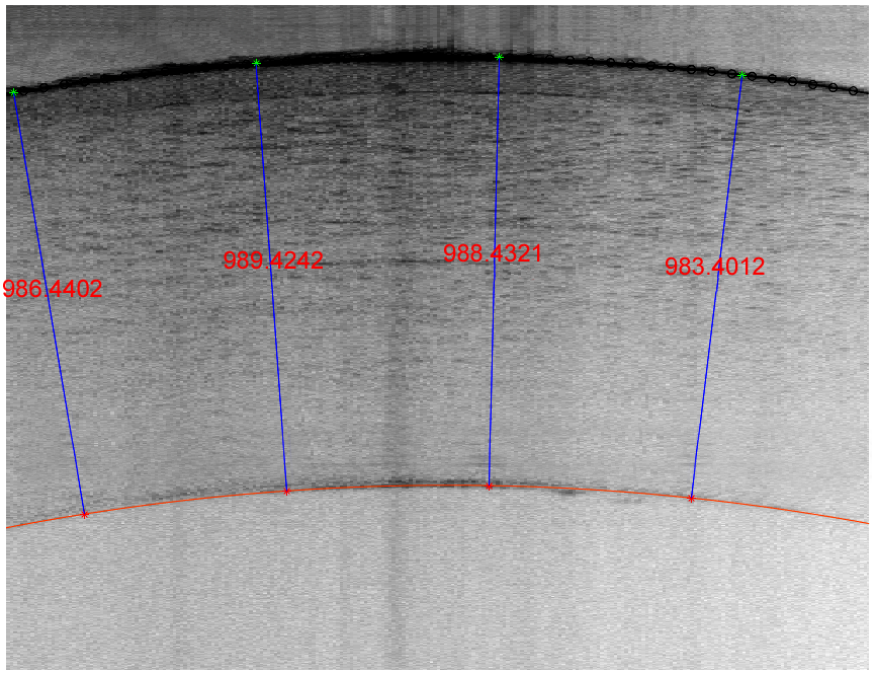

Figure 4.3: Typical LF-OCT images for a cornea at a pressure of 15 mmHg during the first loading phase (Time = 0 hour). The image was reordered at a medium-resolution mode of a 600 lines/mm grating. The epithelium layer is clearly visible and can be identified by the thin arc below the anterior surface of the cornea. The average central corneal thickness (CCT) of this cornea was 986.9 μm.

4.4.1. Geometrical variations

Geometrical variations were detected through the monitoring of the corneal response to changes in IOP. Monitored parameters included cornea thickness, radius of curvature and displacement of

the corneal apex. Figure 4.4 illustrates the thickness change with varying IOP during loading and unloading. Generally, the results show that corneal thickness is inversely proportional to increasing and decreasing internal pressure, and there is a significant difference in the corneal apex thickness between the loading and unloading phases ($p \leq 0.00024$). It was noticed that corneas exhibited the expected curvature at 2 mmHg.

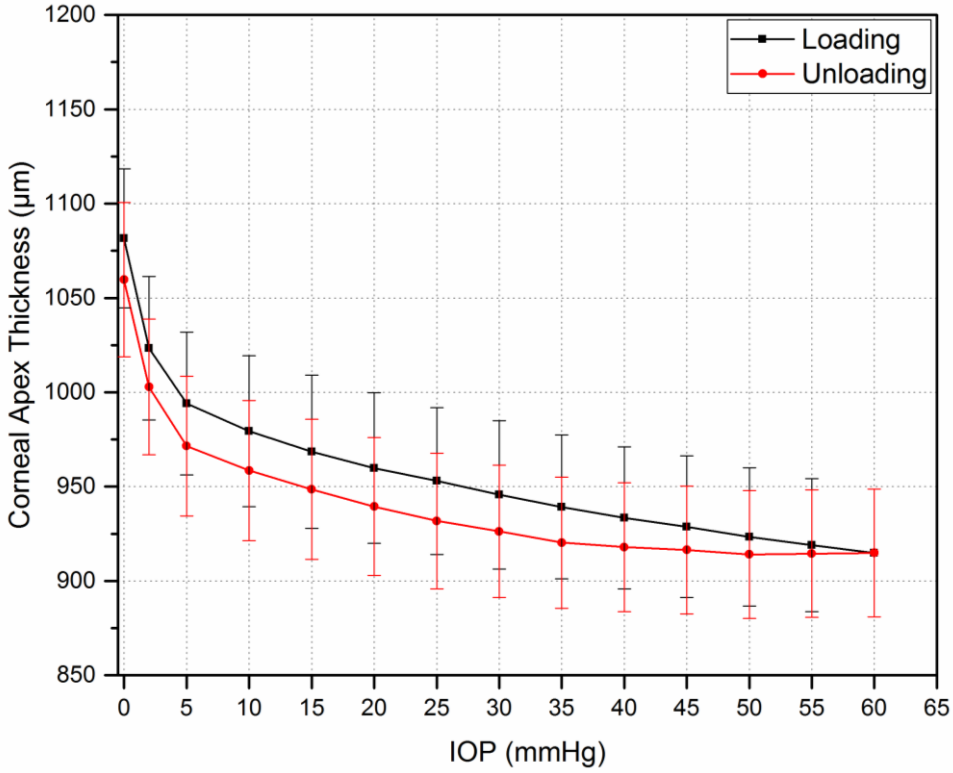

Figure 4.4: Average of thickness change of intact corneas (epithelium, stroma, and endothelium) with varying IOP. Errors bars represent standard deviation (n=8 corneas).

The best fit for the variation in corneal thickness during the loading phase follows a logarithmic equation which is shown in Equation (4.4). However, there is approximately a linear relationship between the thickness of the cornea and the internal pressure of the loading phase from 15 to 60 mmHg. At high IOPs, the average reduction in the apex corneal thickness every 5 mmHg was approximately 1.07%.

$$\mathrm{CCT(IOP)} = \mathrm{CCT_{at\ IOP=0\ mmHg}} - 57.3\ \mathrm{IOP}^{0.265} \tag{4.4}$$

where CCT(IOP) is the thickness of the corneal apex in µm at specific IOP that is measured in mmHg. $\mathrm{CCT_{IOP=0}}$ is central corneal thickness at IOP=0 mmHg, relaxed state.

The percentage reduction in thickness at low internal pressures is significantly greater than that at high internal pressures. In the loading phase, the total change in corneal apex thickness reduced around 14% after the IOP was increased from 0 mmHg to 60 mmHg, which meant that the thickness reduced from 1081±55 μm to 914±33 μm. It was noticed that after the unloading phase finished at 0 mmHg, the corneal thickness did not immediately return to its original thickness i.e. at the point where the loading phase began. However, it was noted that the thickness did eventually recover after approximately 5 min.

The radius of the corneal apex curvature decreased slightly when the IOP increased as shown in Figure 4.5. At each specific IOP, the radius of corneal apex curvature in the loading phase was not significantly different than that in the unloading phase (p=0.945). A linear relationship was observed between radius of corneal apex curvature and IOP, Equation (4.5).

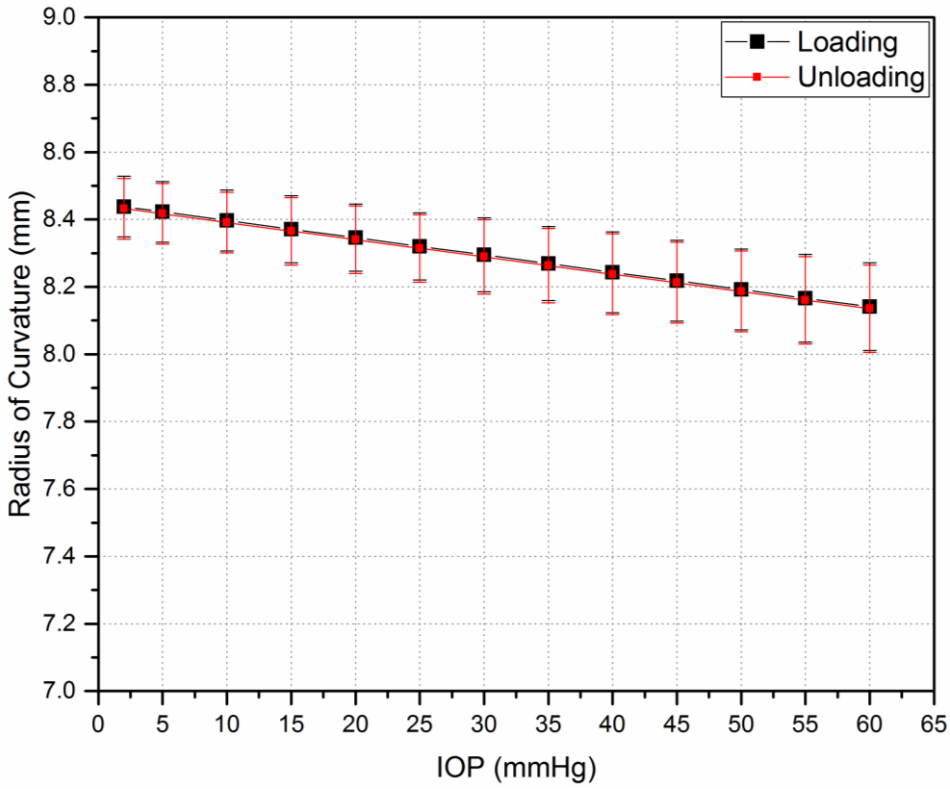

Figure 4.5: Radius of curvature of the corneal apex for corneas which were fixed in an artificial holder. Data is shown from 2 mmHg onwards. Error bars represent standard deviation (n=8 corneas).

$$R(IOP) = 8.448 - 0.005 \times IOP \tag{4.5}$$

The thickness of porcine corneas slightly increased at paracentral and peripheral regions. Corneal thickness (CT) at 3 mm from the centre of the cornea was 1016.28±15.45 μm, recorded at 15 mmHg. In comparison with the centre of the corneas, the thickness was significantly increased by

8.1% near the limbus (p=0.0145). Equation 4.6 describes the changes in the thickness of the cornea.

$$CT(x) = CCT + x + 3x^2 \quad (4.6)$$

where, CT is the thickness of a porcine cornea at point x; x is the location from the centre of the cornea, which ranges as $0 \leq x < 6$ in millimetres; CCT is central corneal thickness. $CT_{x=0} = CCT$.

The displacement of the corneal apex for the first loading and unloading phases is shown in Figure 4.6. An exponential relationship was observed for both loading and unloading phases. The maximum corneal apex displacement was 143±3.78 μm away from the initial position at 2 mmHg. The rate of change in the corneal apex displacement was greater at pressure levels below 20 mmHg.

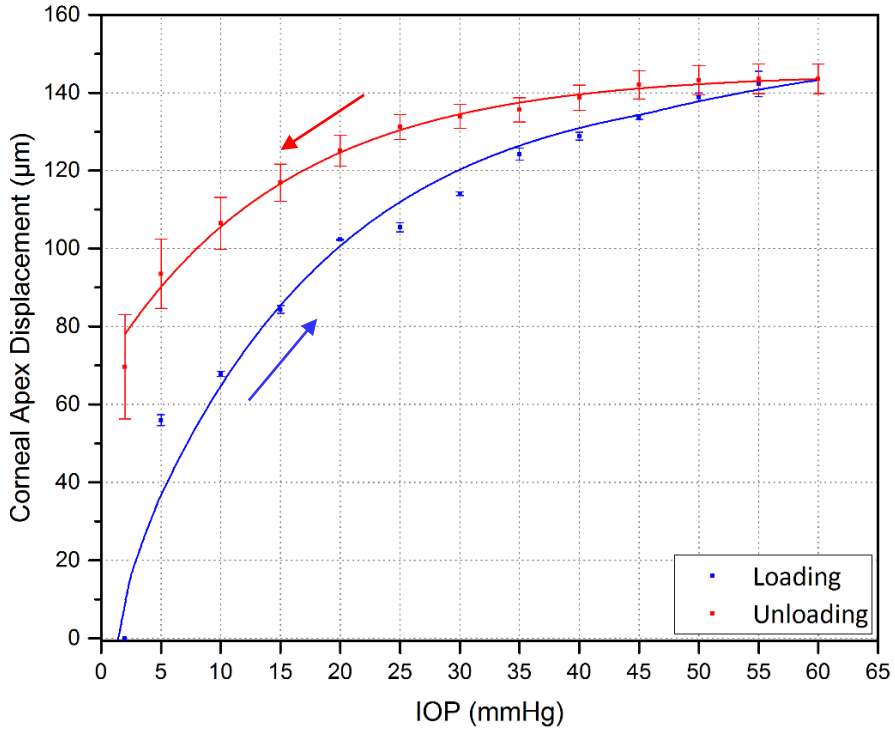

Figure 4.6: Corneal apex displacement with varying IOP loading and unloading. Vertical bars represent the standard deviation (n=8 corneas). The blue arrow indicates the direction in the increase of corneal apex displacement (loading phase). The red arrow shows the direction in the decrease in corneal apex displacement (unloading phase).

4.4.2. Mechanical properties

Elastic properties were calculated by the use of geometrical changes to IOP change and applying Equations 4.1, 4.2 and 4.3. Corneal apex stress-strain curve for the first loading and unloading phases is shown in Figure 4.7. Corneal apex hysteresis from the first loading and unloading phases was 10.5±0.6 mmHg (1.4±0.08 kPa) for the fresh corneas.

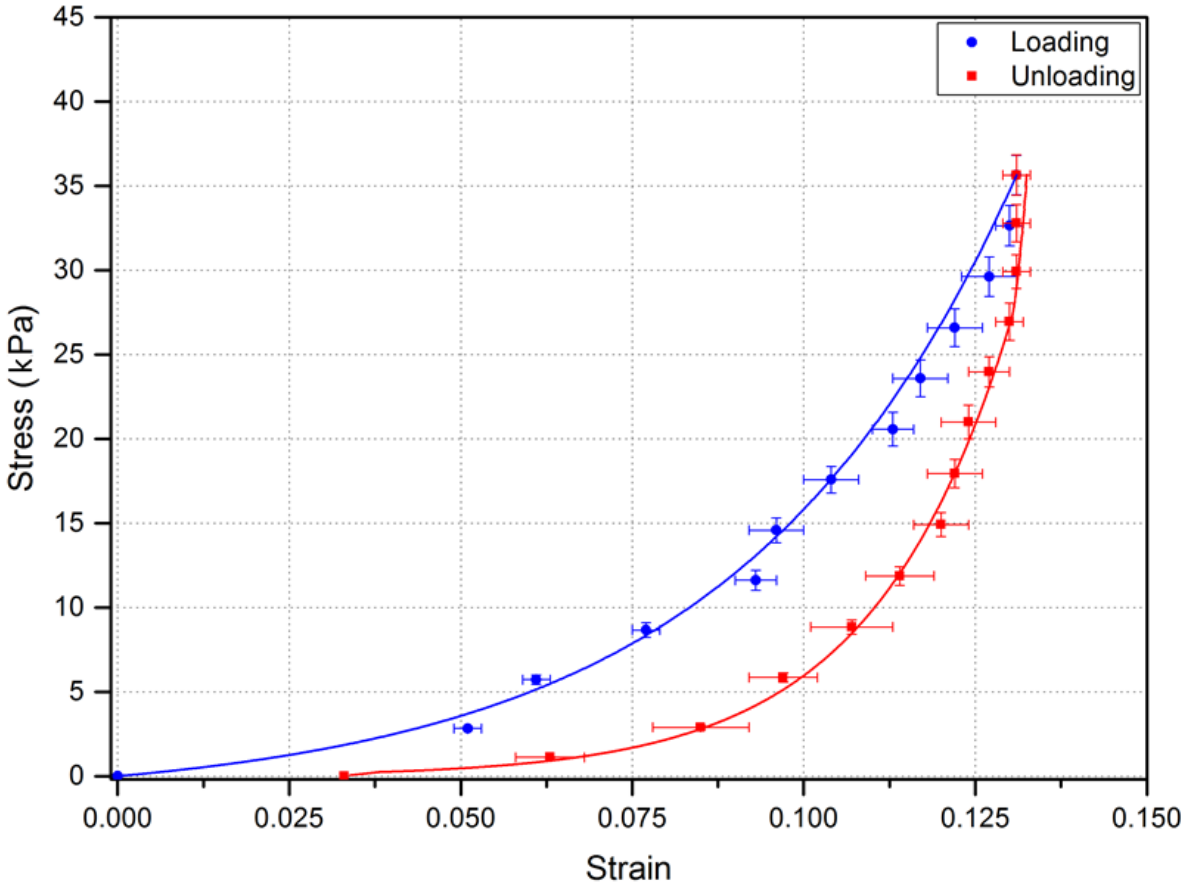

Figure 4.7: Corneal apex stress - strain curves that obtained from the first loading and unloading phases (n=8 corneas).

Elastic modulus of the corneal apex during the first loading and unloading phases is demonstrated in Figure 4.8 where (approximately) a linear relationship can be seen. However, in the loading phase, a non-linear relationship between the elastic modulus and IOP was noticed at pressure levels below 15 mmHg. There was a slight difference between the elastic modulus determined during the loading and unloading phases, which decreased as the IOP increased.

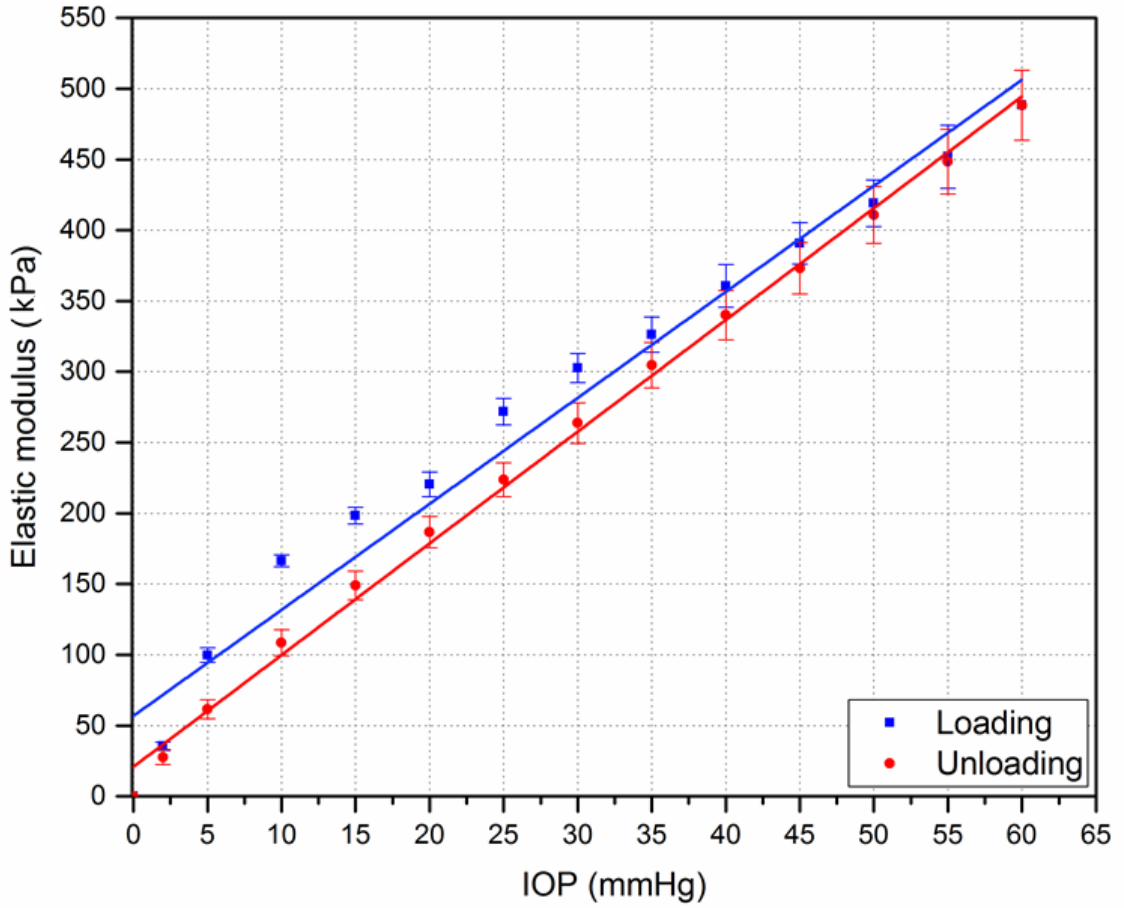

Figure 4.8: Elastic modulus of corneal apex obtained from the first loading and unloading phases (n=8 corneas). There was significant difference between the elastic modulus of loading and unloading phases with varying IOP (tested by Wilcoxon signed ranks test, p=0.0076.

4.4.3. Hydration effects

Figure 4.9 shows that corneal thickness during the loading and unloading phases was affected by two parameters, namely IOP and hydration time. It can be seen that the thickness of the corneas significantly increased over the hydration time ($p \leq 0.0012$). Corneal thickness significantly increased by approximately 6% after the first hour of hydration in PBS. The maximum thickness recorded at 0 mmHg was 1222.47 ± 63.79 μm after four hours of hydration, which is about 14% more than that measured at the initial state. Figure 4.9 also shows that the area between the loading and unloading curves increased every hour, which indicates a change in viscous properties of the corneas. No visual damage was observed to corneas during the repetitive measurement cycles.

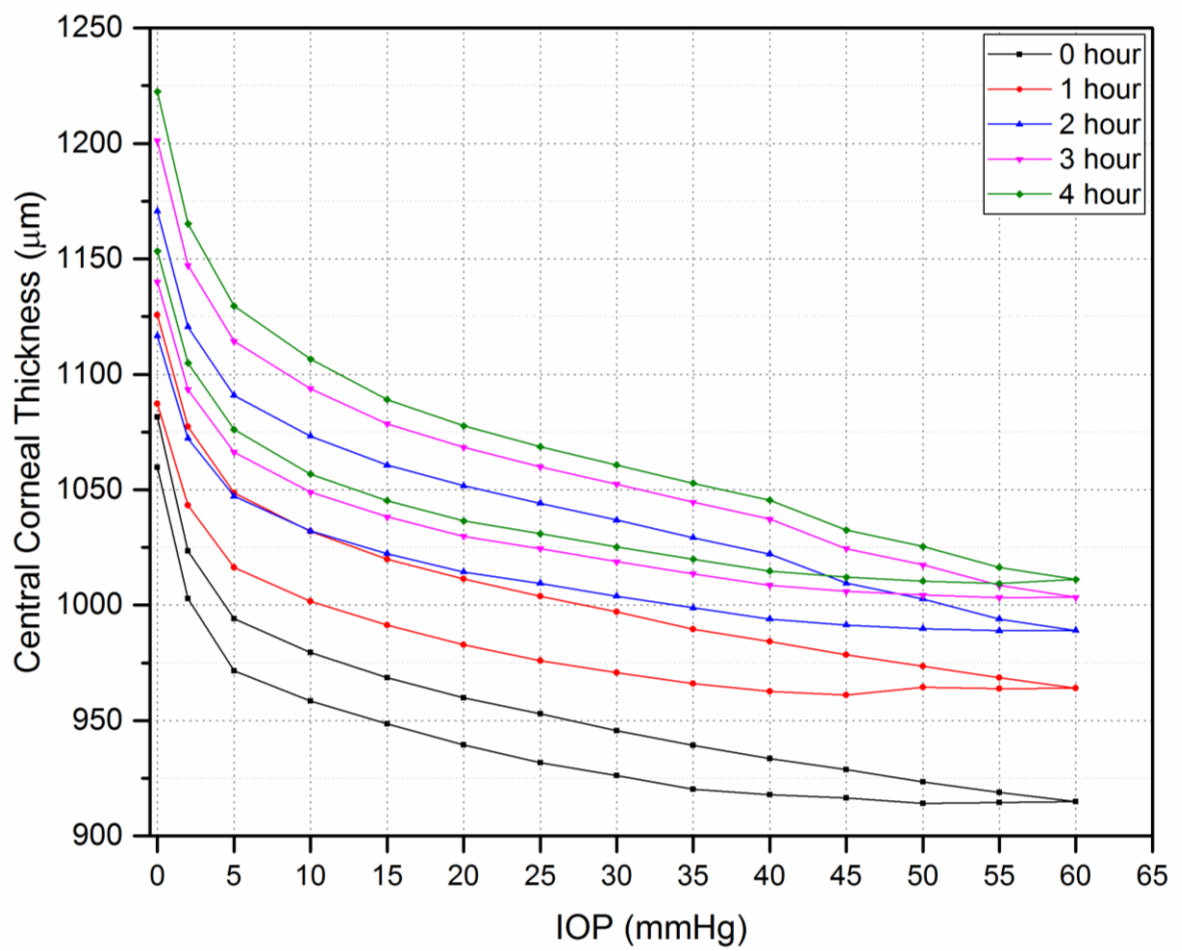

Figure 4.9: Plot showing corneal thickness change of corneas with varying IOP for 0-4 hours. Each loop represents the corneal thickness during loading and unloading phases. Standard deviation values were excluded to allow the trends to be more discernible (n = 8 corneas). There was a significant difference between central corneal thickness of each cycle over time (Wilcoxon signed ranks test, $p < 0.00012$).

The results also show that hydration can affect not only the thickness but also the mechanical properties of the corneas. An increase in the elastic modulus was observed due to geometrical changes of the samples, mainly thickness and corneal apex displacement. Figure 4.10 shows the increase in elastic modulus of the corneas at 15 mmHg with hydration time. Elastic modulus of hydrated corneas after 1 hour was significantly increased by approximately 52% relative to the initial elastic modulus when the corneas were almost fresh (zero hours). Elastic modulus of the corneas increased from 198.25±5.97 kPa at 0 hour to 315.84±18.4 kPa after 1 hour. Elastic modulus of the corneas was found to significantly increase around 2 % each hour after the first hour of hydration ($p \leq 0.0415$).

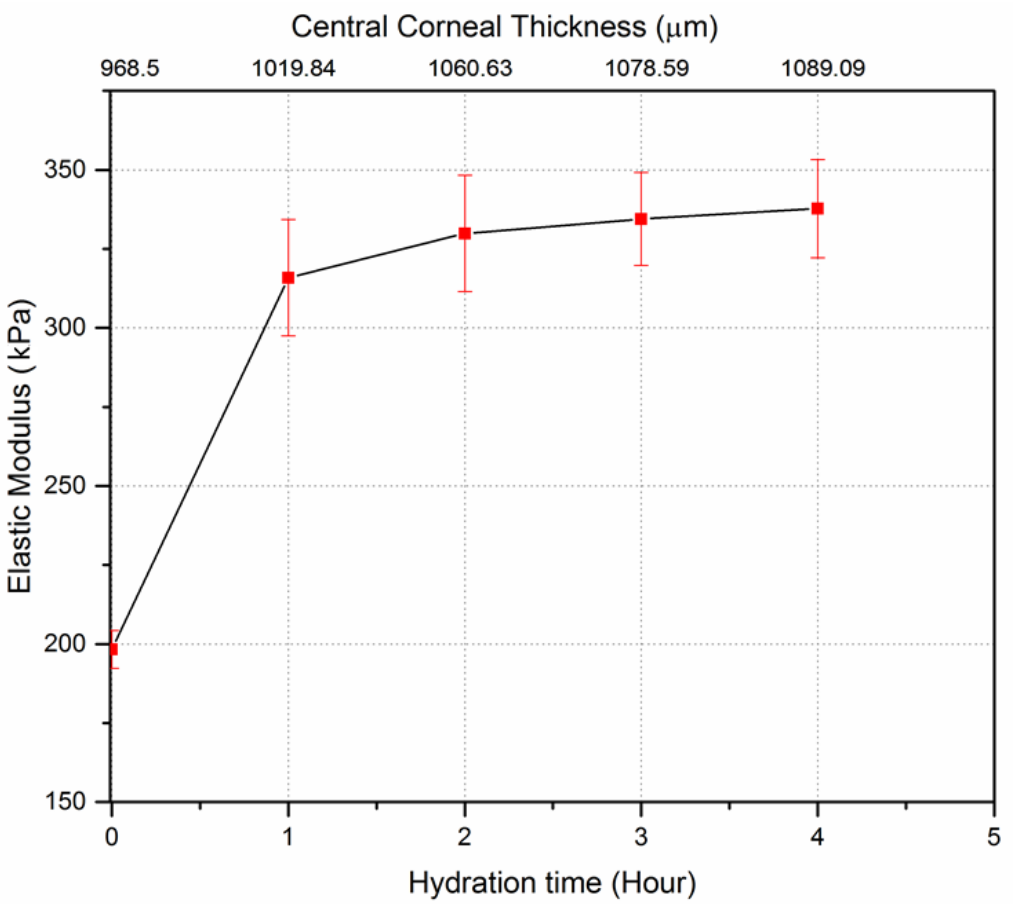

Figure 4.10: The change of elastic modulus during the loading phase with hydration time is correlated with central corneal thickness shown for IOP of 15 mmHg. The top x-axis represents the central corneal thickness at the corresponding hydration time (bottom x-axis) at 15 mmHg. Error bars represent standard deviation (n=8 corneas). There was a significant difference between elastic modulus values between 0 hour and first hour of hydration, $p \leq 0.0026$. Elastic modulus become relatively stable (slight increase) after the first hour of hydration.

An increase in hysteresis was also detected with increasing hydration time. The hysteresis in hydrated corneas after 1 hour significantly increased by about 50% relative to that at initial state; from 1.4±0.08 kPa (10.5±0.6 mmHg) to 2.1±0.12 kPa (15.8±0.9 mmHg) after 1 hour in PBS. Figure 4.11 shows the relation between hysteresis and hydration time. Hysteresis was found to significantly increase around 2.7% from the first hour to the second hour of hydration; this percentage was gradually decreasing by 0.75% each hour ($p \leq 0.0336$).

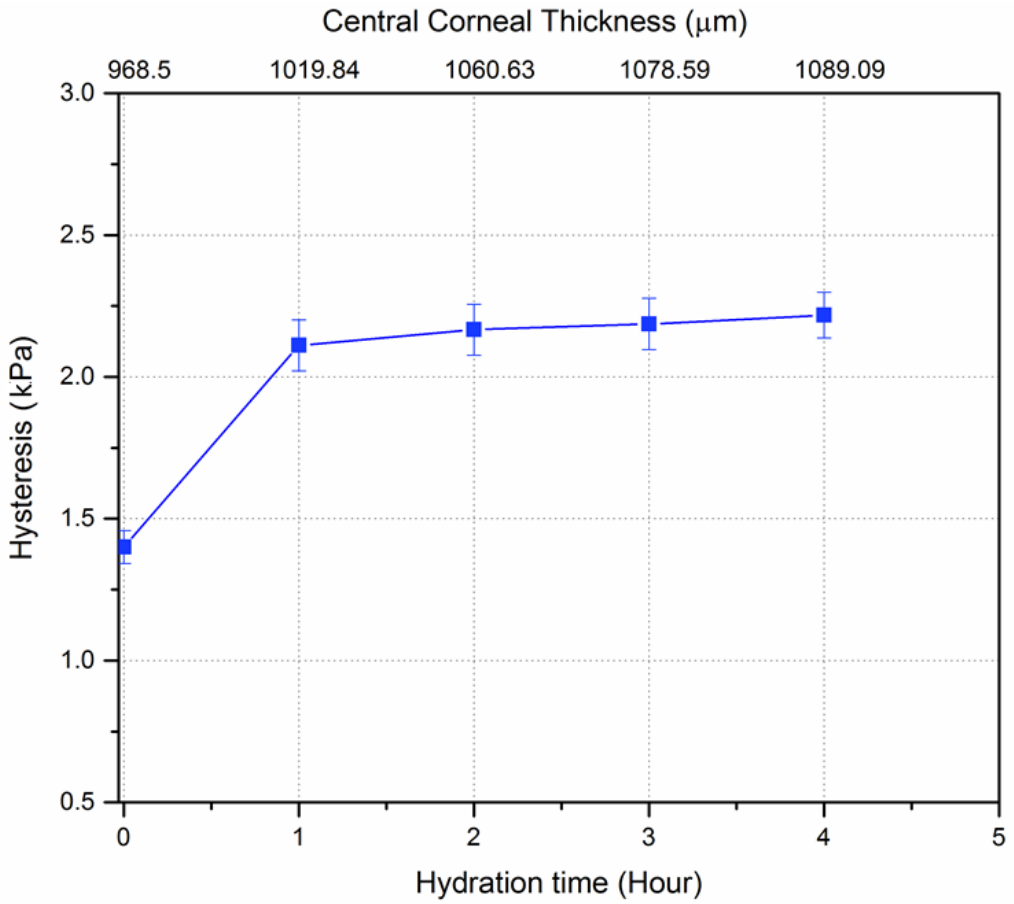

Figure 4.11: Corneal hysteresis and hydration time relationship. (n = 8 corneas). The top x-axis represents the central corneal thickness at the corresponding hydration time (bottom x-axis) at 15 mmHg. There was a significant difference between hysteresis values over time between 0 hour and first hour of hydration, $p \leq 0.0078$. Hysteresis became relatively stable (slight increase) after the first hour of hydration.

4.5. Discussion

This study aimed to investigate the biomechanical properties of the porcine cornea using LF-OCT with application as a corneal inflation test method. The significant advantage of the current approach is that it enables real-time LF-OCT to be used for monitoring corneal geometrical changes during loading and unloading cycles for four hours. One recent study used a spectral domain OCT for corneal inflation tests to obtain elastic deformation (Wang *et al*, 2018). Although this experiment demonstrated a real-time method statical deformation for inflated corneas, the authors underestimated the effects of hydration on corneal thickness change after obtaining post-mortem corneas. This drawback can lead to inaccurate quantitative elastic deformation and unrealistic viscoelastic behaviour as stated previously (Kling and Marcos, 2013; Vantipalli *et al*, 2018). In addition, the role of corneal thickness in strain calculations was not considered since it based on the assumption of axial deformation of corneal apex only with no change in volume of corneal material during applied forces.

Utilising the advantages of LF-OCT system, real-time monitoring of geometrical changes was carried out with an axial resolution of approximately 3.5 μm in corneal tissue. This high-resolution monitoring equipment helped obtain detailed cross-sectional images of the corneas that clearly showed the boundary between the epithelium and stromal layer (see Figure 4.3). Therefore, the LF-OCT system can be considered as a superior imaging modality for monitoring the corneas during inflation testing as it provides both real-time and high-resolution data in a non-destructive manner. In addition, the utilised LF-OCT was more flexible than off the shelf commercial or research swept source systems as this study have used a motorised spectrograph and thus it was possible to select the axial resolution and image depth range suitable for the task in hand. A similar LF-OCT system but with inflexible lower axial resolution was demonstrated by Yasuno *et al*, in which three-dimensional OCT was built for *in vivo* dermatological investigation(Yasuno *et al*, 2006).

The model in this study is based on a basic inflation model proposed by Anderson *et al*(Anderson *et al*, 2004) and further development with the use of the approach that was proposed in the literature (Asejczyk-Widlicka and Pierscionek, 2008) to obtain volumetric strain and tangent elastic modulus. The main limitation of this model was the assumption of zero scleral deformation; where, corneal deformation was recorded only. The cornea and sclera are flexibly connected in the native state, therefore, a whole-eye model including both the cornea and sclera would approximately provide a better demonstration of *in vivo* conditions (Asejczyk-Widlicka and Pierscionek, 2008; Kling *et al*, 2010; Whitford *et al*, 2016). However, the whole-eye model cannot accurately represent the native condition because the eye is an anisotropic structure. Hence, the sclera deformation is different than corneal deformation at the same IOP due to histological differences. Therefore, the corneal deformation in a whole-eye model will be affected by scleral deformation, and therefore complicated analysis is required to measure corneal behaviour (Anderson *et al*, 2004). The whole-eye model can better describe the ocular deformation as a whole structure instead of corneal deformation (Kling *et al*, 2010). In the native state, the eye orbit and surrounding orbital tissues hold the eye ball in place; this acts to limit sclera deformation and the cornea deform differently due to the constraints not being the same (Anderson *et al*, 2004). In addition, the whole-eye model is more complicated to maintain a steady IOP and expensive to run (Elsheikh and Anderson, 2005).

The current study has shown that the radius of the corneal apex decreases slightly with increasing IOP. This trend is similar to that seen in comparable studies (Asejczyk-Widlicka and Pierscionek, 2008; Asejczyk-Widlicka *et al*, 2011; Ko *et al*, 2013; Pierscionek *et al*, 2007). In reality, the radius of

the whole eye, both the cornea and the sclera, would be expected to slightly increase with increasing internal pressure. Unlike the cornea-only model used, the radius of corneal apex was slightly decreased because the free ends of the cornea were mechanically fixed and only its apex was free to deform (Figure 4.2). Consequently, this fixation of the corneas at the limbus could exhibit a non-physiological boundary condition affecting measurements of corneal apex radius during inflation.

In this study, the calculations of elastic behaviour depend on a four-dimension matrix of variables (P, T, R and D) which were varied with time for hydration and hysteresis assessment. The cycle of IOP change was set from 0 to 60 mmHg under which the porcine corneas were monitored for geometrical variations. Geometrical variations were utilised to extract the elastic behaviour during the loading and unloading cycles which was started from 2 mmHg in this study. Other studies have started from different IOPs, 10 mmHg (M. Lombardo *et al*, 2014; Wang *et al*, 2018) and 5 mmHg (Hennighausen *et al*, 1998), depending on the linearity of the IOP-Apex corneal displacement curve. However, the researcher decided to start from 2 mmHg for calculation of the elastic behaviour because the researcher observed that corneas were sufficiently inflated at that minimal internal pressure to remove the initial crimps from the corneal surface, in addition to exhibiting stable geometrical properties and corneal apex displacement. The experiments were performed in the IOP range of 0—60 mmHg and no visual damage was observed. The observation and decision of the present study was in agreement with recent studies (Boschetti *et al*, 2012; Whitford *et al*, 2016).

Corneal thickness is an important parameter that can influence the accuracy of the IOP measurements (Bechmann *et al*, 2000; Ehlers *et al*, 1975; Hansen and Ehlers, 1971). Therefore, corneal thickness is often measured optically to obtain accurate measurements (Hon and Lam, 2013; Singh *et al*, 2016a). In this study, the mean corneal apex thickness measurement was 980±13.5 μm at 15 mmHg. This is comparable to the thickness of 967±76.5 μm at 15 mmHg, which has been reported by other studies that have utilised optical measurements (Asejczyk-Widlicka *et al*, 2008; Kling and Marcos, 2013; Singh *et al*, 2016a). The values also match *in vivo* and *in vitro* studies in which an ultrasound pachymeter was used for the measurements (Bartholomew *et al*, 1997; Jay *et al*, 2008). However, the value in the current study is around 30% lower than an *in vivo* study in which a pachymeter was used for the measurements without considering the effects of IOP on the thickness measurement (Faber *et al*, 2008). The trend of corneal thickness reduction and compression due to IOP has been well-described by other researchers (Asejczyk-Widlicka *et al*, 2008; Ford *et al*, 2011; Tanter *et al*, 2009). The variations in absolute values of corneal apex

thickness reported in the literature can be attributed to many factors including the age of the pigs and hydration method, but the testing instrument and method used are likely to be most significant factors (Faber *et al*, 2008; Sanchez *et al*, 2011).

Corneal apex displacement curves are clearly non-linear throughout the whole IOP range. However, the slope varies slightly at high IOP (> 20 mmHg). This non-linear behaviour demonstrates that the corneas have an average low stiffness at low IOP, and then the stiffness rises as the IOP increases. At low IOPs, the collagen fibrils are not taut, and the mechanical response is mainly dominated by the extracellular matrix of the stromal layer. At high IOPs, collagen fibrils lead the mechanical response. This non-linear response, change of slope rate in corneal apex displacement has also been reported by other researchers (Anderson *et al*, 2004; Ford *et al*, 2011; Wang *et al*, 2018; Whitford *et al*, 2016). In this study, the values of corneal apex displacement with IOP for the porcine corneas are close to those reported by Whitford *et al* (Whitford *et al*, 2016) and Wang *et al* (Wang *et al*, 2018).

The stress-strain relationship exhibits the expected non-linear mechanical behaviour. In the first cycle of the loading and unloading curves, no statistical significance was observed at low IOPs. This non-linear behaviour occurred due to the pre-conditioning phase of the cornea where the collagen fibrils are not aligned. Quinn and Winkelstein (Quinn and Winkelstein, 2011) stated that there is a strong relationship between alignment changes of collagen fibrils and the mechanical response during pre-conditioning as fibrils start to change direction in response to the main deformation point. The porcine corneas tested in this study exhibited a typical viscoelastic response which is expressed by the hysteresis value measured from the area between the loading-unloading phases of the stress-strain curve. The initial hysteresis value for fresh porcine corneas, 10.5±0.6 mmHg, is very close to the human cornea hysteresis measured *in vivo* by Ocular Response Analyser (Firat and Doganay, 2011). The value of hysteresis can be affected by corneal pathology, for example it is low in keratoconic corneas (Luce, 2005). It can also be influenced by the natural aging process (Kotecha, 2007; Kotecha *et al*, 2006).

This study found an approximately linear relationship between the elastic modulus and IOP at IOPs greater than 20 mmHg. The values of elastic modulus are mostly non-linear at low IOPs. To the best of author's knowledge, no previous study has reported the elastic modulus values of porcine corneas based on a similar method. The elastic modulus of the current study is comparable to a study conducted by Asejczyk-Widlicka and Pierscionek (Asejczyk-Widlicka and Pierscionek,

2008), in which high-resolution digital cameras were used to monitor corneal profile changes in response to IOP. In addition, the elastic modulus of the current study are slightly higher to a study conducted by Singh *et al* (Singh *et al*, 2016a), E = 14.7 kPa at 15 mmHg, in which OCE was used to assess the effects of UV-A/riboflavin corneal collagen crosslinking (CXL) on the mechanical anisotropy of in situ porcine corneas at varying IOPs. This difference could be related to the different method used and also due to the hydration effect on corneas. However, the current study is comparable in the trend of increases the elastic modulus with CCT decreases due to high IOP, as was reported in the same study (Singh *et al*, 2016a). Reporting elastic modulus of porcine corneas will help to identify mechanical properties and provide a basis for comparison with treated or unhealthy corneas. One limitation of the current approach is that the elasticity calculation assumes that the corneal samples have an entirely homogenous thickness. In reality, there is an uneven increase in corneal thickness from central area toward the peripheral area (Asejczyk-Widlicka *et al*, 2008). This can lead to a slight inaccuracy in the calculation of volumetric strain since the thickness change of corneal apex (ΔT) is included in the calculation of the volumetric strain. Therefore, building a model to involve regional variation of corneal thickness will help to increase the accuracy of biomechanical properties calculations.

This study also examined the effect of hydration on the biomechanical and geometrical properties of the corneas. Corneal thickness significantly increased after one hour. Since the pressure remained at 0 mmHg IOP between tests, the thickness increase can be attributed to corneal swelling due to hydration. Corneal swelling likely occurred due to the osmolarity difference between the corneal tissue and the PBS. The swelling gradually increased in subsequent test cycles indicating water quantity in the tissue is approaching the equilibrium state of the osmolarity difference. The area between the curves in each cycle gradually increased and hence there was a hysteresis change with each cycle. In the hydrated corneas, the elastic modulus significantly increased after one hour. After 4 hours of hydration, elastic modulus was substantially higher as compared to fresh corneas suggesting that this was due to the swelling (thickness increase). This relation proves that corneal thickness variations can affect the stiffness and then realistic IOP measurements. This is thought to be related to geometrical changes in the extracellular matrix and in particular collagen fibril properties due to swelling. These changes may lead to modifications in material density and molecular spacing, which will affect the biomechanical response. Therefore, corneal thickness should be maintained by appropriate hydration media which can help stabilise corneal elasticity. This finding was also proposed by Kling and Marcos (2013), where they preserved corneas in Dextran solution and found these were less stiff than those in Optisol (tissue

culture media). They also compared corneal thickness preserved in varying storage media, and studied the effect of hydration on porcine corneas. In addition, Dias and Ziebarth (2015) reported that the more swollen corneal samples (higher hydration) were stiffer (greater elastic modulus). They used AFM to examine the impact of corneal hydration on corneal elasticity of *ex vivo* samples. On the other hand, Hatami-Marbini and Etebu, (2013) reported contradictory results to the trend found within the current study; where they showed that elastic modulus decreases with increasing hydration. They used a rheometry to measure elastic response of corneas immersed in 0.9% NaCl solution. The difference may be related to the differences in characterisation method, for example the method used by Hatami-Marbini and Etebu measures a shear response rather than an elastic response as in the current study.

This study also showed hysteresis variations with hydration time. Corneal hysteresis (the area between the loading and unloading phase of stress-strain curve) increased by 59.3% after 4 hours of hydration that made significant changes in corneal thickness. The current data shows that as hysteresis increases as the central corneal thickness increases due to hydration. Since corneal thickness increases are associated with elastic modulus increases (Han *et al*, 2015b; Vantipalli *et al*, 2018), hysteresis may increase with high elastic modulus corneas. Although, there limited studies in the literature which have examined corneal hysteresis as a function of hydration. One previous study has shown that the higher the concentration of Dextran, the greater the hysteresis observed (Kling and Marcos, 2013). In that study, hysteresis was defined as the amount of remaining corneal deformation after a cycle of increased/decreased IOP variation, which differs from the approach of the present study. Interestingly, the slightly swollen corneas in Optisol-GS for 24 hours showed increased hysteresis, which is in the agreement with the current finding.

This chapter aimed to quantify the biomechanical and geometrical properties of porcine corneas and how much these properties vary with IOP and hydration. However, this study is limited to loading/unloading rate (speed of the inflation and testing). The wide variation in biomechanical properties of corneas reported in the literature could be related to the viscoelastic nature of the corneal tissue and its dependence on age, hydration and testing conditions (Elsheikh *et al*, 2007; 2011; Nash *et al*, 1982). The loading/unloading rate in inflation testing is one of the parameters that undoubtedly affects the measured biomechanical (stress-strain and hysteresis) and geometrical (thickness) properties. It is expected that the cornea exhibits higher stiffness and hysteresis at fast pressure application rate (fast loading/unloading rate) than those measured at slow pressure application rate. Elsheikh *et al* (2007) determined mechanical behaviour of the human cornea at

different loading rates in inflation testing. They found that the fast loading rate is associated with higher values of elastic modulus, which could also show high hysteresis values, as would be anticipated from a viscoelastic material such as the cornea.

The approach used in this study is of clinical relevance. For example, keratoconic corneas are characterised by reduced localised thickness with a lower elastic modulus and hysteresis (Bao *et al*, 2017). Furthermore, low corneal hysteresis and thin central corneal thickness are associated with glaucoma damage, which is an acquired optic neuropathy in which destruction of ganglion cells and fibres leads to irreversible visual field loss (Congdon *et al*, 2006). In addition, the findings can help in providing better models for calculating IOP in stiff corneas, and enhance the ability to accurately diagnose many other ocular diseases. Moreover, this study has shown that corneal hydration has a significant influence on the biomechanical response of the cornea and the type of hydrating solution may have significant effects on the biomechanical response depends (Kling and Marcos, 2013). Therefore, geometrical changes due to hydration of corneal samples should be addressed to increase the accuracy of models and improve clinical practice.

4.6. Conclusions

In conclusion, this study has developed an LF-OCT system for corneal inflation testing to provide better assessment for the corneal biomechanical behaviour. This study has validated the current data by comparing the results with other studies that used the same parameters. The results show that the biomechanical properties of the cornea can be influenced by many factors such as IOP, corneal thickness and hydration. Over the loading phase, corneal thickness decreases as the IOP increases. Elastic modulus increases as the IOP increases. Finally, the corneas showed a non-linear increase of elastic modulus, corneal thickness and hysteresis as the hydration time increased. The current method may help build better numerical and mechanical models and thereby help better understand corneal biomechanics. In addition, this study provides information that might help avoid complications in corneal surgical practice which may occur due to inaccurate estimation of the real IOP and corneal thickness.

4.7. References

Anderson, K., Elsheikh, A., Newson, T., 2004. Application of structural analysis to the mechanical behaviour of the cornea. Journal of The Royal Society Interface 1, 3-15.

Asejczyk-Widlicka, M., Pierscionek, B., 2008. The elasticity and rigidity of the outer coats of the eye. British Journal of Ophthalmology 92, 1415-1418.

Asejczyk-Widlicka, M., Schachar, R., Pierscionek, B., 2008. Optical coherence tomography measurements of the fresh porcine eye and response of the outer coats of the eye to volume increase. SPIE 13, 024002-1 - 024002-6.

Asejczyk-Widlicka, Śródka, Schachar, R.A., Pierścionek, B.K., 2011. Material properties of the cornea and sclera: A modelling approach to test experimental analysis. Journal of Biomechanics 44, 543-546.

Bao, F.J., Geraghty, B., Wang, Q.M., Elsheikh, A., 2017. Role of corneal biomechanics in the diagnosis and management of keratoconus. In: Alió J. (eds) Keratoconus (pp. 141-150). Springer, Cham, pp. 141-150. USA.

Bartholomew, L., Pang, D., Sam, D., Cavender, J., 1997. Ultrasound biomicroscopy of globes from young adult pigs. American Journal of Veterinary Research 58, 942-948.

Bechmann, M., Thiel, M., Roesen, B., Ullrich, S., Ulbig, M., Ludwig, K., 2000. Central corneal thickness determined with optical coherence tomography in various types of glaucoma. British Journal of Ophthalmology 84, 1233-1237.

Boschetti, Triacca, Spinelli, Pandolfi, 2012. Mechanical Characterization of Porcine Corneas. Journal of Biomechanical Engineering 134, 031003.

Boyce, B., Grazier, M., Jones, R., Nguyen, T., 2008. Full-field deformation of bovine cornea under constrained inflation conditions. Biomaterials 29, 3896-3904.

Bryant, M., McDonnell, P., 1996. Constitutive laws for biomechanical modeling of refractive surgery. the American Society of Mechanical Engineers 118, 473 - 481.

Congdon, N., Broman, A., Bandeen-Roche, K., Grover, D., Quigley, H., 2006. Central corneal thickness and corneal hysteresis associated with glaucoma damage. American Journal of Ophthalmology 141, 868-875.

Dias, J., Ziebarth, N., 2015. Impact of hydration media on *ex vivo* corneal elasticity measurements. Eye and Contact Lens 41, p, 281-286.

Dorronsoro, C., Pascual, D., Pérez-Merino, P., Kling, S., Marcos, S., 2012. Dynamic OCT measurement of corneal deformation by an air puff in normal and cross-linked corneas. Biomedical Optics Express 3, 473-87.

Ehlers, N., Bramsen, T., Sperling, S., 1975. Applanation tonometry and central corneal thickness. Acta Ophthalmologica 53, 34-43.

Elsheikh, A., Alhasso, D., Rama, P., 2008. Biomechanical properties of human and porcine corneas. Experimental Eye Research 86, 783-790.

Elsheikh, A., Anderson, K., 2005. Comparative study of corneal strip extensometry and inflation tests. Journal of The Royal Society Interface 2, 177-185.

Elsheikh, A., McMonnies, C., Whitford, C., Boneham, G., 2015. *In vivo* study of corneal responses to increased intraocular pressure loading. Eye and Vision 2, 1-10.

Elsheikh, A., Wang, D., Brown, M., Rama, P., Campanelli, M., Pye, D., 2007. Assessment of corneal biomechanical properties and their variation with age. Current Eye Research 32, 11-19.

Elsheikh, A., Kassem, W., Jones, S., 2011. Strain-rate sensitivity of porcine and ovine corneas. Acta of Bioengineering & Biomechanics 13(2), 25-36.

Faber, C., Scherfig, E., Prause, J., Soensen, K., 2008. Corneal thickness in pigs measured by ultrasound pachymetry *in vivo*. Scandinavian Journal of Laboratory Animal Sciences 35, 39-43.

Fernández, D., Niazy, Kurtz, Djotyan, Juhasz, 2005. Finite element analysis applied to cornea reshaping. Journal of Biomedical Optics 10, 064018-064018-11.

Firat, Doganay, 2011. Corneal hysteresis in patients with dry eye. Eye 25, eye2011211.

Ford, M., Dupps, W., Rollins, A., Roy, A., Hu, Z., 2011. Method for optical coherence elastography of the cornea. Journal of Biomedical Optics 16, 016005-016005-7.

Ford, M.R., Roy, A., Rollins, A.M., Dupps, W.J., 2014. Serial biomechanical comparison of edematous, normal, and collagen crosslinked human donor corneas using optical coherence elastography. Journal of Cataract & Refractive Surgery 40, 1041-1047.

Fung, Y.C., 2013. Biomechanics: Mechanical Properties of Living Tissues, 2nd Edition. Springer Science and Business Media. USA.

Gatzioufas, Seitz, 2014. Determination of corneal biomechanical properties *in vivo*: a review. Materials Science and Technology 31, 188-196.

Grehn, F., Stamper, R., 2009. Essentials in Ophthalmology Glaucoma. Springer. USA

Guarnieri, F., 2014. Corneal Biomechanics and Refractive Surgery. Springer, Argentina .

Guirao, A., 2005. Theoretical elastic response of the cornea to refractive surgery: risk factors for keratectasia. Journal of Refractive Surgery 21, 176-85.

Gunvant, P., O'Leary, D.J., Baskaran, M., Broadway, D.C., Watkins, R.J., Vijaya, L., 2005. Evaluation of tonometric correction factors. Journal of Glaucoma, 14(5), 337-343.

Han, Z., Aglyamov, S., Li, J., Singh, M., Wang, S., Vantipalli, S., Wu, C., Liu, C., Twa, M., Larin, K., 2015. Quantitative assessment of corneal biomechanical properties using optical coherence elastography and a modified Rayleigh Lamb-frequency model. International Society for Optics and Photonics: Ophthalmic Technologies XXV 9307. 930719-1-5.

Han, Z., Li, J., Singh, M., Aglyamov, S., Wu, C., Liu, C., Larin, K., 2015. Analysis of the effects of curvature and thickness on elastic wave velocity in cornea-like structures by finite element modeling and optical coherence elastography. Applied Physics Letters 106, 233702.

Han, Z., Li, J., Singh, M., Wu, C., Liu, C., Raghunathan, R., Aglyamov, S., Vantipalli, S., Twa, M., Larin, K., 2017. Optical coherence elastography assessment of corneal viscoelasticity with a modified Rayleigh-Lamb wave model. Journal of the Mechanical Behavior of Biomedical Materials 66, 87-94.

Hansen, F., Ehlers, N., 1971. Elevated tonometer readings caused by a thick cornea. Acta Ophthalmologica 49, 775-778.

Hatami-Marbini, H., Etebu, E., 2013. Hydration dependent biomechanical properties of the corneal stroma. Experimental Eye Research 116, 47-54.

Hennighausen, H., Feldman, S.T., Bille, J.F., McCulloch, A.D., 1998. Anterior-posterior strain variation in normally hydrated and swollen rabbit cornea. Investigative Ophthalmology & Visual Science 39, 253-62.

Hon, Y., Lam, A., 2013. Corneal deformation measurement using Scheimpflug noncontact tonometry. Optometry and Vision Science 90, e1 - e8.

Jay, L., Brocas, A., Singh, K., Kieffer, J., Brunette, I., Ozaki, T., 2008. Determination of porcine corneal layers with high spatial resolution by simultaneous second and third harmonic generation microscopy. Optical Society of America 16, 16284-16293.

Kling, S., Marcos, S., 2013. Effect of hydration state and storage media on corneal biomechanical response from *in vitro* inflation tests. Journal of Refractive Surgery 29, 490-7.

Kling, S., Remon, L., Pérez-Escudero, A., Merayo-Lloves, J., Marcos, S., 2010. Corneal biomechanical changes after collagen cross-Linking from porcine eye inflation experiments. Investigative Ophthalmology & Visual Science 51, 3961-3968.

Ko, M., Leung, L., Lam, D., Leung, C., 2013. Characterization of corneal tangent modulus *in vivo*. Acta Ophthalmologica 91, e263-e269.

Kotecha, A., 2007. What biomechanical properties of the cornea are relevant for the clinician? Survey of Ophthalmology 52, S109-S114.

Kotecha, A., Elsheikh, A., Roberts, C.R., Zhu, H., Garway-Heath, D.F., 2006. Corneal thickness- and age-related biomechanical properties of the cornea measured with the ocular response analyzer. Investigative Ophthalmology & Visual Science 47, 5337-47.

Lai, J., Zhang, Y., Li, Z., Jiang, H., He, A., 2010. Complex refractive index measurement of biological tissues by attenuated total reflection ellipsometry. Optical Society of America 49, 3235 - 3238.

Larin, K.V., Sampson, D.D., 2017. Optical coherence elastography - OCT at work in tissue biomechanics [Invited]. Biomedical Optics Express 8, 1172-1202.

Lawman, S., Dong, Y., Williams, B., Romano, V., Kaye, S., Harding, S., Willoughby, C., Shen, Y.-C., Zheng, Y., 2016. High resolution corneal and single pulse imaging with line field spectral domain optical coherence tomography. Optics Express 24, 12395.

Lawman, S., Madden, P., Romano, V., Dong, Y., Mason, S., Williams, B., Kaye, S., Willoughby, C., Harding, S., Shen, Y.-C., Zheng, Y., 2017a. Deformation velocity imaging using optical coherence tomography and its applications to the cornea. Biomedical Optics Express 8, 5579.

Lawman, S., Williams, B., Zhang, J., Shen, Y.-C., Zheng, Y., 2017b. Scan-less line field optical coherence tomography, with automatic image segmentation, as a measurement tool for automotive coatings. Applied Sciences 7, 351.

Li, J., Han, Z., Singh, M., Twa, M., Larin, K., 2014. Differentiating untreated and cross-linked porcine corneas of the same measured stiffness with optical coherence elastography. Journal of Biomedical Optics 19, 110502-110502.

Li, T., Tian, L., Wang, L., Hon, Y., Lam, A., Huang, Y., Wang, Y., Zheng, Y., 2015. Correction on the distortion of Scheimpflug imaging for dynamic central corneal thickness. Journal of Biomedical Optics 20, 056006-056006.

Liu, C.-H.H., Schill, A., Raghunathan, R., Wu, C., Singh, M., Han, Z., Nair, A., Larin, K.V., 2017. Ultra-fast line-field low coherence holographic elastography using spatial phase shifting. Biomedical Optics Express 8, 993-1004.

Liu, J., Roberts, C., 2005. Influence of corneal biomechanical properties on intraocular pressure measurement Quantitative analysis. Journal of Cataract & Refractive Surgery 31, 146-155.

Lombardo, G., Serrao, S., Rosati, M., Lombardo, M., 2014. Analysis of the viscoelastic properties of the human cornea using scheimpflug imaging in inflation experiment of eye globes. PLoS ONE 9, e112169.

Lombardo, M., Serrao, S., Rosati, M., Ducoli, P., Lombardo, G., 2014. Biomechanical changes in the human cornea after transepithelial corneal crosslinking using iontophoresis. Journal of Cataract & Refractive Surgery 40, 1706-1715.

Luce, D., 2005. Determining *in vivo* biomechanical properties of the cornea with an ocular response analyzer. Journal of Cataract & Refractive Surgery 31, 156-162.

Nash, I., Greene, P., Foster, C.S., 1982. Comparison of mechanical properties of keratoconus and normal corneas. Experimental Eye Research 35, 413-424.

Orssengo, G.J., Pye, D.C., 1999. Determination of the true intraocular pressure and modulus of elasticity of the human cornea *in vivo*. Bulletin of mathematical biology 61, 551-72.

Pierscionek, B.K., journal of … M., Schachar, R.A., 2007. The effect of changing intraocular pressure on the corneal and scleral curvatures in the fresh porcine eye. British Journal of Ophthalmology 91, 801.

Quinn, K., Winkelstein, B., 2011. Preconditioning is correlated with altered collagen fiber alignment in ligament. Journal of Biomechanical Engineering 133, 064506.

Radhakrishnan, H., Miranda, M., O'Donnell, C., 2012. Corneal biomechanical properties and their correlates with refractive error. Clinical and Experimental Optometry 95, 12-18.

Rosales, P., Marcos, S., 2009. Pentacam scheimpflug quantitative imaging of the crystalline lens and intraocular lens. Journal of Refractive Surgery 25, 421-8.

Sanchez, I., Martin, R., Ussa, F., Fernandez-Bueno, I., 2011. The parameters of the porcine eyeball. Graefe's Archive for Clinical and Experimental Ophthalmology 249(4), 475-482.

Singh, M., Li, J., Han, Z., Raghunathan, R., Nair, A., Wu, C., Liu, C.-H., Aglyamov, S., Twa, M., Larin, K., 2016a. Assessing the effects of riboflavin/UV-A crosslinking on porcine corneal mechanical anisotropy with optical coherence elastography. Biomedical Optics Express 8, 349.

Singh, M., Li, J., Han, Z., Wu, C., Aglyamov, S., Twa, M., Larin, K., 2016b. Investigating elastic anisotropy of the porcine cornea as a function of intraocular pressure with optical coherence elastography. Journal of Refractive Surgery 32, 562-567.

Spoerl, E., Seiler, T., 1999. Techniques for stiffening the cornea. Journal of Refractive Surgery 15, 711-3.

Tanter, Touboul, Gennisson, J.-L., Bercoff, J., Fink, M., 2009. High-resolution quantitative imaging of cornea elasticity using supersonic shear imaging. IEEE Transactions on Medical Imaging 28, 1881-1893.

Tuchin, V. V, 2007. Tissue Optics: Light Scattering Methods and Instruments for Medical Diagnosis, Third. ed. SPIE.USA

Tuchin, V. V., Wang, L, Zimnyakov, D.A., 2006. Optical Polarization in Biomedical Applications. Springer Science & Business Media.USA.

Vantipalli, S., Li, J., Singh, M., Aglyamov, S., Larin, K., Twa, M., 2018. Effects of thickness on corneal biomechanical properties using optical coherence elastography. Optometry and Vision Science 95, 299.

Wang, L., Tian, L., Huang, Y., Huang, Y., Zheng, Y., 2018. Assessment of corneal biomechanical properties with inflation test using optical coherence tomography. Annals of Biomedical Engineering 46, 247-256.

Wang, S., Larin, K., 2015. Optical coherence elastography for tissue characterization: a review. Journal of Biophotonics 8, 279-302.

Whitford, C., Joda, A., Jones, S., Bao, F., Rama, P., Elsheikh, A., 2016. *Ex vivo* testing of intact eye globes under inflation conditions to determine regional variation of mechanical stiffness. Eye and Vision 3, 21.

Whitford, C., Studer, H., Boote, C., Meek, K., Elsheikh, A., 2015. Biomechanical model of the human cornea: Considering shear stiffness and regional variation of collagen anisotropy and density. Journal of the Mechanical Behavior of Biomedical Materials 42, 76-87.

Wu, K., Li, S., Lo, A., Ngan, A., Wong, D., So, K., Ellis-Behnke, R., Tang, B., 2013. Micro-scale stiffness change of cornea tissues suffered from elevated intraocular pressure investigated by nanoindentation. Soft Materials 11, 244-253.

Yasuno, Y., Endo, T., Makita, S., Aoki, G., Itoh, M., Yatagai, T., 2006. Three-dimensional line-field Fourier domain optical coherence tomography for *in vivo* dermatological investigation. Journal of Biomedical Optics 11, 014014-014014-7.

Yu, J., Bao, F., Feng, Y., Whitford, C., Ye, T., Huang, Y., Wang, Q., Elsheikh, A., 2013. Assessment of corneal biomechanical behavior under posterior and anterior pressure. Journal of Refractive Surgery (Thorofare, N.J. : 1995) 29, 64-70.

Yuzhakov, A., Sviridov, A., Baum, O., Shcherbakov, E., Sobol, E., 2013. Optical characteristics of the cornea and sclera and their alterations under the effect of nondestructive 1.56-μm laser radiation. Journal of Biomedical Optics 18, 058003-058003.

Chapter 5

In vitro assessment of corneal transparency of inflated porcine corneas

This chapter focusses on applying the spectrophotometric technique to assess corneal transparency of the porcine cornea in the visible spectra. The factors that affect corneal transparency are summarised in this chapter. The effects of an altered corneal ultrastructure on corneal transparency are evaluated by changing intraocular pressure, and hydration. This chapter demonstrates why corneal transparency changes in certain conditions including with varying intraocular pressure, hydration time and de-epithelisation. The method of sample clamping and the location of the incident beam on the sample were controlled in this study in order to obtain regional optical properties of porcine corneas. Furthermore, the testing method utilised in this chapter was optimised, which is applied to assess corneal transparency of enzymatic treated corneas in the subsequent chapter.

Abstract

The cornea is the outermost part of the eye and is characterised for its transparency and refractive power. The need for treating, managing and modelling certain corneal diseases motivates researchers to build extended knowledge about the cornea. This chapter investigates light transmission and the linear absorption coefficient (μ_a) through the porcine cornea in the visible portion of the electromagnetic spectrum as a function of intraocular pressure (IOP) and position across the cornea from the centre to the periphery. Spectrophotometry was used to measure visible light transmission in the wavelength range 380-820 nm across pressurised corneas from 0 - 60 mmHg. Light transmission through corneas that were incubated in phosphate buffer saline (PBS) and tissue culture (TC) solutions for 4 hours was assessed to explore the role of the solutions on corneal transparency. The maximum percentage transmission (%T) of light across porcine corneas was 88.6±0.4% that was recorded at 700 nm and 15 mmHg. At 700 nm and 15 mmHg, the minimum μ_a of 1.27±0.36 cm^{-1} was calculated. Light transmission in central cornea was higher than in other regions. Corneal transparency decreased in corneas that were incubated in PBS and TC. Non-statistically significant differences were observed between light transmission across de-epithelised corneas and intact corneas. Corneal transparency was found to be a function of IOP, a parameter that should be considered in transparency measurement. The method presented can be used to assess corneal absorption for riboflavin *in vitro*. Light transmission through porcine cornea presented in this study could be used to predict corneal ultrastructure changes.

5.1. Introduction

Transparency is an essential property of the cornea, the primary refractive component in the visual system of animals including humans. The cornea combines its interesting optical properties with complex viscoelastic characteristics and thus must have a structure that allows strength, transparency, and maintains an ideal shape simultaneously for clear vision.

5.1.1. Stromal ultrastructure and transparency

The human cornea is composed of five layers, in which the thickest layer is the stroma that is mainly composed of type I collagen fibrils. These fibrils are arranged in layers known as lamellae in which they run in acute angles to each other in the anterior stroma and run parallel to each other in the middle and posterior stroma; all lamellae are parallel to the corneal surface. These lamellae are arranged at all rotational angles throughout the depth of the cornea. Although, human corneas seem to be in preferential orientations in which a larger proportion of fibrils lie in the inferior-superior and medial-lateral directions (Aghamohammadzadeh *et al*, 2004). In other species such as pigs, a larger proportion of stromal collagen fibrils lie in circumferential orientations (Hayes *et al*, 2007). The extracellular matrix (ECM) of the corneal stroma is comprised of keratocytes and collagen fibrils. The collagen fibrils are cross-linked by an interstitial matrix of proteoglycans, by which the interfibrillar spacing is maintained. The collagen fibril and interfibrillar spacing are highly uniform in the central cornea, possessing a diameter of 32.5±1.5 nm with a centre to centre interfibrillar spacing of 61 nm in humans (Meek and Boote, 2004) and almost the same in pigs (Kazaili and Akhtar, 2018). It is widely accepted that they have no role in light scattering because of their small dimensions compared to the wavelengths of visible light (Meek and Boote, 2004).

The stromal cells, known as keratocytes have minor effect on light propagation. Light travelling across the human cornea is thought to pass through approximately 100 layers of keratocytes, as has been estimated according to their density, volume, and size (Møller-Pedersen, 2004). Under physiological conditions, intracellular crystallin proteins act to match the overall refractive index of keratocytes to that of the ECM. This delicate matching makes the cell cytoplasm transparent, with the nuclei and the very tiny mitochondria contributing to specular scatter (Jester *et al*, 1999; Meek *et al*, 2003).

5.1.2. Transparency theories and the affecting parameters

Many attempts have been made to explain why the cornea is transparent. Maurice (1957) suggested that the corneal collagen fibrils were arranged in a hexagonal lattice structure, and that the scattered

light from the collagen fibrils would interfere destructively in all directions except that of the incident beam (the primary visual axis). The study postulated that collagen fibrils in swollen corneas would be disrupted from the perfect hexagonal lattice structure and scattered light would not be removed from the beam leading to a reduction in corneal transparency and corneal haze.

Subsequently, the lattice theory of transparency was assessed by Goldman and Benedek (1967) to elucidate the transparency of the dogfish cornea. They reported that the theory failed to explain the transparency of the dog fish cornea because the cornea consists of a thick Bowman's layer that occupied 15% of CCT and comprises of non-parallel fibres. They concluded that the lattice arrangement of collagen fibrils was not the main role for corneal transparency and that the transparency of Bowman's layer was because of the uniformity of collagen fibrils diameters and the interfibrillar spacing that measures approximately half the wavelength of visible light. Their finding was mathematically validated in a later study (Hart and Farrell, 1969). With the use of X-ray diffraction, it was suggested that collagen fibrils are not totally organised in a perfect lattice structure, but collagen fibrils are arranged in a paracrystalline lattice structure, where there is adequate correlation in the phases scattered from each fibril that destructive interference follows as a simple and elegant theoretical consequence (Sayers *et al*, 1982; Worthington, 1984).

In summary, from the models proposed in literature to explain corneal transparency, the mostly widely recognised studies suggest that the following parameters are important: collagen fibril diameter, Interfibrillar spacing, number density of collagen fibrils, spatial ordering of the fibrillar array, refractive index differential between the interfibrillar or ground substance and the fibrils and stromal thickness.

The role of each of these parameters on corneal transparency, and comprehensive discussions of light propagation and scattering through the cornea, can be found in the literature (Meek and Knupp, 2015; Meek *et al*, 2003) and summarised in Section 2.5 of this thesis. However, it is well known that some of these parameters are affected by physiological conditions such as intraocular pressure (IOP) and hydration. To date, corneal transparency at varying physiological pressure has been neglected; therefore, the present study aims to bridge this gap. In addition, these parameters vary slightly in different species in term of corneal thickness, collagen fibril orientation, and regional structural changes over the cornea (Hayes *et al*, 2007; Koudouna *et al*, 2018; Winkler *et al*, 2015). Therefore, corneal transparency of human corneas might not be as same as in other vertebrate corneas.

5.1.3. Measurement of corneal transparency

Spectrophotometry is the most common method that was used to study the transmission spectrum through the cornea. In spectrophotometry method, a light beam is equally divided into a reference beam and an incident beam. The intensity of the reference beam is measured by using a photodetector. The incident beam is directed perpendicular on a sample, which is placed in front of another photodetector. The intensity of the transmitted beam is measured by the photodetector to be compared to the intensity of reference beam. In the new developed spectrophotometers, a photodetector is added for measuring the reflections from the surface of the cornea.

Spectrophotometry has been adapted to measure and evaluate corneal transparency across the cornea in the visible region (Beems and Best, 1990; Boettner and Wolter, 1962; Doutch *et al*, 2008, 2007; Freegard, 1997) and in the ultraviolet region (Koppen *et al*, 2010; Lombardo *et al*, 2015; Doutch *et al*, 2012; Lembares *et al*, 1997; Lombardo *et al*, 2015). These studies provided valuable data in the field of corneal transparency. However, no study has investigated the optical response of the cornea to varying IOP. Few studies applied a fixed hydrostatic pressure on the cornea to evaluate corneal transparency in visible region (Kostyuk *et al*, 2002; Lombardo *et al*, 2015a). Kostyuk *et al* (2002) used spectrophotometry to measure corneal transparency of deepithelised and deendothelised bovine corneal stromas with a hydration of 3.2 equilibrated at 154 mM NaCl and buffered at pH 7.4. A pressure of 360 Pa (2.7 mmHg) was applied on the samples using silicon oil, and optical density was measured over the range from the 450 to 750 nm range. They found that corneas were progressively more transparent as NaCl increased, relating that to the known increase of fixed negative charge in the corneal matrix when chloride ions are adsorbed onto the matrix. Lombardo and others (2015) evaluated the stromal concentration of transepithelial riboflavin 0.1% solution in human donor corneas soaked either in a 15% dextran-enriched riboflavin 0.1% solution or a hypotonic dextran-free riboflavin 0.1% solution with the use of spectrophotometry. They measured absorbance spectra of human corneas in the 330 to 700 nm range, in which corneas were pressurised at fixed pressure of 18 mmHg using sodium chloride 0.9% solution. The study effectively evaluated the concentration of the absorbed riboflavin in the stromas, concluded that dextran-enriched solutions required complete corneal de-epithelisation to permit effective stromal soaking with riboflavin or other solutions.

5.1.4. Aim

This chapter aims to determine how corneal transparency varies with IOP (0 - 60 mmHg) across the central region of the porcine cornea. In addition, the chapter examines how corneal transparency varies from centre to the limbus of the cornea. Furthermore, corneal transparency for swollen corneas and de-epithelised corneas was assessed.

5.2. Materials and methods

5.2.1. Sample preparation

Thirteen pair of fresh porcine eyes were separately obtained from a local abattoir shortly after slaughter. The pigs were aged from 5 to 6 months. The epithelium layer was peeled off using a cotton-tipped applicator and tweezers. The corneas, with a 2 mm scleral ring, were subsequently dissected and placed in a specially designed artificial anterior chamber, Figure 5.1.

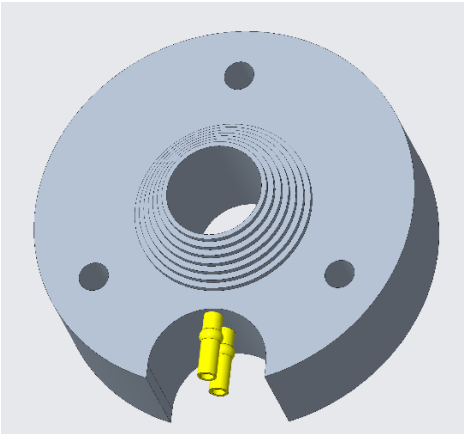

Figure 5.1: 3D sketch of the specially designed artificial anterior chamber. The corneas were clamped at the top of the chamber by a cap, with a 14 mm diameter aperture. The diameter of the anterior aperture of the holder is 13 mm. The diameter of posterior aperture is 25.4 mm, which is covered by a quartz glass disc of thickness 0.25 mm that allows light of 200 to 2500 nm wavelength range across it. The part was drawn using Creo V5 (PTC Inc., MA, USA) and fabricated in the mechanical workshop (School of Engineering, University of Liverpool, UK).

5.2.2. Experimental setup

Corneal transparency was evaluated by measuring the transmitted intensity in the visible region. A double beam spectrophotometer (SYNERGY HT, BioTek, USA) with a detector half-angle acceptance of 3° and a beam size adjusted to 1 mm diameter was utilised to determine the transmitted light intensity (I) through inflated porcine corneas. Percentage transmission (%T) was measured using Equations 5.1 and 5.2. Figure 5.2 demonstrates the setup used for measuring corneal transparency. The corneas were clamped in the specially designed artificial anterior chamber (Figure 5.1) and pressurised simulating intraocular pressures (IOP) in the range 0 to 60

mmHg. The pressure was controlled by the height of the reservoir, which is filled with phosphate buffer saline solution (PBS), and measured using a pressure sensor (ABP series, Honeywell, USA).

$$T = I/I_o \tag{5.1}$$

$$\%T = 100\ T \tag{5.2}$$

where, I and I_o are the transmitted and initial intensity of the light beam, respectively. T is the transmission and $\%T$ is the percentage transmission.

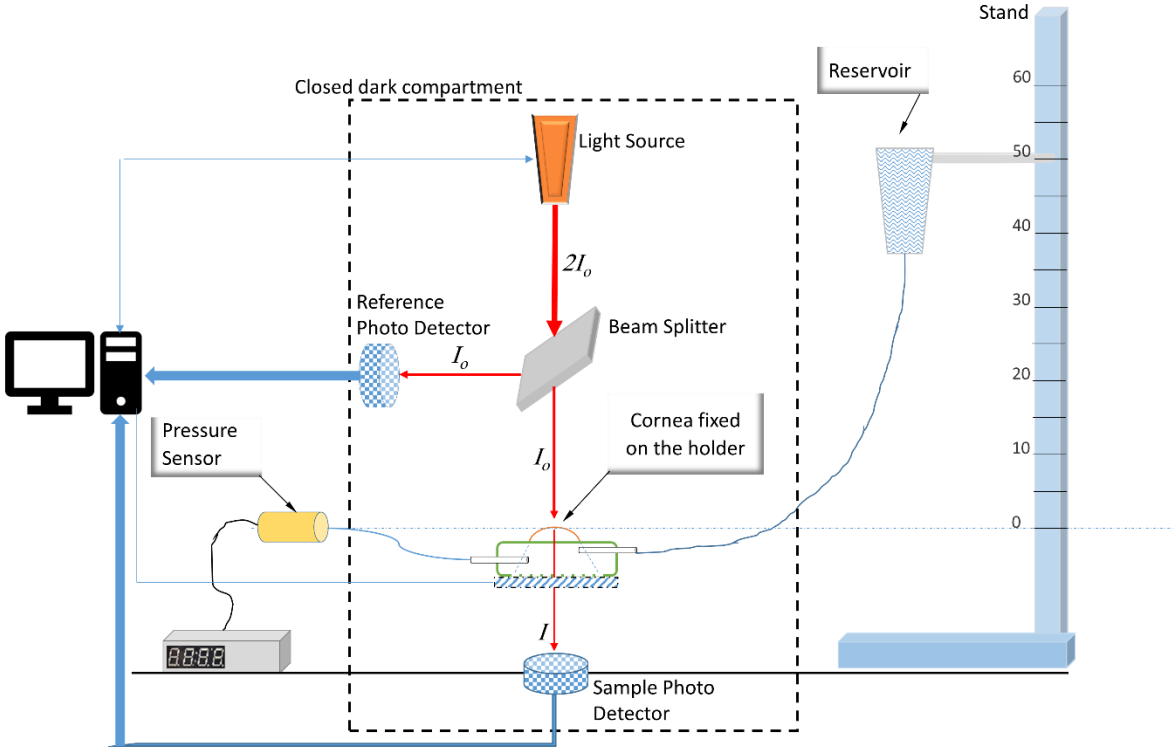

Figure 5.2: Schematic diagram of the spectrophotometric method which was used for measuring corneal transparency. The reservoir was filled with PBS. The light source emits a beam that is equally divided by the beam splitter into reference and incident beams, both I_o. The transmitted beam across the sample I is detected and compared with the initial incident beam. Spectrophotometric components are in closed dark compartment, so that any reflections from the surface of the cornea can be detected. The computer can control the light source and the stage, where the sample is placed. In addition, the computer can detect back reflections from the sample surface.

The artificial corneal chamber was placed in the spectrophotometer such that the light beam was perpendicular to the surface of the corneas during the measurements. Baseline readings were collected from the corneal chamber filled only with PBS, and was recorded before each corneal measurement. Thus, light transmission measurements through the inflated corneas were expressed

as a ratio of the baseline reading. The light beam path could be adjusted in lateral controlled displacements by the operating software (Gen5, BioTek, USA), which can move the stage to any point in Cartesian coordinates. Therefore, measuring the light transmission at predefined points on the cornea could be achieved. The geometrical centre of the corneas was assumed and set as the origin point of the Cartesian coordinates. Reflections from the surface of the cornea were maintained to the minimal level, approximately zero, which means the light beam is perpendicular on the point of incident.

The central corneal thickness (CCT) of the corneas at 0 mmHg was measured by using a Pachymeter (DGH 55 Pachmate, Vision Systems, USA). Corneas of approximately similar thickness were put together in a group to limit the effect of this parameters on the measurements by selecting corneas of approximately similar CCT for each experiment. In addition, corneal thickness was assumed to be equal to the optical path length. The group refractive index of the corneas was assumed to be constant for the entire cornea, 1.389. All of the experiments were performed at room temperature (approximately 22°C) and 45±2.1% relative humidity, as determined with a humidity-temperature meter (OMEGA engineering, USA).

5.2.3. The experiments

A set of four independent experiments were carried to measure corneal transparency in different conditions. Table 5.1 summarises the conditions and number of corneas in each experiment.

Table 5.1: A summary of the four independent experiments showing the condition used in the spectrophotometry method.

	Experiment 1	Experiment 2	Experiment 3	Experiment 4
n	6	5	10	5
Removal of epithelium layer	✓	✓	✓	✗
IOP	Variable	Fixed	Fixed	Fixed
Inflation solution	PBS	PBS	PBS	PBS
Hydration solution	✗	✗	PBS, TC	✗
Hydration period (min)	✗	✗	0 - 240	✗
Scanning region	Central	Central to peripheral	Central	Central
Acquired data	μa, %T	Localised %T	%T(t)	%T

'n' refers to number of corneas. '✓' and '✗' refer to yes and no. IOP is the intraocular pressure applied on the posterior surface of the corneas. 'PBS' and 'TC' are phosphate buffer saline solution and tissue culture, respectively. '%T' and 'μ_a' refer to percentage transmission and the absorption coefficient.

The details of each experiment are as following:

5.2.3.1. Experiment 1: Corneal transparency dependence on IOP and light wavelength

Six corneas of similar CCT from different pigs were chosen to test the effect of variable IOP on corneal transparency. The epithelium layer was peeled off from these corneas. In this group, PBS was used to apply hydraulic pressure to the posterior surface of the corneas, simulating IOP in the range 0 to 60 mmHg, in 5 mmHg increments. Corneal transparency at the centre of cornea was measured at wavelengths from 380 - 820 nm. The total time spent for the measurement of each cornea was about 7 minutes.

Linear absorption coefficient (μa) of inflated porcine corneas can be calculated using Beer-Lambert law (Equation 5.3). Scattering was neglected that was previously estimated to be very small (Meek and Knupp, 2015; Meek *et al*, 2003). CCT of porcine corneas at varying IOPs were mathematically calculated using Equation 5.4, which was obtained from Chapter 4.

$$I = I_o . e^{(-\mu_a . l)} \tag{5.3}$$

$$\mathrm{CCT(IOP)} = \mathrm{CCT_{IOP=\,0\ mmHg}} - 57.3\, IOP^{0.265} \tag{5.4}$$

where, I and Io are the transmitted and initial intensity of the light beam. *l* refers to the optical path length that is the thickness of the cornea (CCT) times the refractive index. T is the transmission and %T is the percentage transmission. CCT(IOP) is the central corneal thickness at IOP at which the cornea is inflated. CCT at IOP = 0 mmHg is the CCT at relaxed state, 0 mmHg.

5.2.3.2. Experiment 2: Regional corneal transparency

Five corneas of approximately similar CCT from different animals were selected to map regional corneal transparency in the visible light. The epithelium layer was peeled off from the corneas. Central corneal thickness was about 905±5.1 μm after the de-epithelisation. The orientation of corneas was marked when the samples were fixed on the holder. The IOP was fixed at 15 mmHg during the testing. Percentage transmittance of visible light through the corneas was measured for a 10 X 10 mm^2 area with 1.5 mm intervals. In points away from the centre, the chamber was titled to make corneal surface in a right angle to the incident beam.

5.2.3.3. Experiment 3: Hydration effect on corneal transparency

Five pairs of porcine corneas, with approximately similar CCT, were elected to detect the changes in corneal transparency following varying incubation times with PBS or tissue culture (TC) solution

(CARRY-C, ALCHIMIA, Italy). The epithelium layer was peeled off from the corneas. Five corneas from different pairs were kept at the relaxed state in a sealed bottle filled with PBS or TC at room temperature, and used to measure %T across the centre of the corneas every 15 min over 4 hours. The IOP was fixed at 15 mmHg during the measurement. The corneas were marked to test at the same point every time.

5.2.3.4. Experiment 4: Epithelium effect on corneal transparency

Five corneas, with approximately similar CCT, were used to assess the effect of the epithelium presence on corneal transparency. Firstly, %T was measured across the intact corneas, with the epithelium on. Afterward, the epithelium was peeled off and %T across the de-epithelised corneas was re-measured. %T through the centre of the corneas was measured at 15 mmHg.

5.2.4. Statistical analysis

All statistical analysis was performed using OriginPro 2016 version 9.3 (OriginLab, USA). Data is presented as mean values and standard deviation (mean ± standard deviation) unless otherwise stated. Homogeneity between the corneas in each group was assumed despite known biological variability between animals because the corneas of approximately similar CCT were selected to be in a group. In order to determine the statistical significance, data distribution in each group and condition was assessed to select the appropriate test. Paired-sample t-tests were used to test the significance of both %T and the absorption coefficient at each IOP with values at other IOPs within the experiment 1 corneas. The same statistical test was utilised between transmissions at different locations in the corneas of experiment 2. Also, the same test was used between transmissions obtained from intact and deepithelised corneas. Unpaired sample t-tests were used to detect the significance between transmissions at the same time and wavelength and in different incubation solutions. The significance level (α) was set as 0.05 for all tests.

5.3. Results

5.3.1. Corneal transparency dependence on IOP and light wavelength

Figure 5.3 demonstrates light transmission through the central region of porcine corneas at varying IOP. The results show that corneal transparency is varying with the wavelength and IOP. For ease of presentation, quantitative measurement of corneal light transmission with varying IOP and wavelength are shown in Figures 5.4, and 5.5, respectively.

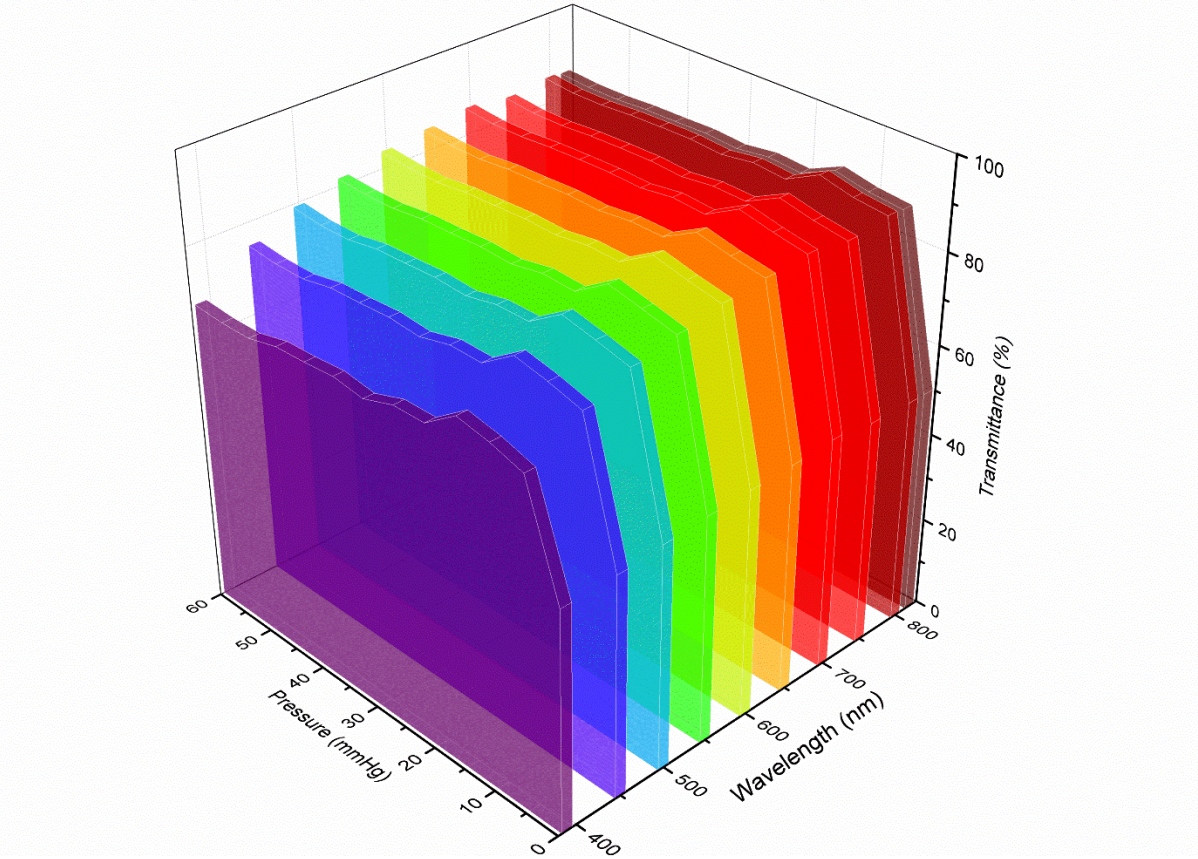

Figure 5.3: 3D plot of light transmittance versus wavelength and IOP of porcine corneas at central region. Linear fitting between points was chosen and standard deviation data were excluded to allow the trends to be more discernible (n = 6 corneas).

Figure 5.4 shows that the maximum light transmission through the central cornea, which was recorded at 15 mmHg. At IOP of 15 mmHg, %T was 73.8±1.8, 84±1.2 and 88.6±2.1 at wavelengths of 400 nm, 500 nm and 700 nm, respectively, and statistically different than %T at all other IOPs ($p \leq 0.028$). At 700 nm, light transmission through the corneas was significantly decreased by approximately 1.8% and 4.6% when the IOP decreased to 10 mmHg and increased to 20 mmHg, respectively, $p \leq 0.021$. %T of the visible light sharply dropped to 29±2 at 0 mmHg, $p \leq 0.001$. A gradual reduction in light transmission was seen, with a decrease of 5.7% at 60 mmHg from the value recorded at 15 mmHg, $p \leq 0.012$.

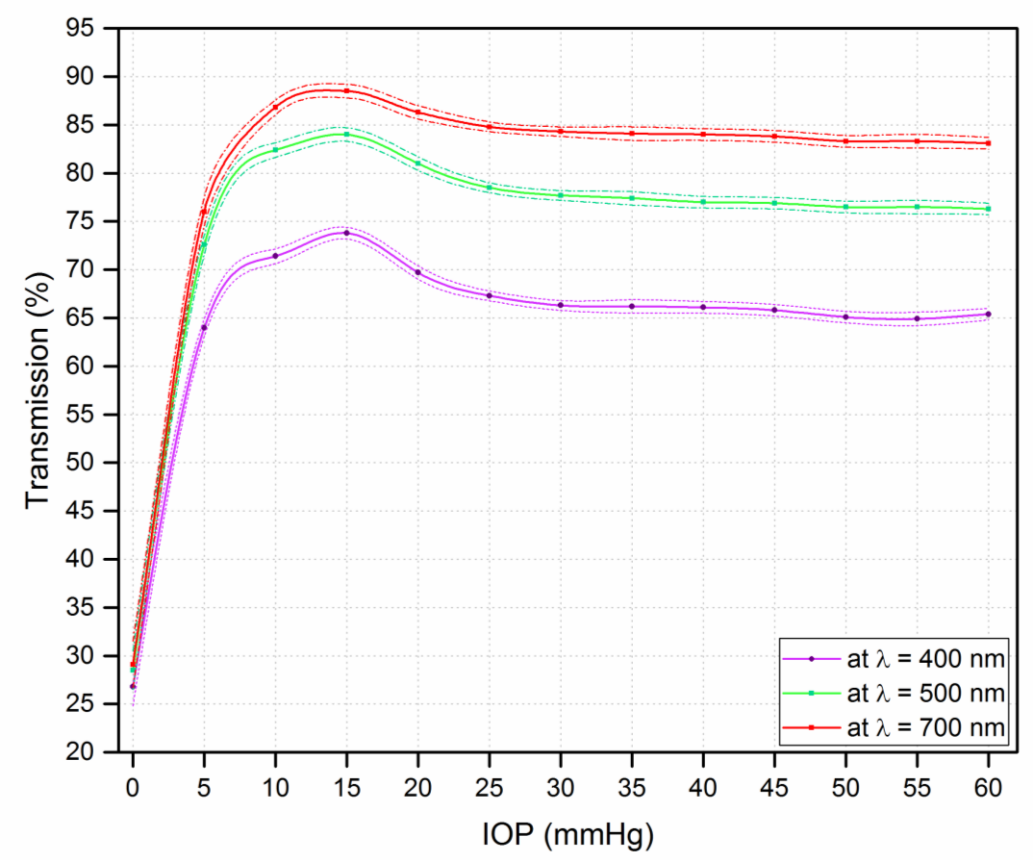

Figure 5.4: Percentage transmission of visible light waves across porcine corneas at varying IOP. The continuous line represents the average of the measurements, while the dotted lines represent the standard deviation (n = 6 corneas).

Figure 5.5 reveals a non-linear dependence of corneal transparency on the wavelength. For simplicity, the transmission at 15 mmHg was selected. The transmission of the light gradually increased as the light wavelength increased from the near ultraviolet region to the red-light region, at which the maximum transmission was recorded. At an IOP of 15 mmHg, the maximum light transmission of 88.6±2.1 through porcine corneas was seen at 700 nm, and the minimum light transmission of 72.9±1.5 was recorded at 410 nm. Light transmission deceased at the beginning of the near-infrared region compared to at 700 nm.

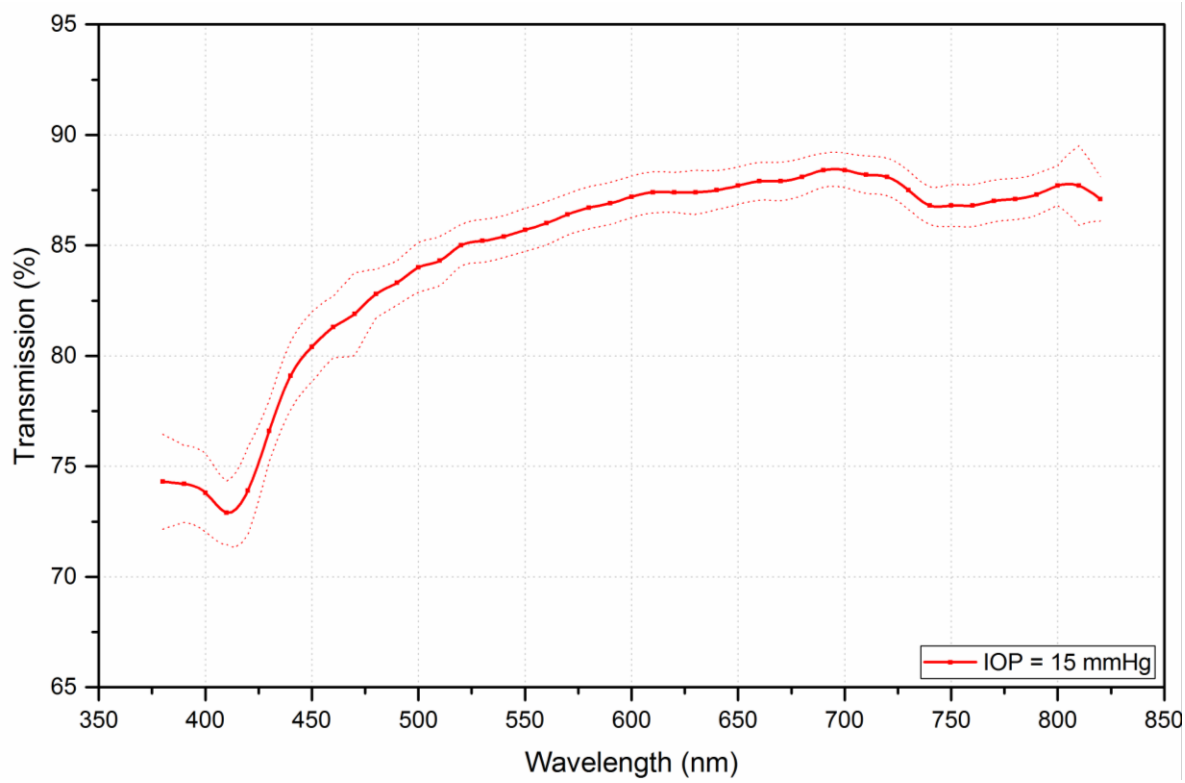

Figure 5.5: Visible light transmittance of the central cornea as a function of wavelength. The dotted lines represent confidence limits of the solid curve (n = 6 corneas).

Figure 5.6: shows the linear absorption coefficient in the centre of the porcine corneas. For simplicity of presentation, three wavelengths are shown in Figure 5.6. The results show that μ_a was 11.5±0.6 cm^{-1} at 700 nm, when the corneas were at relaxed state, 0 mmHg. The absorption coefficient significantly dropped to 1.57±0.4 cm^{-1} as the IOP increased from 0 mmHg to 5 mmHg, p=0.008. The minimum absorption was recorded at 15 mmHg of visible light. For example, the minimum μ_a was 3.13±0.5 cm^{-1}, 1.59±0.45 cm^{-1} and 1.27±0.36 cm^{-1} of wavelengths 400 nm, 550 nm and 700 nm, respectively. Beyond that IOP, the absorption coefficient slightly increased, as the IOP increased. The data also shows that the absorption coefficient of the corneas was dependent on the transmitted light wavelengths, where high absorption of light was seen at shortest wavelengths.

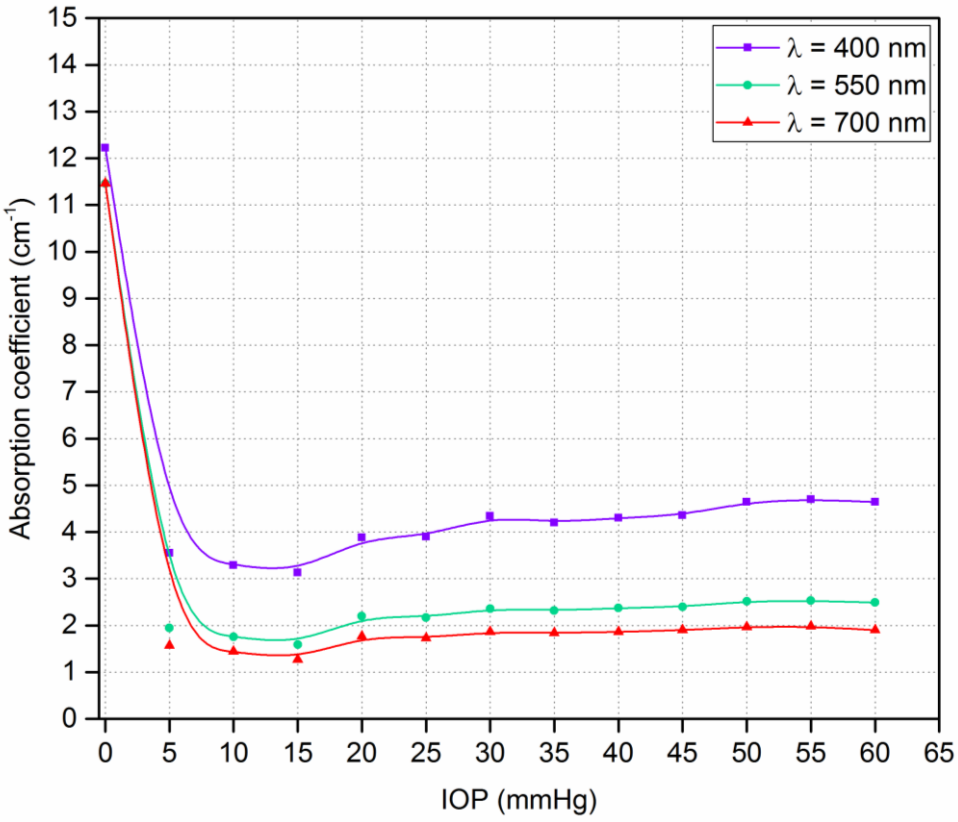

Figure 5.6: Linear absorption coefficient of the central point of inflated porcine corneas. Presentation of standard deviation values were ignored since the absorption coefficient is a calculated parameter (n = 6 corneas).

5.3.2. Regional corneal transparency

The results show distinct light transmission variations between corneal zones. A three-dimensional map of transitional transparency of porcine corneas inflated at 15 mmHg is displayed in Figure 5.7. It was found that light transmission across the corneas gradually decreased when moving away from the central region. The data presented in Figure 5.8 shows that transparency is almost equal in the central cornea (diameter of 3.2 mm). Beyond a 6 mm diameter, paracentral cornea, the decrease in the transparency became more rapid. A significant reduction in corneal transparency on the limbal zone was seen compared with other corneal zones ($p \leq 0.018$), at which %T was 39.2±3.1 at wavelength 700 nm. It was also evident that there appears to be a degree of isotropy in the transparency distribution between the two given meridians around the oval-like central contour. Figure 5.8 shows %T as a function of distance from the nasal-superior point (on the limbus) to the temporal-inferior point (near the limbus), a diagonal axis on the projection of the dome.

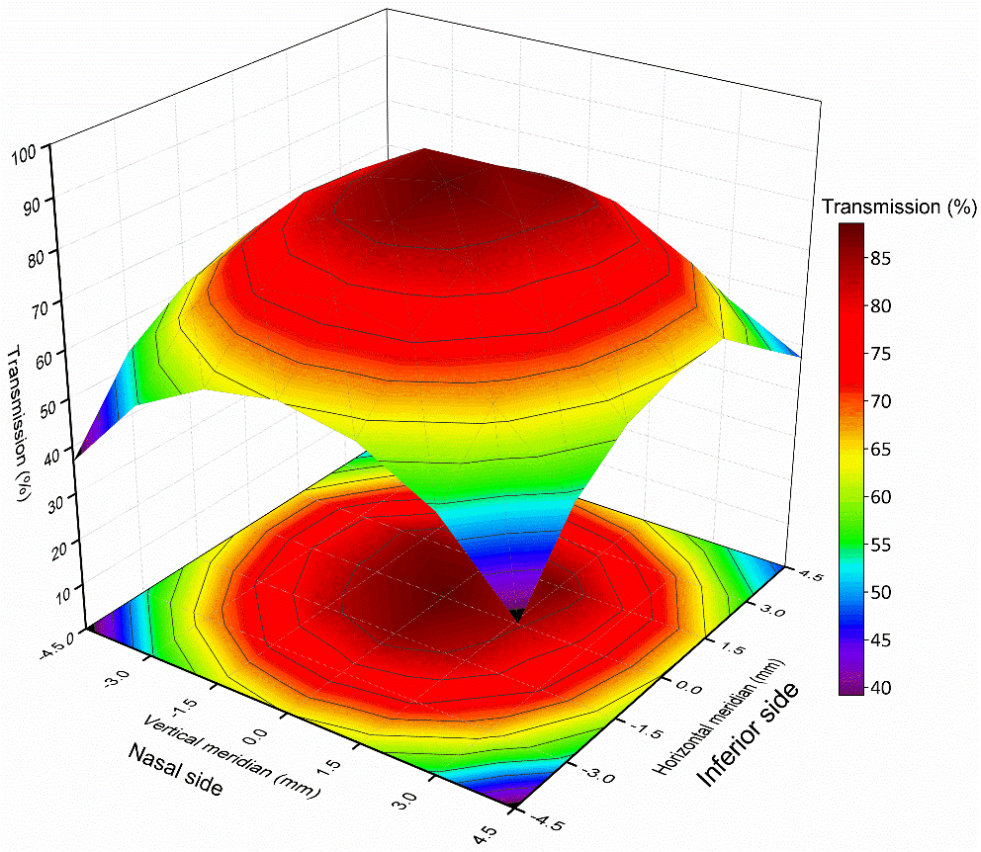

Figure 5.7: Representative three-dimensional plot of regional transparency meridians of inflated porcine corneas at physiological IOP (the dome shape). The two-dimensional shape is the projection of the dome. The contour interval of 5(%). The scale bar represents %T values. Corneal epithelium was peeled off the samples; IOP was 15 mmHg; λ was 700 nm; n = 5 corneas.

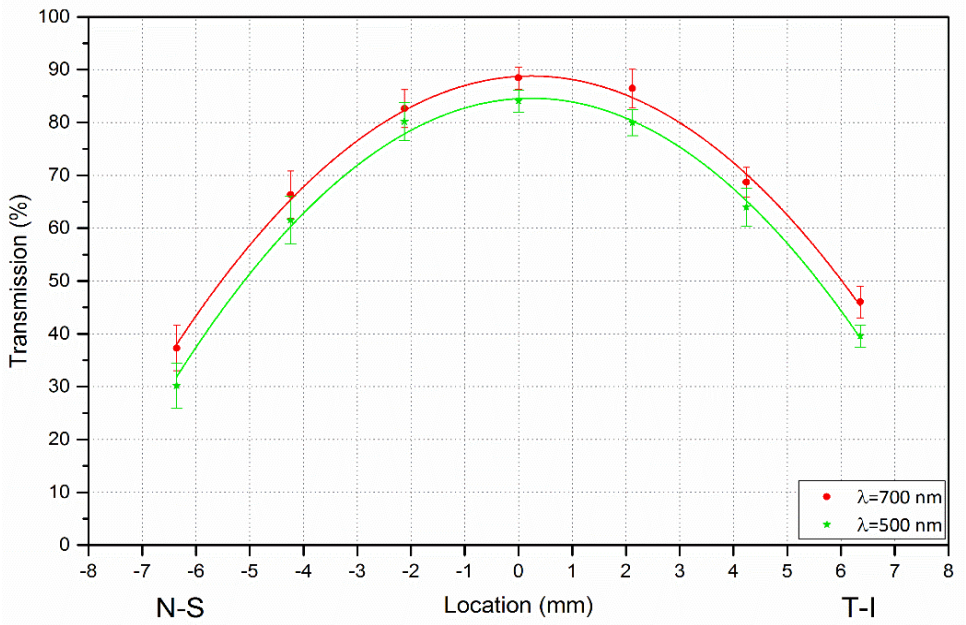

Figure 5.8: Percentage transmission of light at 700 nm and 500 nm as a function of a location on a diagonal line from nasal-superior corner (N-S, the negative side of the x-axis) to the temporal-inferior corner (T-I, the positive side on the x- axis) passing through the optical centre of the cornea (0). Error bars represent standard deviation (n= 5 corneas). Fitting line is a second order function.

5.3.3. Hydration effect on corneal transparency

Figure 5.9 shows %T of light across corneas incubated with PBS or TC. The results show a reduction in corneal transparency of corneas incubated with PBS or TC. %T was significantly less in corneas that were incubated with PBS, 40.2±2.1 % at 600 nm after 240 min, than in corneas that were incubated with TC, 72.5±2.8 % at 600 after 240 min, $p \leq 0.001$. It was noticed that %T of corneas that were incubated with TC and tested at 700 nm, were affected by the dye of the TC solution and that caused additional light attenuation. Therefore, results obtained at 700 nm were excluded from Figure 5.10 to maintain clarity in the results. The maximum light attenuation caused by TC dye was seen at 670 nm, where corneas were found to be stained red after 15 min and transmission reduced significantly when comparing initial state to %T after 30 min, $p=0.0028$.

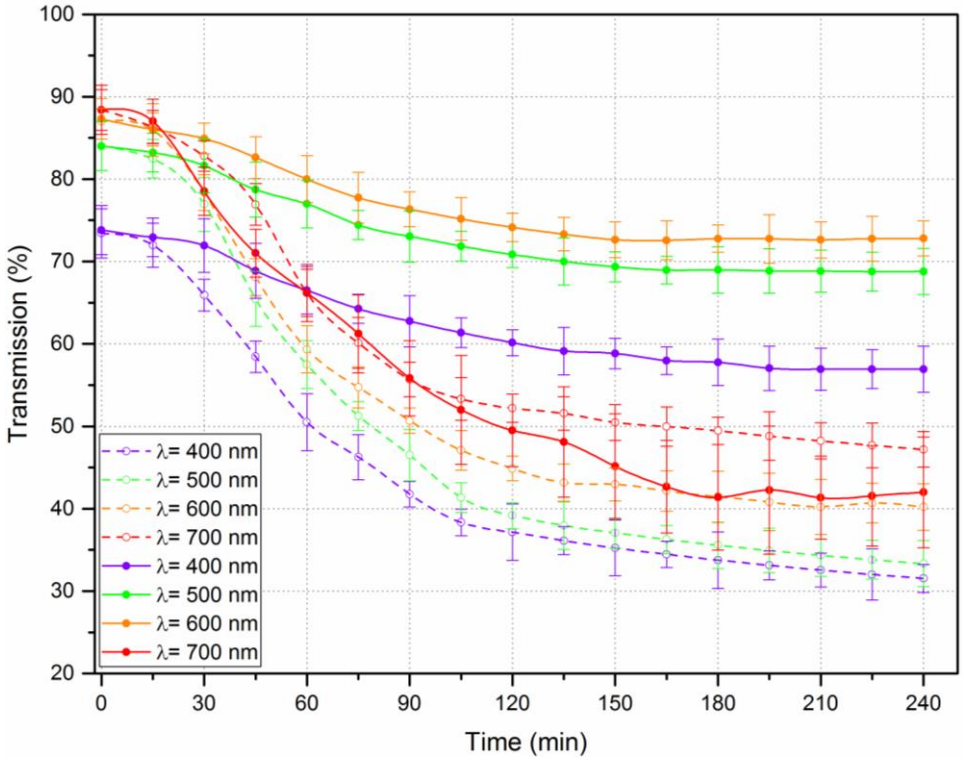

Figure 5.9: Percentage light transmission across corneas were incubated with PBS and TC. The corneas that were incubated with TC are represented by solid circles and lines, whilst the corneas that were incubated with PBS are represented by unfilled circles and dashed lines. Error bars represent standard deviation.

In Figure 5.10, %T of light across corneas decreased with no statistical difference between the value at the initial state, 0 min, and the value after incubation with TC for 30 min. %T of light across corneas incubated with TC at 165 min was significantly reduced by about 18% as compared to the initial state, $p \leq 0.013$. After 165 min, the reduction in %T across the corneas incubated in TC was more stable with no statistical difference seen for the remainder of the experiment, $p \geq 0.19$.

For the corneas incubated with PBS, %T was reduced compared to values from corneas incubated with TC. At 15 min incubation time in PBS, %T was slightly decreased by about 1% with no statistical difference compared to initial state, $p \geq 0.067$. A rapid reduction in %T was observed across corneas incubated with PBS along values between 15 min and 105 min.

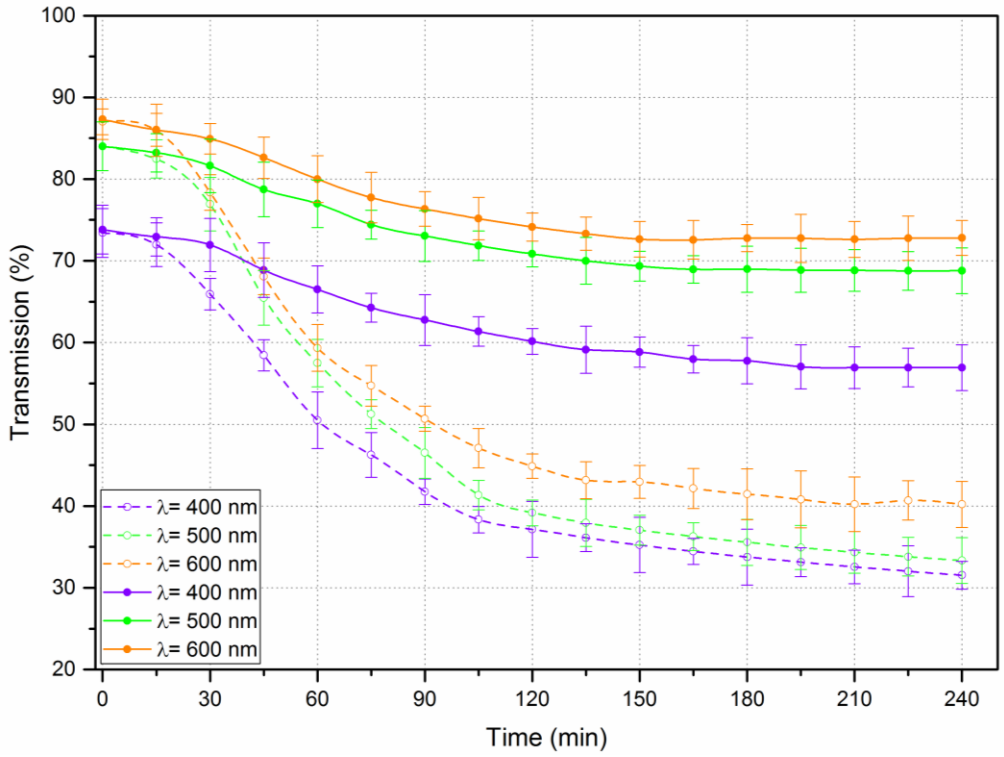

Figure 5.10: Percentage light transmission across corneas were incubated with PBS and TC. The corneas that were incubated with TC are represented by solid circles and lines, while the corneas that were incubated with PBS are represented by unfilled circles and dashed lines. Error bars represent standard deviation. %T at 700 nm were excluded in this graph.

5.3.4. Epithelium effect on corneal transparency

Figure 5.11 compares %T of light across intact and deepithelised corneas. %T of the light across the deepithelised corneas was higher by about 0.8% than %T across the intact corneas. However, the statistical test showed no significant difference between the two groups, $p \geq 0.113$.

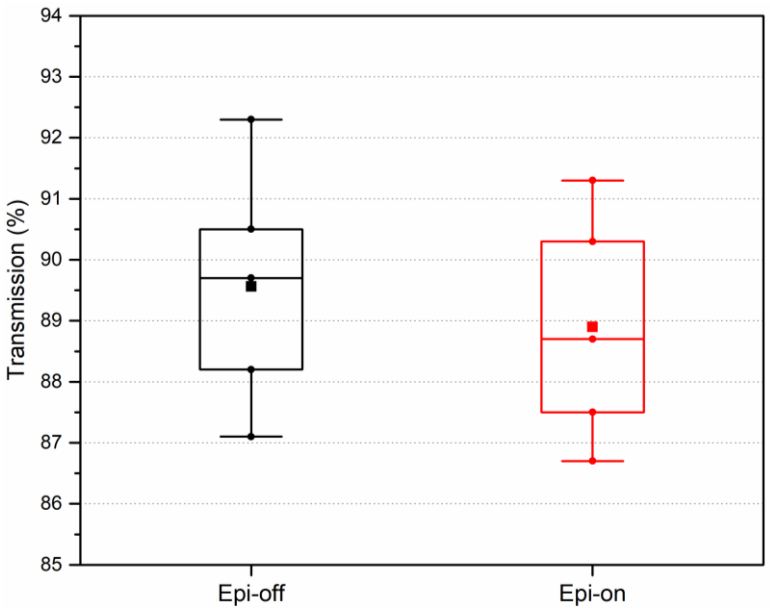

Figure 5.11: Percentage transmission of light across intact and deepithelised porcine corneas. Epi-off refers to de-epithelised corneas; Epi-on represents the intact corneas. Corneas were inflated at 15 mmHg. Data were represented as box plots and data overlaid with lower and upper borders of the box to represent the lower and upper quartiles, and the middle horizontal line to represent the median. The upper and lower whiskers represent 5th and 95th percentile of the data. The solid points represent data points of each group. The square refers to the mean value of the dataset for that group. λ = 700 nm; (n = 5 corneas/box), $p \geq 0.113$.

5.4. Discussion

This chapter aimed to measure the optical properties of porcine corneas under physiological pressures using computerized spectrophotometry. In addition, the study aimed to demonstrate the potential to map the regional %T of the inflated corneas. Since PBS was used to inflate the corneas in previous chapters, it was therefore of interest to assess the corneal transparency changes of hydrated corneas in PBS. This study also investigated the effect of epithelium presence on light transmission across the corneas.

The main advantage of the spectrophotometric method used in this study is measuring the light transmission through inflated porcine corneas in a manner similar to *in-vivo* conditions. Previous spectrophotometric methods (Beems and Best, 1990; Boettner and Wolter, 1962; Doutch *et al*, 2007, 2012, 2008; Freegard, 1997) provided an overview of corneal transparency of clamped relaxed corneas. In contrast to these methods, this method allowed measuring corneal optical properties at varying physiological pressures.

Many factors may affect the validity of the results, including the condition of the eyes, the length of time between enucleation and the measurements, and the accuracy of the method. Therefore, fresh porcine corneas were collected from a local slaughterhouse, and enucleated within 30 minutes from collection to be ready for the measurements immediately. Corneas were selected precisely to be the same thickness. Thus, thickness differences between corneas were eliminated as much as possible. In terms of the accuracy of the method, a limitation could be raised from localising the exact centre point of the cornea.

5.4.1. Corneal transparency dependence on IOP and light wavelength

The results indicate that corneal transparency is affected by IOP, where increased or decreased IOP in comparison to the normal physiological pressure causes reduction in light transmission through the cornea. It is hypothesised that corneal transparency reductions are related to changes in ultrastructural features including intrafibrillar spacing, collagen fibrils diameter and density. It is well known that elevated IOP changes the shape of the cornea (Asejczyk-Widlicka *et al*, 2011), compresses corneal tissue (Kazaili *et al*, 2019) and applies tension forces on collagen fibrils (Wu *et al*, 2013) that leads to a possible reduction in collagen fibril diameters and the interfibrillar spacing (Chang *et al*, 2018). In turn, this reduction therefore causes an increase in the density of the corneal material and thus decreases light transmission across the cornea, which can be explained by another form of Beer- Lambert law (Equation 5.5). Simply, the law implies that any increase in scattering or density of the material decreases the transmitted light. This suggestion is also in agreement with mathematical analyses proposed previously (Freund *et al*, 1986; Doutch *et al*, 2008). Another support of the relation between transmission and ECM organisation was mathematically proven by Doutch *et al* (2008), they proved that interfibrillar spacing reduction leads to increase in fibril number density and proposed Equation 5.6 that can be used for explaining the relation between interfibrillar spacing and corneal transparency.

$$I = I_o . e^{(-\alpha \rho \, l)} \tag{5.5}$$

$$\rho = \frac{1}{(1.06 \; d^2)} \tag{5.6}$$

where α represents the total scattering cross section per fibril. ρ refers to the density of fibrils. l is the optical path length, in which the incident beam traversed the actual thickness of cornea. d is the interfibrillar spacing.

Another possibility for explaining the reduction of corneal transparency with higher IOPs is increased turbidity due to alterations in stromal lamellae orientation. It has been found with the help of nonlinear optical microscopy that the stroma microstructure appeared to be modified by increased IOP, in which lamellae gradually slid and slightly rotated, relative to each other, toward balancing the proportions of lamellae oriented along the two preferential orientations (Benoit *et al*, 2016).

In this study, it was found that corneal transparency is reduced with IOPs lower than the normal physiological pressure. At 0 mmHg (relaxed corneas), the measured light transmittance was very low; this inaccurate result has happened due to the present of wrinkles on corneal surface that increase light reflections. Therefore, a previous study placed the tested corneas between two transparent thick fused quartz to avoid reflections of the light from corneal surface (Boettner and Wolter, 1962). At pressures from 5 to 10 mmHg, the slight reduction in corneal transparency could be attributed to internal turbidity of the cornea, where the absence of proper tension on collagen fibrils could cause folds that affects their normal orientation. It has also been reported that the anterior stromal lamellae slide and rotate, one to each other, as the IOP changes (Meek and Knupp, 2015). These considerations therefore confirm that corneal ultrastructural integrity and distribution influence corneal transparency which can only be optimally achieved at normal IOP level. In addition, it might be required to test corneal transparency at normal IOP values for corneas are mounted in anterior chamber holder because other pressures introduce changes in corneal transparency.

The results showed that corneal transparency depends on light wavelength, confirming that the longer the light wavelength, the higher the light transmission in the cornea. These results are in agreement with (Doutch *et al*, 2008; Farrell *et al*, 1973; Hart and Farrell, 1969; Kostyuk *et al*, 2002).

The linear absorption coefficient of porcine corneas appears to increase as IOP increases. In addition, it is a function of corneal thickness and wavelength. Corneal thickness is an important parameter in calculation of μa, which decreases as the IOP increases. To the best of my knowledge, this chapter reported for the first time a study of the visible light absorption coefficient of porcine corneas that can be used for modelling and laser treatment operations. The absorption coefficient of uninflated porcine corneas measured at 380 nm (12.8 cm^{-1}) seems to be close with absorption coefficients of relaxed human corneas measured at 365 nm (9 cm^{-1}) reported by (Koppen *et al*, 2010). It is important to note that porcine corneas are slightly thicker than human corneas.

The dependence of corneal transparency on IOP may help in explaining some ocular conditions, in particular the conditions associated with high IOP. The current finding may allow putting us to speculate that patients who need higher intensity of light for clearer vision or have low light sensitivity, have symptoms of high or low IOP. Further investigations should include assessing the effect of variable IOPs on lens transparency and how it is correlated to low light sensitivity.

5.4.2. Regional corneal transparency

The current results found a reduction in light transmission through porcine corneas as a function of distance from the centre toward the limbus. Such a feature was also seen in human and bovine corneas using a spectrophotometry (Doutch *et al*, 2007). It was of a great interest to explore the reason of this reduction in corneal transparency and how it is relates to ultrastructural features of the stroma. It is plausible that the transparency of central cornea is higher than the transparency of peripheral and pre-limbal regions, which is attributed to ultrastructural organisation and collagen fibril diameters and intrafibrillar spacing are highly uniform in central cornea than other regions in the stromal (Boote *et al*, 2003; Knupp *et al*, 2009; Meek and Leonard, 1993).

It is known that corneal thickness gradually increases towards the periphery (Faber *et al*, 2008; Sanchez *et al*, 2011), which reduces the transmitted intensity according to the Beer- Lambert law. However, it was previously reported that corneal thickness was not the main reason of transmission reduction in the peripheral region of bovine corneas, speculating that the increase in interfibrillar spacing and diameter in peripheral region mainly contributed in light transmission reduction (Doutch *et al*, 2007).

A simple analysis can be done by using Equations 5.3 and 5.7 (Equation 5.7 obtained from Chapter 4) to evaluate the contribution of the thickness on light transmission reduction in the peripheral cornea. The analysis needs to assume a constant ultrastructural organisation across the cornea by assuming that μ_a is constant. This analysis results in a reduction in light transmission by 1.35% at 5 mm from the centre of the cornea, which is much less than experimentally. Therefore, this analysis emphasizes that the primary factor causing the reduction in the transparency is due to an increase in specular scattering and ultrastructural changes.

$$\mathrm{CT(x)} = \mathrm{CCT} + \mathrm{x} + 3\mathrm{x}^2 \tag{5.7}$$

where, CT is the thickness of a porcine cornea at point x; x is the location from the centre of the cornea at which CCT is measured ,$0 \leq x \leq 5$; CCT is central corneal thickness.

The increased specular scattering in peripheral and limbal regions can be mainly attributed to an increase of the keratocyte density, which was proved to increase progressively toward the periphery and limbal region by a biochemical measurements study (Møller-Pedersen and Ehlers, 2009). Møller-Pedersen and Ehlers (2009) also asserted that the specular scattering was small in central cornea. Therefore, it is suggested that the reduction in light transmission across the peripheral cornea, which caused by increased scattering, takes place due to gradual increase in the keratocyte density.

Corneal transparency reduction in the peripheral region of the cornea could be related to changes in ultrastructural features including collagen fibril diameter and interfibrillar spacing. It was reported that collagen fibril diameter and interfibrillar spacing increases toward the corneal periphery and limbal region of human corneas (Boote *et al*, 2011), which leads to a substantial reduction in the fibril number density by about 27% from the centre to the far periphery (Doutch *et al*, 2008). These changes could be the reason why light transmission decreased across the peripheral and limbal corneal regions.

In addition, the relative refractive index between the fibrils and the interfibrillar matrix increases in case of an increase in collagen fibril diameters and interfibrillar spacing. That increase leads to a reduction %T across the peripheral cornea. The reduction in %T was mathematically estimated to be about 12% in a point located 5 mm away from the centre of the human cornea (Doutch *et al*, 2008).

The results presented in this chapter showed that porcine corneas are characterised by a symmetrical corneal transparency which is distributed around the corneal apex centre. That does not mean the geometrical centre and the corneal apex centre of the cornea are at the same point because the porcine cornea is more like an asymmetrical oval shape with the maximum corneal diameter being 14.88 mm and the shortest corneal diameter being 12.69 mm. The symmetrical distribution of corneal transparency is in agreement with a finding proposed by (Hayes *et al*, 2007), which used x-ray scattering technique and showed highly amount of collagen fibrils in stroma run in circumferential directions that they seem in a centrosymmetric nature around an oval-like centre.

It can be, therefore, concluded that corneal anisotropy of corneal transparency in porcine corneas is affected by spatial ordering of the collagen fibrillar array.

5.4.3. Hydration effect on corneal transparency

The results showed that corneal transparency reduced with incubation time in PBS or TC. It was also shown that corneal transparency reduced less in corneas that were incubated with TC than those incubated in PBS. It is well known that corneas swell in PBS, which causes an increase in corneal thickness (Doughty, 2000), also shown in Chapter 4. While, TC can apparently maintain corneal swelling and slightly decrease the thickness, according to the specification of the solution, as was found in Chapter 3. For the corneas incubated in PBS, it seems that water gradually moved to the stroma and situated between collagen fibrils in unknown distribution changing tissue density by increasing the interfibrillar spacing (Meek and Knupp, 2015). The increase in interfibrillar spacing, due to the swelling, considerably increased the optical path length, which in turn decreased light transmission that can be verified by Equation 5.6 and 5.7. In addition, water in swelling corneas unequally distributed between lamellae leading to an increase in the anisotropy of the collagen fibrils orientation (Freund *et al*, 1991; Meek *et al*, 2003; Møller-Pedersen, 2004), disrupting the lattice organisation of the collagen fibrils (Clark, 2004), and changing normal refractive properties (Patel and Tutchenko, 2019). These factors caused by the abnormal water content in the cornea leads to disruption within the regular array of the collagen fibrils, which is the main reason for corneal haziness. The current results of corneal transparency reduction in swollen corneas are consistent with findings proposed in the literature (Farrell *et al*, 1973; Freund *et al*, 1991).

Another possibility that might affect corneal transparency of the swollen corneas is the increased in light scattering due to a change in the stromal refractive index. It was reported that the stromal refractive index exponentially decreases with hydration due to changes in the ratio of the refractive indices of the fibrils and the matrix following unequal increase in the fibril diameters and interfibrillar spacing (Meek *et al*, 2003). They calculated the reduction in stromal refractive index of swollen corneas (Meek *et al*, 2003) and hypothesised that the reduction in stromal refractive index increases light scattering in a small percentage, about 5% in highly hydrated corneas. Therefore, a small amount of the incident light will scatter in the swollen corneas that leads to a reduction in corneal transparency.

For corneas incubated in TC, a gradual deswelling and staining by red dye was observed in the corneas, associated with a reduction in corneal transparency. Reduction in corneal thickness possibly took place due to a reduction in interfibrillar spacing that in turn increases the fibril number density, which leads to reduction in light transmission according to Equations 5.5 and 5.6. It can be concluded that hydrating deepithelised corneas by either PBS or TC, swelling and deswelling solutions, causes reduction in corneal transparency that is possibly caused by disruption of ECM, particularly interfibrillar spacing.

5.4.4. Epithelium effect on corneal transparency

The results presented in this chapter show that corneal transparency is increased in deepithelised corneas comparing to intact corneas, but without statistical significance. This finding is consistent with results proposed by Ringvold (1998). The study used spectrophotometry to detect light absorbance across intact and deepithelised corneas, found no difference between the two conditions at wavelengths higher than 409 nm, and proposed the epithelium as a UV-protective layer. It is known that the thickness of the epithelium is about 50 μm. This small thickness of the epithelium can increase the optical path by about 3% of the whole corneal thickness. With Equation 5.5 it can be determined that there is an inverse relationship between the optical thickness and the transmitted light, and that a reduction of less than 1% of the transmitted light can be expected. Therefore, the experimental finding matches the mathematical analysis and confirm that the stromal layer plays the main role in corneal transparency, from an optical point of view.

5.5. Limitations

The present study demonstrated corneal transparency based on the light transmission across the corneas by neglecting the back-scattering photons attributing that for their small intensity. These back scattered photons probably diffused in many angles that made them far to be detected by the spectrophotometer. Another limitation in calculation of the absorption coefficient, in which the scattering coefficient was assumed to be zero due to small scattering. Sterically specking, scattering, absorption and reflection of incident photons are taken place in the cornea in certain extents.

5.6. Conclusions

This study investigated how corneal transparency of porcine corneas changes with IOP and wavelength. It was concluded that the optimal transparency of the cornea would be at the normal physiological pressure, which is correlated to the ideal ultrastructure organisation. Here, the linear absorption coefficient at the centre of porcine corneas with variable IOPs was proposed to be

linked to CCT, concluding that porcine corneas absorb a very small portion of incident visible light. In addition, this study has examined corneal transparency in different regions through porcine corneas, and found that a reduced transparency in peripheral region that is mainly attributed to ultrastructural changes based on literature. Transparency of porcine corneas are symmetrically distributed around the corneal apex centre. Moreover, swelling and deswelling solutions principally decrease corneal transparency that is attributed to ultrastructure alterations. The presence or absence of the epithelium will make no statistical difference in terms of transparency in the visible spectrum. Since porcine corneas are usually utilised as biochemical and biomechanical alternatives of human samples, the current results can be utilised for modelling and comparison, and thus achieve better understanding of how ultrastructural changes affect corneal transparency. The current finding of regional corneal transparency may have potential to assess regional corneal absorption for riboflavin *in vitro* corneal-crosslinking treatment.

5.7. References

Aghamohammadzadeh, H., Newton, R., Meek, K., 2004. X-ray scattering used to map the preferred collagen orientation in the human cornea and limbus. Structure 12, 249-256.

Asejczyk-Widlicka, Śródka, Schachar, R.A., Pierścionek, B.K., 2011. Material properties of the cornea and sclera: A modelling approach to test experimental analysis. Journal of Biomechanics 44, 543-546.

Beems, E., Best, J., 1990. Light transmission of the cornea in whole human eyes. Experimental Eye Research 50, 393-395.

Benoit, A., Latour, G., Marie-Claire, S.-K., Allain, J.-M., 2016. Simultaneous microstructural and mechanical characterization of human corneas at increasing pressure. Journal of the Mechanical Behavior of Biomedical Materials 60, 93-105.

Boettner, E.A., Wolter, R., 1962. Transmission of the ocular media. Investigative Ophthalmology & Visual Science 1, 776-783.

Boote, C., Dennis, S., Newton, R., Puri, H., Meek, K., 2003. Collagen Fibrils Appear More Closely Packed in the Prepupillary Cornea: Optical and Biomechanical Implications. Investigative Ophthalmology & Visual Science 44, 2941-2948.

Boote, C., Kamma-Lorger, C.S., Hayes, S., Harris, J., Burghammer, M., Hiller, J., Terrill, N.J., Meek, K.M., 2011. Quantification of collagen organization in the peripheral human cornea at micron-scale resolution. Biophysical Journal 101, 33-42.

Chang, S.-H.H., Mohammadvali, A., Chen, K.-J.J., Ji, Y.-R.R., Young, T.-H.H., Wang, T.-J.J., Willoughby, C.E., Hamill, K.J., Elsheikh, A., 2018. The relationship between mechanical

properties, ultrastructural changes, and intrafibrillar bond formation in corneal UVA/Riboflavin cross-linking treatment for keratoconus. Journal of Refractive Surgery 34, 264-272.

Clark, J., 2004. Order and disorder in the transparent media of the eye. Experimental Eye Research 78, 427-432.

Doughty, M.J., 2000. Swelling of the collagen-keratocytematrix of the bovine corneal stroma *ex vivo* in various solutions and its relationship to tissue thickness. Tissue and Cell 32, 478-493.

Doutch, J., Quantock, A., Smith, V., Meek, K., 2008. Light transmission in the human cornea as a function of position across the ocular surface: theoretical and experimental aspects. Biophysical Journal 95, 5092-5099.

Doutch, J., Quantock, A.J., Meek, K.M., 2007. Changes in visible light transmission across the corneal stroma. International Society for Optics and Photonics 6535, 65350Q.

Doutch, J.J., Quantock, A.J., Joyce, N.C., Meek, K.M., 2012. Ultraviolet light transmission through the human corneal stroma is reduced in the periphery. Biophysical Journal 102, 1258-1264.

Faber, C., Scherfig, E., Prause, J., Soensen, K., 2008. Corneal thickness in pigs measured by ultrasound pachymetry *in vivo*. Scandinavian Journal of Laboratory Animal Sciences 35, 39-43.

Farrell, R.A., McCally, R.L., Tatham, P.E., 1973. Wave-length dependencies of light scattering in normal and cold swollen rabbit corneas and their structural implications. The Journal of Physiology 233, 589-612.

Freegard, T., 1997. The physical basis of transparency of the normal cornea. Eye 11, eye1997127.

Freund, D., McCally, R., Farrell, R.A., 1991. Light scattering tests of structure in normal and swollen rabbit corneas. Johns Hopkins APL Technical Digest 12, 137-143.

Freund, D.E., McCally, R.L., Farrell, R.A., 1986. Direct summation of fields for light scattering by fibrils with applications to normal corneas. Applied Optics 25, 2739.

Goldman, J.N., Benedek, G.B., 1967. The relationship between morphology and transparency in the nonswelling corneal stroma of the shark. Investigative Ophthalmology & Visual Science 6, 574-600.

Hart, R.W., Farrell, R.A., 1969. Light scattering in the cornea. Journal of the Optical Society of America 59, 766.

Hayes, S., Boote, C., Lewis, J., Sheppard, J., Abahussin, M., Quantock, A., Purslow, C., Votruba, M., Meek, K., 2007. Comparative study of fibrillar collagen arrangement in the corneas of primates and other mammals. The Anatomical Record: Advances in Integrative Anatomy and Evolutionary Biology 290, 1542-1550.

Jester, J.V., Moller-Pedersen, T., Huang, J., Sax, C.M., Kays, W.T., Cavangh, H.D., Petroll, W.M., Piatigorsky, J., 1999. The cellular basis of corneal transparency: evidence for "corneal crystallins". Journal of Cell Science 112 (5), 613-22.

Kazaili, A., Akhtar, R.R., 2018. Ultrastructural and nanomechanical changes of the cornea following enzymatic degradation. Journal for Modeling in Ophthalmology 2(2), 24-29.

Kazaili, A., Lawman, S., Geraghty, B., Eliasy, A., Zheng, Y., Shen, Y., Akhtar, R., 2019. Line-Field Optical Coherence Tomography as a tool for *In vitro* characterization of corneal biomechanics under physiological pressures. Scientific Reports 9, 6321.

Knupp, C., Pinali, C., Lewis, P.N., Parfitt, G.J., Young, R.D., Meek, K.M, Quantock, A.J., 2009. The architecture of the cornea and structural basis of its transparency. In Alexander McPherson, A. (ed) Advances in Protein Chemistry and Structural Biology (pp. 25-49). Elsevier: Academic Press. USA.

Koppen, C., Gobin, L., Tassignon, M.-J., 2010. The absorption characteristics of the human cornea in ultraviolet-a crosslinking. Eye Contact Lens 36, 77-80.

Kostyuk, O., Nalovina, O., Mubard, T., Regini, J., Meek, K., Quantock, A., Elliott, G., Hodson, S., 2002. Transparency of the bovine corneal stroma at physiological hydration and its dependence on concentration of the ambient anion. The Journal of Physiology 543, 633-642.

Koudouna, E., Winkler, M., Mikula, E., Juhasz, T., Brown, D., Jester, J., 2018. Evolution of the vertebrate corneal stroma. Progress in Retinal and Eye Research 64, 65-76.

Lembares, A., Hu, X.H., Kalmus, G.W., 1997. Absorption spectra of corneas in the far ultraviolet region. Investigative Ophthalmology & Visual Science 38, 1283-1287.

Lombardo, M., Micali, N., Villari, V., Serrao, S., Pucci, G., Barberi, R., Lombardo, G., 2015a. Ultraviolet A: Visible spectral absorbance of the human cornea after transepithelial soaking with dextran-enriched and dextran-free riboflavin 0.1% ophthalmic solutions. Journal of Cataract & Refractive Surgery 41, 2283-2290.

Lombardo, M., Pucci, G., Barberi, R., Lombardo, G., 2015b. Interaction of ultraviolet light with the cornea: Clinical implications for corneal crosslinking. Journal of Cataract & Refractive Surgery 41, 446-459.

Maurice, 1957. The structure and transparency of the cornea. The Journal of Physiology 136, 263-286.

Meek, K., Boote, C., 2004. The organization of collagen in the corneal stroma. Experimental Eye Research 78, 503-512.

Meek, K., Dennis, S., Khan, S., 2003. Changes in the refractive index of the stroma and its extrafibrillar matrix when the cornea swells. Biophysical Journal 85, 2205-2212.

Meek, K.M., Knupp, C., 2015. Corneal structure and transparency. Progress in Retinal and Eye Research 49, 1-16.

Meek, K.M., Leonard, D.W., 1993. Ultrastructure of the corneal stroma: a comparative study. Biophysical Journal 64, 273-280.

Meek, Leonard, Connon, Dennis, Khan, 2003. Transparency, swelling and scarring in the corneal stroma. Eye 17, 6700574.

Møller-Pedersen, T., 2004. Keratocyte reflectivity and corneal haze. Experimental Eye Research 78, 553-560.

Møller-Pedersen, T., Ehlers, N., 1995. A three-dimensional study of the human corneal keratocyte density. Current Eye Research 14, 459-464.

Patel, S., Tutchenko, L., 2019. The refractive index of the human cornea: A review. Contact Lens Anterior Eye 42(5), 575-580.

Ringvold, A., 1998. Corneal epithelium and UV-protection of the eye. Acta Ophthalmologica Scandinavica 76, 149-53.

Sanchez, I., Martin, R., Ussa, F., Fernandez-Bueno, I., 2011. The parameters of the porcine eyeball. Graefe's Archive for Clinical and Experimental Ophthalmology 249(4), 475-482.

Sayers, Z., Koch, M.H., Whitburn, S.B., Meek, K.M., Elliott, G.F., Harmsen, A., 1982. Synchrotron x-ray diffraction study of corneal stroma. Journal of Molecular Biology 160, 593-607.

Winkler, M., Shoa, G., Tran, S., Xie, Y., Thomasy, S., Raghunathan, V., Murphy, C., Brown, D., Jester, J., 2015. A comparative study of vertebrate corneal structure: The evolution of a refractive lens vertebrate corneal structure. Investigative Ophthalmology & Visual Science 56, 2764-2772.

Worthington, C.R., 1984. The structure of cornea. Quarterly Reviews of Biophysics 17, 423-51.

Wu, K., Li, S., Lo, A., Ngan, A., Wong, D., So, K., Ellis-Behnke, R., Tang, B., 2013. Micro-scale stiffness change of cornea tissues suffered from elevated intraocular pressure investigated by nanoindentation. Soft Materials 11, 244-253.

Chapter 6

In-vitro assessment of biophysical properties of porcine corneas following enzymatic degradation.

This chapter focusses on assessing the biomechanical properties and corneal transparency of the porcine corneas following enzymatic degradation with collagenase and amylase. Oscillatory nanoindentation and optical coherence tomography (OCT) with inflation testing were utilised to determine the biomechanical properties of the corneas. The spectrophotometric technique was used to assess corneal transparency of the treated corneas in the visible spectra. This chapter demonstrates how viscoelastic and optical properties of porcine corneas change following enzymatic treatment with different concentrations of amylase and collagenase, and with different incubation times. The measured biomechanical and optical properties of the treated corneas are discussed and compared with other studies.

Abstract

The cornea is a collagenous structure that show distinctive viscoelastic and optical properties. Some digestive enzymes such as alpha-amylase and collagenase are found in the cornea and can affect the proteoglycan-collagen fibril complex. This study aims to investigate the viscoelastic and optical properties of corneas following enzymatic degradation of proteoglycans and collagen fibrils with alpha-amylase and collagenase. Corneas were incubated with different concentrations of amylase (10, 20, and 30 mg/ml), crude collagenase (1, and 2 mg/ml) and purified collagenase (1, and 2 mg/ml) for varying periods. Oscillatory nanoindentation was used to measure microscale biomechanical properties including shear storage modulus (G′) and shear loss modulus (G″)of inflated corneas (15 mmHg) following enzymatic incubation. Inflation testing with optical coherence tomography (OCT) was utilised to measure the macroscale viscoelastic properties, including tangential elastic modulus (E_t) and corneal hysteresis (CH), and central corneal thickness (CCT) of the treated corneas. Corneal transparency and absorption coefficient (μ_a) were examined using spectrophotometry. The results showed that the amylase and collagenase reduced the viscoelastic properties (G′, G″, E_t, CH) of the corneas. The viscoelastic properties and CCT of the treated corneas decreased as a function of the enzyme concentrations and incubation periods. There is a positive correlation between microscale and macroscale elastic moduli of the control and treated corneas. The results in this chapter may be useful to build an empirical animal model of keratoconic corneas with different progression levels.

6.1. Introduction

The cornea combines optical properties with complex viscoelastic characteristics and thus must have a structure that allows strength, transparency, and ideal shape to be achieved simultaneously for clear vision. These properties are compromised with certain diseases such as keratoconus, which is thought to progress due to disruption of the enzymatic balance in the cornea (Volatier *et al*, 2019). Collagenase is one of these enzymes that was found to increase its activity in keratoconus (Balasubramanian *et al*, 2010). An in-depth investigation of how these enzymes affect biomechanical properties and transparency of the cornea may help in better understanding the course of the keratoconus.

In vivo, the cornea is subjected to many factors that influence its material properties. For example, the cornea is inflated at physiological pressures, which was found to affect its viscoelasticity and transparency (Chapter 3, 4 and 5), and hydrated by tear fluid and aqueous humour that both play an essential role in the health of the cornea. The tear fluid contains nutrients and active enzymes such as α-amylase, which was found to reduce the stiffness of collagenous tissue such as in the temporomandibular joint disc (Tanaka *et al*, 2003) and the cornea (Wollensak *et al*, 2011).

6.1.1. Stromal ultrastructure

As discussed in Chapter 2, the human cornea is composed of five layers, of which the thickest layer is the stroma that is mainly composed of type I collagen fibrils. These fibrils are arranged in layers known as lamellae that run in acute angles to each other in the anterior stroma and run parallel to each other in the middle and posterior stroma; all lamellae are parallel to the corneal surface. These lamellae are arranged at numerous rotational angles throughout the depth of the cornea. In the case of human corneas, the preferred orientations seem to consist of a larger proportion of fibrils lying in the inferior-superior and medial-lateral directions (Aghamohammadzadeh *et al*, 2004). However, in porcine corneas, the larger proportion of stromal collagen fibrils lie in circumferential orientations (Hayes *et al*, 2007). The extracellular matrix (ECM) of the corneal stroma primarily consists of collagen fibrils that are associated with proteoglycans, expressing a collagenous structure characterised by distinctive biomechanical properties.

There are a number of cells that are situated between the collagen lamellae in the stroma called keratocytes, also known as fibroblasts. These are mesencyhmal-derived cells of the corneal stroma that are normally quiescent, but they can readily respond and transition into healing phenotypes

following injury (West-Mays and Dwivedi, 2006). These cells serve to maintain the extracellular environment by reabsorbing and resynthesizing collagen molecules and glycosaminoglycans (GAGs), and also produce matrix metalloproteases (MMPs) such as collagenase (DelMonte and Kim, 2011). Changes in MMP expression are believed to be responsible for remodelling of the ECM, where collagenase and gelatinase activities were found to increase in keratoconic corneas (Kao *et al*, 1982; Zhou *et al*, 1998). In this chapter, collagenase and amylase are used to alter the biomechanical properties of the porcine corneas.

6.1.2. Collagenase

Collagenase is an enzyme that breaks the peptide bonds of the triple helix region in collagen. In corneas, it is secreted by corneal epithelial cells and stromal cells in response to repeated micro-traumas (eye rubbing, UV, contact lenses, allergy) and genetically susceptible individuals (Balasubramanian *et al*, 2010; Collier *et al*, 2000; Collier, 2001; Kaiserman and Sella, 2019). Commercially, collagenase is mainly extracted from vertebrates and bacterial sources such as *Clostridium Histolyticum*. Depending on preparation method, collagenase can be classified into 6 classes. Crude collagenase type I is normally mixed with other enzymes when it is extracted from its source. Crude collagenase may contain several collagenases (such as II, III, IV and V) but also a sulfhydryl protease, clostripain (Mitchell 1968), a trypsin-like enzyme, and an aminopeptidase (Bond and Van Wart, 1984). Collagenase type V is chromatographically purified collagenase, which is specifically purified to decrease the caseinase activity and provide high specific activity. Thus, purified collagenase has been typically used in collagen structural and biosynthetic studies.

Collagenase has been used in some studies for clinical treatment of collagenous tissues as well as for experimental studies that aim to degrade tissue properties to understand pathology. For example, collagenase has been used in the treatment of severely burned tissues, chronic dermal ulcers, and has also been tested in the treatment of herniated lumbar disks (Durmus *et al*, 2009; Sethi *et al*, 2000; Vaalamo *et al*, 1997). Purified collagenase has been approved for the treatment of pathological fibrotic tissues like Dupuytren's cords in the hand (Hurst *et al*, 2009) and penile fibrous plaques in Peyronie's disease (Honig, 2014). Jayes and colleagues (2016) used purified collagenase to digest interstitial collagen in uterine fibroids and reduce their stiffness. In that study, uterine samples were incubated with a variety of concentrations of collagenase for different periods. They found that the uterine fibroids were degraded by collagenase with significant reduction in tissue stiffness, which might result in an ultimate reduction of fibroid symptoms including pain and bleeding (Jayes *et al*, 2016). Another recent study utilised collagenase (crude and

purified) to identify strain dependent degradation behaviour and mechanical factors affecting collagen degradation in arterial tissue (Gaul *et al*, 2018). The study identified the strain dependent degradation behaviour of arterial tissue, and found an increase in collagen fibre crimp of tissues that were treated with crude collagenase that was not seen in samples that were treated with purified collagenase.

In the cornea, researchers have addressed collagenase implication in the pathology of keratoconic corneas. Studies found higher concentrations of collagenase and smaller concentrations of other degradation enzymes in tear fluid of patients with keratoconus, suggesting that collagenase activity was the main cause of keratoconus progression (Lema *et al*, 2008; Pannebaker *et al*, 2010). Other studies used immunohistochemical methods to investigate histopathological changes and expression differences in biochemical factors of collagenase in corneas with keratoconus (Collier *et al*, 2000; *et al*, 2015; Mackiewicz *et al*, 2006; Seppälä *et al*, 2006). They found that collagenase expression in keratoconic corneas was slightly increased around epithelial cells and also appeared locally in a scattered manner in the stroma. They concluded that collagenase expression increases in keratoconus, but it might not be the only tissue-destructive enzyme. Thus, researchers also suggested that the increase of collagenase activity in keratoconus is due to reduction of proteinase inhibitors leading to unbalance between MMPs and their inhibitors (Romero-Jiménez *et al*, 2010; Volatier *et al*, 2019). To the best of the author's knowledge, no biomechanical or optical study has investigated the influence of collagenase on corneal tissue.

6.1.3. Amylase

Amylase is an enzyme present in the saliva of humans and some other mammals that catalyses the hydrolysis of starch into sugars (disaccharides and trisaccharides). It is classified into three types depending on the type of proteins (α-amylase, β-amylase, and γ-amylase). In animals, α-amylase is secreted by salivary, pancreatic and lacrimal glands. While, gamma-amylase (γ-amylase) is secreted by the small intestine of animals. In this study, α-amylase was utilised to treat corneas because it is abundantly present in tear fluid as an active enzyme (Mylius, 1961; van Haeringen *et al*, 1975). That finding makes it of great interest for further investigation into the role amylase plays in keratoconus. Amylase secretion was recently found to increase in patients with early stages of keratoconus (Legkikh *et al*, 2018).

α-amylase affects various connective tissues and releases acidic GAGs. Generally, α-amylase randomly cleaves polysaccharides at α-1,4 glycosidic bonds. The glycosaminoglycan is linked to

proteoglycans by a tetrasaccharide linker. Thus, it was found that α-amylase releases GAGs from various connective tissues such as ligaments, cornea, sclera, and skin (Quintarelli *et al*, 1969). That finding drove Tanaka and colleagues (2003) to treat temporomandibular joint disc samples with different concentrations of amylase to remove proteoglycans. Their study aimed to investigate the role of the proteoglycans on the viscoelastic properties of the discs, and found that increasing the concentration of amylase significantly decreases viscoelasticity of the discs.

Few studies have investigated the mechanical response of the cornea following incubation with amylase (Spoerl *et al*, 2012; Wollensak *et al*, 2011). One such example, which involved treating porcine corneal strips with α-amylase was conducted by Wollensak *et al* (2011) using an extensometer to measure stiffness of the samples. The study found a significant reduction in stiffness of samples following the enzymatic treatment, suggesting alterations in optical properties of the corneas that were also observed in a later study (Spoerl *et al*, 2012). However, in both of these previous studies, corneal strips were dissected and stiffness measured regardless of the collagen fibrils orientation and physiological tension. In addition, it was not clear how the amylase activity of the treated corneas was inhibited after the incubation.

Therefore, investigating of the biomechanical and optical properties of corneas following enzymatic treatment in a manner similar to *in-vivo* conditions may help in providing better understanding of the effect of increased expression of amylase and collagenase on viscoelasticity, thickness and transparency of the cornea.

6.1.4. Aim

This chapter focuses on assessing viscoelastic properties of corneas following enzymatic treatment with amylase and collagenase. In this chapter, the effect of the enzymatic treatment on corneal transparency is examined by measuring visible light transmission and central corneal thickness of the treated corneas. Finally, this chapter examines the correlation between the microscale and macroscale elastic response of the corneas following enzymatic treatment.

6.2. Materials and methods

Within this section, preparation and enzymatic treatment of the corneas will be explained. The specific experimental parameters used for the studies in this chapter are described which followed the process illustrated in Figure 6.1.

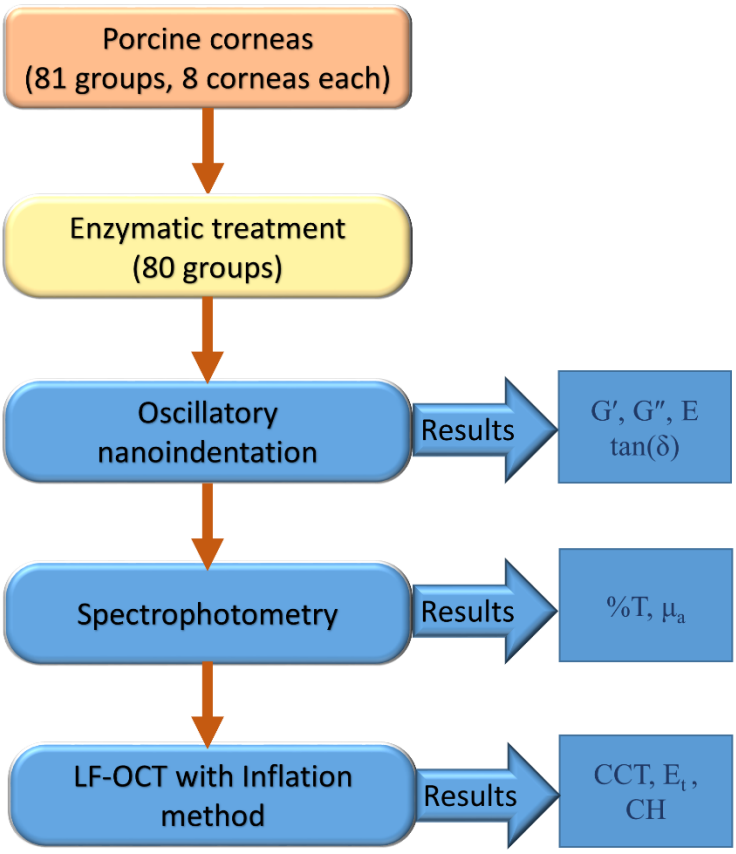

Figure 6.1: A summary showing the sequence of the measurements on the treated corneas. G', G", E, tan(δ), %T, μ_a, CCT, E_t, and CH refer to shear storage modulus, loss modulus, elastic modulus, percentage transparency, absorption coefficient, central corneal thickness, tangent elastic modulus, and corneal hysteresis, respectively.

6.2.1. Sample preparation

Eighty-one groups of fresh porcine eyes (8 eyes each) were separately obtained from a local abattoir shortly after slaughter. The pigs were aged from 5 to 6 months. The epithelium layer was peeled off using a cotton-tipped applicator and tweezers, to allow the enzymes to easily diffuse into the tissue. The corneas, with a 3 mm scleral ring, were subsequently dissected and placed in artificial anterior chambers that have been described previously in Chapters 3-5. The anatomical orientation of corneas was marked when the samples were fixed on the holders. In this study, no significant difference in the mass of the corneas was assumed.

The 81 groups were divided into a control group of 8 corneas and 80 treated groups (8 corneas each), in which the treated groups were treated with different concentrations of amylase and collagenase, tabulated in the next section. The control corneas were tested directly after dissection. The treated corneas were divided into 80 subgroups, depending on the type of treatment solution in which the corneas were incubated.

6.2.2. Enzymatic treatment

Treatment solution was prepared by mixing 8 ml tissue culture (TC) solution (CARRY-C, ALCHIMIA, Italy) with varying quantities of α-amylase (Amy) extracted from Aspergillus oryzae, crude collagenase (CC) and purified collagenase (PC) from *Clostridium histolyticum* (Bacteria). All the chemicals, including the enzymes and their inhibitors, were obtained from Sigma-Aldrich, Dorset, UK, unless stated otherwise. The concentrations of amylase in the treatment solution were either 10, 20, or 30 mg/ml, CC in the treatment solution was either 1, or 2 mg/ml and PC in the treatment solution was either (1, or 2 mg/ml). The treatment solution was filled in a sealed container that was placed on a controlled hotplate stirrer (Stuart US152, Bibby Scientific, UK) with a digital temperature controller sensor (SCT1, Bibby Scientific, UK) was immersed in the treatment solutions. This setup helped control the incubation temperature at 37.5±1°C for different incubation periods (0.5, 1, 2, 3, 4, 24, 48 hours). Table 6.1 summarises the concentrations of the enzymes and the incubation times that were used in treating the corneas. Some experiments were excluded because the treated corneas were excessively digested and became unsuitable for this study, marked as 'X' in Table 6.1. After incubation, corneas were rinsed with phosphate buffered saline solution (PBS), and soaked in enzymatic inhibitor solutions for 3 minutes. An aqueous solution of Dichloromethylenediphosphonic acid disodium (NaDTA) at a concentration of 5 mg/ml was used to inhibit the activity of the collagenase in the treated corneas. α-amylase inhibitor of concentration 1 mg/ml in aqueous solution was used to inhibit the activity of the α-amylase in treated corneas. A pilot study was conducted to assess the effect of these inhibitors on mechanical properties, in which the concentrations of the inhibitors and the soaking time had no significant effects on the storage shear modulus and loss shear modulus, shown in Appendix III. Another pilot study was performed to investigate the effect of incubating corneas in TC on biomechanical properties and CCT. There was no significant difference in biomechanical properties between fresh corneas and samples that were incubated for 4 and 24 hours in TC, but CCT was decreased after 4 hours, shown in Appendix IV.

The treated groups were given titles denoting the incubation time and the concentration of the enzymes used. For example, the treated group that was labelled as '3h-Amy10+CC2' refers to corneas that were incubated in a solution consisting of amylase (10 mg/ml) and crude collagenase (2 mg/ml).

Table 6.1: Enzyme concentrations and incubation time used in this study.

Concentration (mg/ml)	Incubation time (hours)						
	0.5	1	2	3	4	24	48
Amy 10	✓	✓	✓	✓	✓	✓	✓
Amy 20	✓	✓	✓	✓	✓	✓	✓
Amy 30	✓	✓	✓	✓	✓	✓	✓
CC 1	✓	✓	✓	✓	✓	✓	✓
CC 2	✓	✓	✓	✓	✓	✓	✗
Amy 10 + CC 1	✓	✓	✓	✓	✓	✓	✓
Amy 20 + CC 1	✓	✓	✓	✓	✓	✓	✗
Amy 30 + CC 1	✓	✓	✓	✓	✓	✗	✗
Amy 10 + CC 2	✓	✓	✓	✓	✓	✗	✗
Amy 20 + CC 2	✓	✓	✓	✓	✓	✗	✗
Amy 30 + CC 2	✓	✓	✓	✓	✓	✗	✗
PC 1	✓	✓	✓	✓	✓	✓	✓
Amy 10 + PC 1	✓	✓	✓	✓	✓	✓	✓
Amy 10 + PC 2	✓	✓	✓	✓	✓	✓	✗
Amy 30 + PC 2	✓	✓	✓	✓	✓	✗	✗

'Amy' refers to alpha-amylase enzyme. 'CC' represents crude collagenase enzyme. 'PC' refers to purified collagenase. 10, 20 and 30 refer to 10, 20 and 30 mg/ml amylase concentrations, respectively. 1, and 2 refer to 1, and 2 mg/ml collagenase concentrations, respectively. '✓' and 'X' represent the included and excluded experiments, respectively.

6.2.3. Microscale viscoelastic properties: Oscillatory nanoindentation

The storage shear modulus (G′) and the loss shear modulus (G") of the treated corneas were measured using oscillatory nanoindentation, which was explained in Chapter 3. The treated corneas were fixed in a holder and pressurised at normal intraocular pressure (15 mmHg) during the indentation using PBS as an inflation solution. Each cornea in every group was indented with 2 indents on the apex, in which a 1000 μm distance was set between the indents. All other parameters were the same as in Chapter 3. The testing and tip cleaning took approximately 6 min.

6.2.4. Corneal transparency: Spectrophotometry

Corneal transparency of the treated corneas was evaluated using spectrophotometry to measure percentage transmission (%T) through the central cornea. This method was detailed in Chapter 5, where the transparency of the fresh porcine corneas was evaluated. The treated corneas were

placed in a custom designed holder, in which the corneas were inflated at 15 mmHg using an elevated reservoir filled with PBS. Two types of reference corneas were measured, firstly, control corneas that were normal and untreated corneas. Secondly, corneas were incubated with TC for 4 hours (4h-TC). The total time spent for the measurement of each cornea was less than 1 min.

6.2.5. Corneal thickness and biomechanical properties: Inflation test by LF-OCT

Line-field optical coherence tomography (LF-OCT) was used to measure macroscale biomechanical properties, including E_t and CH, and tomographical values of each group, including displacement of corneal apex and CCT. The method was explained in detail in Chapter 4.

6.2.6. Statistical analysis

All statistical analysis was performed using OriginPro 2016 version 9.3 (OriginLab, USA). Data is expressed as mean values and standard deviation (mean ± standard deviation) unless otherwise stated. Heterogeneity between the corneas in each group was assumed. In order to determine the statistical significance, the distribution of each dataset was assessed using quantile-quantile plot and normality test to select the appropriate test. Since the groups were unpaired and the statistical significance was chosen to be between two datasets, the two-sample t-test was used to test the statistical difference between G′, G", E, CCT, E_t, CH and %T of the treated corneas and those obtained from the control corneas. The significance level (α) was set as 0.05 for all tests. Pearson's correlation test was used to assess the relationship between elastic modulus of the treated corneas obtained from LF-OCT and oscillatory nanoindentation methods.

6.3. Results

In this section, the key results are presented. All the results are tabulated in Appendix II. It was noticed that the colour of the corneas changed from transparent-clear to transparent-pink following incubation in treatment solutions. Example of treated corneas are shown in Figure 6.2. Treated corneas appeared to be softer and more transparent; these changes are reported in the next sections. In Figure 6.2 (C), the text was apparently magnified as the cornea worked as a transparent lens.

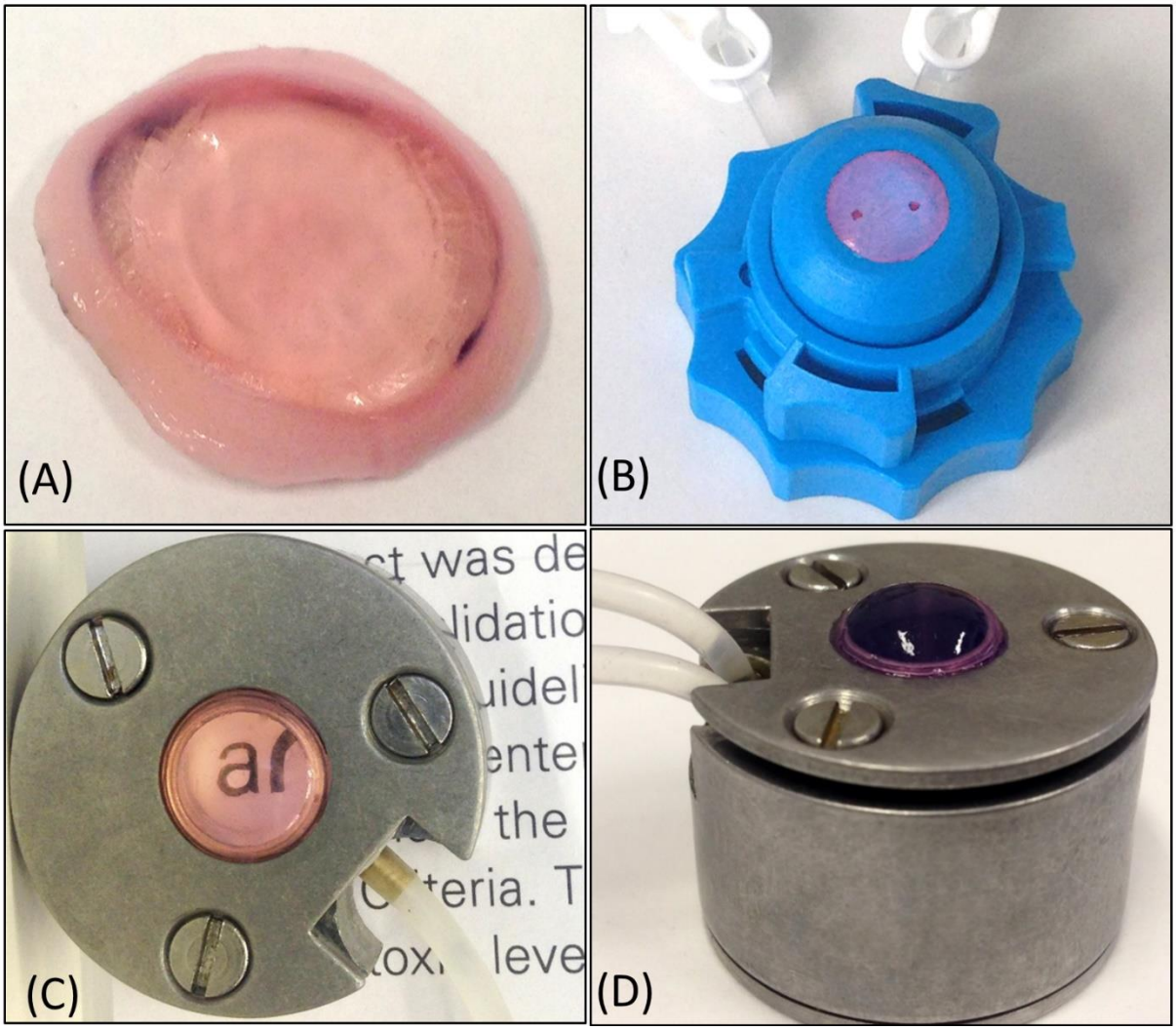

Figure 6.2: Typical treated corneas. (A) An uninflated treated cornea. (B) A treated cornea held in a Barron artificial anterior chamber for LF-OCT inflation testing. (C) A treated cornea fixed in a special designed holder and inflated at 15 mmHg for testing corneal transparency. The text is shown magnified by the cornea (D) A treated cornea fixed in a special designed holder and inflated at 15 mmHg for micromechanical viscoelastic property determination.

6.3.1. Microscale viscoelastic properties: Oscillatory nanoindentation

6.3.1.1. Amylase treated groups.

In this section, G′ and G″ of groups that were incubated with amylase will be presented, which help evaluate the influence of amylase on the corneas.

G′ was decreased following incubation of the corneas in varying concentrations of amylase and collagenase. Figure 6.3(A) shows the G′ of different groups that were incubated in amylase (10 mg/ml) for different periods. G' of the control group were 85.1±9.5 kPa. G' of 0.5h-Amy10 group decreased by 1.8±0.1% after 30 min incubation in amylase solution (10 mg/ml) in comparison with the control group. However, the reduction in G' was not statistically significant, p=0.6804.

The statistical significance in G′ of the control and the 24h-Amy10 groups was detected after incubating the treated corneas in the same concentration of amylase (10 mg/ml) for 24 hours ($p=0.0374$). Graphs showing E values of the corneas are presented in Appendix II.

It was found that higher concentrations of amylase in the treatment solutions led to a greater reduction in G′. G′ of corneas that were incubated in varying amylase concentrations (10, 20, and 30 mg/ml) for 2 hours decreased by 6.3±2.9%, 8.3±2.8% and 9.9±2.1%, respectively. Figure 6.3(B) shows the reduction in G′ with time for corneas that were incubated in varying amylase concentrations. The rate of change in the reduction of G′ seems to be affected by incubation time and amylase concentration, in which greater reduction was seen within the first 4 hours compared to after 24 hours. The rate of change in G′ considerably decreased in the period from 24 to 48 hours. In the period from 24 to 48 hours, the rate of G′ reduction was greater in the high amylase concentration (30 mg/ml) than in the low amylase concentrations (10 and 20 mg/ml).

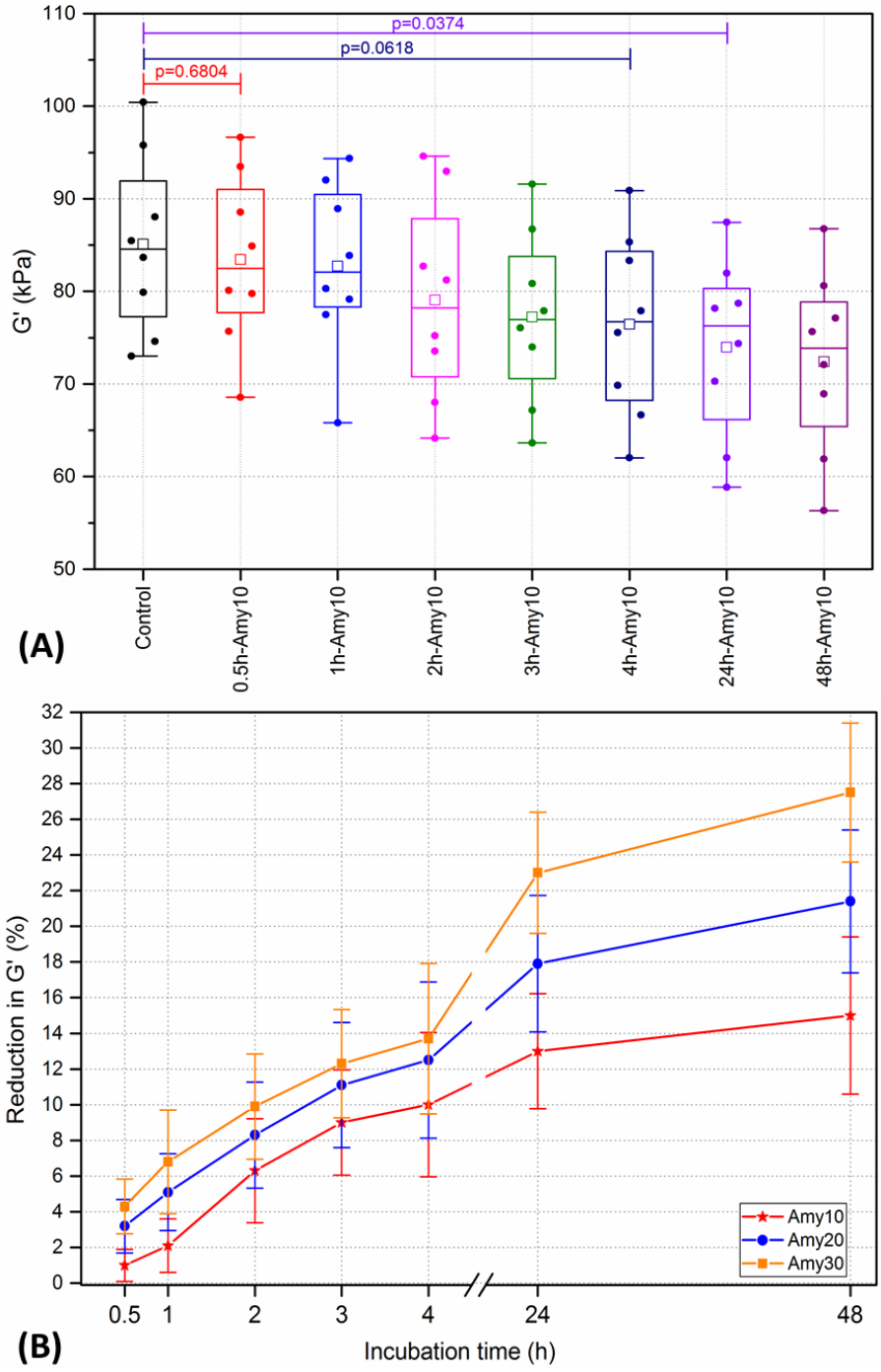

Figure 6.3: Shear storage modulus (G′) of inflated corneas that were incubated in amylase solutions for varying incubation periods. Corneas were inflated at 15 mmHg. (A) G′ of corneas were incubated in amylase (10 mg/ml). Data were represented as box plots and data overlaid with lower and upper borders of the box to represent the lower and upper quartiles, and the middle horizontal line to represent the median. The upper and lower whiskers represent 5th and 95th percentile of the data. The solid points represent data points of each group. The square refers to the mean value of the dataset for that group. 'p' refers to the statistical significance value. (n=8 corneas/box). (B) Percentage reduction in G′ over time for corneas that were incubated in varying amylase concentrations. Each data point represents one treatment group that consisted of 8 corneas. Error bars represent standard deviations. A break in the *X*-axis between 4.5 and 21 was set to enhance the representation of the graph.

The shear loss modulus (G") decreased in groups that were incubated in a solution containing amylase. Figure 6.4(A) shows G" of different groups that were incubated in amylase (10 mg/ml) for different periods. G″ of the control group were 13.34±2.49 kPa. G" was decreased with incubation time, where it decreased from 13.34±2.49 kPa (control group) to 12.52±2.7 kPa (2h-Amy10 group) when the corneas were incubated for two hours in amylase (10 mg/ml), p= 0.273.

G" was slightly decreased with increased incubation time and enzyme concentration (Figure 6.4(B)). However, the trend became statistically significant after incubation of the corneas in amylase (20 mg/ml) solution for 3 hours, in which G" of 3h-Amy20 group had significantly decreased by 15.2% in comparison to the control corneas, p=0.0461.

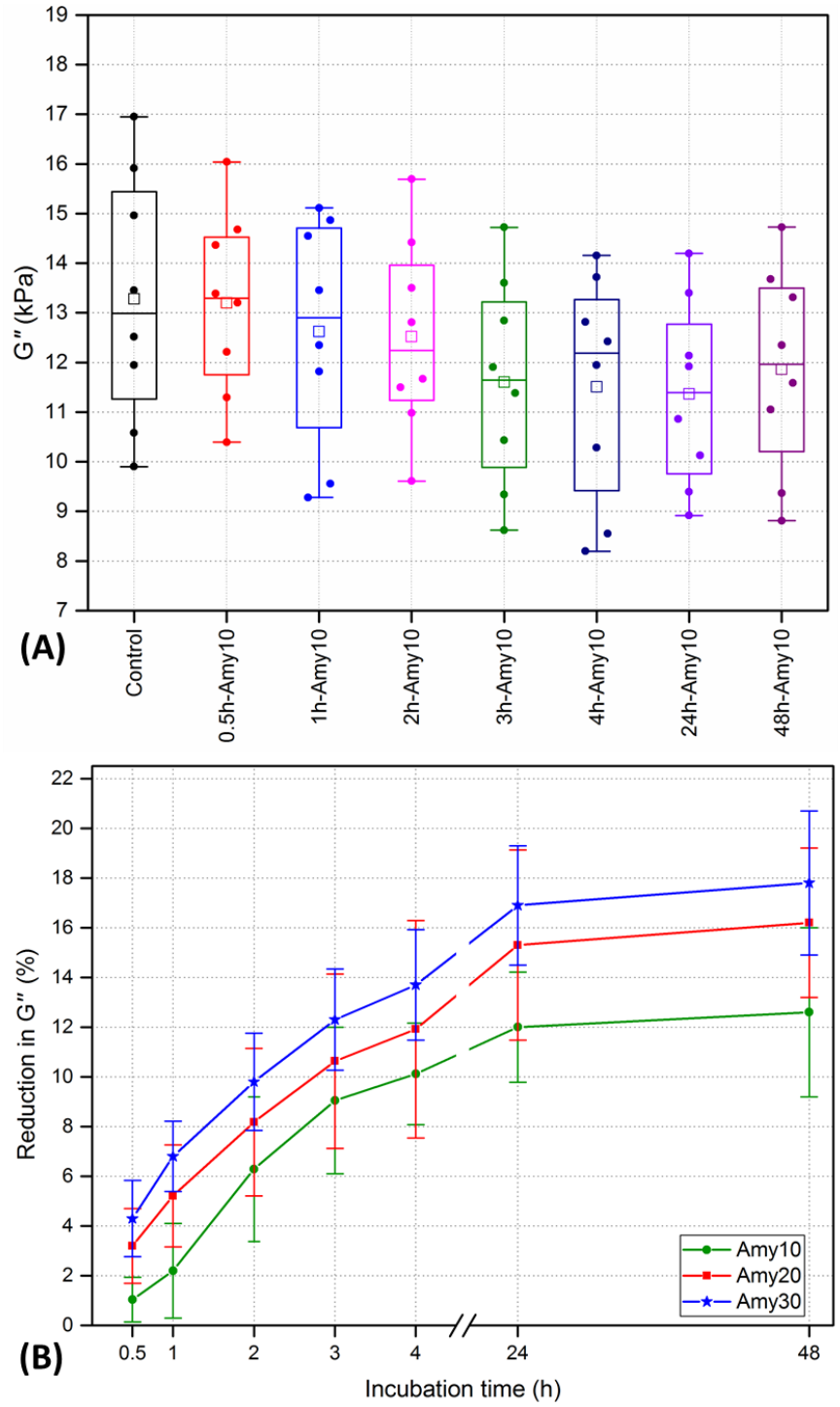

Figure 6.4: Shear loss modulus (G′) of inflated corneas that were incubated in amylase solutions for varying incubation periods. Corneas were inflated at 15 mmHg. (A) G′ of corneas were incubated in amylase (10 mg/ml). Data were represented as box plots and data overlaid with lower and upper borders of the box to represent the lower and upper quartiles, and the middle horizontal line to represent the median. The upper and lower whiskers represent 5th and 95th percentile of the data. The solid points represent data points of each group. The square refers to the mean value of the dataset for that group. 'p' refers to the statistical significance value. (n=8 corneas/box). (B) Percentage reduction in G′ over time for corneas that were incubated in varying amylase concentrations. Each data point represents one treatment group that consisted of 8 corneas. Error bars represent standard deviations. A break in the *X*-axis between 4.5 and 21 was set to enhance the representation of the graph.

6.3.1.2. Collagenase treated group

In this section, mechanical properties of the treated corneas will be presented for all the groups in which collagenase was used. In some cases, amylase treatment will be also shown in graphs for comparison. The loss factor will be presented in this section to compares the proportional relationship of the viscous to elastic contribution of treated corneas that were incubated with varying enzymes for 4 hours.

The addition of collagenase to the treatment solution led to dramatic reductions in G′ of the treated corneas. For ease of data presentation and comparison, groups that were incubated in varying concentrations of amylase and collagenase (crude and purified) for 4 hours are presented in Figure 6.5. The reduction in G′ was found to increase with increasing concentration of the enzymes (amylase and collagenase). The increase of collagenase in the treatment solution led to a further decrease in G′. For example, increasing the crude collagenase from 1 to 2 mg/ml (in the groups 4h-Amy10+CC1 and 4h-Amy10+CC2) further decreased G′ from 46.92±9.35 kPa to 34.98±6.76 kPa. This also indicates that the increase of collagenase in the treatment solution has a bigger influence on G′ than increasing the amylase concentration. The maximum reduction in G′ was found in 4h-Amy30+CC2 group, with a significant reduction of approximately 63.8% relative to the control group ($p<0.0001$).

The results show that purified collagenase had a lower effect on corneal stiffness than crude collagenase. At the same incubation conditions, G′ of corneas (4h-Amy30+CC2 group) that were treated with a solution containing crude collagenase (2 mg/ml) was significantly less (<33.45%) than that of corneas (4h-Amy30+PC2 group) that were incubated with a solution containing purified collagenase (2 mg/ml) ($p<0.0001$).

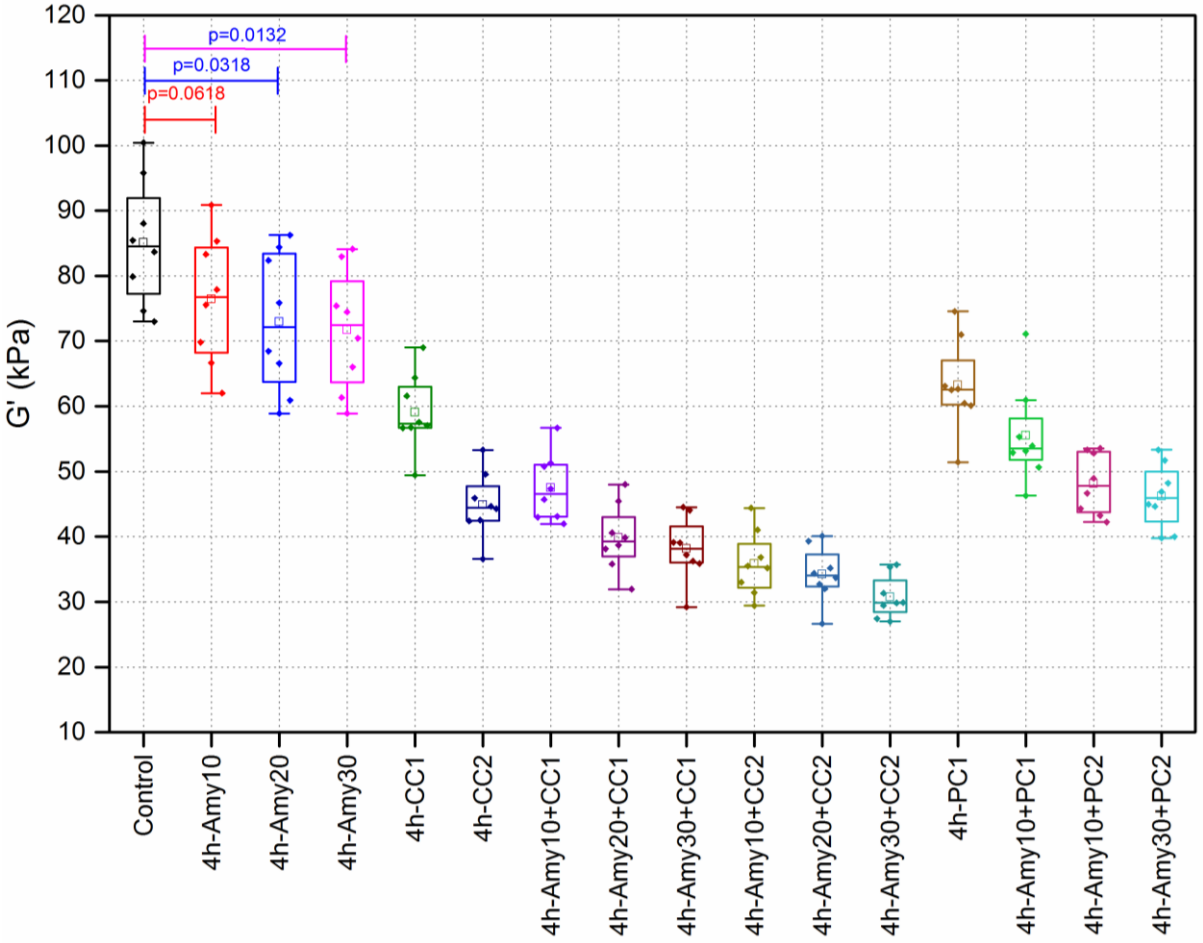

Figure 6.5: Shear storage modulus (G′) of inflated corneas that were incubated in varying amylase and collagenase solutions for 4 hours. Corneas were inflated at 15 mmHg. Data were represented as box plots and data overlaid with lower and upper borders of the box to represent the lower and upper quartiles, and the middle horizontal line to represent the median. The upper and lower whiskers represent 5th and 95th percentile of the data. The solid points represent data points of each group. The square refers to the mean value of the dataset for that group. 'p' refers to the statistical significance value. (n=8 corneas/box).

Figures 6.6 shows the percentage reduction in G′ of all the groups, where corneas were treated with varying concentration of the enzymes for different incubation periods. The results illustrate that the rate of G′ reduction was affected by the incubation time and enzyme concentrations. The higher rate of change in G′ was seen in corneas that were incubated with a solution consisting of amylase (30 mg/ml) and crude collagenase (2 mg/ml). In some experiments, extensive incubation time of corneas up to 24 hours in treatment solutions containing collagenase caused structural damage to the tissue; in particular, corneas that were incubated in amylase (30 mg/ml) and crude collagenase (2 mg/ml) for more than 4 hours.

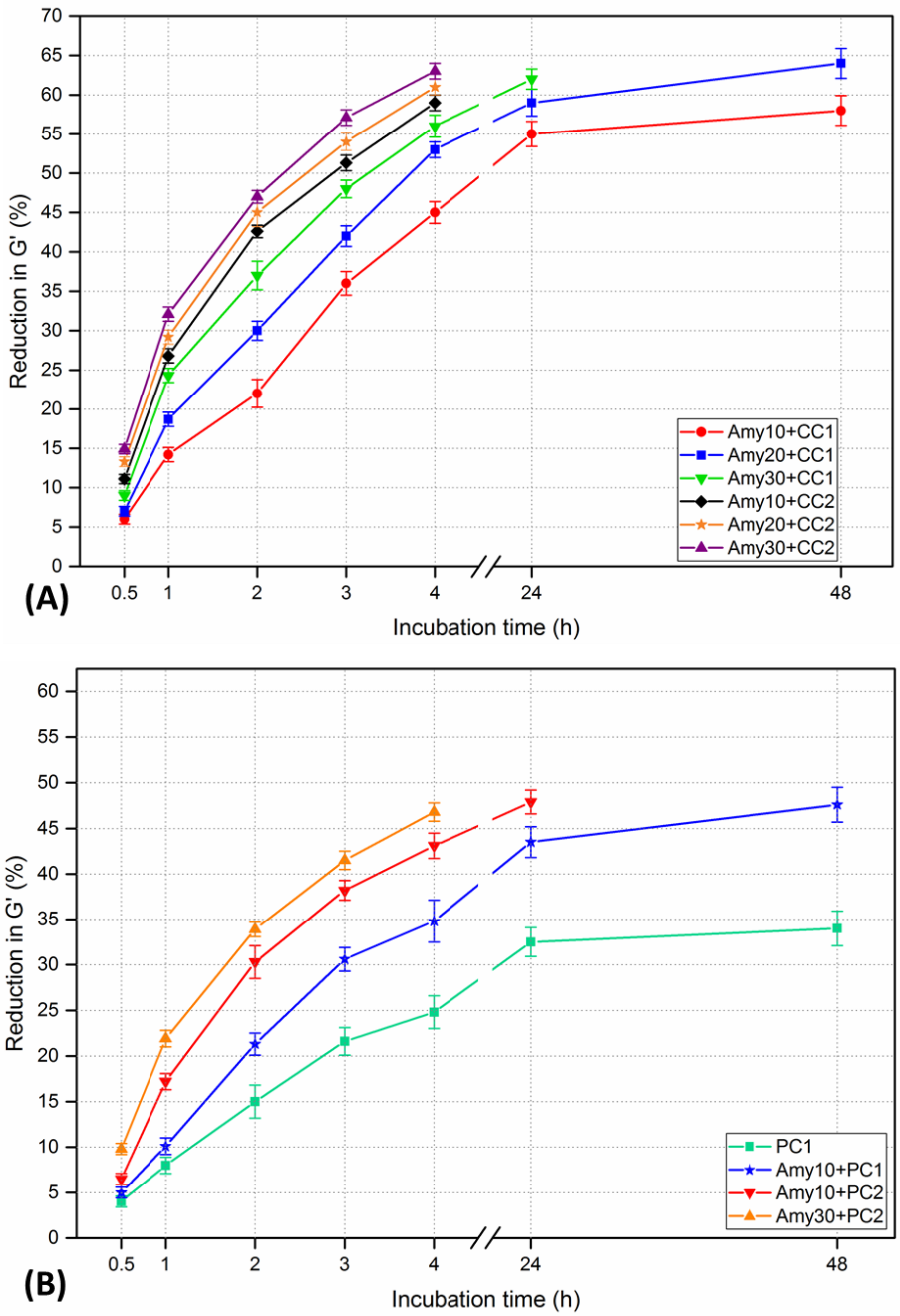

Figure 6.6: Percentage reduction in the shear storage modulus (G′) of corneas over incubation time for all groups that were incubated in varying treatment solutions of different amylase and crude collagenase concentrations. Treatment solutions are presented in the legend box. (A) Groups treated with varying concentrations of amylase and crude collagenase. (B) Groups treated with varying concentrations of amylase and purified collagenase. Error bars represent standard deviations (n = 8 corneas/point). A break in the *X*-axis between 4.5 and 21 was set to enhance the representation of the graph.

The shear loss modulus of the treated corneas significantly decreased after adding the collagenase (crude and purified) to the treatment solution. Figure 6.7 compares G" of corneas that were incubated in varying treatment solutions for 4 hours. Corneas that were treated with amylase (10 and 20 mg/ml) did not show significant changes in G" values compared to the control group ($p>0.2489$). G" was significantly reduced by 18.3% for corneas incubated with amylase (30 mg/ml) for 4 hours, compared to control group, $p=0.0492$. The greatest reduction in G" was seen following incubating the corneas (4h-Amy30+CC2) in a solution containing amylase (30 mg/ml) and crude collagenase (2 mg/ml); 82.2% compared to control samples ($p<0.0001$). Corneas that were incubated in a solution containing crude collagenase showed a higher reduction in G" than those corneas treated with purified collagenase.

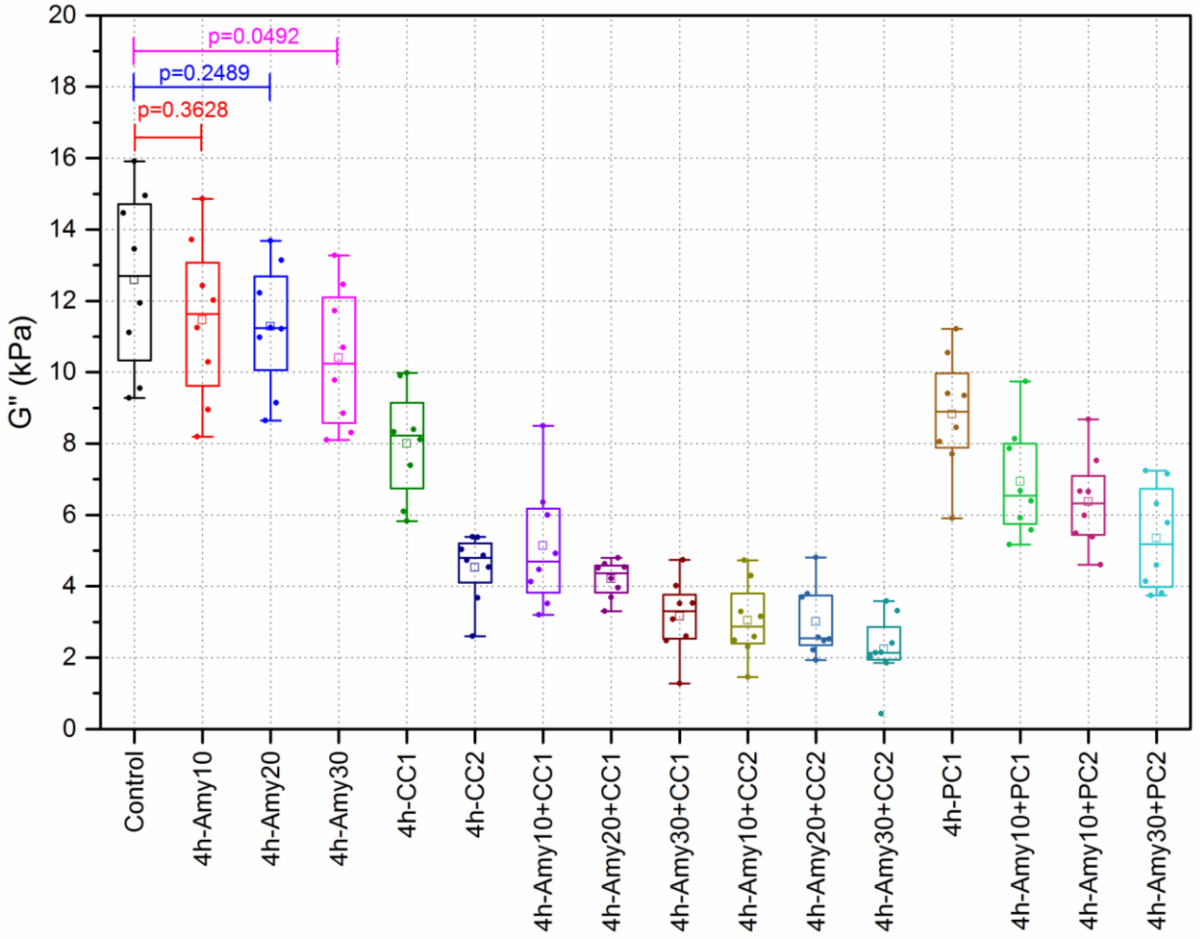

Figure 6.7: Shear loss modulus (G") of inflated corneas that were incubated in varying amylase and collagenase solutions for 4 hours. Corneas were inflated at 15 mmHg. Data were represented as box plots and data overlaid with lower and upper borders of the box to represent the lower and upper quartiles, and the middle horizontal line to represent the median. The upper and lower whiskers represent 5th and 95th percentile of the data. The solid points represent data points of each group. The square refers to the mean value of the dataset for that group. 'p' refers to the statistical significance value. (n=8 corneas/box).

The proportional importance of viscous to elastic contribution (loss factor) of the treated corneas showed significant changes in corneas treated with solutions containing crude collagenase ($p<0.0481$). No statistical difference was detected between tan(δ) of corneas that were incubated in solutions consisting of purified collagenase and amylase and tan(δ) of the control group. Figure 6.8 shows the changes in tan(δ) of corneas that were incubated in varying amylase and collagenase solutions for 4 hours. tan(δ) of the control group was 0.146±0.02. The greatest reduction in loss factor of treated corneas (4h-Amy30+CC2 group) was 50.5% compared to the control samples.

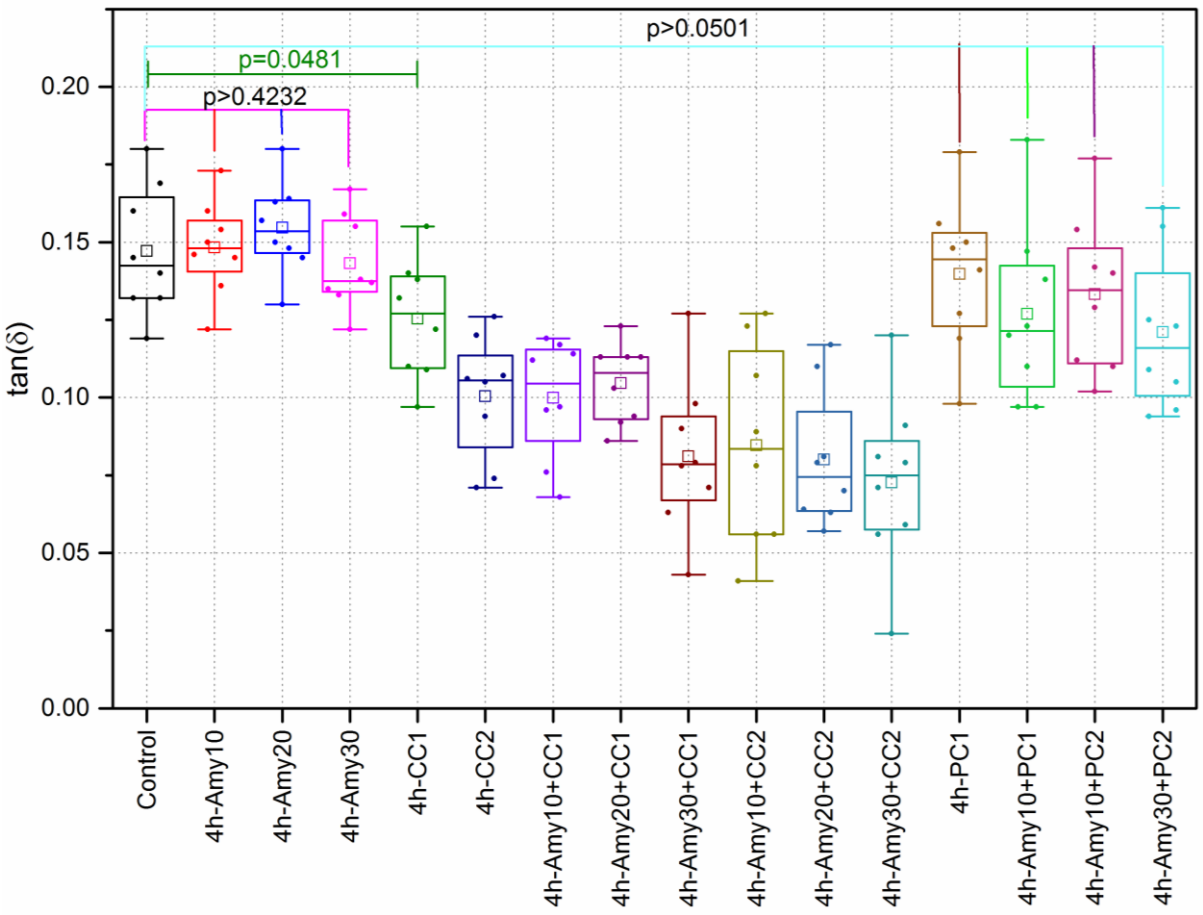

Figure 6.8: Loss factor (tan(δ)) of corneas that were incubated in varying amylase and collagenase solutions for 4 hours. Corneas were inflated at 15 mmHg. Data were represented as box plots and data overlaid with lower and upper borders of the box to represent the lower and upper quartiles, and the middle horizontal line to represent the median. The upper and lower whiskers represent 5th and 95th percentile of the data. The solid points represent data points of each group. The square refers to the mean value of the dataset for that group. 'p' refers to the statistical significance value. (n=8 corneas/box).

6.3.2. Corneal transparency: Spectrophotometry

The results show that corneal transparency increased following enzymatic treatment. For ease of data presentation, percentage transmission (%T) at a wavelength of 600 nm through corneas that were incubated in varying concentrations of amylase and collagenase (crude and purified) have been presented in this section (Figure 6.9). The percentage transmission (%T) through the central region of the control group was 87.03±0.76 at 600 nm, whilst, %T of corneas incubated with TC for 4 hours (4h-TC) was significantly decreased by approximately 13% relative to the control group ($p<0.0001$). The results show that %T was significantly increased by 11.9% relative to 4h-TC group following incubation of corneas in a solution containing amylase (10 mg/ml). Furthermore, %T slightly increased with increased concentration of amylase in the treatment solution. Likewise, the presence of collagenase (crude and purified) increased %T through corneas. The results found that %T was slightly increased with increased concentration of enzymes in the treatment solution.

It was also found that the presence of purified collagenase led to a greater increase in %T across the corneas than the crude collagenase. For example, %T through corneas that were treated with purified collagenase (1 mg/ml) for 4 hours increased by 12.1% relative to the 4h-TC group ($p>0.0001$), whilst, %T across corneas that were treated with crude collagenase (1 mg/ml) for 4 hours increased by 8.2% relative to the 4h-TC group ($p>0.0001$). The maximum %T was 88.4±0.69, which was recorded in corneas that were incubated in treatment solutions containing purified collagenase (2 mg/ml) and amylase (30 mg/ml).

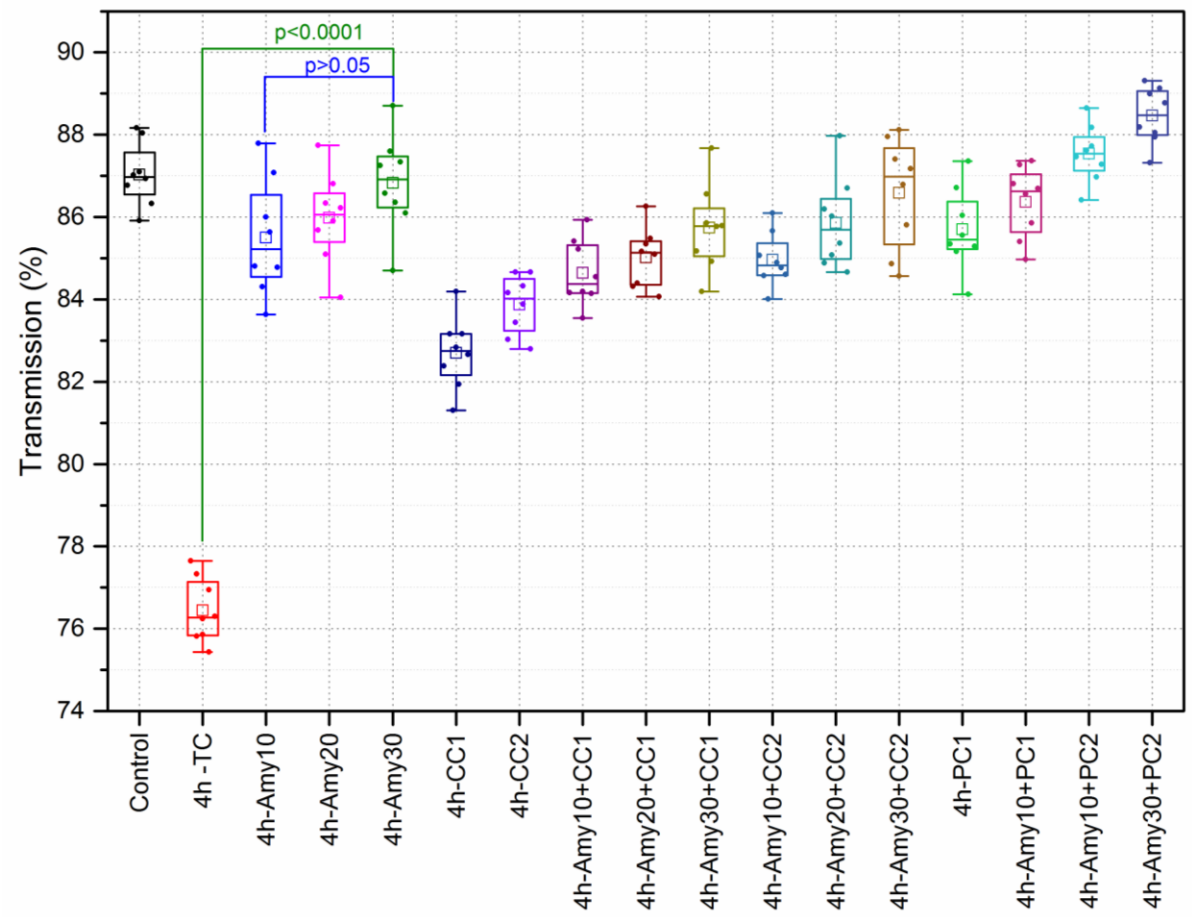

Figure 6.9: Percentage transmission (%T) of a 600nm-light through corneas that were incubated in varying amylase and collagenase solutions for 4 hours. Corneas were inflated at 15 mmHg. Data were represented as box plots and data overlaid with lower and upper borders of the box to represent the lower and upper quartiles, and the middle horizontal line to represent the median. The upper and lower whiskers represent 5th and 95th percentile of the data. The solid points represent data points of each group. The square refers to the mean value of the dataset for that group. 'p' refers to the statistical significance value. (n=8 corneas/box).

The results showed that the absorption coefficient (μ_a) of the treated corneas decreased relative to 4h-TC group and increased relative to the control group (Figure 6.10). μ_a of the central region of the control group was 1.53±0.08 cm^{-1} at a wavelength of 600 nm, whilst, μ_a of corneas incubated with TC for 4 hours was significantly increased to 3.37±0.15 cm^{-1} ($p<0.0001$). The presence of amylase and collagenase (crude and purified) significantly decreased μ_a ($p<0.0001$). Relative to 4h-TC group, μ_a of treated corneas decreased as the collagenase concentration in the treatment solutions increased, whilst, increasing the concentration of the amylase in treatment solutions significantly decreased the values of absorption coefficient ($p>0.149$).

Amylase reduced μ_a of the treated corneas more than collagenase (crude and purified) for the same incubation time. For example, μ_a of corneas incubated in amylase (10 mg/ml) for 4 hours was

1.77±0.17 cm^{-1}. In comparison, μ_a of corneas incubated in crude collagenase (1 mg/ml) and purified collagens for the same period were 2.5±0.12 cm^{-1} and 2±0.15 cm^{-1}, respectively.

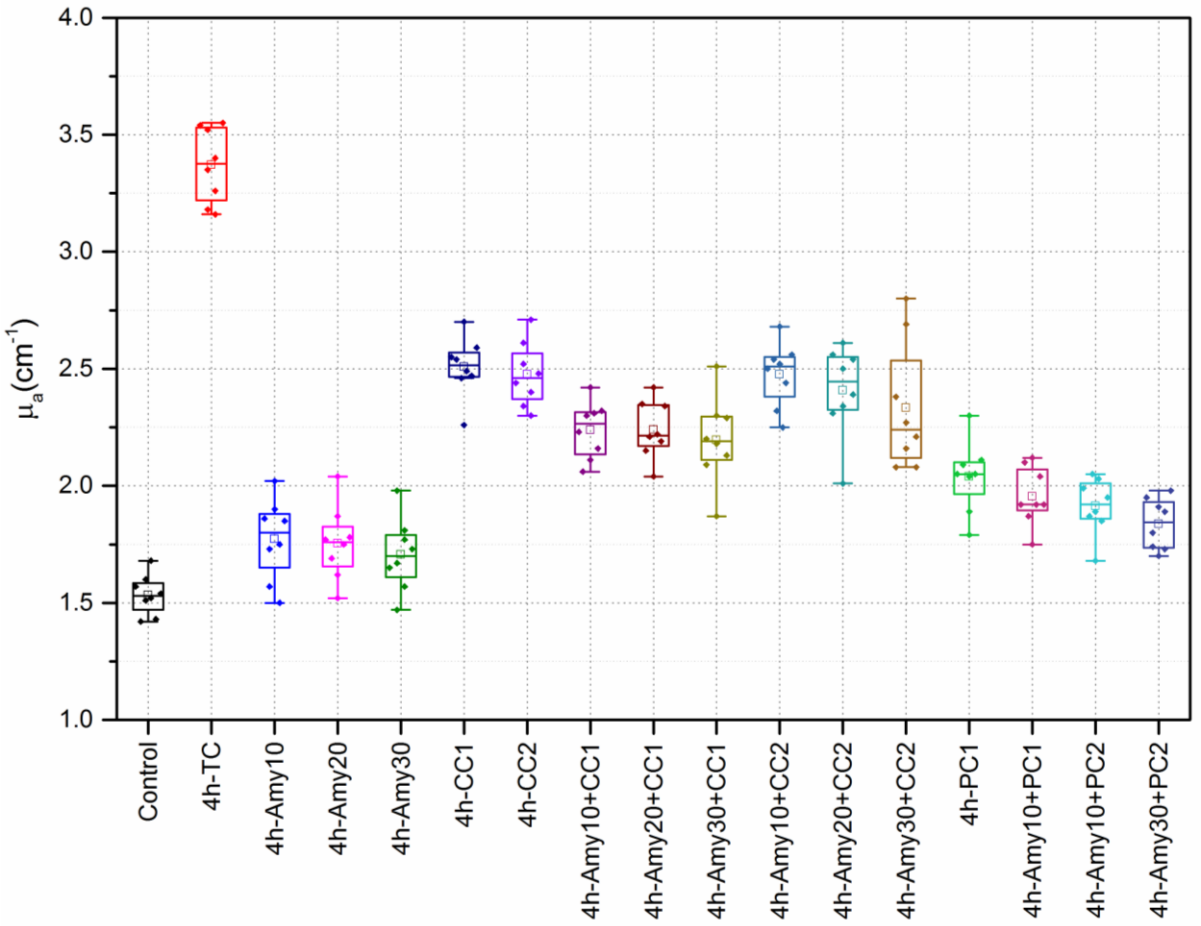

Figure 6.10: Absorption coefficient (μ_a) of corneas that were incubated in varying amylase and collagenase solutions for 4 hours. The wavelength was 600 nm. Corneas were inflated at 15 mmHg. Data were represented as box plots and data overlaid with lower and upper borders of the box to represent the lower and upper quartiles, and the middle horizontal line to represent the median. The upper and lower whiskers represent 5th and 95th percentile of the data. The solid points represent data points of each group. The square refers to the mean value of the dataset for that group. 'p' refers to the statistical significance value. (n=8 corneas/box).

6.3.3. Corneal thickness and biomechanical properties: LF-OCT

Figure 6.11 shows a representative LF-OCT image of a control and treated cornea inflated at 15 mmHg. The results showed that CCT decreased following enzymatic treatment. The dome shape was steeper in treated corneas (4h-Amy10+CC2 group) than in the control corneas. The reduction in thickness following enzymatic incubation affect the whole cornea.

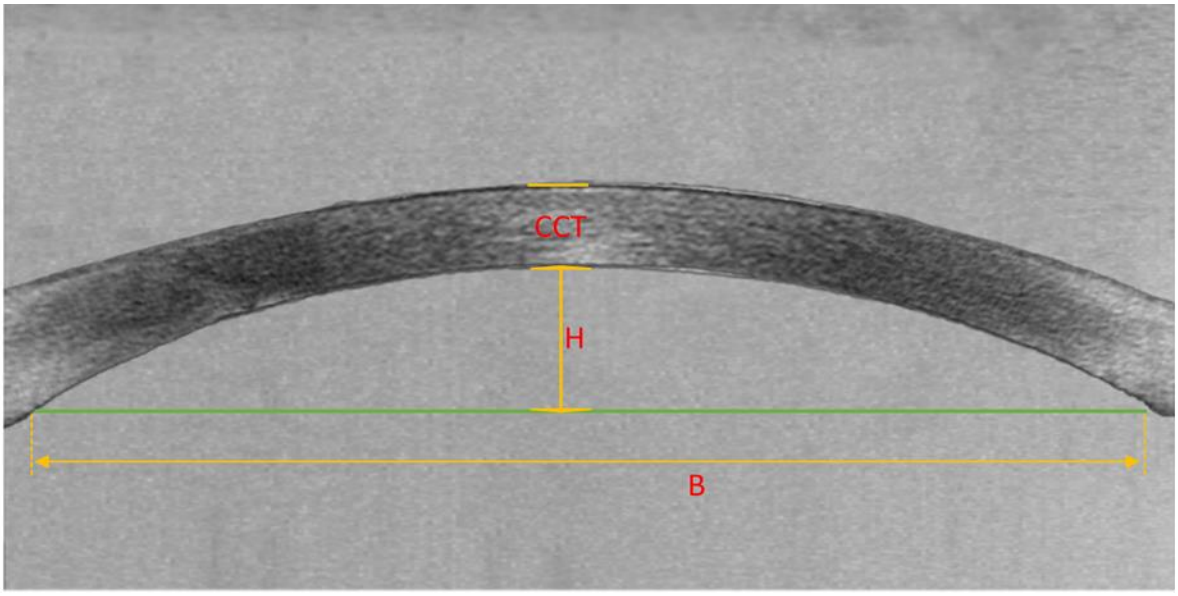

(A)

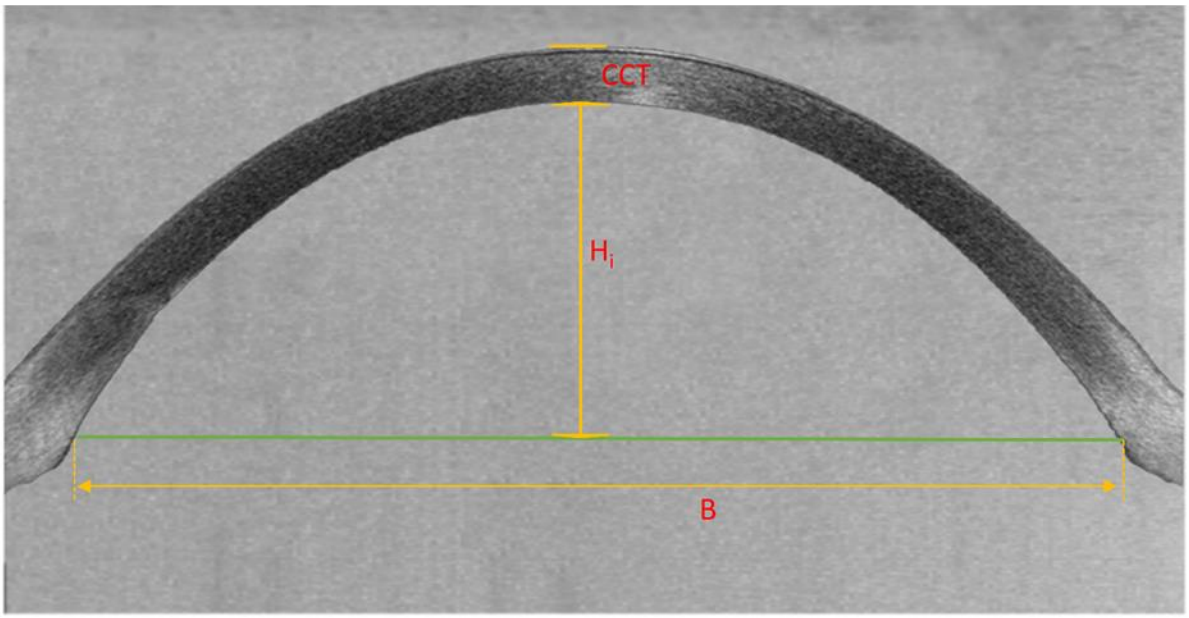

(B)

Figure 6.11: A typical LF-OCT image for inflated control and enzymatic-treated corneas at a pressure of 15 mmHg during the loading phase. (A) A control cornea. Central corneal thickness (CCT) of this cornea was 986.9 μm. The height (H) from the base was 1.92 mm. The base (B) was 12.5 mm. (B) Enzymatic-treated cornea of 4h-Amy10+CC2 group, where the cornea was incubated in amylase (10 mg/ml) and crude collagenase (2 mg/ml) for 4 hours. The central corneal thickness (CCT) of this cornea was 714.34±13.45 μm. The height (H_i) from the base was 5.92±0.72 mm. The base (B) was 12.54 mm. Corneas were placed in an artificial anterior chamber, shown in Figure 6.2(B). In both images, the epithelium layer had been removed. High pass filter was used to enhance the contrast of the corneal boundaries.

6.3.3.1. Corneal thickness

It was found that the CCT reduced as incubation time in amylase solution increased. CCT of the control group was found to be 992.5±10.41 μm. Corneas incubated in TC for 30 min (0.5h-TC) showed no significant difference from control group ($p=0.468$), whilst prolonged incubation of corneas in TC for 4 hours significantly reduced CCT by approximately 10% relative to the control group ($p<0.0001$). CCT of corneas incubated in amylase (10 mg/ml) decreased with increased incubation time (Figure 6.12). For example, CCT of corneas incubated with amylase (10 mg/ml) for 30 min was significantly decreased by approximately 2% relative to 0.5h-TC group, whilst increasing incubation time of the corneas to 4 hours in the same amylase concentration decreased CCT of the corneas more than at their initial state. At the same concentration of amylase (10 mg/ml), the reduction in CCT of the corneas was not found to be statistically significant after incubation of the corneas for more than 24 hours ($p=0.274$).

CCT of the treated corneas reduced significantly when both amylase and collagenase were added to treatment solutions. For ease of data presentation, groups that were incubated in varying concentrations of amylase and collagenase (crude and purified) for 4 hours are presented in Figure 6.13. The results also showed that collagenase (crude and purified) significantly reduced CCT. The CCT of the treated corneas significantly decreased as the concentration of enzymes in the treatment solutions increased. For example, increasing the concentration of the amylase in the treatment solution from 10 to 20 mg/ml increased the reduction percentage of CCT from 2% to 4.3%, respectively, relative to the control group. For the same incubation time, the presence of collagenase (purified and crude) reduced the CCT more than amylase. For instance, the corneas that were incubated in a treatment solution of crude collagenase (1 mg/ml) for 4 hours reduced CCT by 14.6% relative to the control group, whilst incubating the corneas in a treatment solution of amylase (30 mg/ml) for the same period significantly reduced CCT by 7.6% relative to the control group, $p<0.0001$. The maximum reduction in CCT was recorded in the 4h-Amy30+CC2 group. It had significantly decreased by approximately 28.5% relative to the control group ($p<0.0001$).

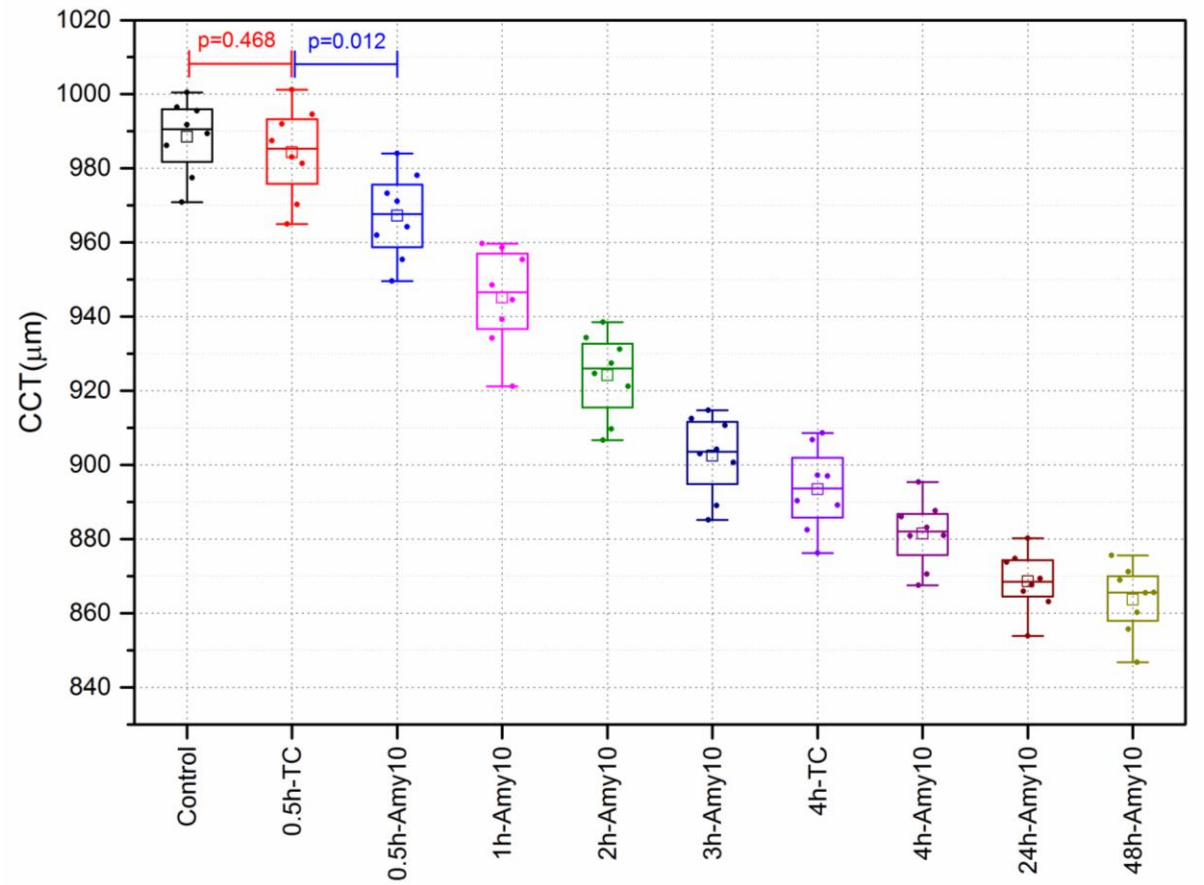

Figure 6.12: Central corneal thickness of inflated corneas that were incubated in amylase (10 mg/ml) for varying incubation time. Corneas were inflated at 15 mmHg. Data were represented as box plots and data overlaid with lower and upper borders of the box to represent the lower and upper quartiles, and the middle horizontal line to represent the median. The upper and lower whiskers represent 5th and 95th percentile of the data. The solid points represent data points of each group. The square refers to the mean value of the dataset for that group. 'p' refers to the statistical significance value. (n=8 corneas/box).

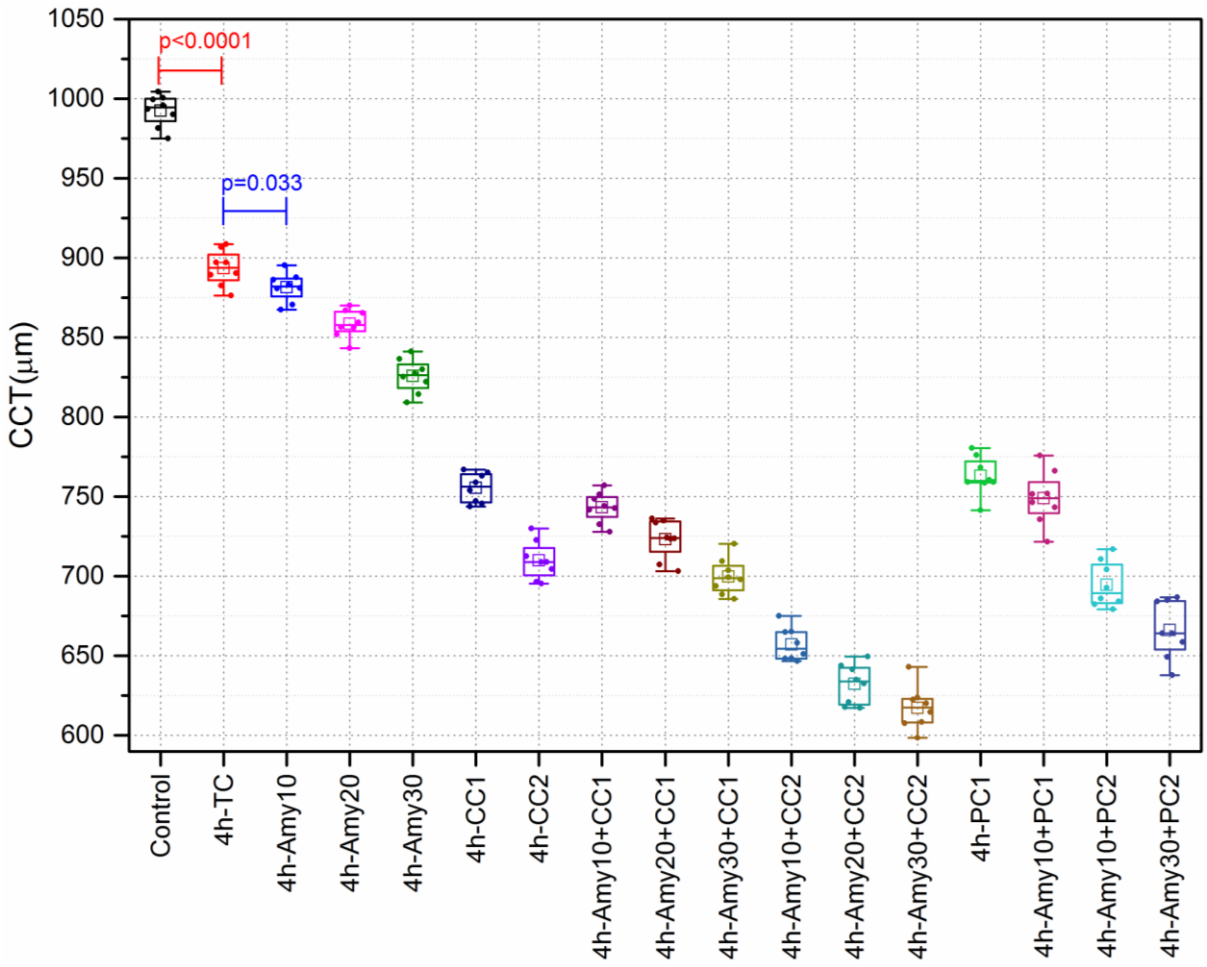

Figure 6.13: Central corneal thickness of inflated corneas that were incubated in solutions of varying concentrations of amylase and collagenase (crude and purified) for 4 hours. Corneas were inflated at 15 mmHg. Data were represented as box plots and data overlaid with lower and upper borders of the box to represent the lower and upper quartiles, and the middle horizontal line to represent the median. The upper and lower whiskers represent 5th and 95th percentile of the data. The solid points represent data points of each group. The square refers to the mean value of the dataset for that group. 'p' refers to the statistical significance value. (n=8 corneas/box).

6.3.3.2. Biomechanical properties

The corneas showed nonlinear elastic behaviour. An example stress-strain curve is shown in Figure 6.14. The deformation (strain) of the treated corneas was more than the control group for the same stress. The slope of the stress-strain curves of the 4h-Amy30+CC2 group had decreased more than the slope of the curves in the control group.

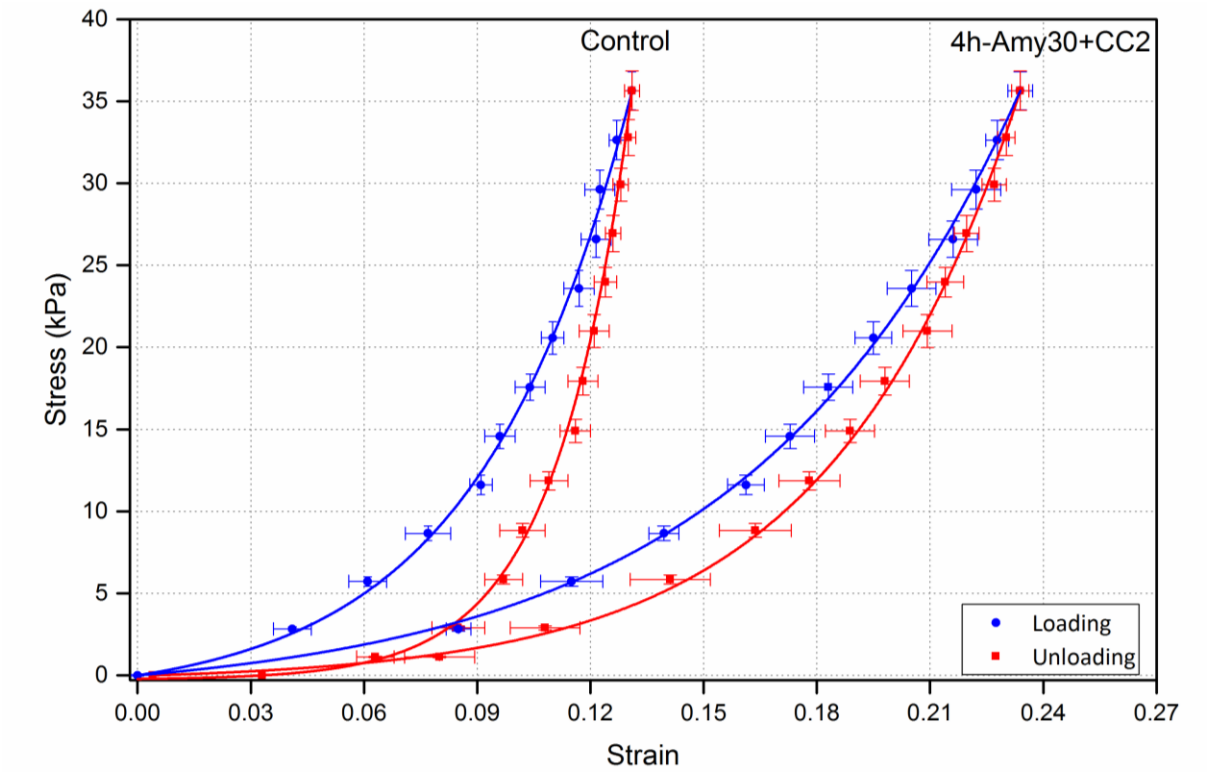

Figure 6.14: Stress-strain curves of the control and enzymatic treated corneas in loading and unloading phases obtained by inflation testing with LF-OCT. The left cycle was obtained from the control group. The right cycle was measured from corneas that were incubated in a solution containing amylase (30 mg/ml) and crude collagenase (2 mg/ml) for 4 hours. Error bars represent standard deviations. n= 8 corneas each group. The use of inflation testing with LF-OCT technique that used to determine the stress-strain curves of corneas was explained in Chapter 4.

The tangential elastic modulus (E_t) was reduced following incubation of the corneas in varying concentrations of amylase and collagenase. Figure 6.15 shows E_t of corneas that were incubated in varying treatment solutions of amylase and collagenase for 4 hours. E_t of the control group was 204.59±12.52 kPa. Following incubation of the corneas for 4 hours in amylase solution (10 mg/ml), E_t of 4h-Amy10 group had decreased by 6.6% relative to the control group, however, the reduction was not statistically significant, $p=0.0861$. E_t of the treated corneas had significantly reduced with increased concentration of enzymes in the treatment solutions. In 4h-CC1 group, E_t reduced by 30.5% relative to the control group when crude collagenase (1 mg/ml) was used to treat the corneas for 4 hours. For the same incubation time, the reduction in E_t was increased by 44.4% relative to the control group when the concentration of the crude collagenase increased to 2 mg/ml in the treatment solution. The maximum reduction in E_t was found in 4h-Amy30+CC2 group. It had significantly decreased by approximately 62.7% relative to the control group ($p<0.0001$).

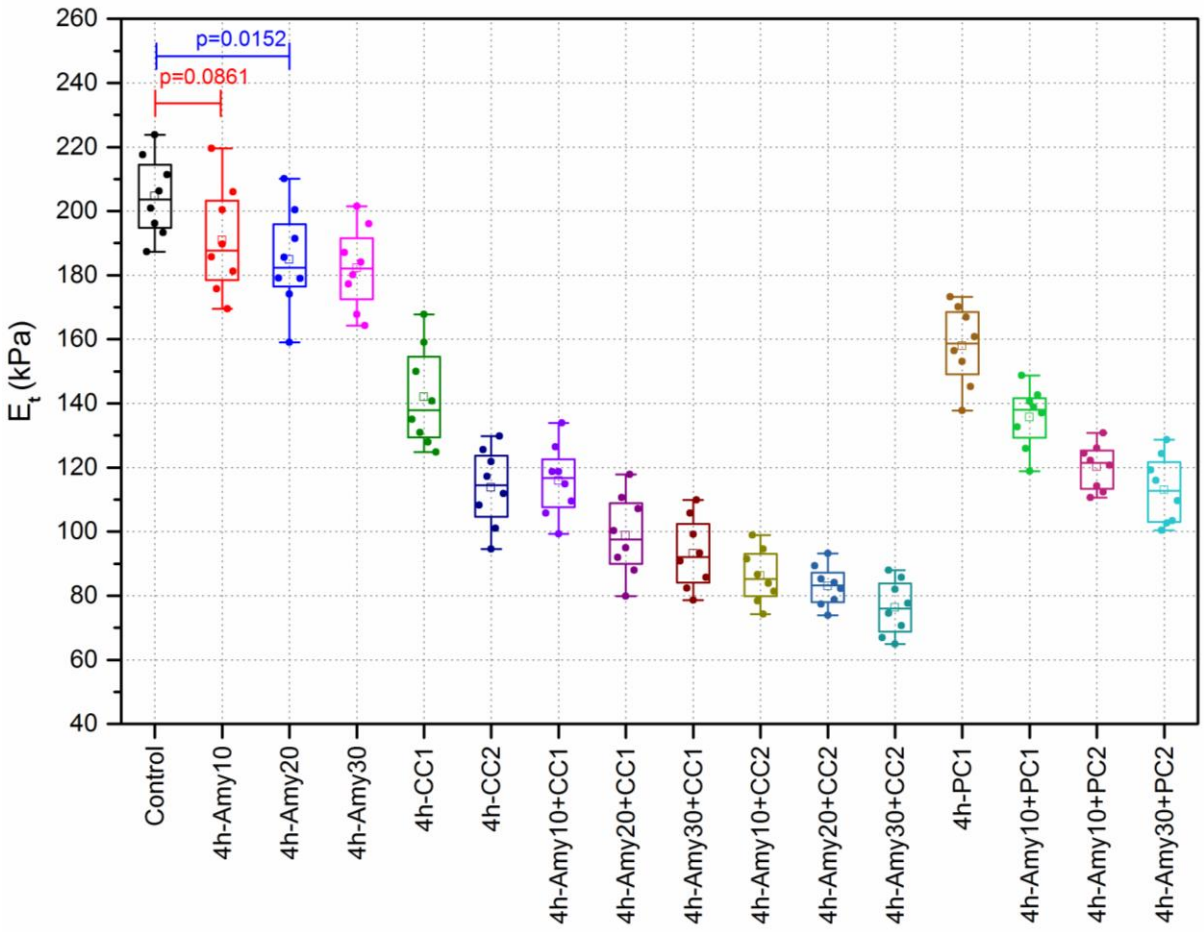

Figure 6.15: Tangential elastic modulus (E_t) of corneas that were incubated in varying amylase and collagenase solutions for 4 hours. Corneas were inflated at 15 mmHg. Data were represented as box plots and data overlaid with lower and upper borders of the box to represent the lower and upper quartiles, and the middle horizontal line to represent the median. The upper and lower whiskers represent 5th and 95th percentile of the data. The solid points represent data points of each group. The square refers to the mean value of the dataset for that group. 'p' refers to the statistical significance value. (n=8 corneas/box).

The tangential elastic modulus of the control and treated corneas obtained from inflation testing showed a very high consistency in the trends observed with oscillatory nanoindentation, Figure 6.16 (A). For example, E_t of the control group varied from 187.32 to 223.84 kPa, whilst E of the same corneas ranged from 204.4 to 281.18 kPa when they were measured by oscillatory nanoindentation. A significant statistical difference and a positive correlation relationship were found between the elastic modulus of the control corneas obtained by the two methods (y=0.46 x+94.7, Pearson's correlation coefficient=0.988, p=0.0051). A positive correlation relationship was also detected between E_t and E of the treated corneas (Pearson's correlation coefficient > 0.818, p>0.01). An example of the comparison between elastic modulus of treated corneas with the two techniques is shown in Figure 6.16(B).

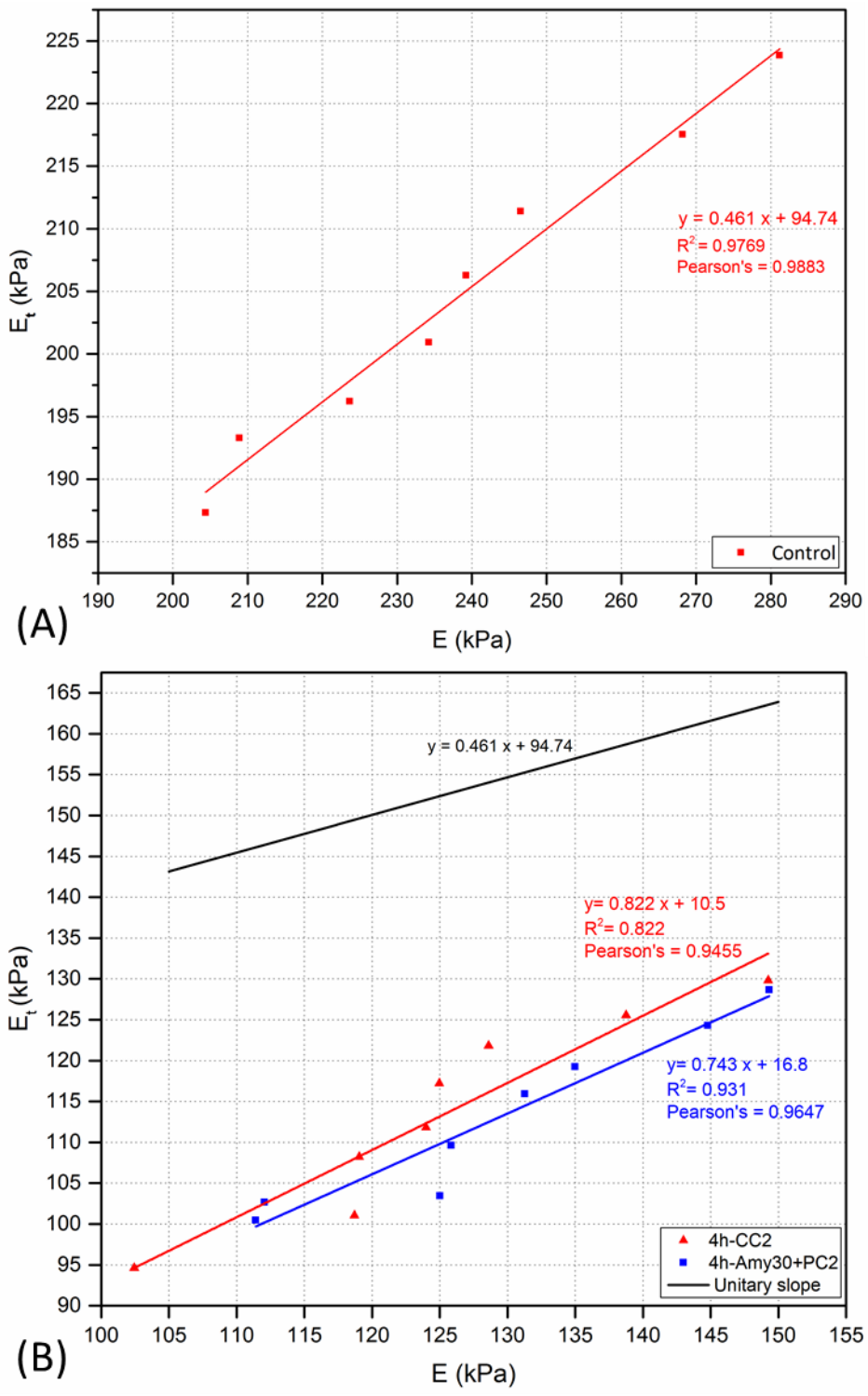

Figure 6.16: Comparison of the elastic modulus of corneas obtained by the inflation test and the oscillatory nanoindentation. (A) Control group and (B) treated corneas. E_t refers to tangential elastic modulus obtained by the inflation test. E represents elastic modulus acquired by the oscillatory nanoindentation. The least squares regression equation is shown on the plots. R^2 is the coefficient of determination. Unitary slope was extended from the control group to show the discrepancies with treated groups in the graphs.

Corneal hysteresis (CH) of the treated groups was decreased following the enzymatic treatment, shown in Figure 6.17. However, in some groups, the reduction was not statistically significant in many groups where the amylase (10, 20 and 30 mg/ml) was only used for the treatment ($p>0.1492$). The addition of collagenase (crude and purified) to treatment solutions caused significant reduction in CH of the treated corneas. CH of the control group was 1.457±0.06 kPa (10.97±0.46 mmHg). The maximum reduction in CH was found in 4h-Amy30+CC2 group. It had significantly decreased by approximately 35.5% relative to the control group ($p<0.0001$).

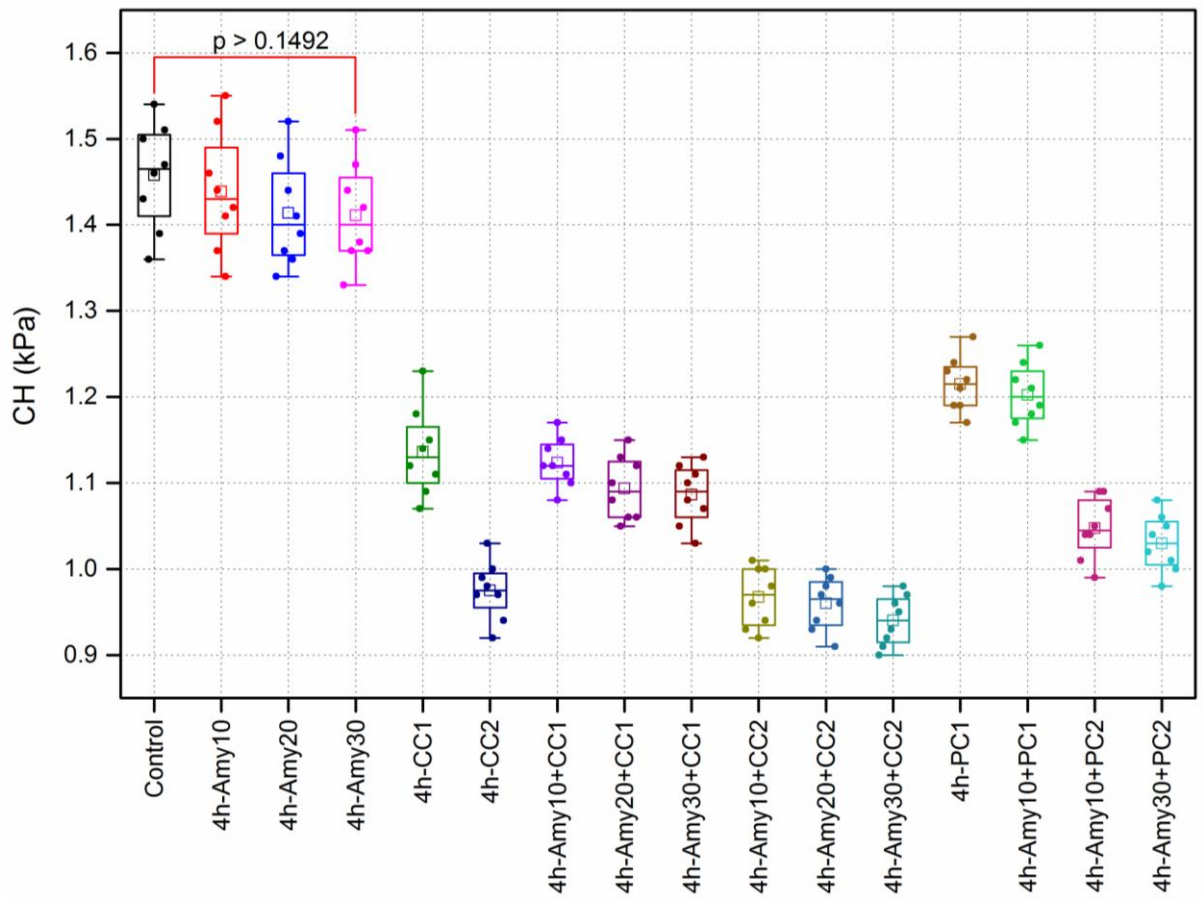

Figure 6.17: Corneal hysteresis (CH) of corneas that were incubated in varying amylase and collagenase solutions for 4 hours. Corneas were inflated at 15 mmHg. Data were represented as box plots and data overlaid with lower and upper borders of the box to represent the lower and upper quartiles, and the middle horizontal line to represent the median. The upper and lower whiskers represent 5th and 95th percentile of the data. The solid points represent data points of each group. The square refers to the mean value of the dataset for that group. 'p' refers to the statistical significance value. (n=8 corneas/box).

6.4. Discussion

This chapter aimed to assess the biomechanical and optical properties of porcine corneas following enzymatic degradation. In addition, the study aimed to determine how different concentrations of

the degradation enzymes (amylase and collagenase) and incubation time affect biomechanical and optical properties of porcine corneas.

Two studies have previously examined the effect of amylase (Spoerl *et al*, 2012; Wollensak *et al*, 2011) on the biomechanical stiffness of corneal strips using an extensometer. In these two studies, the corneas were dissected and mechanically tested using an extensometer where the corneas were cut in destructive way for the experiments. In addition, it was not clear how the amylase activity of the treated corneas was controlled after the incubation. In contrast, the current study used more precise techniques, in which the corneas were measured in a manner similar to *in-vivo* conditions, where no distraction in the collagen network of the corneas took place. To the best of the author's knowledge, no previous studies have assessed biomechanical and optical properties of corneas following collagenase (crude or purified) digestion.

Corneal hydration is an important factor that affects the calculations of biomechanical and optical properties, as explained in Chapters 3-5. Therefore, treated corneas were tested directly after the enzymatic treatment. The results of the treated corneas from the three methods are discussed in the following sections.

6.4.1. Microscale viscoelastic properties: Oscillatory nanoindentation

The results indicate that corneal stiffness was decreased following incubation of the corneas in aqueous solutions containing degradation enzymes (amylase and collagenase). This finding is in general agreement with those obtained previously by studies that have utilised different methods for the study of collagen degradation of tissues. The reduction in elastic modulus following incubation of collagenous tissues in amylase has been reported for a number of collagen-rich tissues, such as corneas (Spoerl *et al*, 2012; Wollensak *et al*, 2011), periodontal ligament of the rat molar (Watanabe and Komatsu, 2009), and the temporomandibular joint disc (Tanaka *et al*, 2003). The collagenolytic activity of bacterial collagenase has been previously proven in several studies to lead to a reduction in tissue stiffness (Gaul *et al*, 2018; Huang and Yannas, 1977). Thus, it has been utilised for tissue modelling and treatment for a number of different diseases (Shekhter *et al*, 2017).

The results presented in this chapter showed that the viscoelastic properties (G′ and G") of the treated corneas decreased with increasing concentration of degradation enzymes. This trend was also found by Tanaka *et al* (2003), where the viscoelastic properties of the disc of the temporomandibular joint significantly decreased with increasing concentration of amylase. It was

also reported by Huang and Yannas (1997) that increasing the concentration of collagenase significantly decreased the stiffness of insoluble collagen fibres immersed in a solution of purified collagenase. In addition, the results found that the viscoelastic properties (G′ and G") were decreased when increasing the incubation time. This trend is also consistent with a study conducted by Jayes *et al* (2016) that showed that the stiffness of uterine fibroid tissues incubated with purified collagenase decreased with increased incubation times. Hayes and Bodine (1978) also reported that viscoelastic shear moduli (G′ and G") of bovine articular cartilage decreased following incubation in crude collagenase solution; and the reduction increased with increasing incubation time from one to four days.

The current study shows that collagenase effectiveness in reduction of the viscoelastic properties (G′ and G") of the treated corneas was higher than that with amylase. In addition, amylase treated corneas did not show a significant difference in G" with reference to control corneas. The reason could be related to the differences between the amylase and collagenase activity in degradation sites on ECM. It was reported that amylase can release proteoglycans from collagenous tissues, such as cartilage, following incubation with α-amylase (0.3 mg/ml) for 7 hours at 38°C (Quintarelli *et al*, 1969). That depletion of proteoglycans affects the cross-links between the collagen fibrils that weakens the stiffness of the collagenous structure (Spoerl *et al*, 1998), which is in agreement with the results of this study, for the groups that were incubated with amylase. There is no evidence in the literature, to the author's knowledge, that amylase affects collagen fibrils. Collagenase, on the other hand, digests collagen fibrils of the tissue (Cronlund and Woychik, 1987), exhibits moderate to extreme reduction in the stiffness of collagenous tissues and results in a reduction of tissue shear viscoelastic properties (Hayes and Bodine, 1978).

In this study, it was found that crude collagenase demonstrated higher specific activities and more reduction in the tissue stiffness than that of the more costly purified collagenase. This outcome is comparable with Gaul *et al* (2018) who found that arterial samples incubated with crude collagenase exhibited more deformation than those incubated with purified collagenase. This strong reduction can be attributed to contamination of the crude collagenase with other proteolytic enzymes such as clostripain, which is a proteinase that cleaves proteins (Hanoune *et al*, 1977).

The loss factor, or tan(δ), (G"/G′) of the treated corneas significantly decreased following incubation with crude collagenase, and no significant difference was detected following incubation

with amylase and purified collagenase. In other words, incubation of the corneas with crude collagenase increased the dominance of the elastic properties to the viscous properties. This refers to the energy that is stored (storage modulus G′) in the treated corneas being higher than the energy that is dissipated (loss modulus G"), meaning that damping of the treated corneas decreased. Similar outcomes were reported in the literature (Hayes and Bodine, 1978; Tanaka *et al*, 2003). Tanaka and colleagues found that tan(δ) of the temporomandibular joint disc samples incubated with an α-amylase solution decreased with an increase of the enzyme concentration in the solution. They attributed the reduction in the loss factor to reduction of water quantity due to amylotic depletion of proteoglycans. Thus, the reduction of water quantity in the treated corneas made them more elastic-solid than the control corneas, which was evident in the results.

Hayes and Bodine (1978) found that tan(δ) of bovine articular cartilage significantly decreased following incubation of the samples with crude collagenase and related this to the enzymatic cleavage of macromolecules. Since the significant reduction in tan(δ) of the treated corneas was only in the groups where the crude collagenase was used, it can be hypothesised that the significant reduction in tan(δ) of corneas incubated in crude collagenase was not caused by collagenase alone, but also by other digestive enzymes that were in the treatment solution. Therefore, purified collagenase would be more suitable for reducing the stiffness of corneas without effecting the viscous to elastic ratio. Interestingly, purified collagenase (*Clostridium histolyticum*) is approved for local injection into the shortened, abnormal fibrous tendons of the hand in Dupuytren's contracture (Jayes *et al*, 2016).

6.4.2. Corneal transparency: Spectrophotometry

In this chapter, it was found that corneal transparency of corneas decreased following incubation with TC for 4 hours, which was also detailed in Chapter 5. Therefore, the comparison took place between the enzymatic treated corneas and the 4h-TC group to detect the effect of the enzymes on corneal transparency. Histologically, corneas including keratocytes and fibroblasts are not expected to die in such media. The reduction in corneal transparency of 4h-TC group is likely to have been caused due to changes in the extracellular matrix of the stroma, especially, the interfibrillar spacing. Since TC decreases corneal thickness and limits corneal swelling, the volumetric density of the tissue is expected to increase that leads to decrease light transmission through the corneas. The relation between the volumetric density of the collagen fibril and %T was explained in Chapter 5.

Percentage transmission was increased following the incubation of corneas in amylase and collagenase (crude and purified) solutions for 4 hours. This finding is consistent with outcomes reported by (Spoerl *et al*, 2012; Wollensak *et al*, 2011). Wollensak and colleagues (2011) found that corneal strips treated with amylase appeared more transparent than the untreated control group. They attributed this to the amylotic digestion of proteoglycans in the treated corneal strips. Presence of collagenase in the treatment solution increased corneal transparency, which is mainly attributed to a reduction of corneal thickness and reduction of collagen fibrils density. According to Equation 6.1, the reduction in corneal thickness could lead to increase in %T.

It was found that purified collagenase increases corneal transparency more than crude collagenase. It is known that purified collagenase digests the collagen fibrils, whilst crude collagenase is contaminated with other digestive enzymes that digest collagen fibrils and other components of the ECM (Hanoune *et al*, 1977). It is likely, therefore that crude collagenase strongly affected the regular arrangement of the collagenous structure of the cornea. It was also reported that collagen fibrils of arterial sections digested by crude collagenase appeared with more crimps than those digested by purified collagenase (Gaul *et al*, 2018). In that work, Gaul *et al* showed that the collagenous structure of the arterial sections of samples digested by purified collagenase was intact with no crimps. Unlike the samples that were digested with crude collagenase. Their findings corroborate the results in this work that show corneal transparency is higher in corneas that were incubated with purified collagenase than those incubated with crude collagenase.

The enhancement of corneal transparency requires some further discussion. First, it is possible that the regular arrangement of collagen fibrils of the treated corneas was not affected following enzymatic degradation. However, it was experimentally observed that amylase (Zhoula, 2018) and collagenase (Chapter 7) slightly affect the arrangement of collagen fibrils, which in turn would decrease corneal transparency according to transparency theories (explained in Chapter 2). Therefore, it seems there were other factors that caused enhancement in corneal transparency, but the arrangement of collagen fibrils was not one of them. Second, it is possible that corneal transparency was enhanced following enzymatic treatment due to reduction in collagen fibril diameters and increase in interfibrillar spacing, where both parameters can affect light transmission (explained in Chapter 5). It was found that collagen fibril diameters in the sclera were decreased, and splitting up between fibrils were increased, following incubation with amylase (Zhuola, 2018) and collagenase (shown in Chapter 7). These changes led to a decrease in fibril density that in turn enhanced light transmission through the treated corneas according to Equations 5.5 and 5.6

(Chapter 5). The fourth factor that may have enhanced corneal transparency of treated corneas was the reduction of corneal thickness following enzymatic treatment. It was explained previously that a reduction in corneal thickness can increase light transmission according to Beer- Lambert law (Equation 5.5, Chapter 5). Finally, enzymatic treatment of the corneas with amylase and collagenase is very likely to cause damages to fibroblasts and keratocytes. Corneal transparency seems to be increased by this possible phenomenon because keratocytes and fibroblasts are known to have a minor effect on light propagation; they are responsible for backscattering (explained in Chapters 2 and 5). Since this backscattering was decreased due to elimination of the keratocytes and fibroblasts following the enzymatic treatment, especially collagenase, this could also be a reason why the light transmission through the corneas increased.

6.4.3. Corneal thickness and biomechanical properties: LF-OCT

The use of LF-OCT helped obtain detailed cross-sectional images of the treated corneas during the inflation testing. The corneas were monitored in real-time and high resolution, which made tracking the geometrical changes (CCT and R) of the treated corneas easier than using other equipment. The main advantage of the LF-OCT system was the flexible ability to select suitable axial resolution and image depth. This property was important for monitoring the treated corneas, characterised by a steeper dome shape than in the control groups. The long image depth (>10 mm) was suitable for capturing the whole cornea with clear boundaries. Commercial OCT systems can scan high axial resolution images for the cornea. However, the maximum image depth is limited (Fercher, 2010). Thus, commercial OCTs would not be a suitable choice to scan the apex displacement of the treated corneas during the inflation. An example of a developed OCT systems that was able to scan long image depth, 12 mm, with high axial resolution has been reported by (Shao *et al*, 2018).

6.4.3.1. Corneal thickness

CCT decreased following the enzymatic treatment of the corneas for all groups. CCT reduction following incubation of corneal samples in amylase was previously reported (Wollensak *et al*, 2011). Wollensak and co-workers incubated corneal samples of a 400 μm thickness with amylase and found that the thickness of amylase-treated samples decreased by approximately 6.5% relative to the control group. They attributed the reduction in thickness of the enzymatic treated samples to the depletion of proteoglycans. In this study, the dimethylmethylene blue assay (DMMB) was used to prove the depletion of proteoglycans from the corneal samples following incubation with amylase (Appendix VII). The results obtained from the DMMB assay proved the presence of

GAGs in the solution where corneal samples were incubated with amylase. GAGs are unbranched chains of polysaccharides made up of repeat units of sulphated disaccharides, which are linked to proteoglycans.

OCT images revealed that the treated corneas were thinner in the collagenase-treated groups compared with the amylase-treated groups after equal incubation time. This may mean that the collagenolytic activity is stronger than amylotic activity. To the best of the author's knowledge, CCT of corneas following incubation in collagenase has not been reported in the literature. By analogy, however, collagenase digests collagen fibrils that leads to reduction in their density, which in turn leads to a reduction in the thickness of the whole tissue. Spoerl *et al*, (2004) evaluated the influence of the crosslinking treatment on the resistance of the cornea against enzymatic degradation with pepsin, trypsin and collagenase solutions. They treated porcine corneas with the photosensitiser riboflavin and used UVA-irradiation for corneal crosslinking. Subsequently, the cross-linked and control corneas were incubated with the digestive enzymes. They assessed the changes in the diameter and histology of corneal buttons before and after enzymatic incubation. They found that the control corneas were digested and reductions in cross-sectional diameter occurred faster than the cross-linked corneas.

6.4.3.2. Biomechanical properties

The results showed non-linear stress-strain relationships of both control and treated corneas. Amylase-treated corneas showed more elastic deformation than the control-untreated corneas. A similar trend was reported by Spoerl *et al* (2012), where amylase treated corneas showed bigger strain deformations than the control corneas for the same stress. A similar trend was found in keratoconic corneas when compared to healthy eyes. Andreassen *et al*, (1980) used uniaxial tensile testing to determine the stress-strain relationship between normal and keratoconic corneas and found that the keratoconus group showed more deformation than in the normal group.

In this study, a fixed loading-unloading rate was chosen to characterise the biomechanical properties of the treated corneas. It is expected that the higher loading rate exhibits larger elastic modulus and corneal hysteresis values, due to the inability of the liquid in the cornea to be rapidly repelled from the loaded region. This leads to the cornea showing an extra resistant force in response to the loading, which increases the measured elastic modulus (Boyce *et al*, 2008).

The tangential elastic modulus (E_t) of the treated corneas decreased following enzymatic incubation of corneas. To the best of the author's knowledge, the elastic modulus of enzymatic treated corneas based on inflation tests has not been reported in the literature. Within this study, E_t from inflation testing was found to be in agreement with the elastic modulus (E) obtained by oscillatory nanoindentation. E_t of the control and treated corneas from the inflation test (using LF-OCT) were significantly correlated with that from oscillatory nanoindentation testing, validating the measured elastic modulus from both methods.

E_t determined from the inflation tests, was significantly smaller than that from the oscillatory nanoindentation test. This can be attributed to the difference between the testing scales, where E_t reflects the bulk elastic response of the corneas in the tangential direction, whilst the localised E measures the elastic response of microscale structures of the cornea. It has been reported that differences in testing scales from macro- to the micro- scale leads to an increase in Young's modulus of the same tissue, which can be attributed to the tissue components being probed at each length scale (Akhtar *et al*, 2011; Crichton *et al*, 2013).

In this study, CH was assessed to reflect the viscoelastic response of the treated corneas. There is a growing interest in assessing CH of the corneas. CH is an assessment of the cornea's ability to absorb and dissipate energy, which was commonly observed through biomechanical tests. CH reflects the viscoelastic behaviour of the corneas, where it is a loading rate-dependent parameter and can be used to characterise the change of biomechanical properties in various diseases or for treatment assessment such as in keratoconus (Boyce *et al*, 2008). It has been reported that CH is associated with glaucoma and its progression (Deol *et al*, 2015) decreases in keratoconus (Shah *et al*, 2007), and increases in cross-linked corneas (Kling *et al*, 2010).

The results presented in this chapter showed that CH of the treated corneas decreased following enzymatic treatment. No previous studies have reported corneal hysteresis of enzymatically-degraded corneas. A similar trend of reduction in G", from earlier results, could be correlated to a reduction of CH following enzymatic treatment. In Chapter 4, the results showed that hydration increases CCT and CH. By analogy, CH reduction in the treated corneas likely indicates a reduced water content in ECM, which is possibly the reason for a decrease in measured G" also. This is hypothesised due to the observed reduction of proteoglycan in the enzymatic treated corneas, where proteoglycans are also responsible for the water content in ECM of the corneal stroma. In particular, the sulfate groups of proteoglycans chains (chondroitin/dermatan sulfate) bind water

and the keratan sulfate acts as a reservoir for hydration (Massoudi *et al*, 2016; Meek and Knupp, 2015).

6.5. Limitations

In this study, the active units of the amylase and collagenase per the mass of tissue were not precisely known as the manufacturer specification provides a large range for these values. That also led to the assumption that there is no significant difference between the mass of the corneas before the enzymatic treatment. The Poisson's ratio and group refractive index of the control and treated corneas were assumed to be fixed, whereas they are expected to change in the treated corneas following the incubation with the digestion enzymes.

6.6. Conclusions

In this chapter, oscillatory nanoindentation, spectrophotometry, and inflation test using LF-OCT were utilised to investigate biomechanical properties and corneal transparency of porcine corneas that were incubated in amylase and collagenase. Amylase and collagenase (crude and purified) reduce corneal stiffness, its ability to absorb and dissipate energy, and also its thickness. Interestingly, the enzymatic treatment of the corneas causes an increase in corneal transparency. Purified collagenase is more suitable for stiffness reduction and transparency of the treated corneas than crude collagenase, raising suggestions for further investigation of the ultrastructure of the corneas. Increase in the concentration of the digestive enzymes and incubation time significantly reduces viscoelastic properties of the treated corneas, where the higher the concentration of enzymes (or more incubation time), the more reduction in viscoelastic properties is expected. This enzymatic treatment of the corneas has potential to be utilised to obtain an animal model of keratoconic corneas with different progression levels. It is possible that the reduction in viscoelastic properties of the cornea might contribute to the pathogenesis of keratoconus; therefore, keratoconus progression might be stopped if the amount of amylase in the tear fluid and the activity of collagenase in the cornea are controlled.

6.7. References

Aghamohammadzadeh, H., Newton, R., Meek, K., 2004. X-ray scattering used to map the preferred collagen orientation in the human cornea and limbus. Structure 12, 249-256.

Akhtar, R., Sherratt, M.J., Cruickshank, J.K., Derby, B., 2011. Characterizing the elastic properties of tissues. Materials Today 14, 96-105.

Andreassen, T., Simonsen, A., Oxlund, H., 1980. Biomechanical properties of keratoconus and normal corneas. Experimental Eye Research 31, 435-441.

Balasubramanian, S., Pye, D., Willcox, M., 2010. Are proteinases the reason for keratoconus? Current Eye Research 35, 185-191.

Bond, M.D., Van Wart, H.E., 1984. Characterization of the individual collagenases from Clostridium histolyticum. Biochemistry 23(13), 3085-3091.

Boyce, B., Grazier, M., Jones, R., Nguyen, T., 2008. Full-field deformation of bovine cornea under constrained inflation conditions. Biomaterials 29, 3896-3904.

Collier, S., Madigan, M., Penfold, P., 2000. Expression of membrane-type 1 matrix metalloproteinase (MT1-MMP) and MMP-2 in normal and keratoconus corneas. Current Eye Research 21, 662-668.

Collier, S.A., 2001. Is the corneal degradation in keratoconus caused by matrix-metalloproteinases? Clinical & Experimental Ophthalmology 29, 340-4.

Crichton, M., Chen, X., Huang, H., Kendall, M., 2013. Elastic modulus and viscoelastic properties of full thickness skin characterised at micro scales. Biomaterials 34, 2087-2097.

Cronlund, A.L., Woychik, J.H., 1987. Solubilization of collagen in restructured beef with collagenases and α-amylase. Journal of Food Science 52, 857-860.

DelMonte, D., Kim, T., 2011. Anatomy and physiology of the cornea. Journal of Cataract & Refractive Surgery 37, 588-598.

Deol, M., Taylor, D., Radcliffe, N., 2015. Corneal hysteresis and its relevance to glaucoma. Current Opinion in Ophthalmology 26, 96-102.

Durmus, A., Han, M., Yaman, I., 2009. Comperative evaluation of collagenase and silver sulfadiazine on burned wound healing in rats. Firat Universitesi Saglik Bilimleri Veteriner Dergisi 23, 135-139.

Fercher, A.F., 2010. Optical coherence tomography-development, principles, applications. Zeitschrift für Medizinische Physik 20(4), 251-276.

Gaul, R.T., Nolan, D.R., Ristori, T., Bouten, C.V.C., Loerakker, S., Lally, C., 2018. Strain mediated Enzymatic Degradation of arterial tissue: Insights into the role of the non-collagenous tissue matrix and collagen crimp. Acta Biomaterialia 77, p.301-310.

Hanoune, J., Stengel, D., Lacombe, M.L., Feldmann, G., Coudrier, E., 1977. Proteolytic activation of rat liver adenylate cyclase by a contaminant of crude collagenase from Clostridium histolyticum. Journal of Biological Chemistry 252, 2039-45.

Hayes, S., Boote, C., Lewis, J., Sheppard, J., Abahussin, M., Quantock, A., Purslow, C., Votruba, M., Meek, K., 2007. Comparative study of fibrillar collagen arrangement in the corneas of primates and other mammals. The Anatomical Record: Advances in Integrative Anatomy and Evolutionary Biology 290, 1542-1550.

Hayes, W.C., Bodine, A.J., 1978. Flow-independent viscoelastic properties of articular cartilage matrix. Journal of Biomechanics 11, 407-419.

Honig, S.C., 2014. Intralesional collagenase in the treatment of Peyronie's disease. Therapeutic Advances in Urology 6(2), 47-53.

Huang, C., Yannas, I.V., 1977. Mechanochemical studies of enzymatic degradation of insoluble collagen fibers. Journal of Biomedical Materials Research 11(1), 137-54.

Hurst, L.C., Badalamente, M.A., Hentz, V.R., Hotchkiss, R.N., Kaplan, F.T., Meals, R.A., Smith, T.M., Rodzvilla, J., 2009. Injectable collagenase clostridium histolyticum for Dupuytren's contracture. New England Journal of Medicine 361, 968-79.

Jayes, F., Liu, B., Moutos, F., Kuchibhatla, M., Guilak, F., Leppert, P., 2016. Loss of stiffness in collagen-rich uterine fibroids after digestion with purified collagenase Clostridium histolyticum. American Journal of Obstetrics and Gynecology 215, 596.e1-596.e8.

Kaiserman I., Sella S., 2019. Chronic ocular inflammation and keratoconus. In: Barbara A. (eds) Controversies in the Management of Keratoconus (pp. 17-27). Springer, Cham. USA

Kao, W.W., Vergnes, J.P., Ebert, J., Sundar-Raj, C.V., Brown, S.I., 1982. Increased collagenase and gelatinase activities in keratoconus. Biochemical and Biophysical Research Communications 107, 929-36.

Kling, S., Remon, L., Pérez-Escudero, A., Merayo-Lloves, J., Marcos, S., 2010. Corneal biomechanical changes after collagen cross-Linking from porcine eye inflation experiments. Investigative Ophthalmology & Visual Science 51, 3961-3968.

Legkikh, L., Koledintsev, M., Semenova, A., Okuyama, K., 2017. Biochemical investigations of lacrima in early diagnosis of keratoconus. (Abstract) Sangubashi Eye Clinic, Japan. [available on: www.sangubashi.com/English/report/syanhai.htm] (accessed on:12th January 2020).

Lema, I., Durán, J., Ruiz, C., Díez-Feijoo, E., Acera, A., Merayo, J., 2008. Inflammatory response to contact lenses in patients with keratoconus compared with myopic subjects. Cornea 27, 758-763.

Mackiewicz, Z., Määttä, M., Stenman, M., Konttinen, L., Tervo, T., Konttinen, Y., 2006. Collagenolytic proteinases in keratoconus. Cornea 25, 603-610.

Massoudi, D., Malecaze, F., Galiacy, S., 2016. Collagens and proteoglycans of the cornea: importance in transparency and visual disorders. Cell and Tissue Research 363, 337-349.

Meek, K.M., Knupp, C., 2015. Corneal structure and transparency. Progress in Retinal and Eye Research 49, 1-16.

Mylius, E.A., 1961. Amylase in tears? A histochemical study. Acta pathologica et microbiologica Scandinavica 148, 143-147.

Pannebaker, C., Chandler, H.L., Nichols, J.J., 2010. Tear proteomics in keratoconus. Molecular Vision 16, 1949-57.

Quintarelli, G., Dellovo, M.C., Balduini, C., Castellani, A.A., 1969. The effects of alpha amylase on collagen-proteoglycans and collagen-glycoprotein complexes in connective tissue matrices. Histochemie 18, 373-375.

Romero-Jiménez, M., Santodomingo-Rubido, J., Wolffsohn, J., 2010. Keratoconus: A review. Contact Lens and Anterior Eye 33(4), 157-166.

Seppälä, H., Määttä, M., Rautia, M., Mackiewicz, Z., Tuisku, I., Tervo, T., Konttinen, Y., 2006. EMMPRIN and MMP-1 in keratoconus. Cornea 25, 325-330.

Sethi, C.S., Bailey, T.A., Luthert, P.J., Chong, N.H., 2000. Matrix metalloproteinase biology applied to vitreoretinal disorders. British Journal of Ophthalmology 84, 654-66.

Shah, S., Laiquzzaman, M., Bhojwani, R., Mantry, S., Cunliffe, I., 2007. Assessment of the biomechanical properties of the cornea with the ocular response analyzer in normal and keratoconic eyes. Investigative Ophthalmology & Visual Science 48, 3026-3031.

Shao, Y., Tao, A., Jiang, H., Shen, M., Zhu, D., Lu, F., Karp, C., Ye, Y., Wang, J., 2018. Long scan depth optical coherence tomography on imaging accommodation: impact of enhanced axial resolution, signal-to-noise ratio and speed. Eye and Vision 5(1), 16.

Shekhter, A., Balakireva, A., Kuznetsova, N., Vukolova, M., Litvitsky, P., Zamyatnin, A., 2017. Collagenolytic enzymes and their applications in biomedicine. Current Medicinal Chemistry 24.

Spoerl, E., Huhle, M., Seiler, T., 1998. Induction of cross-links in corneal tissue. Experimental Eye Research 66, 97-103.

Spoerl, E., Teral, N., Raiskup, F., Pillunat, L., 2012. Amylase reduces the biomechanical stiffness of the cornea. Investigative Ophthalmology & Visual Science 53(14), 1531-1531.

Spoerl, E., Wollensak, G., Seiler, T., 2004. Increased resistance of crosslinked cornea against enzymatic digestion. Current Eye Research 29, 35-40.

Tanaka, E., Aoyama, J., Tanaka, M., Van Eijden, T., Sugiyama, M., Hanaoka, K., Watanabe, M., Tanne, K., 2003. The proteoglycan contents of the temporomandibular joint disc influence its dynamic viscoelastic properties. Journal of Biomedical Materials Research 65, 386-92.

Vaalamo, M., Mattila, L., Johansson, N., Kariniemi, A.L., Karjalainen-Lindsberg, M.L., Kähäri, V.M., Saarialho-Kere, U., 1997. Distinct populations of stromal cells express collagenase-3 (MMP-13) and collagenase-1 (MMP-1) in chronic ulcers but not in normally healing wounds. Journal of Investigative Dermatology 109, 96-101.

Van Haeringen, N.J., Ensink, F., Glasius, E., 1975. Amylase in human tear fluid: Origin and characteristics, compared with salivary and urinary amylases. Experimental Eye Research 21, 395-403.

Volatier, T.L., Figueiredo, F.C, Connon, C.J., 2019. Keratoconus at a molecular level: A review. The Anatomical Record 1,1-5. [doi:10.1002/ar.24090].

Watanabe, Y., Komatsu, K., 2009. Biomechanical and morphological studies on the periodontal ligament of the rat molar after treatment with α-amylase *in vitro*. Connective Tissue Research 36, 35-49.

West-Mays, J., Dwivedi, D., 2006. The keratocyte: Corneal stromal cell with variable repair phenotypes. The International Journal of Biochemistry & Cell Biology 38, 1625-1631.

Wollensak, G., Spörl, E., Mazzotta, C., Kalinski, T, Sel, S., 2011. Interlamellar cohesion after corneal crosslinking using riboflavin and ultraviolet A light. British Journal of Ophthalmology 95, 876-880.

Zhou, L., Sawaguchi, S., Twining, S.S., Sugar, J., Feder, R.S., Yue, B.Y., 1998. Expression of degradative enzymes and protease inhibitors in corneas with keratoconus. Investigative Ophthalmology & Visual Science 39, 1117-24.

Zhuola, 2018. The role of proteoglycans in the ultrastructure and mechanical properties of the sclera. (PhD thesis), University of Liverpool, United Kingdom.

Chapter 7

Ultrastructural and nanomechanical changes of the cornea following enzymatic degradation

This chapter focusses on assessing the ultrastructural and nanomechanical changes of porcine corneas following enzymatic degradation with collagenase and amylase. Atomic force microscopy (AFM) was used to measure collagen fibril diameter and D-periodicity. Peak Force Quantitative Nanomechanical Mapping (PF-QNM) AFM mode was used to determine the elastic modulus of the corneal samples. The effects of enzymes on collagenous tissues are summarised in this chapter. This chapter focusses on the use of the AFM characterisation for ultrastructural and nanomechanical property measurement of corneas change following enzymatic treatment with different concentrations of amylase and collagenase. Treatment of the corneas and incubation time are illustrated. The obtained ultrastructural and nanomechanical details of the treated cornea samples are discussed and compared with other studies.

Abstract

Under physiological conditions, the cornea is exposed to various enzymes, some of them have digestive actions, such as amylase and collagenase. These digestive enzymes might change the ultrastructure (collagen morphology) of the cornea, which sequentially changes the mechanical response of the cornea and distort vision, such as in keratoconus. The aim of this study is to investigate the ultrastructure and nanomechanical properties of the porcine cornea following incubation with α-amylase and collagenase. Atomic force microscopy (AFM) was used to capture nanoscale topographical details (diameters and D-periodicity of collagen fibrils) of air-dried cryosectioned anterior stromal sections and calculate their elastic modulus. Samples were incubated with varying concentrations of α-amylase for 40 min or with collagenase (crude and purified) for 15 min at approximately 37.5°C. The results showed that the diameter and D-periodicity of control samples were 55.5±2.4 nm and 67.46±2.3 nm, respectively. Collagen fibril diameters were decreased following incubation with amylase, but not their D-periodicity. Elastic modulus of control samples was 2.27±0.15 GPa, which gradually decreased with enzyme concentration in amylase-treated samples. Elastic modulus, collagen fibril diameters and D-periodicity were greatly reduced in collagenase-treated samples. The effect of crude collagenase on corneal samples was more pronounced than purified collagenase, where significant deterioration was observed in samples that were incubated with high concentrations of crude collagenase. This enzymatic treatment may help in answering some questions related to keratoconus, and possibly be used to build an empirical animal model of keratoconic corneas with different progression levels.

7.1. Introduction

There is a need to investigate and develop a better understanding of corneal ultrastructure and biomechanics at the nano-level. Understanding corneal ultrastructure and its response to chemicals is important for a number of ocular disorders, such as keratoconus that is characterised by a significant deterioration in the collagenous network resulting in a cone-shape cornea.

The human cornea consists of five layers, in which the stroma represents about 90% of its thickness (Chapter 4). At the microscale, the stroma is composed of many lamellae that run in acute angles to each other in the anterior stroma and run parallel to each other in the middle and posterior stroma; all lamellae are parallel to the corneal surface. The thickness of each lamella is approximately 2 μm and mainly consists of type I collagen fibrils. These fibrils seem to be arranged with a high degree of lateral order and run in the same direction as their lamella. Collagen fibrils consist of a number of collagen molecules that are aligned together in staggered arrangement to form a banding pattern, which is called D-periodicity. Collagen fibrils have relatively uniform diameters of 32.5±1.5 nm and D-periodicity of 65 nm in human corneas (Meek, 2009; Meek and Knupp, 2015), which seems to be slightly higher in porcine corneas (Xia *et al*, 2014). Collagen fibrils of the stroma are associated with by proteoglycans that keep them aligned and give support to provide the overall shape and strength of the cornea. Proteoglycans contain chains of glycosaminoglycans (GAGs), which are polysaccharide molecules that attract water and are thought to provide the extracellular matrix with additional physical properties not provided by collagen fibrils alone (Zhang *et al*, 2009). To the best of the author's knowledge, no study has been conducted to visualise and investigate the ultrastructural topography (collagen fibril diameters, spacing, alignment and D-periodicity) of keratoconic corneas, which can be attributed to unavailability of the samples. Therefore, it is of great importance to visualise and investigate ultrastructural topography of collagenous structure in keratoconus, and possibly building an empirical model.

In terms of microscale mechanical properties of keratoconus, a recent study has assessed the micromechanical changes of collagen cross-linking on keratoconic corneas *in vitro* with minimal sample destruction (Beshtawi *et al*, 2015). Beshtawi and colleagues assumed the cornea had isotropic properties and utilised scanning acoustic microscopy (SAM) to measure the speed of sound across the stroma of six keratoconic corneal buttons to indicate the stiffness. They successfully found an increase in speed of sound between the cross-linked and control corneas, which makes their method promising for other *in vitro* applications.

The cornea is exposed to a number of enzymes that are either secreted by lacrimal gland or produced by the corneal cells, such as keratocytes. Some of these enzymes, such as amylase (Van Haeringen *et al*, 1975) and collagenase (Kaiserman and Sella, 2019) are believed to have digestive actions in the stromal layer of the corneas. It was also found that these enzymes cause a reduction in collagenous tissue stiffness; therefore, they may contribute somehow in progression of keratoconus (Galvis *et al*, 2015).

Alpha-amylase is an active enzyme in the tear fluid that has been suggested to increase in patients with keratoconus (Legkikh *et al*, 2018), where it was found that it can decrease corneal section stiffness (Spoerl *et al*, 2012). Previous studies used extensometers to examine the effect of alpha-amylase on corneal sections (Spoerl *et al*, 2012; Wollensak *et al*, 2011). They found that the elastic modulus of corneal strips (about 200 μm thick) decreases following incubation with alpha-amylase. These studies provided the basic information on the effect of the amylase on the cornea regardless of how the ultrastructural details will change following the incubation with the enzyme, which have not been investigated yet.

The other digestive enzyme in the cornea is collagenase, which attacks the peptide bonds of the triple helix region on collagen. It is found in epithelial and stromal cells and can be released into the stromal layer in response to traumas for biomechanical modulation of the collagenous network (Balasubramanian *et al*, 2010; Collier *et al*, 2000; Collier, 2001; Kaiserman and Sella, 2019), where it has been approved for the modelling of few collagenous tissues to reduce their stiffness such as in Dupuytren's contracture (Hurst *et al*, 2009). It was found to increase in patients with keratoconus (Collier *et al*, 2000; *et al*, 2015; Mackiewicz *et al*, 2006; Seppälä *et al*, 2006) due to reduction of its inhibitor (Romero-Jiménez *et al*, 2010; Volatier *et al*, 2019). However, no ultrastructural or nanomechanical investigation has been conducted to show its activity on corneal tissues.

The investigation of ultrastructural topography and biomechanical properties of the cornea requires a technique that is less destructive to the samples, such as the atomic force microscope (AFM). Other techniques such as scanning electron microscopy (SEM) and transmission electron microscopy (TEM) may provide ultrastructural details of the cornea but samples need to be sputter-coated and dried extensively, which may affect the realistic measurement of diameters and axial D-periodicity of collagen fibrils (Last *et al*, 2010) that were found to change with dehydration (Jastrzebska *et al*, 2016). Therefore, AFM has been selected to capture the *in vitro* ultrastructural

topography and nanomechanical properties without extensive dehydration and sputter-coating that lead to changes in ultrastructural details (Jastrzebska *et al*, 2016; Last *et al*, 2010; Xia *et al*, 2014).

The use of AFM in the investigation of corneal diseases can help in addressing many questions. Early AFM studies focused on the collagen fibrils characterisation in mammalian corneas (Fullwood *et al*, 1996). Other studies gave insights to determine the elastic properties of the corneal layers (Last *et al*, 2012; Lombardo *et al*, 2012) that may help in obtaining the basic knowledge for compression with unhealthy corneas. For example, AFM was used to analyse the photoablated stromal corneas in comparison to untreated samples (Lombardo *et al*, 2006). The study showed undulations and granule-like features on the ablated stromal surface when 193 nm excimer laser was used and confirmed the precision of laser surgery in removing submicrometric amounts of the stroma. AFM was also utilised to investigate the ultrastructural topography in stromal layer of human corneas following collagen cross-linking treatment with riboflavin and ultraviolate-A light (Choi *et al*, 2013). However, to date, no AFM study have examined ultrastructural changes in either keratoconic or enzymatic treated corneas.

7.2. Aim

This chapter utilises AFM to investigate of ultrastructural and nanomechanical changes following enzymatic incubation of sections of porcine corneal tissue with amylase and collagenase. In this study, the effect of varying concentrations of alpha-amylase and collagenases on ultrastructural topography of corneal tissue sections is examined by measuring collagen fibril diameter and D-periodicity. Nanoscale elastic maps of the corneal sections are presented to indicate tissue stiffness following incubation with varying concentrations of alpha-amylase and collagenases. Finally, the difference between crude collagenase and purified collagenase on corneal samples is considered.

7.3. Materials and methods

7.3.1. Sample preparation

Eighteen eyes of pigs aged from 5 to 6 months were obtained from a local abattoir shortly after slaughter. They were divided into three main groups (6 corneas each group); amylase-group, crude collagenase group, and purified collagenase group. Corneas were dissected immediately on arrival (within an hour from slaughter) at the University of Liverpool. Corneal samples were chosen from the apex (3 mm diameter) after desquamating the epithelial layer using a cotton-tipped applicator and tweezers. The preparation procedure included snap freezing and cryosectioning to make the corneal sample ready for AFM experiments.

After dissecting, the samples were carefully rinsed with Phosphate Buffered Saline (PBS) (Sigma-Aldrich, Dorset, UK). Afterwards, each sample was placed in a cryomold with an appropriate orientation and amount in the optimum cutting temperature resin (Tissue-Tek, CellPath, Powys, UK). The resin was added to hold the sample's place and orientation in the cryomold. Subsequently, the cryomolds were wrapped with aluminium foil to protect the corneal samples and the resin from direct contact with the freezing liquid. Wrapped cryomolds were then completely immersed in isopentane (2-methyl butane) for 2 min. The isopentane was frozen at -80°C using liquid nitrogen. After that, specimens were stored in -80°C freezer until cryosectioning.

Cryosectioning was performed by utilising a Leica cryostat (model CM1850, Leica Microsystems Ltd, UK) to section the frozen corneal samples. Depending on literature, AFM section thickness should be in range from 5 to 10 μm (Fischer *et al*, 2008); in this project, the AFM section thickness was 5 μm. In the amylase group (6 corneas), eleven sections of 5 μm thickness were taken from the first third of each cornea. The first third was defined as the anterior stromal layer of 150 μm after the epithelium. In the crude collagenase group (6 corneas), five sections of 5 μm thickness were taken from the first third of each cornea. A similar number of sections were prepared from the purified collagenase group. In all corneas, sections were taken after 20 μm from the anterior surface of the stroma. Sections were then stored in -80°C freezer until they were tested.

7.3.2. Enzymatic treatment

The cryosectioned tissue of amylase group (n=66) was treated with α-amylase (type Aspergillus oryzae, Sigma-Aldrich, Dorset, UK) for 40 min. Amylase was diluted in PBS to varying concentrations (0.2, 0.4, 0.6, 0.8, 1, 1.2, 1.4, 1.6, 1.8, and 2 mg/ml), see Table 7.1. The control sections in this group (n=6) were incubated in PBS only for the same period. One drop (40 ml) of amylase at 37.5°C was applied on the amylase treated group and kept at 37.5±1.1°C for 40 min. Afterwards, the corneal sections were washed with cold PBS (4°C) and left in air for 18 min in preparation for AFM testing. Samples of amylase group were incubated in amylase solution for 40 min.

The cryosectioned samples of the crude collagenase group (n= 30) were incubated with crude collagenase (type *Clostridium histolyticum*, Sigma-Aldrich, Dorset, UK) for 15 min at 37.4±1.8°C. The treated samples of this group (n=24) were incubated with one drop (40 ml) of crude collagenase (0.05, 0.1, 0.15, and 0.2 mg/ml) at 37.5°C that were diluted in PBS. Those samples were snap-washed firstly by a cold (4°C) aqueous solution of dichloromethylene diphosphonic

acid disodium (NaDTA) at a concentration of 1 mg/ml to inhibit the activity of the collagenase; and subsequently by PBS twice and tested after 18 min. The control samples of this group (n=6) were incubated in PBS for 15 min and snap-washed with NaDTA and PBS.

The cryosectioned samples of the purified collagenase group (n=30) were treated with varying concentrations of purified collagenase (type *Clostridium histolyticum*, Sigma-Aldrich, Dorset, UK) at 37.5°C (0.05, 0.1, and 0.15 mg/ml) for 15 min. Six samples served as controls, which were incubated in PBS only, for 15 min to investigate the effect of snap-washing the sections with cold (4°C) NaDTA. The treated samples (n=24) of this group were also snap-washed with cold NaDTA and PBS following the enzymatic incubation and tested after 18 min. Table 7.1 summarises these groups and treatment solutions.

Table 7.1: A summary of the groups and treatment parameters.

	Amylase group	Crude collagenase group	Purified collagenase group
No. of porcine eyes	6	6	6
No. of sections	66	30	30
Incubation time (min)	40	15	15
Enzyme concentrations (mg/ml)	0.2, 0.4, 0.6, 0.8, 1, 1.2, 1.4, 1.6, 1.8, and 2	0.05, 0.1, 0.15, and 0.2	0.05, 0.1, 0.15, and 0.2
Washing solution	PBS	NaDTA	NaDTA

PBS: Phosphate buffered saline solution; NaDTA: Dichloromethylenediphosphonic acid disodium solution.

7.3.3. AFM in air

A Bruker MultiMode 8 AFM with E-piezoelectric scanner (Bruker Nano Inc., Nano Surfaces Division, CA, USA) was utilised to investigate the topographical and elastic property changes of the cryosectioned samples following enzymatic treatment. Peak Force quantitative nanomechanical mapping (PF-QNM) mode in air was used, which is most suited for biological samples with structural heterogeneity (Dokukin and Sokolov, 2012; Pittenger *et al*, 2010). This mode is characterised by its ability to control the applied forces to the sample (or the peak force), which allows indentations to be limited to several nanometres that both maintains resolution and prevents sample damage. In addition, Peak Force QNM mode allows measurements at an extremely wide range of elastic moduli (1 MPa to 50 GPa) (Pittenger *et al*, 2010). This mode uses the Derjaguin-Muller-Toporov (DMT) model and a curve fitting process of the unloading portion of the force - separation curve, see Figure 7.1, to calculate elastic modulus (Pittenger *et al*, 2010).

This model uses the loading forces plus the adhesive forces between the tip and the surface of the sample (Dokukin & Sokolov, 2012). In PF-QNM mode, the cantilever is oscillated at a frequency of 1 to 4 kHz with peak-to-peak amplitudes of 100 - 300 nm. When the tip touches the sample surface, the applied force gradually increases to the peak force and the displacement is recorded. The tip then is withdrawn and the force decreases.

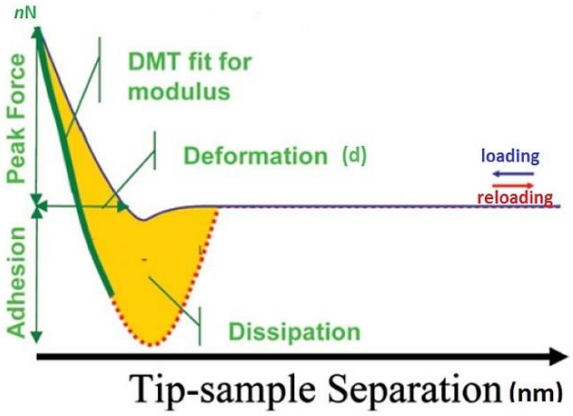

Figure 7.1: A schematic force-separation curve. The loading refers to the loading force on the tip, while the unloading curve refers to adhesion force. Deformation is the indentation depth into the sample. Dissipation represents energy dissipated in a cycle of interaction. The adhesion force can be any attractive force between the tip and sample (Pittenger *et al*, 2010).

According to this model, elastic modulus (Young's modulus) can be calculated using equation 7.1 (Young *et al*, 2011).

$$E = \frac{3\left(F_{tip} - F_{adh}\right)}{4\sqrt{R\,d^3}} \quad \ldots (7.1)$$

where E is reduced Young's modulus, F_{tip} is the applied force on the tip, F_{adh} is the adhesion force between the tip and the sample surface, R is the tip radius, and d is the deformation depth (indentation depth).

The AFM was uploaded with a silicon probe with a rectangular tip, type RTESPA-300 (Bruker Nano Inc., CA, USA). It was used due to its capabilities of capturing high resolution topographical images and its ability to measure a wide elastic modulus range of the samples being tested (200 MPa - 5000 MPa). The specifications and geometry of the probe are shown in Table 7.2.

Table 7.2: Cantilever and tip used in this study.

Cantilever schematic	Parameter	Details
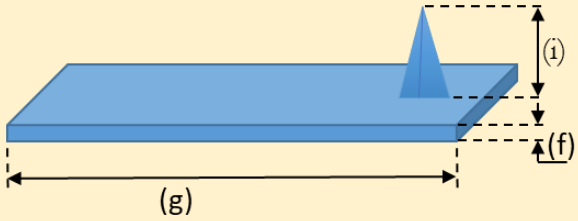	(a) Probe reference	RTESPA-300
	(b) Resonant frequency	~ 300 kHz
	(c) Spring constant	~ 40 N/m
	(d) Cantilever geometry	Rectangular
	(e) Cantilever material	0.01 - 0.025 Ωcm Antimony (n) doped Si
	(f) Cantilever thickness	3.4 µm
	(g) Cantilever length	125 µm
	(h) Cantilever back side coating	Reflective aluminium
	(i) Tip height	10 - 15 µm
	(j) Tip radius (Nom)	8 nm

Relative calibration of the AFM was performed before every test. The calibration procedure was used to define the parameters of the PF-QNM mode. These parameters were measured relative to a known reference sample, which was a Vishay Photostress PS1 Polymer (Vishay; Wendell, NC, USA). This reference sample had a known elastic modulus of 2.7±0.1 GPa, which was utilised to calibrate the AFM and estimate the tip radius. A direct method of thermal tuning was carried out to measure the spring constant of the cantilever. Finally, deflection sensitivity was calibrated to convert volts measured on the photodetector to nanometres of motion, which was performed by measuring a force curve on an "infinitely stiff" surface relative to the chosen cantilever. Therefore, a sapphire sample (Sapphire-12M; Bruker Nano Inc., Nano Surfaces Division, CA, USA) was utilised, by which the cantilever does not indent it during the force curve measurement. Further details on PF-QNM calibration are presented in Appendix V. The PF-QNM mode can be used to determine mechanical properties using a range of different models. In this study, the DMT model was used to generate elastic modulus maps (Pittenger *et al*, 2010). This channel was used to measure the elastic modulus of the scanned area. Further details on PF-QNM mode operation procedure are discussed in literature (Young *et al*, 2011).

With the use of the optical microscopy integrated with the AFM machine, AFM images of the cryosectioned corneas were captured on 3 different locations on each sample. These locations were chosen with the assistance of an integrated optical microscope. Topographical images were collected at 5x5 μm^2 and also 1x1 μm^2. The 1x1 µm images were suitable to visualise collagen fibrils in more detail. The peak force frequency and amplitude were set to 2 kHz and 150 nm. All images were scanned at a scan rate of 0.799 Hz. The 1x1 μm^2 images were captured in 256 horizontal lines, and each line was scanned at a resolution of 256 pixel/line. Whereas, the 5x5 μm^2 images were scanned in 512 horizontal lines, and each line was scanned at a resolution of 512 pixel/line. These setting were chosen following many trials to obtain good quality images with minimal

artefacts. In addition, these settings were recommended by the manufacturer for biological tissues for optimum results.

Topographical features of collagen fibrils, diameter and D-periodicity, were measured after processing the images using NanoScope Analysis 1.7 software (Bruker Nano Inc., Nano Surfaces Division, CA, USA). This software extracts the surface profiles of a selected collagen fibril by using 'section' tool. In this study, collagen fibrils that were straight, high contrast and at approximately zero inclination angle, manually selected from each height image to measure their diameter and D-periodicity. The collected values then were averaged for each image. Figure 7.2 demonstrates the surface profile analysis for collagen fibrils using the NanoScope Analysis software.

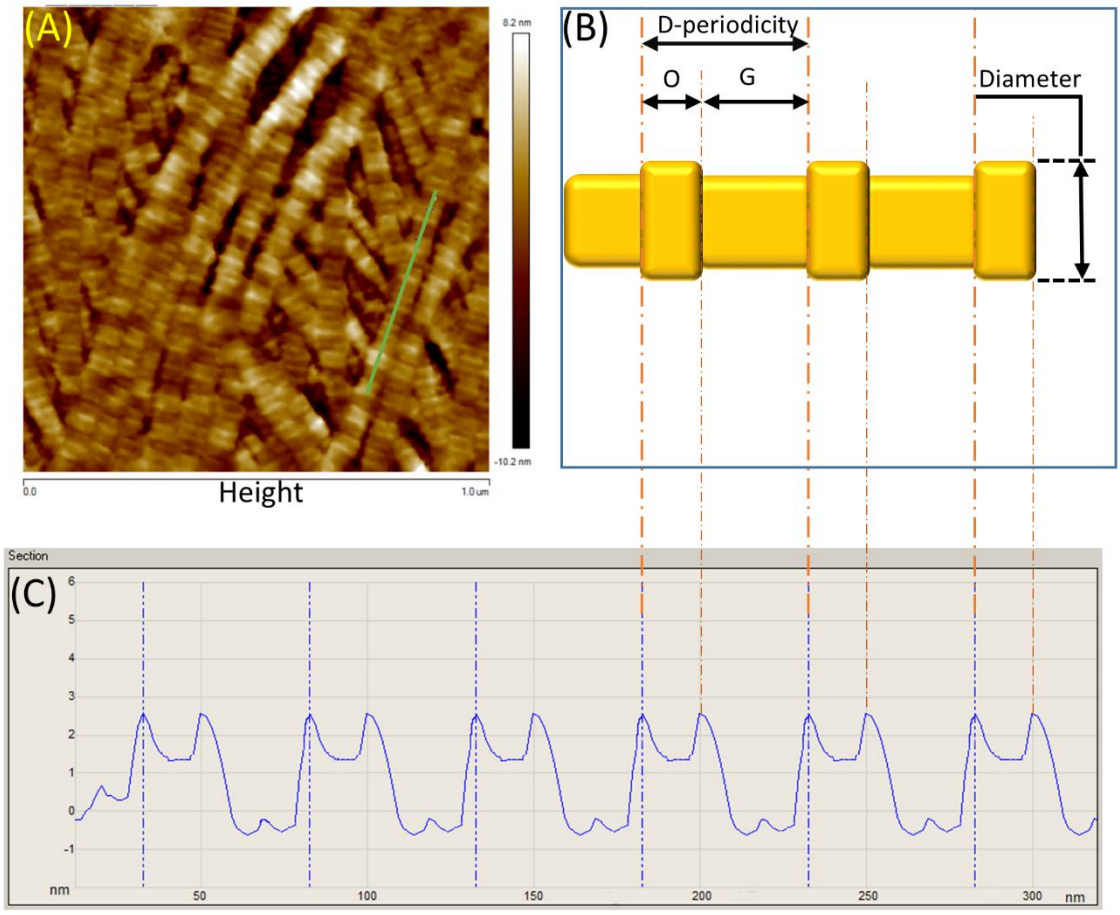

Figure 7.2: Analysis representation of collagen fibril surface profile with using the NanoScope analysis software. (A) Height image of the anterior lamella of a porcine cornea obtained by AFM. The green line in image (A) was drown using 'section' tool of the Nanoscope software. This tool then generates a curve that mimic the collagen surface profile along the line, shown in image (C). The peak to peak distance then is manually placed to measure the distance, which represents the D-periodicity. (B) Schematic diagram explains collagen fibril morphology. 'O' and 'G' refer to overlap and gap zones. This analysis process was repeated for three times, at least, to calculate the average value of collagen fibril diameter and D-periodicity in each image. In this image collagen fibril diameter and D-periodicity were 55.5±2.4 nm and 67.8±1.1 nm, respectively.

7.3.4. Data analysis and statistics

All statistical analysis was performed using OriginPro 2016 version 9.3 (OriginLab, USA). Data is expressed as mean values and standard deviation (mean ± standard deviation) unless otherwise stated. Since the groups and subgroups were unpaired and the statistical significance was chosen to be between two datasets, the two-sample t-test was used to test the statistical difference. The significance level (α) was set as 0.05 for all tests.

7.4. Results

The effect of incubating the corneal sections in amylase and collagenase solutions on the ultrastructure and nanomechanical elastic modulus are presented in the following sub-sections.

7.4.1. Amylase group

Figures 7.3 shows representative topographical images of control samples of the amylase group. In control samples, collagen fibrils seemed packed together and run in a direction. The control samples of the amylase group had shown that the collagen fibrils had diameters of 55.5±2.4 nm and axial D-periodicity of 67.46±2.3 nm. In Figure 7.3(A), one bundle of collagen fibrils ran in a similar direction, whilst in the same image, there was another bundle of collagen fibrils ran in a completely different direction to the previous bundle.

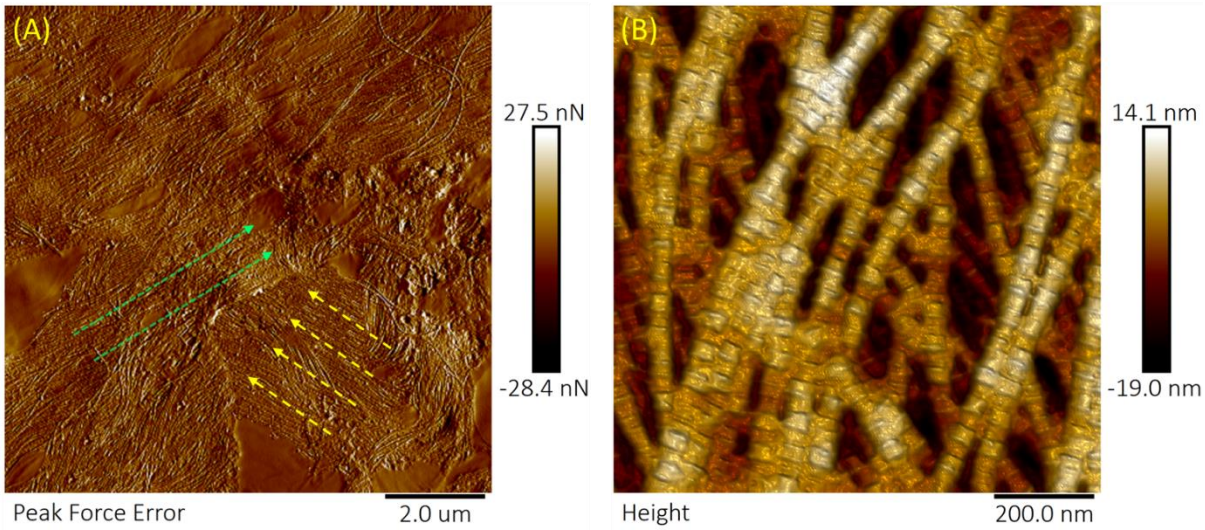

Figure 7.3: Typical topographical images showing collagen fibrils of the anterior lamella of a porcine cornea (control samples). (A) A peak force error image of a control sample was washed and incubated in PBS for 40 min, then left to dry in air at room temperature for 18 min. scan size was 10 μm. The yellow arrows show the direction of a lamella that apparently run in a right angle to another bundle of collagen fibrils (the green arrows). In each bundle, collagen fibrils appear to pack together. (B) A height image of collagen fibrils of a control sample. Scan size was 1 μm. "Height" represents the type of AFM image. A '3D effect' filter was applied for enhancement.

Topographical images of the amylase treated sections revealed a reduction in collagen fibril diameter. Figure 7.4 presents topographical images of porcine corneal sections treated with different concentrations of amylase (0.2 - 2mg/ml). This reduction was found to significantly increase with high amylase concentrations ($p<0.0.498$). The bar graph in Figure 7.5 shows corneal collagen fibril diameters were treated with different amylase concentrations. The maximum reduction in collagen fibril diameter was found in samples treated with 2 mg/ml amylase concentration, with a significant reduction of approximately 26% relative to the control group ($p<0.0001$). There were no statistical differences ($p>0.05$) found in D-periodicity following incubation with varying concentrations of amylase, Figure 7.6. The maximum and minimum values of D-periodicity of amylase treated samples were 70.8 nm and 63.1 nm.

It was also noticed in amylase treated samples that collagen fibril 'splitting up' or fusion was observed. The alignment and regularity of collagen fibrils in the same lamella gradually decreased with increased amylase concentrations, see Figure 7.4 (A, C, and E). Some collagen fibrils seemed to fuse with another adjacent fibril, as shown in Figure 7.4 (B and F).

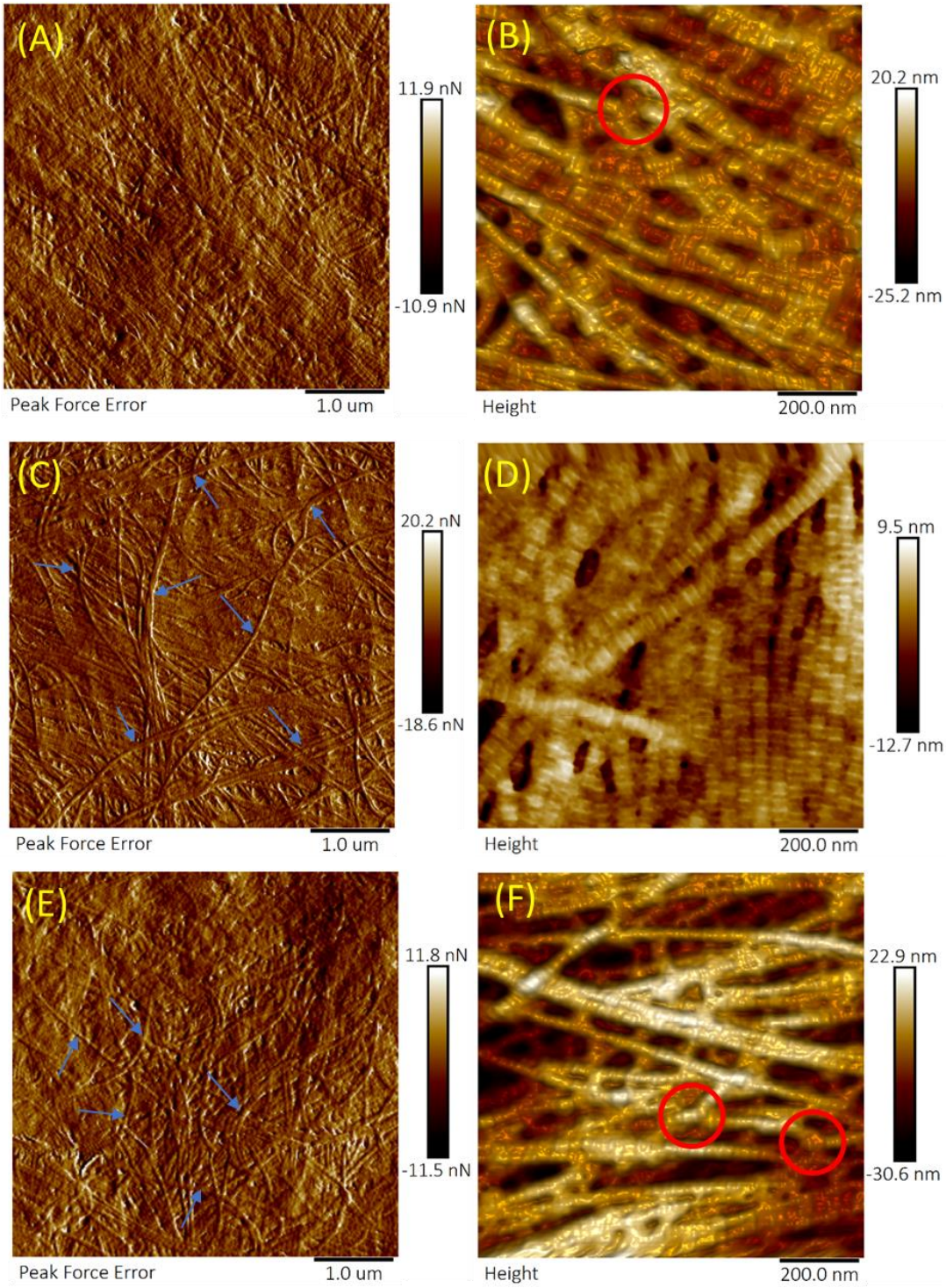

Figure 7.4: Topographical images showing collagen fibrils of the anterior lamella of porcine corneas following incubation with varying concentration of amylase. The sections were incubated in amylase for 40 min, then left to dry in air at room temperature for 18 min. The arrows mark collagen fibrils that ran in irregular directions to other collagen fibrils following amylase incubation. Circles mark the places where the collagen fibril underwent fusion and splitting up. Sections (A) and (B) were incubated with 0.2 mg/ml amylase. The samples in (C) and (D) were incubated with 1 mg/ml amylase. Samples in (E) and (F) were incubated with 2 mg/ml amylase. The scan size for A, C, and F was 5 μm. The scan size for B, D, and F was 1 μm.

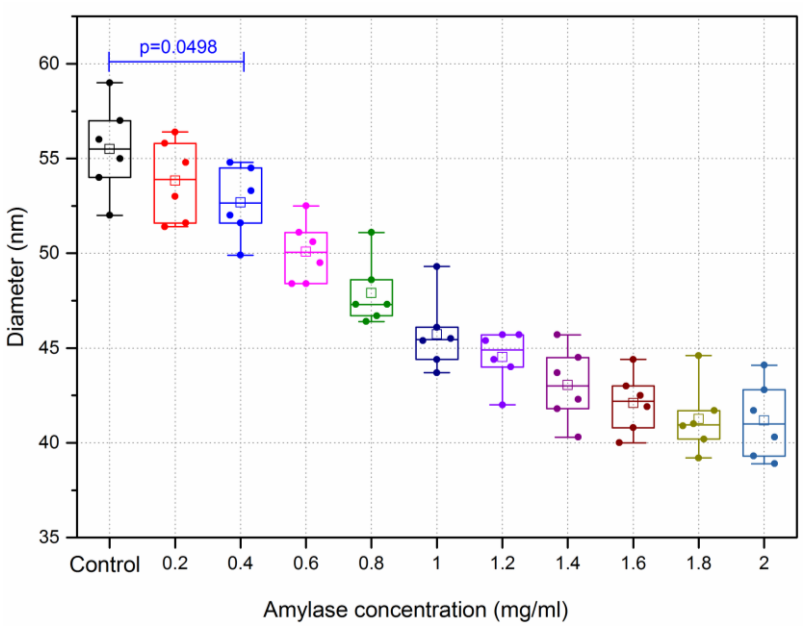

Figure 7.5: Collagen fibril diameters of the anterior lamella of porcine cornea samples following incubation with varying concentrations of amylase. 'Control' represents collagen fibril diameters of control group in which tissue sections were incubated in PBS for 40 min. All data was represented as box plots and data overlaid with lower and upper borders of the box to represent the lower and upper quartiles, and the middle horizontal line to represent the median. The upper and lower whiskers represent 5th and 95th percentile of the data. n = 6 porcine eyes/box. 'p' refers to the statistical significance value.

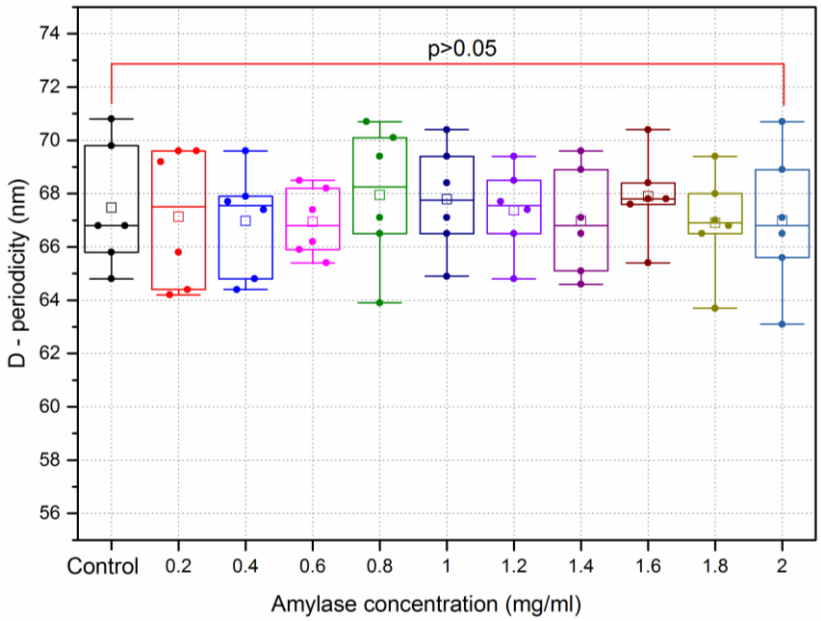

Figure 7.6: D-periodicity of collagen fibrils of porcine cornea sections following incubation with varying concentrations of amylase 'Control' represents collagen fibril diameters of control group in which tissue sections were incubated in PBS for 40 min. All data was represented as box plots and data overlaid with lower and upper borders of the box to represent the lower and upper quartiles, and the middle horizontal line to represent the median. The upper and lower whiskers represent 5th and 95th percentile of the data. n = 6 porcine eyes/box. 'p' refers to the statistical significance value.

It was found that the elastic modulus of corneal treated sections reduced following incubation with amylase. Elastic modulus images (DMT modulus images) of control and amylase-treated samples with different amylase concentrations are shown in Figure 7.7. Elastic modulus of control samples was 2.27±0.15 GPa. Elastic modulus of treated corneas was decreased by 2.2% when samples were incubated with amylase (0.2 mg/ml). The greatest reduction in elastic modulus of 50.2% was seen following amylase (2 mg/ml) treatment for 40 min ($p<0.0001$). The results show that elastic modulus values decreased as the amylase concentration increased. However, no significance difference was detected in elastic modulus of samples that were incubated with amylase of 1.4, 1.6, 1.8, and 20 mg/ml ($p>0.086$).

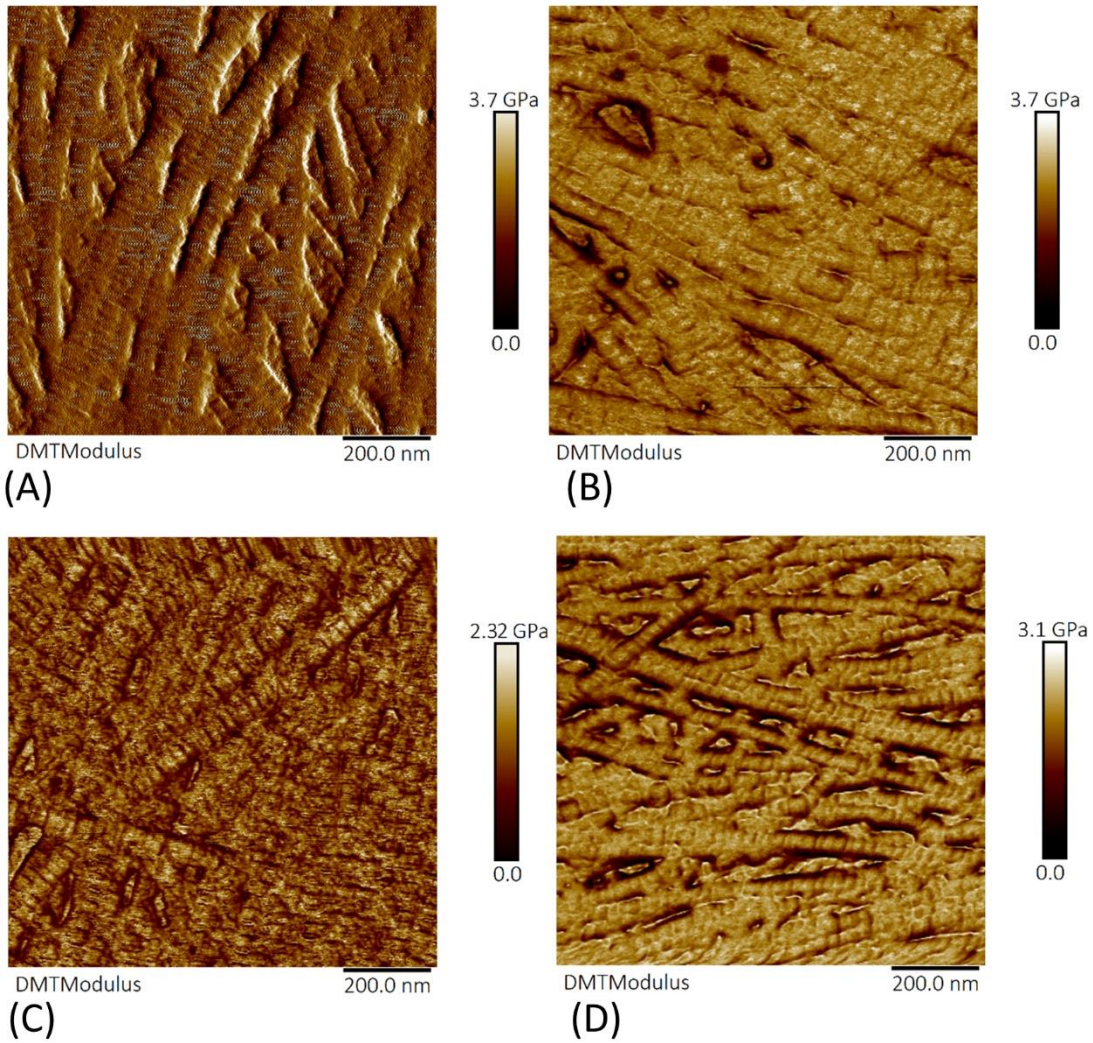

Figure 7.7: Elastic modulus images of the anterior lamella of porcine corneas of control and amylase-treated samples. (A) Control sample was incubated with PBS for 40 min then left to dry in air at room temperature for 18 min. Amylase-treated samples (B, C and D) were incubated with amylase of concentrations 0.2, 1, and 2 mg/ml, respectively.

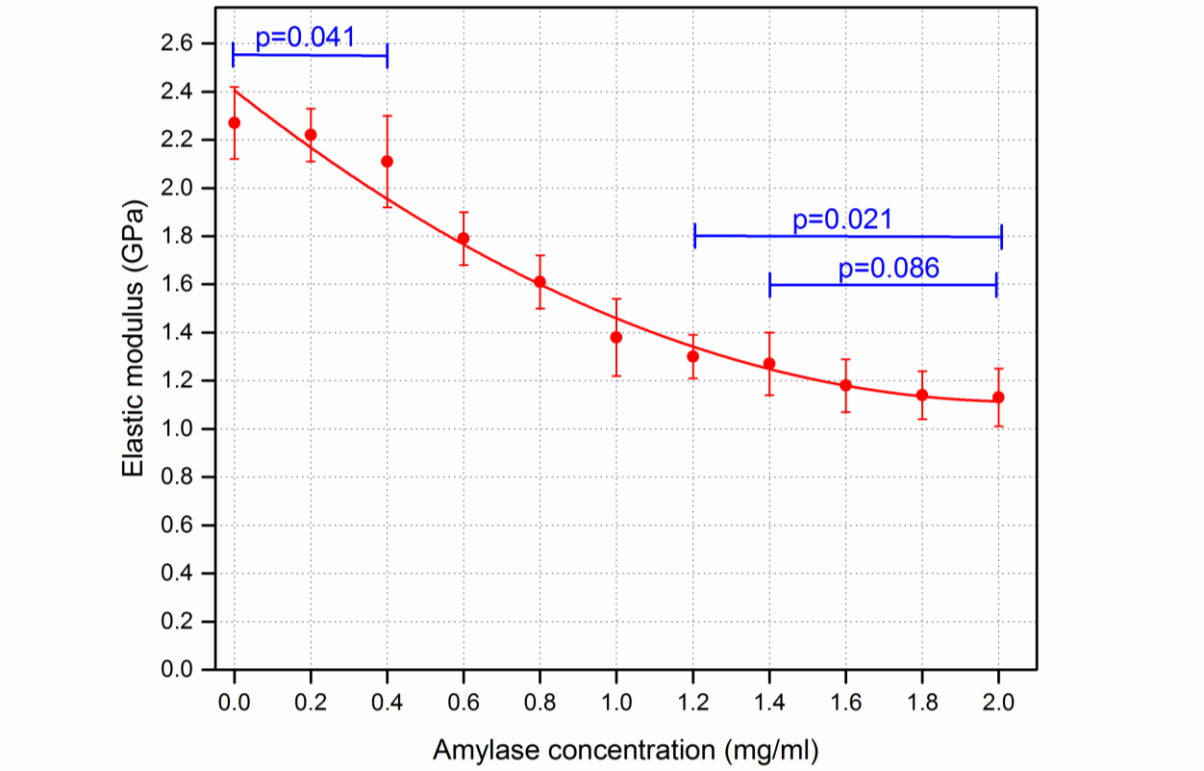

Figure 7.8: Mean values of elastic modulus of corneal samples treated with varying concentrations of amylase. The curve fits a second order equation. Zero amylase concentration refers to control samples. n = 6 porcine eyes/point. 'p' refers to the statistical significance value. Error bars represent the standard deviation.

7.4.2. Crude and purified collagenase groups

Topographical images of sections treated with crude (Figure 7.9) and purified (Figure 7.10) collagenase revealed a significant deterioration with increased concentration of the enzymes from 0.05 to 0.2 mg/ml. Topographical details (collagen fibril diameter and D-periodicity) were not possible to be identified in sections that were incubated with crude and purified collagenases of concentration 0.2 mg/ml, as shown in Figure 7.9(D) and 7.10(D). The sections treated with crude collagenase (0.2 mg/ml) showed traces of degradated collagen fibrils; however, it was possible to identify collagen fibrils in samples that were treated with the lower concentrations of the enzymes.

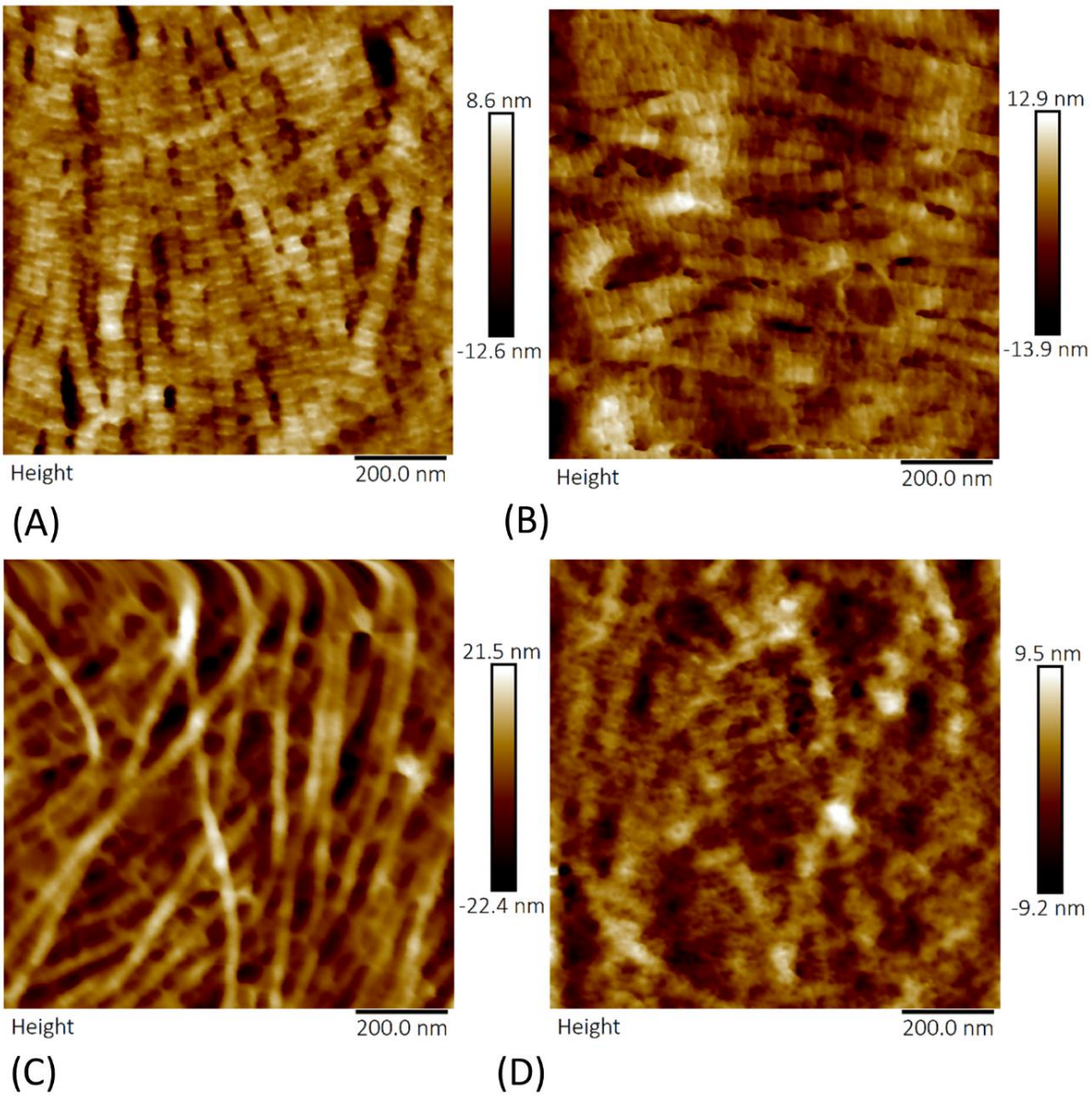

Figure 7.9: Topographical images demonstrating collagen fibrils of anterior lamella of porcine corneas following incubation with varying concentration of crude collagenase. Samples (A, B, C and D) were incubated with crude collagenase of concentrations 0.05, 0.01, 0.15 and 0.2, respectively. The scan size was 1 μm for each image.

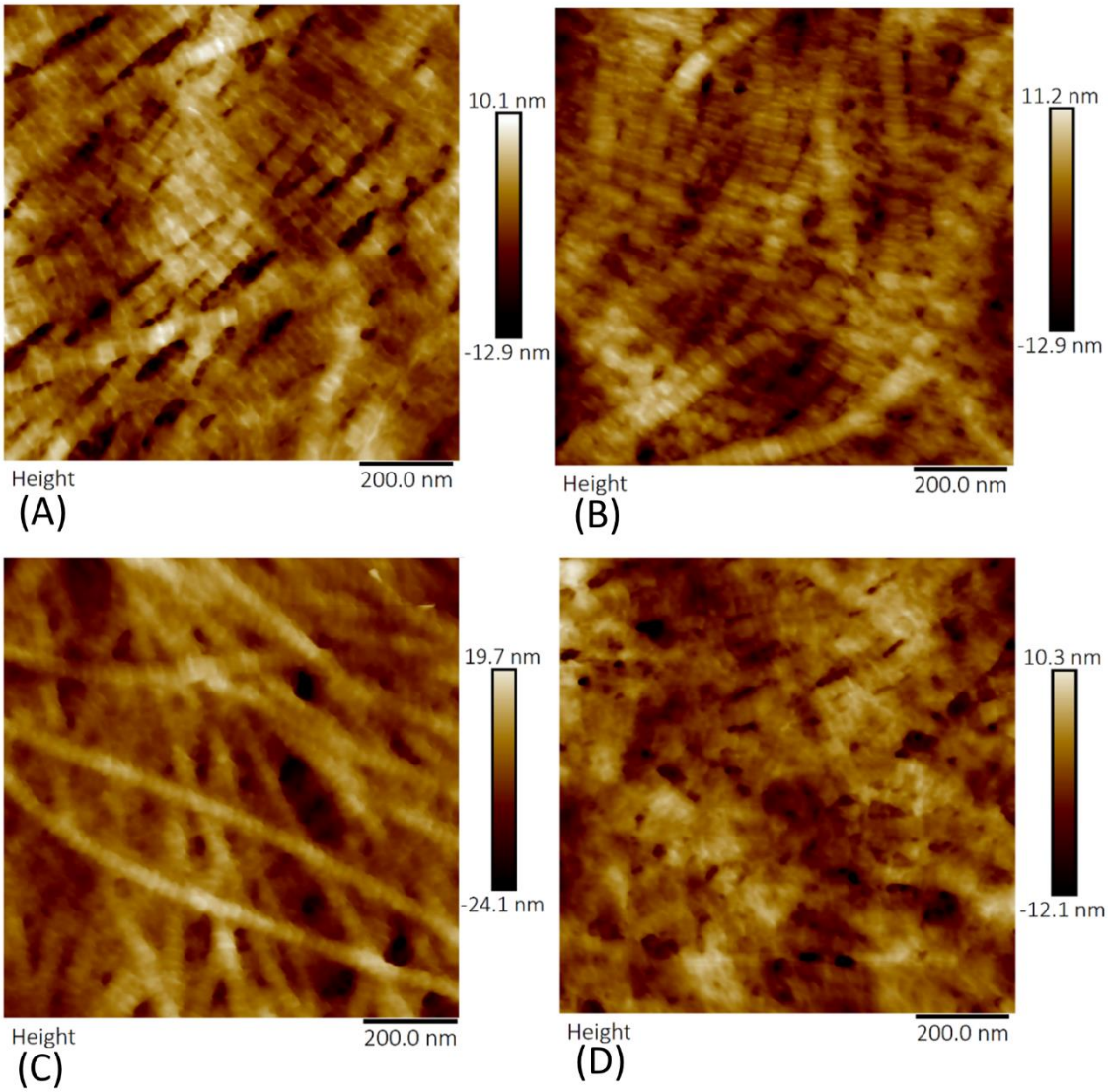

Figure 7.10: Topographical images presenting collagen fibrils of anterior lamella of porcine corneas following incubation with varying concentration of purified collagenase. Samples (A, B, C and D) were incubated with purified collagenase of concentrations 0.05, 0.01, 0.15 and 0.2, respectively.

Topographical images following treatment with crude and purified collagenase showed a significant reduction in collagen fibril diameter, Figure 7.11. The reduction in the diameters of collagen fibril increased with increased concentrations of the enzymes ($p<0.0001$). The mean collagen fibril diameter of the control sections of the crude collagenase group was 57.63±2.12 nm, whilst the control sections of the purified collagenase group had collagen fibril diameter of 58.71±2.26 nm. No significant difference was found between the control sections of both groups ($p=0.41$). The minimum collagen fibril diameter was 39.16±2.1 nm, seen in purified collagenase treated sections of 0.2 mg/ml, whilst no topographical details of collagen fibrils were visible in tissue sections in which the highest crude collagenase was used.

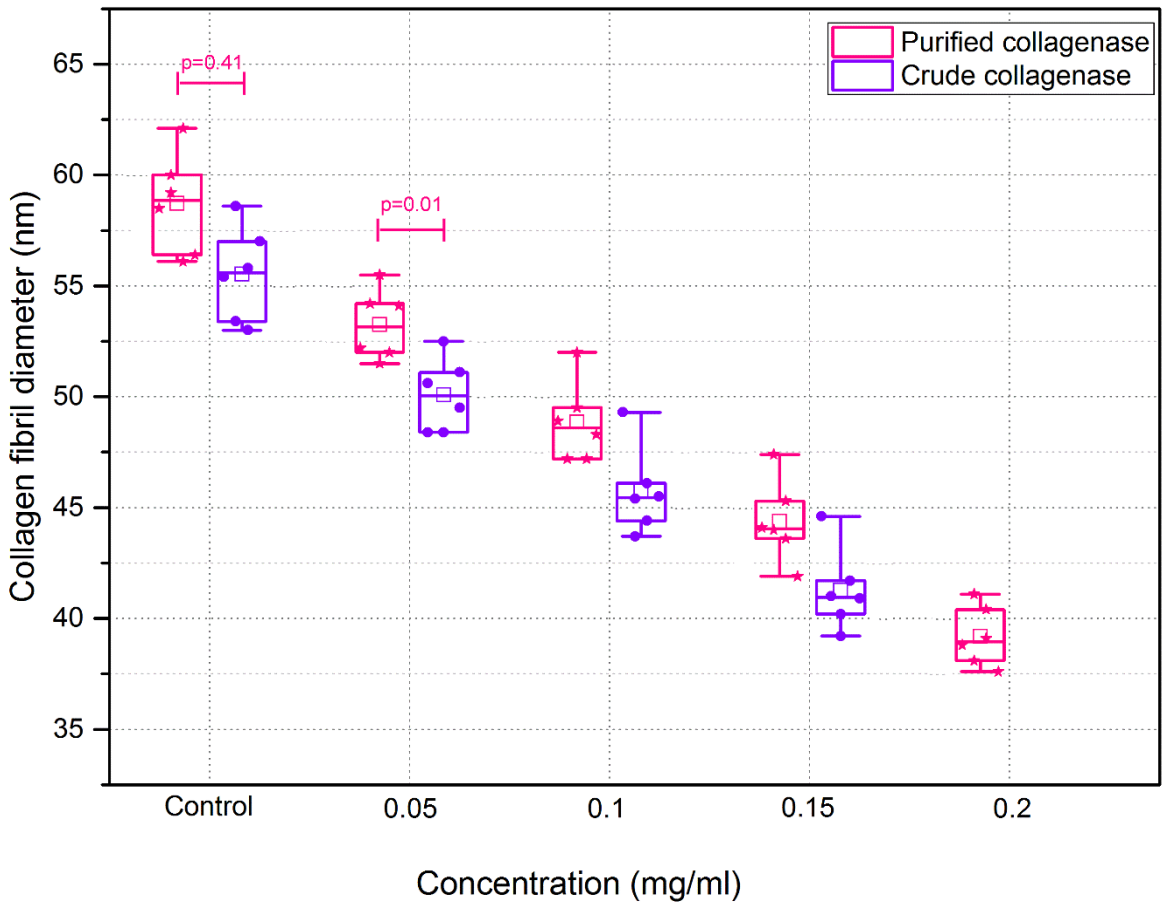

Figure 7.11: Collagen fibril diameters of porcine corneal sections following incubation with varying concentrations of crude and purified collagenase. n = 6 porcine eyes/box. 'Control' represents mean value of collagen fibrils diameters of control sections, where the control sections of the crude collagenase group were incubated in PBS for 15 min and then snap-washed with NaDTA and PBS. The control sections of the purified collagenase group were incubated in PBS for 15 min only. All data was represented as box plots and data overlaid with lower and upper borders of the box to represent the lower and upper quartiles, and the middle horizontal line to represent the median. The upper and lower whiskers represent 5th and 95th percentile of the data. 'p' refers to the statistical significance value. At each concentration, the statistical significance was found between the two groups ($p<0.01$) except in the control samples.

The results also showed that PBS slightly decreased collagen fibril diameter. Figure 7.12 shows that the sections that were incubated in PBS (control sections for 40 min) had collagen fibril diameters (55.5±2.4 nm) significantly less than those tissue sections that were incubated for 15 min (control sections of crude and purified collagenase groups).

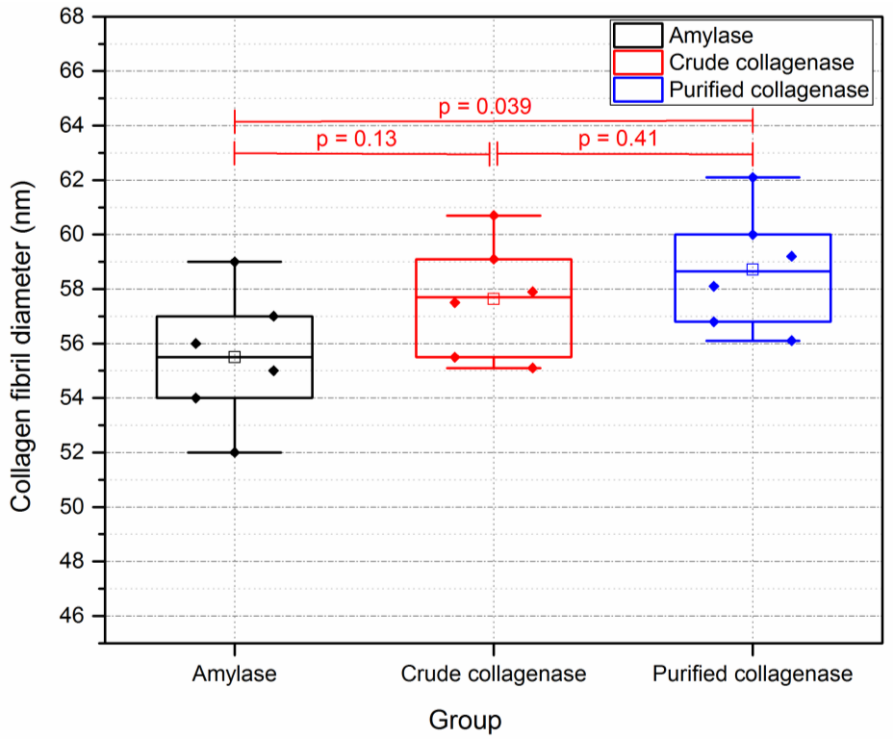

Figure 7.12: Collagen fibril diameters of control sections following incubation with PBS for 15 and 40 min. n = 6 porcine eyes/bar. Control sections of amylase group were incubated with PBS for 40 min. Controls in the crude and purified collagenase groups were incubated with PBS only for 15 min. 'p' refers to the statistical significance value.

Topographical images revealed that D-periodicity had significantly changed following the incubation with crude and purified collagenases ($p>0.03$). Figure 7.13 shows the mean values of D-periodicity of collagen fibrils following degradation with the enzymes. No significant difference was found in D-periodicity of collagen fibrils of the control sections of both the crude and purified collagenase groups, which were 67.6±2.3 nm and 67.4±2.6 nm, respectively. The D-periodicity was significantly reduced by approximately 8.2% in treated samples that were incubated with 0.05 mg/ml crude collagenase in comparison to the control sections ($p<0.0001$), whilst at the same concentration of 0.05 purified collagenase, the D-periodicity was decreased by approximately 4.2% in contrast to control sections. The D-periodicity was significantly decreased with increased concentration of the collagenases ($p<0.0001$), where it was reduced to 45.1±2.4 nm (approximately 33.1% relative to control sections) at the highest concentration of purified collagenase. It was not possible to measure D-periodicity of collagen fibrils in samples that were treated with 0.2 mg/ml crude collagenase because no obvious topographical features were obtained from those sections.

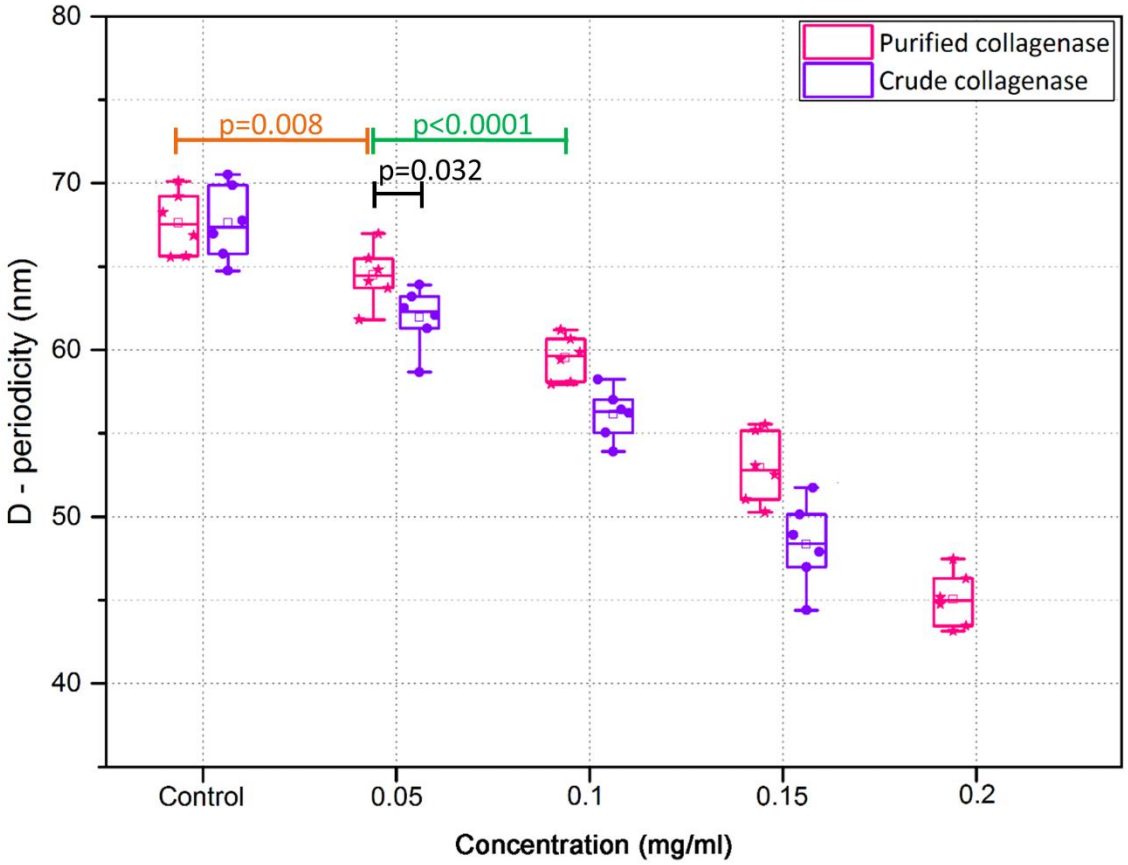

Figure 7.13: D-periodicity of collagen fibrils of porcine cornea sections following incubation with varying concentrations of crude and purified collagenase. (n = 6 porcine eyes/box). 'Control' represents mean value of collagen fibrils diameters of the control sections, where the control sections of the crude collagenase group were incubated in PBS for 15 min and then snap-washed with NaDTA and PBS. The control sections of the purified collagenase group were incubated in PBS for 15 min only.

The elastic modulus significantly decreased in sections that were incubated with crude collagenase for 15 min, and it decreased more when the concentration increases ($p<0.001$), see Figure 7.14. Elastic modulus of control sections was 2.21±0.16 GPa. These sections were incubated in PBS for 15 min and then snap-washed with NaDTA and PBS. Elastic modulus significantly decreased by 27.6% when the sections were incubated with 0.05 mg/ml crude collagenase ($p<0.001$). The maximum reduction of the elastic modulus was 76.5%, which was seen following incubating the sections in 0.2 mg/ml crude collagenase for 15 min.

It was also found that elastic modulus of the purified collagenase-treated sections was significantly decreased following incubation with varying concentrations of the enzyme ($p<0.05$), Figure 7.14. Elastic modulus of the controls was 2.16±0.18 GPa; these samples were incubated in PBS for 15 min. The elastic modulus seemed to decrease linearly with an increase in purified collagenase concentration.

The results also show that the elastic modulus of sections that were treated with crude collagenase were reduced more than in tissue sections that were incubated with purified collagenase. This difference was statistically significant at each concentration ($p<0.001$). There was no significant difference found in elastic moduli of controls when comparing the crude and purified collagenase groups ($p=0.92$).

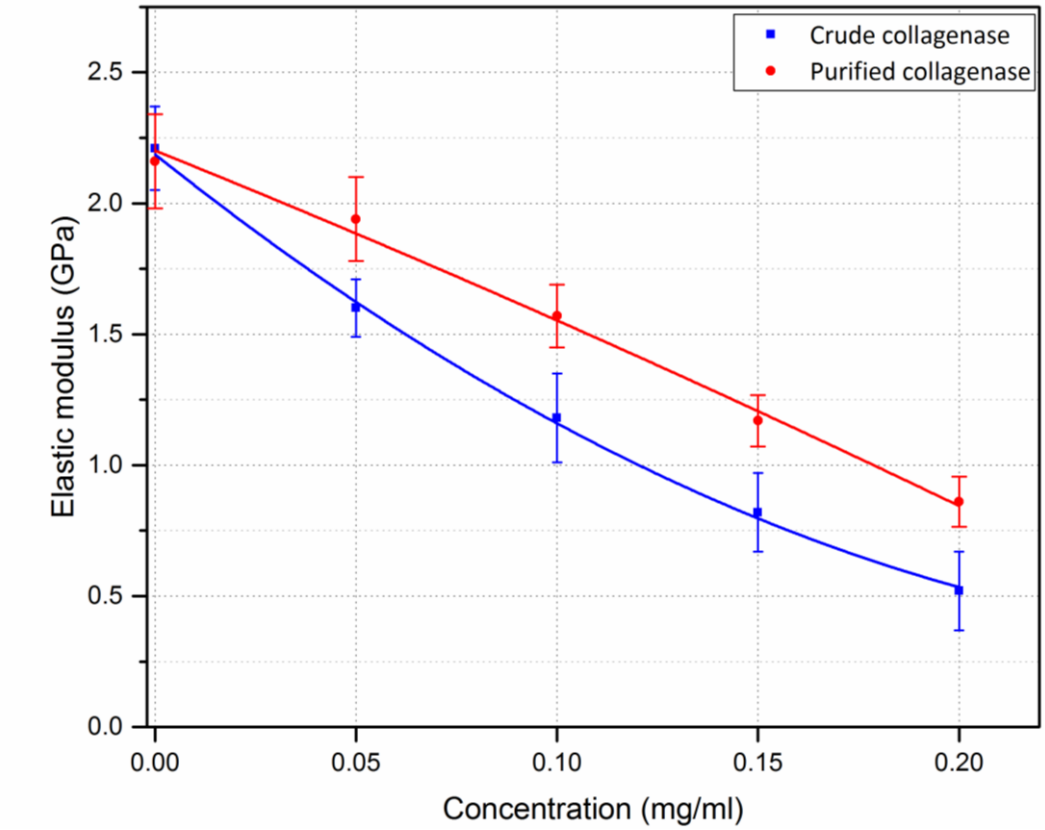

Figure 7.14: Mean values of elastic modulus of corneal samples treated with varying concentrations of crude and purified collagenase. Zero concentration refers to control samples. n = 6 porcine eyes/point. Error bars represent the standard deviation.

7.5. Discussion

This chapter aimed to use *in vitro* enzymatic degradation to understand how the ultrastructure and nanomechanical changes in the collagen fibril network and extracellular matrix may affect corneal properties. The effect of different concentrations of the degradation enzymes (amylase, crude collagenase and purified collagenase) on nanomechanical and ultrastructural properties of porcine corneas was investigated.

AFM was used to determine the ultrastructure and nanomechanical properties of the porcine corneas. The main advantage of AFM over other nano-imaging techniques (such as scanning electron microscopy, SEM) is that topographical details of samples can be visualised without the

need of special treatments (such as metal/carbon coatings) that would irreversibly alter or damage the samples. Unlike with SEM, AFM samples do not need to be coated and or require an expensive vacuum environment for proper operation. AFM can also be used to quantify the mechanical properties of samples (Alessandrini and Facci, 2005; Last *et al*, 2010), especially with the introduction of PF-QNM mode that offers a link between samples topography and its mechanical properties in nanoscale (Pittenger *et al*, 2010). However, a few disadvantages that are associated with using AFM include limited scan image size and scanning speed (Jalili and Laxminarayana, 2004). In addition, there was the possibility of image artefacts that could be induced by steep zones on the samples. In this study, these artefacts were avoided by moving to other testing sites on the samples. Moreover, other issues include the lack of certainty in the calculated elastic modulus values that might be happened due to the machine calibration, cantilever geometry and tip contamination during testing (Picas *et al*, 2012). Calibration was checked after each experiment to ensure the accuracy of the obtained elastic modulus values. The new probes, RTESPA-300, were utilised due to their versatile specifications in cantilever stiffness stability. Tip contamination due to interaction with the samples was regularly assessed during the experiments through the shape of the generated force-separation curve and the consistency of the results.

7.5.1. Amylase group

The results indicate that collagen fibril diameters of corneal sections were decreased following incubation with amylase. In an earlier AFM study, it was found that the collagen fibril diameter in the porcine corneal stroma is 55.6±5.2 nm of hydrated sections (Xia *et al*, 2014), which is consistent with collagen fibrils diameters of the air-dried control sections in the current study. The reduction of collagen fibril diameters following incubation with amylase suggests the contribution of proteoglycans in maintaining the collagen fibril diameter. It was found that the sclera of highly myopic human eyes is associated with reduction of proteoglycans, and contained an increased number of smaller diameter collagen fibrils in comparison with normal human sclera, which leads to increase in sclera elasticity (Harper and Summers, 2015). That finding might justify the current change of collagen fibril diameters following the proposed depletion of proteoglycans with amylase. Another study has observed the nanostructure of collagen fibrils of sclera sections following incubation with amylase, found that collagen fibrils were significantly decreased (Zhoula, 2018). This finding also verifies the enhancement of corneal transparency was measured following incubation corneas with amylase and collagenase (Chapter 6).

The current study also showed that the axial collagen fibril D-periodicity did not change following the treatment with amylase. It was found that the axial periodicity of type I collagen fibrils in normal human corneal stroma was approximately 65 nm obtained by x-ray diffraction method (Meek and Boote, 2003) and 67 nm obtained by AFM (Jastrzebska *et al*, 2016), which appears to be very close to the mean values of collagen fibril D-periodicity in the control samples from this study. The current study found non-significant changes in collagen fibril D-periodicity of amylase treated samples. That apparently suggests the collagen fibrils were not digested by the amylase.

The regularity loss in directions, splitting-up and fusion of collagen fibrils were observed following enzymatic treatment with amylase. A similar finding was also seen in sclera samples following incubation with amylase (Zhuola, 2018) that suggested depletion of proteoglycans between collagen fibrils, which was also confirmed by an immunohistochemical pilot study where proteoglycans were found in amylase solutions were used for corneal samples incubation (Appendix III). Some collagen fibrils, therefore, appeared to lack connection to other bundles of fibrils. No analysis methods were built to quantify this observation; therefore, it would be of great help to design a logical procedure to detect collagen fibril randomness.

The elastic modulus was significantly decreased in amylase treated sections. Proteoglycans act as cross-linkers between the collagen fibrils forming an organisation that exhibits the mechanical properties of the tissue. By analogy, the depletion or break down of these cross-linkers leads to deterioration of the normal ultrastructural organisation of the tissue, and subsequently reduction of tissue stiffness (Murienne *et al*, 2015). The reduction of stiffness in collagenous tissue following amylase incubation was also reported in a number of studies (Tanaka *et al*, 2003; Spoerl *et al*, 2012; Wollensak *et al*, 2011), where amylase was utilised to deplete proteoglycans of collagenous tissues. The same trend for elastic modulus reduction was also found in amylase treated corneas (Chapter 6).

The results showed that as the concentration of the amylase increased, the more reduction in elastic modulus was measured in treated corneal sections. That implies the high concentrations of the amylase increase the number of the random attacks on α-1,4 glycosidic bonds. These bonds link the glycosaminoglycan to the core protein of the proteoglycans (Quintarelli *et al*, 1969). The relation between amylase concentration and elastic modulus of corneas was also found in Chapter 6, where increased concentration of amylase depletes more proteoglycans and then more reduction in elastic modulus.

7.5.2. Collagenase groups

It was found that crude and purified collagenase both significantly degraded corneal samples, with significant changes in the ultrastructure which were manifested by alterations in collagen fibril diameters and their structural organisation. Collagen fibrils in the collagenase treated samples (crude and purified) exhibited reduction in diameters with increased enzyme concentration. The reduction in diameter is mainly attributed to digestion of collagen fibrils by collagenases as is the established function of this enzyme (Gaul *et al*, 2018; Hanoune *et al*, 1977; Jayes *et al*, 2016; van der Kraan *et al*, 1990). The current finding is in agreement with a previous study that used AFM to measure the adhesion force and ultrastructure of the collagen fibrils on the Achilles tendons of rats following injection of collagenase (Lee *et al*, 2011).

It was found that D-periodicity of collagen fibrils significantly decreased following incubation with collagenases (crude and purified). That implies the collagen fibrils of corneal sections experienced significant digestion by collagenases, where collagen molecules were particularly affected and became shorter with increased concentration of the enzymes. In support of the current results, Lee *et al* (2011) found that D-periodicity of collagen fibrils on the Achilles tendons of rats were significantly reduced after collagenase incubation. Therefore, it can be said the collagenase did not break down the collagen fibrils in fragments but digested them along each fibril axis, which decreased the fibril diameter. This suggestion has been supported in previous studies, where it was reported the collagenase did not cut the collagen fibril into parts after enzymatic treatment but only decreased their diameter and D-periodicity (Lee *et al*, 2011; Långsjö *et al*, 2002).

Snap-washing corneal samples with NaDTA for very short time has not affected stiffness of the tissue. NaDTA was introduced as an effective corneal collagenase inhibitor (Hook *et al*, 1971) and been used to decalcified of femoral bone mineral content, samples were incubated for prolonged time, and reducing its stiffness (Shah *et al*, 1995). Therefore, snap-washing corneal sample with NaDTA was assessed. The results showed no significant difference in elastic moduli of samples were snap-washed with NaDTA and PBS and other samples were only washed with PBS. This confirms that elastic modulus of enzymatic treated samples was not been changed following snap-washing with NaDTA.

The results presented in this chapter revealed that collagenase decreased the stiffness of the corneal tissue, and this reduction increases with the increase of the enzyme concentration. These results are in agreement with previous studies in which bacterial collagenase reduced tissue stiffness (Lyyra

et al, 1999; Långsjö *et al*, 2002; Stolz *et al*, 2004). It is well known that collagen fibrils serve as the smallest units that exhibit the mechanical property of the tissue and their deterioration causes a reduction in stiffness and subsequent geometrical modifications in the tissue (Fratzl, 2008; Meek and Boote, 2004; Sherman *et al*, 2015). This deterioration can be interpreted as a reduction in collagen fibril diameters, which was found to be correlated with their stiffness (Papi *et al*, 2014). Therefore, it would be useful to investigate the relationship of collagen fibril diameters with stages of stiffness reduction in keratoconic corneas, for future work.

The results presented in this chapter also showed that the crude collagenase has stronger effect on ultrastructural details and mechanical properties than purified collagenase. This result is in agreement with Gaul *et al* (2018) that found arterial tissue incubated with crude collagenase showed more deformation than those incubated with purified collagenase. This effect was also seen in corneal samples were treated by crude and purified collagenase, where elastic modulus decreased more in crude collagenase treated corneas than those treated with purified collagenase (Chapter 6) that attributed to contamination of the crude collagenase with other proteolytic enzymes. (Hanoune *et al*, 1977). Therefore, the ultrastructural details were not possible to be observed in samples where high concentration of cured collagenase was used.

Elastic modulus values presented in Chapters 3, 4 and 6 were less than those measured by AFM. Elastic modulus values of control corneas (whole thickness) tested by nanoindentation and inflation testing were in range of 40 to 700 kPa depending on testing conditions such as internal pressure and hydration. Whereas, elastic modulus values of corneal sections (5 μm thick) were in range of 2 to 2.45 GPa. This can be attributed to many factors including testing scale, air-dried samples, and sample thickness. Testing scale was previously explained in Chapter 6. Air-drying of sclera samples was found to increase their stiffness (Zhuola, 2018). Sample thickness seems to affect the obtained elastic modulus values. The thicker the sample, the less effect of substrate on sample stiffness is expected (Picas *et al*, 2012; Zhuola, 2018). However, increasing the thickness of the AFM sections reduces the quality of the topographical images. Therefore, an optimal tissue thickness was required to balance image quality and reduction of substrate effects.

7.6. Limitations

It was hypothesised that the thickness of the tissue sections after the enzymatic treatment would decrease and since there was no precise techniques to measure cryosection thickness, the thickness was unknown in enzymatic treated sections. The reduction in thickness of the tissue sections tends

to cause an increase in elastic modulus of the tissue due to contribution of the stiff substrate. Another limitation includes testing the samples in air that resulted in elevated values of corneal elastic modulus. Hence, for future work, testing corneal samples in liquid should be conducted to obtained more physiologically relevant mechanical properties. Therefore, the current study suggests that the real stiffness of treated corneas is much less than what was obtained in the results.

This study aims to investigate the corneal nanostructure and mechanical properties in one region of the cornea. The results are limited to the changes in cornea following amylase treatment only, which was not precisely understood because it is still unknown which type of proteoglycans were depleted. Therefore, an immunohistochemical study is suggested to determine the type of the depleted proteoglycans following the amylase incubation which could not be made in this study.

7.7. Conclusions

In this chapter, AFM was employed to examine ultrastructural changes and elastic modulus of corneal sections following incubation with amylase and collagenase. Amylase treatment reduces collagen fibril diameter and corneal stiffness, but not D-periodicity of collagen fibrils. The reduction in corneal stiffness and collagen fibril diameter increased with amylase concentration. This amylase treatment is thought to break-down proteoglycans linkages with collagen fibrils that leads to deterioration in corneal stiffness. This deterioration in the corneas suggests contribution of amylase in the progression of keratoconic corneas, which increases the need for further investigations on the depleted types of proteoglycans.

Treatment of corneal sections with collagenase gradually deteriorates the ultrastructure and the stiffness of the tissue. These changes are significantly higher than the changes obtained with amylase treatment. The deterioration of the ultrastructure includes reduction in both the diameter and the D-periodicity of collagen fibrils, and increases in high concentrations of collagenases (crude and purified). Incubation with crude collagenase has a stronger effect on corneal samples than purified collagenase. The disruption of collagen fibrils' morphology lead to a reduction in elastic modulus at the nanoscale, and that proves there is a correlation between the morphology and stiffness of collagenous tissues. This enzymatic treatment of the corneal sections may serve as an empirical animal model for understanding keratoconus at different progression levels.

7.8. References

Alessandrini, A, Facci, P, 2005. AFM: a versatile tool in biophysics. Measurement Science and Technology 16(6), p.R65.

Balasubramanian, S., Pye, D., Willcox, M., 2010. Are Proteinases the Reason for Keratoconus? Current Eye Research 35, 185-191.

Beshtawi, I., Akhtar, R., Hillarby, M., O'Donnell, C., Zhao, X., Brahma, A., Carley, F., Derby, B., Radhakrishnan, H., 2015. Biomechanical changes of collagen cross-linking on human keratoconic corneas using scanning acoustic microscopy. Current Eye Research 1-7.

Choi, S., Lee, S.-C., Lee, H.-J., Cheong, Y., Jung, G.-B., Jin, K.-H., Park, H.-K., 2013. Structural response of human corneal and scleral tissues to collagen cross-linking treatment with riboflavin and ultraviolet A light. Lasers in Medical Science 28, 1289-1296.

Collier, S., Madigan, M., Penfold, P., 2000. Expression of membrane-type 1 matrix metalloproteinase (MT1-MMP) and MMP-2 in normal and keratoconus corneas. Current Eye Research 21, 662-668.

Collier, S.A., 2001. Is the corneal degradation in keratoconus caused by matrix-metalloproteinases? Clinical & Experimental Ophthalmology 29, 340-4.

Dokukin, M., Sokolov, I., 2012. Quantitative mapping of the elastic modulus of soft materials with HarmoniX and PeakForce QNM AFM modes. Langmuir 28, 16060-16071.

Fischer, A., Jacobson, K., Rose, J., Zeller, R., 2008. Preparation of cells and tissues for fluorescence microscopy. In: Spector, D., Goldman, R. (eds) Basic Methods in Microscopy (pp. 105-124). Cold Spring Harbor Laboratory Press. USA.

Fratzl P., 2008. Collagen: Structure and mechanics, an introduction. In: Fratzl P. (eds) Collagen (pp. 1-13). Springer, Boston. USA.

Fullwood, N.J., Hammiche, A., Pollock, H.M., Hourston, D.J., Song, M., 1996. Atomic force microscopy of the cornea and sclera. Current Eye Research 14, 529-535.

Galvis, V, Sherwin, T, Tello, A, Merayo, J, Eye, B.-R., 2015. Keratoconus: an inflammatory disorder? Eye 29(7), 843-852.

Gaul, R.T., Nolan, D.R., Ristori, T., Bouten, C.V.C., Loerakker, S., Lally, C., 2018. Strain mediated Enzymatic Degradation of arterial tissue: Insights into the role of the non-collagenous tissue matrix and collagen crimp. Acta Biomaterialia 77, 301-310.

Hanoune, J., Stengel, D., Lacombe, M.L., Feldmann, G., Coudrier, E., 1977. Proteolytic activation of rat liver adenylate cyclase by a contaminant of crude collagenase from Clostridium histolyticum. Journal of Biological Chemistry 252, 2039-2045.

Harper, A.R., Summers, J.A., 2015. The dynamic sclera: extracellular matrix remodeling in normal ocular growth and myopia development. Experimental Eye Research 133, 100-11.

Hook, C.W., Brown, S.I., Iwanij, W., Nakanishi, I., 1971. Characterization and inhibition of corneal collagenase. Investigative Ophthalmology & Visual Science 10, 496-503.

Hurst, L.C., Badalamente, M.A., Hentz, V.R., Hotchkiss, R.N., Kaplan, F.T., Meals, R.A., Smith, T.M., Rodzvilla, J., 2009. Injectable collagenase clostridium histolyticum for Dupuytren's contracture. New England Journal of Medicine 361, 968-79.

Jalili, N., Laxminarayana, K.K., 2004. A review of atomic force microscopy imaging systems: application to molecular metrology and biological sciences. Mechatronics 14, 907-945.

Jastrzebska, M., Tarnawska, D., Wrzalik, R., Chrobak, A., Grelowski, M., Wylegala, E., Zygadlo, D., Ratuszna, A., 2016. New insight into the shortening of the collagen fibril D-period in human cornea. Journal of Biomolecular Structure and Dynamics 35(3) 551-563.

Jayes, F., Liu, B., Moutos, F., Kuchibhatla, M., Guilak, F., Leppert, P., 2016. Loss of stiffness in collagen-rich uterine fibroids after digestion with purified collagenase Clostridium histolyticum. American Journal of Obstetrics and Gynecology 215, 596.e1-596.e8.

Kaiserman I., Sella S., 2019. Chronic ocular inflammation and keratoconus. In: Barbara A. (eds) Controversies in the Management of Keratoconus (pp. 17-27). Springer, Cham. USA.

Last, J., Russell, P., Nealey, P., Murphy, C., 2010. The applications of atomic force microscopy to vision science. Investigative Ophthalmology & Visual Science 51, 6083-6094.

Last, J., Thomasy, S., Croasdale, C., Russell, P., Murphy, C., 2012. Compliance profile of the human cornea as measured by atomic force microscopy. Micron 43, 1293-1298.

Lee, G.-J.J., Choi, S., Chon, J., Yoo, S., Cho, I., Park, H.-K.K., 2011. Changes in collagen fibril pattern and adhesion force with collagenase-induced injury in rat Achilles tendon observed via AFM. Journal of Nanoscience and Nanotechnology 11, 773-7.

Legkikh, L., Koledintsev, M., Semenova, A., Okuyama, K., 2017. Biochemical investigations of lacrima in early diagnosis of keratoconus. (Abstract) Sangubashi Eye Clinic, Japan. [available on: www.sangubashi.com/English/report/syanhai.htm] (accessed on: 12th January 2020).

Lombardo, M., Lombardo, G., Carbone, G., De Santo, M.P., Barberi, R., Serrao, S., 2012. Biomechanics of the anterior human corneal tissue investigated with atomic force microscopy. Investigative Ophthalmology & Visual Science 53, 1050-7.

Lombardo, M., Santo, M., Lombardo, G., Barberi, R., Serrao, S., 2006. Atomic force microscopy analysis of normal and photoablated porcine corneas. Journal of Biomechanics 39, 2719-2724.

Lyyra, T., Arokoski, J.P., Oksala, N., Vihko, A., Hyttinen, M., Jurvelin, J.S., Kiviranta, I., 1999. Experimental validation of arthroscopic cartilage stiffness measurement using enzymatically degraded cartilage samples. Physics in Medicine & Biology 44, 525-35.

Långsjö, T., Rieppo, J., Pelttari, A., Oksala, N., Kovanen, V., Helminen, H., 2002. Collagenase-induced changes in articular cartilage as detected by electron-microscopic stereology, quantitative polarized light microscopy and biochemical assays. Cells Tissues Organs 172(4), 265-275.

Mackiewicz, Z., Määttä, M., Stenman, M., Konttinen, L., Tervo, T., Konttinen, Y., 2006. Collagenolytic proteinases in keratoconus. Cornea 25, 603-610.

Meek, K., 2009. Corneal collagen—its role in maintaining corneal shape and transparency. Biophysical Reviews 1, 83-93.

Meek, K., Boote, C., 2004. The organization of collagen in the corneal stroma. Experimental Eye Research 78, 503-512.

Meek, K.M., Knupp, C., 2015. Corneal structure and transparency. Progress in Retinal and Eye Research 49, 1-16.

Murienne, B., Jefferys, J., Quigley, H., Nguyen, T., 2015. The effects of glycosaminoglycan degradation on the mechanical behavior of the posterior porcine sclera. Acta Biomaterialia 12, 195-206.

Papi, M., Paoletti, P., Geraghty, B., Akhtar, R., 2014. Nanoscale characterization of the biomechanical properties of collagen fibrils in the sclera. Applied Physics Letters 104, 103703.

Picas, L., Milhiet, P.-E.E., Hernández-Borrell, J., 2012. Atomic force microscopy: a versatile tool to probe the physical and chemical properties of supported membranes at the nanoscale. Chemistry and Physics of Lipids 165, 845-60.

Pittenger, B, Erina, N, Su, C, 2010. Quantitative mechanical property mapping at the nanoscale with Peak Force QNM. Application Note Veeco Instruments Inc. p, 1-12. [Available on: https://www.bruker.com/fileadmin/user_upload/8-PDF-Docs/SurfaceAnalysis/AFM /ApplicationNotes/AN128-RevB0Quantitative_Mechanical_Property_Mapping_at_the_ Nanoscale_with_PeakForceQNM-AppNote.pdf] (Accessed on: 12th January 2020).

Quintarelli, G., Dellovo, M.C., Balduini, C., Castellani, A.A., 1969. The effects of alpha amylase on collagen-proteoglycans and collagen-glycoprotein complexes in connective tissue matrices. Histochemie 18, 373-375.

Romero-Jiménez, M., Santodomingo-Rubido, J., Wolffsohn, J., 2010. Keratoconus: A review. Contact Lens and Anterior Eye 33(4), 157-166.

Seppälä, H., Määttä, M., Rautia, M., Mackiewicz, Z., Tuisku, I., Tervo, T., Konttinen, Y., 2006. EMMPRIN and MMP-1 in Keratoconus. Cornea 25, 325-330.

Shah, K., Goh, J., Karunanithy, R., Low, S., Das, S., Bose, K., 1995. Effect of decalcification on bone mineral content and bending strength of feline femur. Calcified Tissue International 56(1), 78-82.

Sherman, V.R., Yang, W., Meyers, M.A., 2015. The materials science of collagen. Journal of the Mechanical Behavior of Biomedical Materials 52, 22-50.

Spoerl, E., Teral, N., Raiskup, F., Pillunat, L., 2012. Amylase reduces the biomechanical stiffness of the cornea. Investigative Ophthalmology & Visual Science 53(14), 1531-1531.

Stolz, M., Raiteri, R., Daniels, A.U., VanLandingham, M., Baschong, W., Aebi, U., 2004. Dynamic elastic modulus of porcine articular cartilage determined at two different levels of tissue organization by indentation-type atomic force microscopy. Biophysical Journal 86(5), 3269-3283.

Tanaka, E., Aoyama, J., Tanaka, M., Van Eijden, T., Sugiyama, M., Hanaoka, K., Watanabe, M., Tanne, K., 2003. The proteoglycan contents of the temporomandibular joint disc influence its dynamic viscoelastic properties. Journal of Biomedical Materials Research 65, 386-92.

Van der Kraan, P.M., Vitters, E.L., van Beuningen, H.M., van de Putte, L.B., van den Berg, W.B., 1990. Degenerative knee joint lesions in mice after a single intra-articular collagenase injection. A new model of osteoarthritis. Journal of Experimental Pathology (Oxford, England) 71(1), 19-31.

Van Haeringen, N.J., Ensink, F., Glasius, E., 1975. Amylase in human tear fluid: Origin and characteristics, compared with salivary and urinary amylases. Experimental Eye Research 21, 395-403.

Volatier, T.L., Figueiredo, F.C, Connon, C.J., 2019. Keratoconus at a molecular level: A review. The Anatomical Record 1,1-5. [doi:10.1002/ar.24090].

Wollensak, G., Spörl, E., Mazzotta, C., Kalinski, T, Sel, S., 2011. Interlamellar cohesion after corneal crosslinking using riboflavin and ultraviolet A light. British Journal of Ophthalmology 95, 876-880.

Xia, D., Zhang, S., Hjortdal, J., Li, Q., Thomsen, K., Chevallier, J., Besenbacher, F., Dong, M., 2014. Hydrated human corneal stroma revealed by quantitative dynamic atomic force microscopy at nanoscale. ACS Nano 8(7), 6873-6882.

Young, Monclus, Burnett, Broughton, Ogin, Smith, 2011. The use of the PeakForce™ quantitative nanomechanical mapping AFM-based method for high-resolution Young's modulus measurement of polymers. Measurement Science and Technology 22, 125703.

Zhang, F., Zhang, Z., Linhsrdt, R.J., 2009. Glycosaminoglycans. Elsevier, USA, p. 59-80.

Zhuola, 2018. The role of proteoglycans in the ultrastructure and mechanical properties of the sclera. (PhD thesis), University of Liverpool, United Kingdom.

Chapter 8

Discussion, conclusions and further Work

This chapter summarises the main outcomes of this thesis. In this chapter, an empirical biomechanical model for keratoconus is proposed. Conclusions of the thesis are summarised in this chapter. Suggestions for future work are also made in this chapter.

8.1. Summary of findings

Literature showed that the cornea plays an important role in ocular system, which acts as the primary infectious and structural barrier of the internal delicate contents of the eye. It is characterised by its transparency and geometrical features such as corneal thickness, in which its ultrastructural details are greatly responsible for these features. The ultrastructure of the corneal stroma consists of organised collagenous bundles that are associated with proteoglycans. This organisation exhibits the cornea its unique shape and strength. Investigation of ultrastructural details, including collagen fibril diameter and D-periodicity, might help better understand the progress of corneal diseases and aid in development of therapeutic methods.

Many diseases affect the cornea and distort vision such as keratoconus. It is characterised by localised reduction in corneal thickness that develops a conical protrusion near the apex. Keratoconus deteriorates the cornea gradually and distorts the vision if no treatment procedure is performed such as ultraviolet corneal cross-linking with Riboflavin (CXL). It is wildly believed that the initial progress of keratoconus starts at the nanoscale structure, at which the collagenous network suffers of ultrastructural changes. However, these changes have not been fully investigated in keratoconic corneas due to limited availability of the samples.

The cornea is exposed to varying enzymes, some of them have digestive actions such as amylase and collagenase. Both enzymes were found to increase in Keratoconus. Amylase has been found to deplete proteoglycans from collagenous tissues such as tendons, discs, and corneas. Collagenase has been approved for modelling of collagenous tissue (Honig, 2014) such as Dupuytren's cords in the hand (Hurst *et al*, 2009). Therefore, in this thesis, both enzymes were utilised to initially investigate their effect on the corneas in terms of biomechanical and optical properties. For investigating these properties, therefore, different methods were needed to measure biomechanical properties at different scales along with spectrophotometric method for measuring corneal transparency. Ultrastructural changes in collagen fibril diameters and D-periodicity were assessed following incubation of corneal samples with varying concentration of amylase and collagenase.

Measurements of biomechanical properties of the cornea are influenced by many factors such as testing scale, hydration, and initial applied forces. In Chapter 3, microscale biomechanical properties (shear storage modulus (G') and shear loss modulus (G'')), for inflated corneas at intraocular pressures (IOPs) from 0 - 60 mmHg, were measured with oscillatory nanoindentation. Elastic modulus (E) was calculated at different locations on the corneas (central cornea to limbus).

The effect of using varying inflation solutions (tissue culture (TC) and phosphate buffered saline (PBS) solutions) on viscoelastic properties and central corneal thickness (CCT) were assessed. It was found that G′ and G″ were increased in an approximate linear relationship with IOP. The loss factor, or tan(δ), (G"/G′) was decreased as the IOP increased. Biomechanical and CCT of corneas were affected in prolonged incubation with PBS. It was found that TC was more appropriate for incubation the corneas than PBS. The central cornea appeared to have a higher elastic modulus than the peripheral region, but much less than in the limbus. The anisotropy of biomechanical properties of the cornea is a function of IOP, where anisotropy increases at lower IOPs.

In Chapter 4, biomechanical properties and geometrical features of inflated porcine corneas were measured using Line field-optical coherence tomography (LF-OCT). Geometrical properties, including CCT and corneal radius, tangential elastic modulus (E_t) and corneal hysteresis (CH) were measured at different IOPs (0 - 60 mmHg) for 4 hours. CCT was decreased with IOP, whereas Et was increased in a linear function with IOP. CCT, Et and CH were increased in prolong hydration in PBS. This finding verifies the obtained results in Chapter 3, where G′ and G″ were also increased with IOP and raised with hydration time.

In Chapter 5, percentage light transmission (%T) and the linear absorption coefficient (μa) of the visible spectrum through inflated porcine corneas at varying IOPs was assessed using a spectrophotometry. The role of TC and PBS (used for corneas incubation) on %T was investigated for 4 hours. %T was quantitatively mapped for inflated corneas. The contribution of epithelium layer to the total %T of the cornea was assessed. The maximum %T was found at wavelength of 700 nm and 15 mmHg. The %T was decreased whether the IOP increased or decreased. %T in central cornea was higher than in other regions. Incubation of corneas in PBS and TC for more than 30 min decreases corneal transparency. The epithelium has a negligible effect on %T across the corneas.

In Chapter 6, the above parameters were then measured following incubation of porcine corneas in varying concentrations of alpha amylase and collagenase (crude and purified). The corneas were incubated in TC contained varying concentrations of the enzymes for different periods (0.5, 1, 2, 3, 4, 24 and 48 hours) at 37.5°C. Since the anisotropy of biomechanical and optical properties was less in inflated corneas (Chapter 3), all samples were measured at 15 mmHg and only at corneal apex. It was found that the viscoelastic parameters (G′, G″, E_t and CH) and CCT were decreased as a function of enzyme concentration and incubation period. tan(δ) was only decreased in corneas

following incubation with crude collagenase. Collagenase (crude and purified) has stronger effect in reduction of the viscoelastic parameters and CCT than amylase. Incubation of corneas with crude collagenase led to a greater reduction in viscoelastic parameters and CCT than incubation with purified collagenase. Corneal transparency was decreased in samples incubated with TC (only) for 4 hours. The transparency was increased in theses corneas following incubation with amylase and/or collagenase (crude and purified). The maximum transparency was seen in corneas incubated with purified collagenase, in which corneal transparency was higher than the normal-untreated corneas.

In chapter 7, collagen fibril morphological changes following incubation with amylase and collagenase (crude and purified) was assessed and correlated to elastic modulus of the samples. Anterior stromal sections were treated with varying of concentration of the enzymes and then tested by atomic force microscopy (AFM) to capture nanoscale topographical details (diameter and D-periodicity of collagen fibrils) along with their elastic modulus. Collagen fibril diameter was decreased in samples which were incubated with either enzyme. However, collagen fibril D-periodicity was only reduced following incubation with collagenase (crude and purified). Elastic modulus was reduced in all corneal samples following incubation with the enzymes. This reduction in diameter and D-periodicity of collagen fibrils and the elastic modulus of the samples was a function of enzyme concentration. The effect of collagenase effect was more pronounced than amylase. Crude collagenase has stronger effect on the samples than purified collagenase. A direct correlation was found between collagen fibril morphology and elastic modulus of the samples. The outcomes of this chapter verify those from Chapter 6.

The work presented here has significant potential for glaucoma research. However, a detailed coverage of glaucoma is beyond the scope of this thesis. In Chapters 3 and 4 measurements combined IOP, CCT and corneal biomechanics along with enzymatic degradation that can easily be applied to understand the impact of glaucoma and various other corneal diseases. Increased IOP is a primary risk factor for glaucoma development, where IOP evaluation is used to assess glaucoma control and treatment response, and lowering IOP has resulted in reducing the rates of glaucoma progression over 5 years (Bolivar *et al*, 2013). Therefore, accurate IOP measurement is critical in glaucoma. Goldmann applanation tonometry, which is the gold standard for measuring IOP, estimates the IOP based on the force needed to flatten the corneal apex. This measurement is then based on a number of assumptions about corneal deformability (corneal biomechanics), which is affected by collagen types, corneal hydration, collagen fibril density, ECM, CCT and other

factors that vary among individuals. These factors determine, to some extent, the response of the corneoscleral shell to the force applied during the measurement of IOP, where it was found that corneal viscoelastic properties including CH decrease in glaucomatous eyes (Congdon *et al*, 2006; Demea *et al*, 2015).

Studies also found that CCT is associated with glaucoma progression. Based on the ocular hypertension studies, CCT has become an important factor in glaucoma, where CCT was significantly decreased in patients with ocular hypertension who are at higher risk of developing glaucoma. (Congdon *et al*, 2006; Medeiros and Weinreb, 2012). The reduction of CCT in patients with glaucoma was attributed to involvement of collagen genes influencing CCT and thus, possibly the pathogenesis of glaucoma (Vithana *et al*, 2011). Corneal enzymatic degradation, proposed in Chapter 6, digests collagen fibrils and other ECM that leads to reduction in both corneal thickness and stiffness. This empirical model then can be also utilised to study how the geometrical and biomechanical changes of the cornea with elevated IOP could affect the measurements and management of glaucoma

8.2. Empirical biomechanical model for keratoconus

Keratoconus is a disorder where the cornea becomes progressively thinner causing the cornea to bulge outwards in an irregular cone shape and that deteriorate the vision. The earliest signs of this disease are often diagnosed in young age individuals. Early stages of keratoconus are normally treated with lenses and corneal cross-linking (CXL) technique that has become a widely available treatment to stop progression of the disease. In patients with advanced keratoconus, corneal transplant surgery aims to restore sight. With early detection of keratoconus in youths, physicians prioritise the CXL treatment, which limits the need for corneal transplant surgery. Therefore, the effective contribution of CXL treatment in stopping the progression of keratoconus has reduced the availability of the corneal samples for *ex vivo* biomechanical experiments (Vellara and Patel, 2015).

In this study, porcine corneas were chosen due to their availability and high degree of similarity to the human corneas. In many *ex vivo* studies, where further investigation is needed or the sample size is large, porcine corneas have been utilised as an alternative for human corneas (Asejczyk-Widlicka *et al*, 2008; Boschetti *et al*, 2012; Elsheikh *et al*, 2008; Kling and Hafezi, 2017; Menduni *et al*, 2018; Wollensak and Spoerl, 2004; Zeng *et al*, 2001) .

A few studies have used human keratoconic corneas for measuring the elasticity using different approaches. These studies are summarised in Chapter 2, Table 2.2. These studies cannot provide a complete information to build a model, in which parameters for grading the severity of the disease were missing. Most of the studies that have assessed viscoelasticity of keratoconus in human corneas were *in vivo* experiments using Ocular Response Analyzer (ORA) and CorVis ST dynamic Scheimpflug analyser (CST) (Ortiz *et al*, 2007; Shah *et al*, 2007; Touboul *et al*, 2011). Progression of keratoconus was presented by Shah *et al* (2007) and sorted in grades at which CH and CCT decreased with severity of the disease (Chapter 2, Table 2.1). This grading for progression will be used to build an empirical model of enzymatic treated porcine corneas that reflect the biomechanical and optical properties of the human keratoconus at different progression stages. This model was based on using CH and CCT to grade progression conditions of the keratoconus.

Table 8.1 presents enzymatic treated porcine corneas as an empirical biomechanical model for keratoconus. This was made on the bases of the outcomes from Chapter 6. In this table, the ratio of CH and CCT reduction in keratoconus to the normal human corneas was utilised as guideline to select the most appropriate enzymatic treatment on porcine cornea that generates similar reduction in CH and CCT, at which the corresponding viscoelastic parameters were presented in the table.

A pilot study was conducted to assess the response of the enzymatic treated corneas to CXL treatment (Appendix IV). The study examined G' and G" of enzymatic treated corneas in normal, moderate and severe keratoconus stage. Following applying Riboflavin and ultraviolet light doses on corneas, G' and G" were increased by approximately 40% and 20%, respectively. This pilot study confirms the response of the enzymatic degraded corneas to CXL treatment; hence this suggested enzymatic treatment can be utilised to provide corneas for CXL *ex vivo* research.

Table 8.1: A suggested enzymatic treatment for porcine corneas that match biomechanical properties of varying keratoconus grading.

Condition	Human corneas				Porcine corneas						
	CH (mmHg)	CCT (µm)	Reduction in CH (%)	Reduction in CCT (%)	CH (mmHg)	CCT (µm)	G' (kPa)	G" (kPa)	Et (kPa)	%T	Enzymatic incubation summary
Normal cornea	10.7±2.0	545.0±36	0	0	10.87±0.4	988.3±15	85.2±9.7	12.9±2.3	204.5±12	86.8±0.76	Normal corneas
Mild keratoconus	10.3±2.1	523.1±44	3.7	4	10.28±0.7	909±17	78.5±9.8	11.9±2	190.1±24	86.01±0.5	A cornea button needs to be incubated and slightly shaken in a solution for 2 hours at 37.5oC. The solution consists of amylase (30 mg/ml) in 4 ml TC. The cornea should be snap-washed with PBS(4ºC) then washed with α-amylase inhibitor (1 mg/ml) for 3 min.
Moderate keratoconus	9.7±2.4	487.0±52	9.3	10.6	9.82±0.8	890±13.2	70.7±7.8	10.2±1.8	178.01±19	86.19±0.8	A cornea button needs to be incubated and slightly shaken in a solution for 1 hour at 37.5oC. The solution consists of amylase (10 mg/ml) and purified collagenase (1 mg/ml) in 4 ml TC. The cornea should be snap-washed with PBS(4ºC) then washed with NaEDTA (5 mg/ml) for 3 min.
Severe keratoconus	9.0±2.1	470.2±53	15.8	13.7	9.16±0.5	860.2±18	59.9±6.7	8.5±1.9	150.5±17	86.9±0.91	A cornea button needs to be incubated and slightly shaken in a solution for 2 hours at 37.5oC. The solution consists of amylase (30 mg/ml) and purified collagenase (1 mg/ml) in 4 ml TC. The cornea should be snap-washed with PBS(4ºC) then washed with NaEDTA (5 mg/ml) for 3 min.

'CH', 'CCT', 'G'', 'G'", 'Et', '%T', 'PBS', 'TC', and 'NaEDTA' refer to corneal hysteresis, central corneal thickness, share storage modulus, shear loss modulus, tangential elastic modulus, percentage light transmission, phosphate buffer saline solution, corneal tissue culture, and dichloromethylene diphosphonic acid disodium, respectively. Human corneas section of the table was adopted from Shah *et al* (2007), explained in Chapter 2. Whereas, porcine corneas section was obtained from Chapter 6, in which n = 8 corneas/cell. The values are presented in 'mean ± standard deviation' form.

One limitation of this approach is that the corneas in this empirical model were totally immersed in the enzymes, which causes reduction in biomechanical properties and CCT of whole the corneas (no localised conical protrusion and stiffness changes as expected clinically). However, keratoconic corneas are clinically characterised by a localised thinning with reduction in stiffness (Rabinowitz, 1998). Another limitation in the current enzymatic treatment is the corneas were subjected to enzymes from the anterior and posterior surfaces of the corneas and diffused into the tissue, which makes the outer lamellae of the stroma more affected than the central lamellae. Whereas, in keratoconic corneas, it is expected the enzymes are released inside the tissue and the anterior lamellae are more subjected the effect of the enzymes (Seppälä *et al*, 2006). Histopathologically, Keratoconic corneas can be diagnosed by observing iron deposition in basal cells of corneal epithelium (Fleischer's ring), as explained in section 2.9.6 (Chapter 2). One more limitation of this model is removal of the epithelium layer from the corneas, which made it impossible to examine a possible relationship between iron deposition and the reduction in the thickness and stiffness of the treated corneas. These three limitations of the current treatment could be overcome with localised injection for the enzymes using a microneedle.

The work presented here has significant potential for glaucoma research. However, a detailed coverage of glaucoma is beyond the scope of this thesis. In Chapters 3 and 4 measurements combined IOP, CCT and corneal biomechanics along with enzymatic degradation that can easily be applied to understand the impact of glaucoma and various other corneal diseases. Increased IOP is a primary risk factor for glaucoma development, where IOP evaluation is used to assess glaucoma control and treatment response, and lowering IOP has resulted in reducing the rates of glaucoma progression over 5 years (Bolivar *et al*, 2013). Therefore, accurate IOP measurement is critical in glaucoma. Goldmann applanation tonometry, which is the gold standard for measuring IOP, estimates the IOP based on the force needed to flatten the corneal apex. This measurement is then based on a number of assumptions about corneal deformability (corneal biomechanics), which is affected by collagen types, corneal hydration, collagen fibril density, ECM, CCT and other factors that vary among individuals. These factors determine, to some extent, the response of the corneoscleral shell to the force applied during the measurement of IOP, where it was found that corneal viscoelastic properties including CH decrease in glaucomatous eyes (Congdon *et al*, 2006; Demea *et al*, 2015).

Although raised IOP has traditionally been thought to be the major risk factor for glaucoma, emerging evidence suggests that corneal thickness could also be a predictor of glaucoma

development, particularly in individuals with higher baseline IOP. Studies also found that CCT is associated with glaucoma progression. Based on the results of ocular hypertension studies, CCT has become an important factor in glaucoma, where CCT was significantly decreased in patients with ocular hypertension who are at higher risk of developing glaucoma. (Congdon *et al*, 2006; Medeiros and Weinreb, 2012). The reduction of CCT in patients with glaucoma was attributed to involvement of collagen genes influencing CCT and thus, possibly the pathogenesis of glaucoma (Lu *et al*, 2010; Vithana *et al*, 2011). Corneal enzymatic degradation, proposed in Chapter 6, digests collagen fibrils and other ECM that leads to reduction in both corneal thickness and stiffness. Therefore, this empirical model could also be utilised to study how the geometrical and biomechanical changes of the cornea with elevated IOP could affect the measurements and management of glaucoma.

8.3. Conclusions

There are key findings and conclusions in this work that may contribute to the fields of corneal biomechanics, corneal ultrastructure, *in vitro* enzymatic degradation of the cornea and pathogenesis of keratoconus.

The first objective of this thesis was to explore the utility of the oscillatory nanoindentation for measuring localised nanomechanical properties of porcine corneas, and how these properties are changed with IOP and swelling of the corneas. This thesis found that the biomechanical properties of the cornea are a function of IOP and hydration. Corneas seem to be stiffer with increased swelling. Corneal apex was found to be stiffer than paracentral and peripheral regions of the cornea.

The second objective of this thesis was to combine inflation testing with LF-OCT to provide a better assessment for the corneal biomechanical behaviour at macroscale length. This method validated the biomechanical behaviour of corneas obtained from oscillatory nanoindentation. Corneal hysteresis was found to increase with corneal swelling. IOP has an important role in determination of biomechanical and geometrical properties of the corneas. The corneas show non-linear elastic behaviour, where corneas seem to be stiffer at high deformations.

The third objective was to assess the optical properties of the cornea that were found to be a function of IOP and hydration. The optimal transparency of the cornea was found to be

physiological pressure and hydration. IOPs higher than the physiological pressure were found to decrease corneal transparency. The corneal apex was found to be more transparent than other regions of the cornea, and corneal thickness was not the major parameter for this behaviour.

The fourth objective was examined the effect of amylase and collagenase on biomechanical (at microscale and macroscale), optical and geometrical properties of corneas that were found to be influenced by digestive enzymes (α-amylase and collagenase). Ultrastructural details and nonmechanical properties were also investigated using AFM that was found to validate the biomechanical properties at larger scales. α-amylase was found to deplete proteoglycans of the corneal stroma, which can cause a disruption in collagen fibrils distribution and a reduction in collagen fibril diameter without affecting molecular structure of collagen fibrils (D-periodicity). Collagenases (crude and purified) degraded the molecular structure of collagen fibrils and reduced their diameters, and incubation of corneas with collagenases was found to lead to more reduction in stiffness than incubation with α-amylase. Crude collagenase has more aggressive action on corneal tissue than purified collagenase. Proteoglycans depletion and collagen degradation, following incubation with the enzymes resulted in significant reduction in nanoscale, microscale and macroscale mechanical properties of the cornea. However, the enzymatic treatment increased corneal transparency. Proteoglycans depletion and collagen degradation are a function of enzyme (amylase and collagenase) concentrations and treatment periods. Collectively, the data obtained in this thesis suggest that keratoconus may commence with nanoscale alterations which include molecular changes in extracellular matrix.

8.4. Future work

Based on the findings of this study, some suggestions are recommended for the future. Oscillatory nanoindentation was utilised to assess micromechanical properties of the anterior surface the stromal layer of inflated porcine corneas (Chapter 3). Applying this method to quantify micromechanical properties of other layers can help build more accurate numerical models of the cornea. In addition, the setup used for varying IOP could be used for other tissues e.g. for arterial samples to help assessing viscoelastic properties of the arteries in response to varying blood pressures.

The oscillatory nanoindentation has potential to be used to study localised differences between regions of healthy and diseased tissue. Utilising this method to assess viscoelastic properties of human corneas at varying IOP and to differentiate between healthy and diseased locations such as

in keratoconus and other disorders may contribute in providing better characterisation of the diseases.

Inflation testing with LF-OCT addressed geometrical changes and calculated biomechanical properties with varying IOP based on volumetric deformation of the cornea. The regional biomechanical properties of the intact eye globe (cornea and sclera) using inflation testing were assessed using a set of three cameras to monitor the deformation to the continuous increase in the eye globe volume (PBS injections) (Whitford *et al*, 2016). The study provided key findings; developing the test rig by employing LF-OCTs instead of the cameras can overcome the effect of optical and geometrical distortions caused by cameras that was explained by Li *et al* (2015). In addition, employing OCTs can provide the geometrical changes that can be correlated to biomechanical properties of the cornea and sclera.

Spectrophotometry of inflated porcine corneas quantified light transmission through different regions of the cornea, and provided a correlation between corneal transparency and IOP. The method can be utilised further to investigation of riboflavin absorption in human corneas, and to assess corneal transparency of other ocular diseases such as dry cornea and keratoconus.

Amylase can deplete proteoglycans that reduces biomechanical properties (Chapter 6 and 7). It was found that amylase secreted by lacrimal gland in tear fluid (Mylius, 1961; van Haeringen *et al*, 1975) and increase in patients with early stages of keratoconus (Legkikh *et al*, 2018). However, to the best of author's knowledge, the normal levels and concentration of amylase in tear fluid has not been well investigated, which can help in avoiding keratoconus progression. In addition, researches are needed to investigate the association of increased levels of amylase in tear fluid with other systematic diseases where the amylase activity increases such as in diabetes mellitus. Moreover, the type of affected proteoglycans by amylase is still unknown and it should be examined that can help understanding the collagen-proteoglycan interaction in connective tissue.

Collagenase is well known to digest collagen fibrils and been approved in connective tissue remodelling, where it reduces tissue stiffness (Honig, 2014). However, the role of this enzyme on other extracellular matrix components and proteome interactions has not been investigated.

Morphology of extracellular matrix of the cornea, including collagen fibril dimension and distribution, can provide important information about corneal disorders such as keratoconus. AFM is a very useful tool to investigate the morphological details of the cornea at nanoscale level. However, this tool has not been utilised to examine the ultrastructural details (collagen fibril diameters and D-periodicity) in keratoconic corneas samples.

8.5. References

Asejczyk-Widlicka, M., Schachar, R., Pierscionek, B., 2008. Optical coherence tomography measurements of the fresh porcine eye and response of the outer coats of the eye to volume increase. SPIE 13, 024002-1 - 024002-6.

Bolivar, G., Moreno-Arrones, J.P., Teus, M.A., 2013. Cornea and glaucoma. In: Rumelt, S. (eds) Glaucoma–Basic and Clinical Aspects (pp. 227- 249). IntechOpen. [DOI: 10.5772/53017].

Boschetti, Triacca, Spinelli, Pandolfi, 2012. Mechanical characterization of porcine corneas. Journal of Biomechanical Engineering 134, 031003.

Congdon, N., Broman, A., Bandeen-Roche, K., Grover, D., Quigley, H., 2006. Central corneal thickness and corneal hysteresis associated with glaucoma damage. American Journal of Ophthalmology 141, 868-875.

Demea, H., Demea, S., Holonec, R., Demea, A., 2015. The biophysical properties of cornea in analyzing glaucoma risk. Biophysics 67, 987-994.

Elsheikh, A., Alhasso, D., Rama, P., 2008. Biomechanical properties of human and porcine corneas. Experimental Eye Research 86, 783-790.

Honig, S.C., 2014. Intralesional collagenase in the treatment of Peyronie's disease. Therapeutic Advances in Urology 6(2), 47-53.

Hurst, L.C., Badalamente, M.A., Hentz, V.R., Hotchkiss, R.N., Kaplan, F.T., Meals, R.A., Smith, T.M., Rodzvilla, J., 2009. Injectable collagenase clostridium histolyticum for Dupuytren's contracture. New England Journal of Medicine. 361, 968-79.

Kling, S., Hafezi, F., 2017. Corneal biomechanics - a review. Ophthalmic & physiological optics : the journal of the British College of Ophthalmic Opticians (Optometrists) 37, 240-252.

Legkikh, L., Koledintsev, M., Semenova, A., Okuyama, K., 2017. Biochemical investigations of lacrima in early diagnosis of keratoconus. (Abstract) Sangubashi Eye Clinic, Japan. [available on: www.sangubashi.com/English/report/syanhai.htm] (accessed on: 12th January 2020).

Li, T., Tian, L., Wang, L., Hon, Y., Lam, A., Huang, Y., Wang, Y., Zheng, Y., 2015. Correction on the distortion of Scheimpflug imaging for dynamic central corneal thickness. Journal of Biomedical Optics 20, 056006-056006.

Lu, Y., Dimasi, D.P., Hysi, P.G., Hewitt, A.W., Burdon, K.P., Toh, T.Y., Ruddle, J.B., Li, Y.J., Mitchell, P., Healey, P.R., Montgomery, G.W., 2010. Common genetic variants near the brittle cornea syndrome locus ZNF469 influence the blinding disease risk factor central corneal thickness. PLoS Genetics 6(5).

Medeiros, F.A., Weinreb, R.N., 2012. Is corneal thickness an independent risk factor for glaucoma?. Ophthalmology, 119(3), pp.435-436.

Menduni, F., Davies, L., Madrid-Costa, Fratini, A., Wolffsohn, J., 2018. Characterisation of the porcine eyeball as an in-vitro model for dry eye. Contact Lens and Anterior Eye 41, 13-17.

Mylius, E.A., 1961. Amylase in tears? A histochemical study. Acta pathologica et microbiologica Scandinavica 148, 143-147.

Ortiz, D., Piñero, D., Shabayek, M., Arnalich-Montiel, F., Alió, J., 2007. Corneal biomechanical properties in normal, post-laser in situ keratomileusis, and keratoconic eyes. Journal of Cataract & Refractive Surgery 33, 1371-1375.

Rabinowitz, Y., 1998. Keratoconus. Survey of Ophthalmology 42(4), 297-319.

Seppälä, H., Määttä, M., Rautia, M., Mackiewicz, Z., Tuisku, I., Tervo, T., Konttinen, Y., 2006. EMMPRIN and MMP-1 in keratoconus. Cornea 25, 325-330.

Shah, S., Laiquzzaman, M., Bhojwani, R., Mantry, S., Cunliffe, I., 2007. Assessment of the biomechanical properties of the cornea with the ocular response analyzer in normal and keratoconic eyes. Investigative Ophthalmology & Visual Science 48, 3026-3031.

Touboul, D., Bénard, A., Mahmoud, A., Gallois, A., Colin, J., Roberts, C., 2011. Early biomechanical keratoconus pattern measured with an ocular response analyzer: Curve analysis. Journal of Cataract & Refractive Surgery 37, 2144-2150.

Van Haeringen, N.J., Ensink, F., Glasius, E., 1975. Amylase in human tear fluid: Origin and characteristics, compared with salivary and urinary amylases. Experimental Eye Research 21, 395-403.

Vellara, H., Patel, D., 2015. Biomechanical properties of the keratoconic cornea: a review. Clinical and Experimental Optometry 98, 31-38.

Vithana, E.N., Aung, T., Khor, C.C., Cornes, B.K., Tay, W.T., Sim, X., Lavanya, R., Wu, R., Zheng, Y., Hibberd, M.L., Chia, K.S., 2011. Collagen-related genes influence the glaucoma risk factor, central corneal thickness. Human Molecular Genetics 20(4), 649-658

Whitford, C., Joda, A., Jones, S., Bao, F., Rama, P., Elsheikh, A., 2016. *Ex vivo* testing of intact eye globes under inflation conditions to determine regional variation of mechanical stiffness. Eye and Vision 3(21), 1-12.

Wollensak, G., Spoerl, E., 2004. Collagen crosslinking of human and porcine sclera. Journal of Cataract & Refractive Surgery 30, 689-695.

Zeng, Y., Yang, J., Huang, K., Lee, Z., Lee, X., 2001. A comparison of biomechanical properties between human and porcine cornea. Journal of Biomechanics 34, 533-537.

Appendix I

Corneal holder used for oscillatory nanoindentation

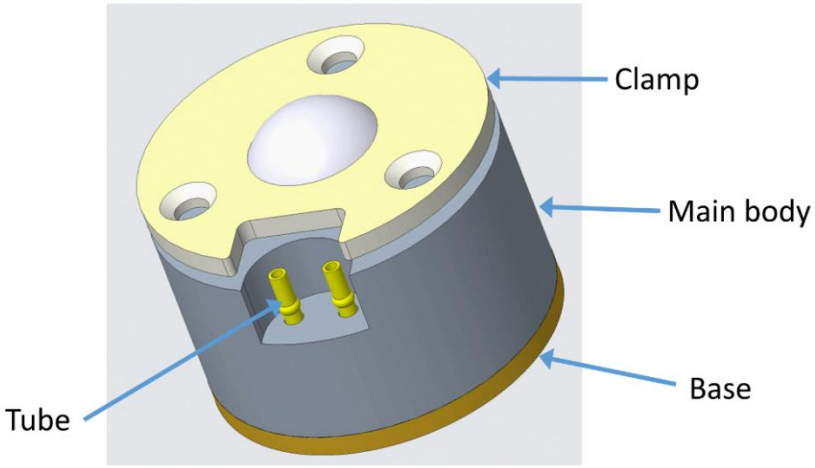

3D-view of the corneal holder

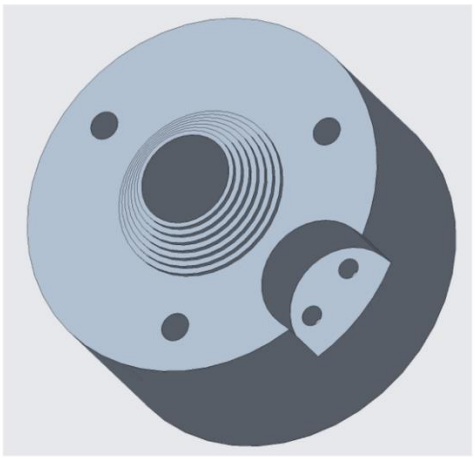

3D-view of the Main body

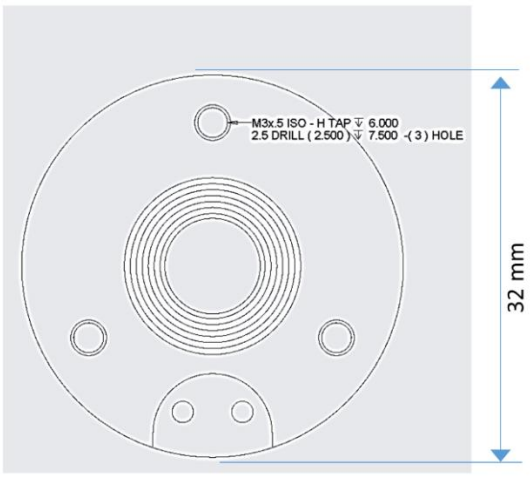

Top-view of the Main body

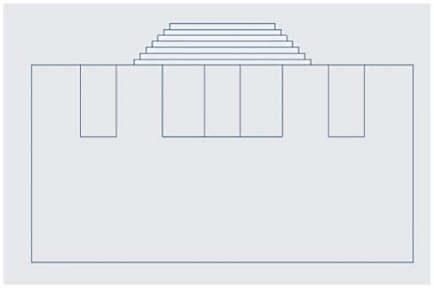

side-view of the Main body

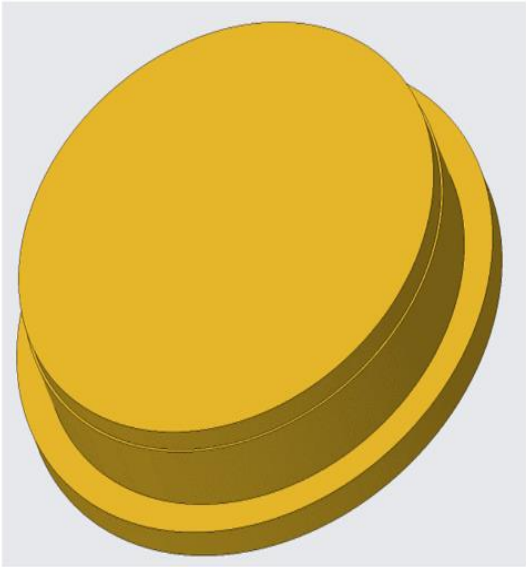

3D-view of the base

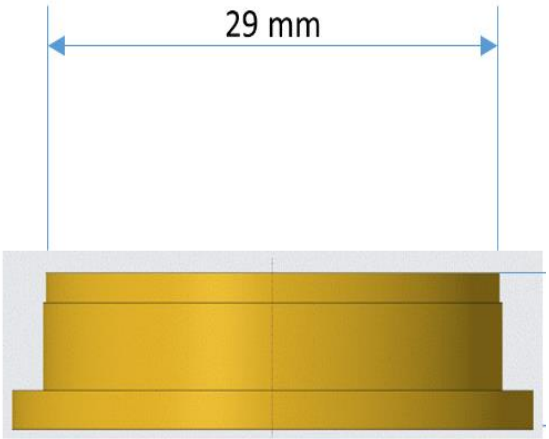

side-view of the base

3D-view of the clamp

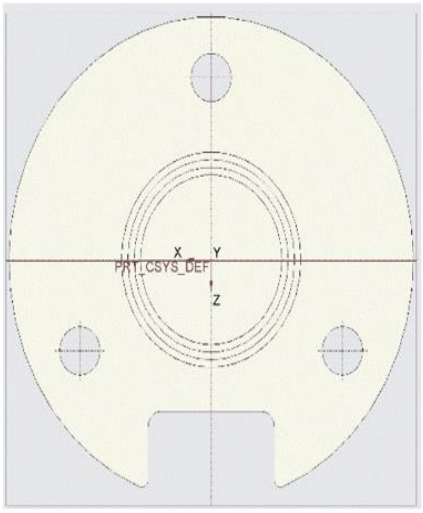

Bottom-view of the clamp

Appendix II

Viscoelastic properties and thickness of porcine corneas following enzymatic degradation

Table A2.1: Shear storage modulus (G') of porcine corneal buttons following incubation with varying concentrations of amylase and collagenases for different incubation periods.

Concentration (mg/ml)	Incubation time (hour)						
	0.5	1	2	3	4	24	48
Amy_10	84.46±16.28	83.52±17.16	79.94±15.88	77.64±16.11	76.78±15.04	74.22±14.07	72.52±15
Amy_20	82.59±16.55	80.96±15.62	78.23±16.48	75.85±15.36	74.65±14.35	70.04±14.08	67.06±13.25
Amy_30	81.65±17.11	79.51±16.28	76.87±15.37	74.82±15.41	73.63±14.7	65.69±13.85	61.85±11.87
CC_1	80.96±16.42	74.99±14.16	71.92±14.8	61.77±12.76	58.12±11.03	50.59±9.53	49.05±10.73
CC_2	78.23±15.05	67.31±13.87	55.97±11.37	49.65±10.59	44.96±9.52		
Amy_10+CC_1	80.2±15.74	73.2±14.19	66.55±13.99	54.6±11.59	46.92±9.35	38.39±7.82	35.83±6.72
Amy_20+CC_1	79.34±16.75	69.36±13.33	59.72±12.55	49.48±9.42	40.1±8.12	34.98±7.04	30.71±6.41
Amy_30+CC_1	77.64±16.18	64.58±13.27	53.75±11	44.36±9.35	37.54±8.16	32.42±5.95	
Amy_10+CC_2	75.5±15.57	62.96±13.35	48.88±9.61	41.55±7.39	34.98±6.76		
Amy_20+CC_2	73.97±15.66	60.4±12.47	46.92±9.48	39.24±7.04	33.27±6.89		
Amy_30+CC_2	72.6±13.92	57.93±11.78	45.22±8.62	36.6±6.8	31.43±5.79		
PC_1	81.9±15.43	78.49±15.91	72.52±13.98	66.55±13.2	63.64±12.5	57.59±12.2	56.31±11.53
Amy_10+PC_1	81.05±17	76.7±16.18	67.14±13.05	58.87±12.6	55.11±11.32	46.49±8.4	43.51±7.84
Amy_20+PC_1	79.77±15.8	70.64±14.78	59.46±11.89	52.72±9.83	48.54±10.53	46.15±9.44	
Amy_10+PC_2	77.89±15.67	68.08±14.1	57.76±12.4	50.93±9.47	46.41±8.43		
Amy_30+PC_2	76.95±15.61	66.63±13.91	56.39±11.9	49.91±10.68	45.39±9.29		

'Ámy', 'CC' and 'PC' refer to α-amylase, crude collagenase and purified collagenase, respectively. The number after the enzyme abbreviations refers to the concentration of the enzyme in the incubation solution. The values of G' are in kPa unit and represented in mean ±standard deviation. n = 8 corneas/cell. Corneas were inflated at 15 mmHg and measured using an oscillatory nanoindenter at corneal apex. Epithelium was removed. n = 8 corneas/cell.

Table A2.2: Shear loss modulus (G") of por10.8cine corneal buttons following incubation with varying concentrations of amylase and collagenases for different incubation periods.

Concentration (mg/ml)	Incubation time (hour)						
	0.5	1	2	3	4	24	48
Amy_10	13.1±2.6	12.5±2.5	12.5±2.7	11.6±2.6	11.5±2.9	11.4±2.1	11.9±2.5
Amy_20	12.2±2.3	12.7±3	11.3±2.8	11.3±2.5	11.6±1.8	10.9±2.1	11.2±2.1
Amy_30	11.9±2.4	12.2±2.7	11.9±2.1	10.8±2.4	10.8±2.6	11.5±2.2	10.7±2.3
CC_1	12.5±2.9	11.3±2.4	9.6±2.2	9.1±1.5	8.1±1.5	7.3±1.3	5.4±1.2
CC_2	12.7±2.7	10.5±1.9	8.2±1.7	5.4±1.1	4.5±0.9		
Amy_10+CC_1	12.1±2.5	11.1±2.7	7.5±3.4	5.4±1.4	5.1±1.7	4.6±1.5	4.3±1.3
Amy_20+CC_1	11.8±2.6	10.5±1.8	5.6±0.9	4.5±1.1	4.2±0.5	3.1±0.9	2.9±1.1
Amy_30+CC_1	12.1±2.3	9.3±2.5	6.5±1.3	4.08±0.9	3.1±1.1	3.1±1.1	
Amy_10+CC_2	12.1±1.9	10.7±2.3	7.4±1.6	4.1±1.3	3.1±1.1		
Amy_20+CC_2	12.1±2.2	7.8±2.1	5.455±1.1	3.4±1.1	3.1±0.9		
Amy_30+CC_2	11.2±2.3	6.5±1.4	4.1±1.2	1.6±0.9	2.2±0.9		
PC_1	12.7±2.6	12.5±2.5	10.9±1.9	9.2±2.4	8.8±1.6	7.5±1.3	6.4±1.4
Amy_10+PC_1	13.3±3.1	12.1±2.3	9.9±1.7	7.7±1.9	6.9±1.5	6.3±1.3	
Amy_20+PC_1	12.6±2.3	11.7±2.7	8.5±1.9	7.4±1.3	6.3±1.3	6.2±1.2	
Amy_10+PC_2	12.1±2.9	10.9±2.1	7.5±1.8	6.7±1.1	5.6±1.4	4.7±1.3	
Amy_30+PC_2	12.3±2.8	10.1±2.3	7.2±1.9	6.3±1.4	5.3±1.4		

'Ámy', 'CC' and 'PC' refer to α-amylase, crude collagenase and purified collagenase, respectively. The number after the enzyme abbreviations refers to the concentration of the enzyme in the incubation solution. The values of G" are in kPa unit and represented in mean ±standard deviation. Corneas were inflated at 15 mmHg and measured using an oscillatory nanoindenter at corneal apex. Epithelium was removed. n = 8 corneas/cell. Enzymes were mixed with tissue culture.

Table A2.3: Tangential elastic modulus (E_t) of porcine corneal buttons following incubation with varying concentrations of amylase and collagenases for different incubation periods.

Concentration (mg/ml)	Incubation time (hour)						
	0.5	1	2	3	4	24	48
Amy_10	210.6±24.5	205±24.6	199.7±24.6	190.8±23.9	190.2±21	184.6±21.8	178.2±23.1
Amy_20	204.4±26.4	202.2±23.2	191.8±25.1	189.4±23.5	184.5±24.2	174.7±21.3	164.3±19.1
Amy_30	204.1±26	198.9±23.3	190±24.6	183.4±22.1	182.4±20.5	161.5±20.6	152.2±18.2
CC_1	200.8±25.2	184.4±23.1	180±23.3	153.2±17.1	142.5±16.7	124.4±14.9	120.9±15.7
CC_2	195.4±22.7	167.1±21.9	136.6±19.2	123±14	113.2±15.4	112.7±13	
Amy_10+CC_1	198.5±23.8	182±21.3	164±20.3	134.6±15.3	115.9±13	93.5±11.3	87.7±13.4
Amy_20+CC_1	198±23.6	170.5±22.8	148.7±19.1	121.3±14.4	99.4±11.6	87±10.5	77.2±10.3
Amy_30+CC_1	194.1±23.5	161.8±20.1	131.9±16.9	109.1±13.7	93.2±11.2	79.6±12.3	
Amy_10+CC_2	186±21.7	156.3±20.5	122.9±14	101.2±13.8	86.2±13.5		
Amy_20+CC_2	183.4±23.6	151.1±17.5	118.1±13.3	99.1±11.5	83.2±12.4		
Amy_30+CC_2	180.1±21	142.2±18.8	113.1±13.2	90.7±12	76.3±8.6		
PC_1	201.9±26.3	194.8±21.4	179.8±20.5	165.6±19	157.9±20.2	141.6±19.1	141.1±16.8
Amy_10+PC_1	199±24.4	190.3±21.3	165.3±22.2	144.7±18.6	135.6±17.9	115.8±16.2	108.8±15.3
Amy_20+PC_1	197.9±23.9	175.7±20	145.5±17.9	128.8±17.8	120.3±16.9	113.2±13.8	108.9±12.6
Amy_10+PC_2	192.3±21.6	167.7±20.1	144.3±17.3	125.2±17.5	115.8±15.9	91.9±13.2	
Amy_30+PC_2	188.2±23.2	164.1±21.3	140±18.2	124.9±16.5	113±13.2		

'Ámy', 'CC' and 'PC' refer to α-amylase, crude collagenase and purified collagenase, respectively. The number after the enzyme abbreviations refers to the concentration of the enzyme in the incubation solution. The values of E_t are in kPa and represented in mean ±standard deviation. Corneas were inflated at 15 mmHg and measured using an inflation method and OCT. Epithelium was removed. Enzymes were mixed with tissue culture. n = 8 corneas/cell.

Table A2.4: Corneal hysteresis (CH) of porcine corneal buttons following incubation with varying concentrations of amylase and collagenases for different incubation periods.

Concentration (mg/ml)	Incubation time (hour)						
	0.5	1	2	3	4	24	48
Amy_10	10.57±0.52	10.57±0.52	10.05±0.5	10.57±0.52	10.8±0.54	10.8±0.54	10.87±0.54
Amy_20	10.27±0.51	11.02±0.55	11.02±0.55	10.27±0.51	10.42±0.52	9.97±0.49	10.42±0.52
Amy_30	10.72±0.53	11.02±0.55	10.65±0.53	9.52±0.47	9.6±0.48	9.52±0.47	10.5±0.52
CC_1	10.05±0.5	9.3±0.46	10.05±0.5	9.07±0.45	9.52±0.47	9.15±0.45	8.77±0.43
CC_2	10.42±0.52	8.92±0.44	8.17±0.4	8.17±0.4	7.2±0.36		
Amy_10+CC_1	10.27±0.51	9.6±0.48	8.92±0.44	8.55±0.42	8.25±0.41	7.95±0.39	7.87±0.39
Amy_20+CC_1	10.2±0.51	9.67±0.48	8.92±0.44	8.55±0.42	8.17±0.4	7.87±0.39	7.8±0.39
Amy_30+CC_1	10.27±0.51	9.6±0.48	8.92±0.44	8.47±0.42	8.17±0.4	7.95±0.39	
Amy_10+CC_2	9.97±0.49	9.07±0.45	8.02±0.4	7.27±0.36	6.97±0.34		
Amy_20+CC_2	10.05±0.5	9±0.45	8.02±0.4	7.27±0.36	6.9±0.34		
Amy_30+CC_2	9.97±0.49	9±0.45	7.95±0.39	7.27±0.36	6.82±0.34		
PC_1	10.5±0.52	10.05±0.5	9.6±0.48	9.37±0.46	9.15±0.45	8.92±0.44	8.92±0.44
Amy_10+PC_1	10.35±0.51	9.82±0.49	9.3±0.46	8.85±0.44	8.62±0.43	8.4±0.42	8.32±0.41
Amy_20+PC_1	10.2±0.51	9.52±0.47	8.7±0.43	8.25±0.41	7.87±0.39	7.5±0.37	
Amy_10+PC_2	10.12±0.5	9.45±0.47	8.7±0.43	8.17±0.4	7.87±0.39		
Amy_30+PC_2	10.12±0.5	9.37±0.46	8.7±0.43	8.17±0.4	7.87±0.39		

'Ámy', 'CC' and 'PC' refer to α-amylase, crude collagenase and purified collagenase, respectively. The number after the enzyme abbreviations refers to the concentration of the enzyme in the incubation solution. The values of CH are in mmHg and represented in mean ±standard deviation. Corneas were inflated at 15 mmHg and measured using an inflation method and OCT. Epithelium was removed. Enzymes were mixed with tissue culture. n = 8 corneas/cell.

Table A2.5: Central corneal thickness (CCT) of porcine corneal buttons following incubation with varying concentrations of amylase and collagenases for different incubation periods.

Concentration (mg/ml)	Incubation time (hour)						
	0.5	1	2	3	4	24	48
Amy_10	989.1±11.5	999.1±11.4	936.2±11.2	909.5±10.7	898.5±9.1	850.9±7.8	845.1±10.3
Amy_20	967.1±10.8	950.2±15.4	916±9.4	889.1±10.8	878.8±9.10	848.7±11.7	849.5±12.2
Amy_30	956.8±11.5	932.1±10.8	901.3±10.1	876.7±10.1	862.7±10.6	768.8±8.2	768.7±8.6
CC_1	961.2±17	917.3±18.4	856.3±11.5	811.4±14.9	758.4±9.4	758±15.5	761.4±15.5
CC_2	972.8±20.1	882±20.4	823.2±8.6	757±13.1	721.9±11.9		
Amy_10+CC_1	945.6±12.6	919.1±10.7	889.5±9.8	849.8±10.1	840.2±9.4	869.7±51.8	834.7±16.3
Amy_20+CC_1	959.8±11	920.1±10.7	877.6±12.7	850.8±9.4	820.3±12.3	796.4±7.3	796.4±7.3
Amy_30+CC_1	928.1±14.9	893.5±11	883.7±14.9	813.8±19.1	796.8±11.2	772±16.7	
Amy_10+CC_2	950.1±14.1	891.4±15.9	839.9±11.7	798.5±19	754.2±10.2		
Amy_20+CC_2	942.2±14.4	872.7±12.9	820.9±15.9	784.8±13.8	729.3±12.4		
Amy_30+CC_2	898.3±18.1	847.1±10.8	804.6±14.5	762±17.1	714.3±13.4		
PC_1	970.7±12.7	947±19.4	897±18.4	829±7.5	791.8±12	785.3±15.4	758.1±13.6
Amy_10+PC_1	981.8±18.7	927.3±15	897.8±18.8	847.8±14.5	809±16.8	781.7±14	
Amy_20+PC_1	974.8±14.8	906.4±18.6	851.3±8.4	817.6±15.4	791.4±14.3	759±7.8	
Amy_10+PC_2	967.2±11.8	864.6±16	805.5±11.5	781.4±17	756.7±18	741.9±10.5	
Amy_30+PC_2	961.3±18.9	838±17.9	795.7±11.3	762.3±12.5	763.2±17.8		

'Ámy', 'CC' and 'PC' refer to α-amylase, crude collagenase and purified collagenase, respectively. The number after the enzyme abbreviations refers to the concentration of the enzyme in the incubation solution. The values of CCT are in μm and represented in mean ±standard deviation. Corneas were inflated at 15 mmHg and measured using an OCT. Epithelium was removed. Enzymes were mixed with tissue culture. n = 8 corneas/cell.

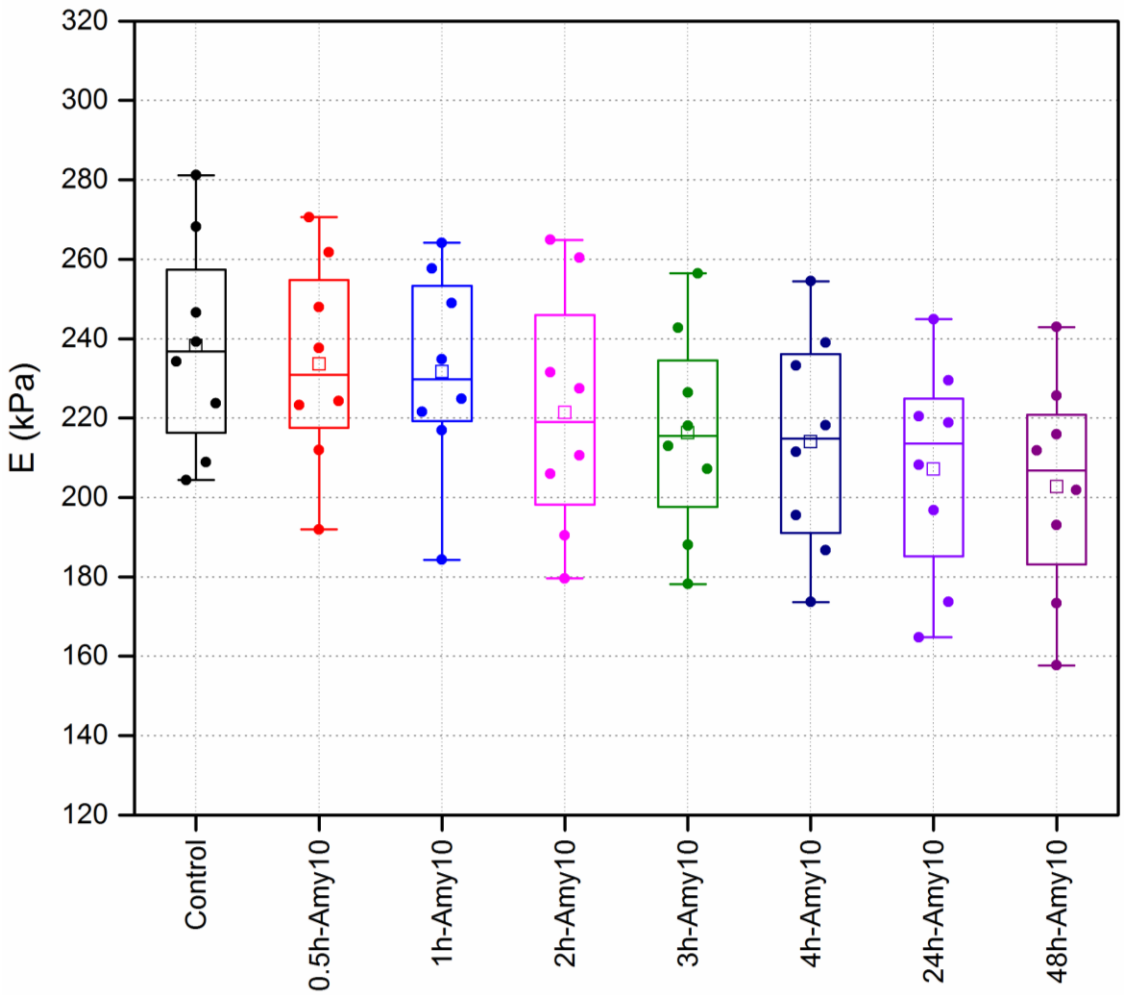

Figure 2A.1: Elastic modulus (E) of inflated corneas that were incubated in amylase solution (10 mg/ml) for varying incubation periods. Corneas were inflated at 15 mmHg. Data were represented as box plots and data overlaid with lower and upper borders of the box to represent the lower and upper quartiles, and the middle horizontal line to represent the median. The upper and lower whiskers represent 5th and 95th percentile of the data. The solid points represent data points of each group. The square (in the box) refers to the mean value of the dataset for that group. (n=8 corneas/box).

Appendix III

Biomechanical properties following snap-washing of the corneas with collagenase inhibitor (NaDTA)

1. Introduction

Collagenase inhibitor Dichloromethylene diphosphonic acid disodium (NaDTA) at a concentration of 5 mg/ml was used to inhibit the activity of the enzyme following enzymatic incubation of porcine corneas. α-amylase inhibitor of concentration 1 mg/ml in aqueous solution was used to inhibit the activity of the α-amylase following the enzymatic incubation of corneas. The corneas following the treatment were incubated in cold enzyme inhibitors (4°C) for 3 min. This pilot study aims to assets the effect of these inhibitors on viscoelastic properties.

2. Method

Fifteen fresh porcine corneas were divided into three groups; control (n=5), NaDTA (n=5) and amylase-inhibitor (n=5) groups. The epithelium of the corneas was removed. The corneas were inflated at 15 mmHg and indented 3 indents at the corneal apex. Table A3.1 below summaries experiment parameters. Shear storage modulus (G') and loss storage modulus (G") were measured using the G200 Nanoindenter.

Table A3.1: A summary of the experiment showing the condition used in the measurments.

	Groups		
	Control	**NaDTA**	**Amylase-inhibitor**
n	5	5	5
Incubation solution	PBS	NaDTA	α-amylase inhibitor
Incubation solution concentration (mg/ml)	----------	5	1
Incubation solution volume (ml)	10	10	10
Incubation solution temperature (°C)	4	4	4
Incubation time (min)	5	5	5
Inflation pressure (mmHg)	15	15	15
Measuring location	Corneal apex	Corneal apex	Corneal apex
Number of indents	3	3	3
Acquired data	G' and G"	G' and G"	G' and G"

3. Results

Figure A3.1 demonstrates G' and G" of porcine corneas were incubated in PBS, NaDTA and α-amylase inhibitor. The results show there were no significant difference between groups ($p>0.05$).

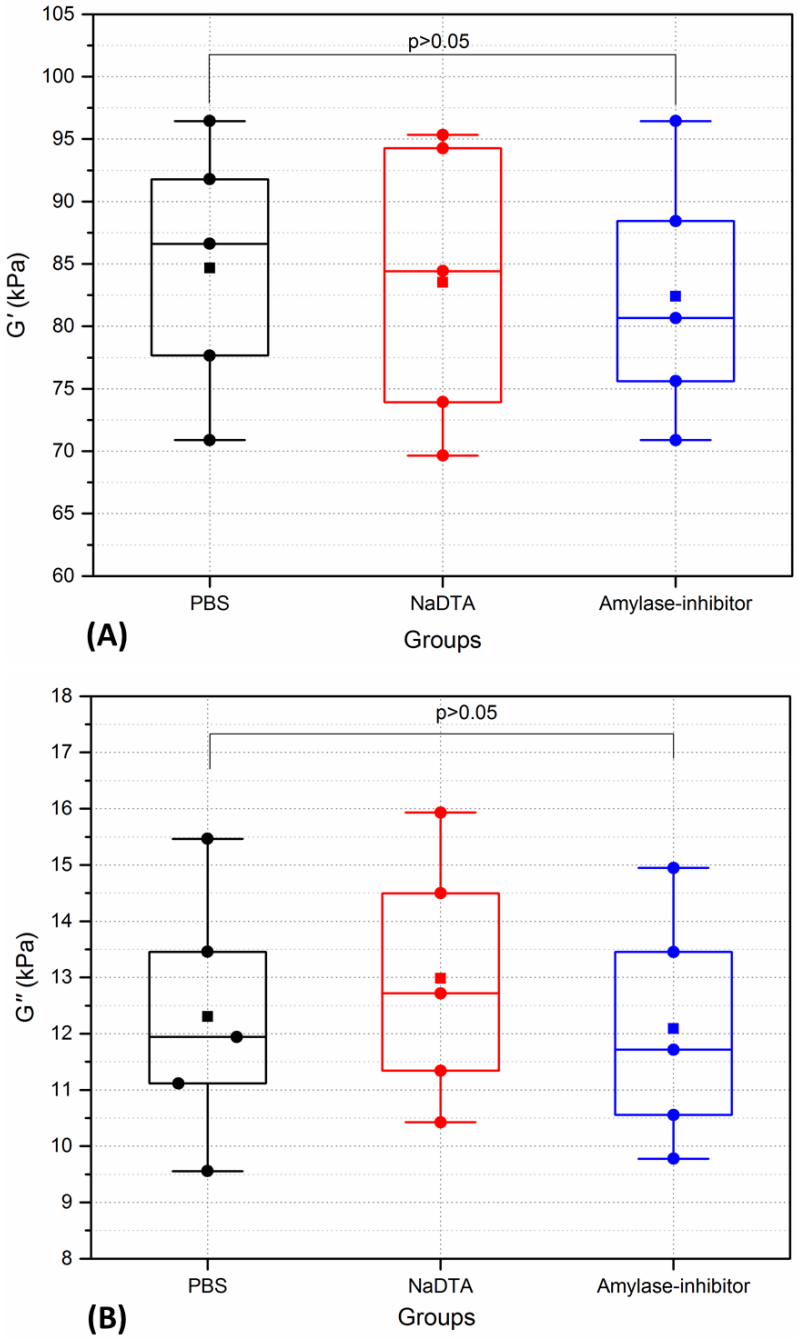

Figure A3.1: G' (A) and G" (B) of porcine corneas were incubated in PBS, NaDTA and α-amylase inhibitor for 5 min. corneas were inflated at 15 mmHg. All data was represented as box plots and data overlaid with lower and upper borders of the box to represent the lower and upper quartiles, and the middle horizontal line to represent the median. The upper and lower whiskers represent 5th and 95th percentile of the data. n=5 porcine eyes/box. 'p' refers to the statistical significance value.

4. Conclusion

Rinsing the corneas with the NaDTA or α-amylase inhibiter for 3 min make no significant change in viscoelastic properties.

Appendix IV

Biomechanical properties and CCT of porcine corneas following incubation with tissue culture

1. Introduction

Tissue culture (TC) was used to incubate porcine corneas for varying periods. It was shown in Chapter 3 that there was no statistically significant increase in shear storage modulus (G') and shear loss modulus (G") of corneas that were initially inflated by TC and the same corneas when retested after 4 hours of incubation in TC. In addition, Chapter 3 showed that central corneal thickness was significantly decreased after 4 hours of incubation in TC. This pilot study aims to quantify the changes in viscoelastic properties and CCT following incubation of porcine corneas in TC for 4 and 24 hours.

2. Method

Eight fresh porcine corneas were incubated in TC and measured at three different periods (0, 4, and 24 hours). The epithelium of the corneas was removed. The corneas were inflated at 15 mmHg and indented 3 indents at the corneal apex. Corneas were incubated at 37.5°C. Shear storage modulus (G') and loss storage modulus (G") were measured using a Nanoindenter G200 system with a DCM-II head (more details are shown in Chapter 3). CCT of the inflated corneas was measured using a Pachymeter. Paired samples t test was used to detect the statistical deference at (α=0.05)

3. Results

Figure A4.1 demonstrates G' and G" of porcine corneas were incubated in PBS, NaDTA and α-amylase inhibitor. The results show there were no significant difference in G' and G" between groups ($p>0.1$). Figure A4.2 shows CCT of porcine corneas significantly decreases following incubation in TC ($p<0.01$).

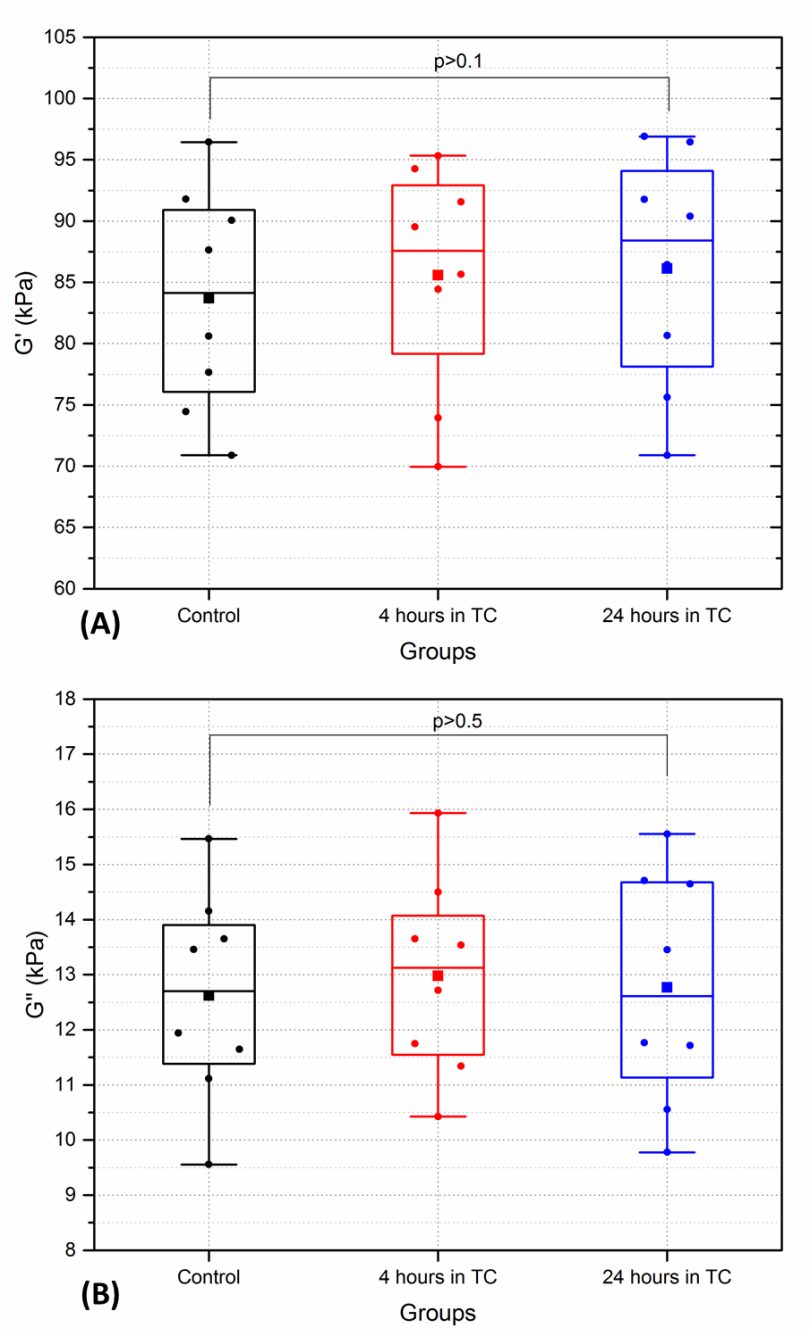

Figure A4.1: G' (A) and G" (B) of porcine corneas were incubated in tissue culture (TC) for 4 and 24 hours. Control group were tested without incubation in TC. Corneas were inflated at 15 mmHg. All data was represented as box plots and data overlaid with lower and upper borders of the box to represent the lower and upper quartiles, and the middle horizontal line to represent the median. The upper and lower whiskers represent 5th and 95th percentile of the data. The solid square in the box represents mean value of the data. n=8 porcine eyes/box. 'p' refers to the statistical significance value.

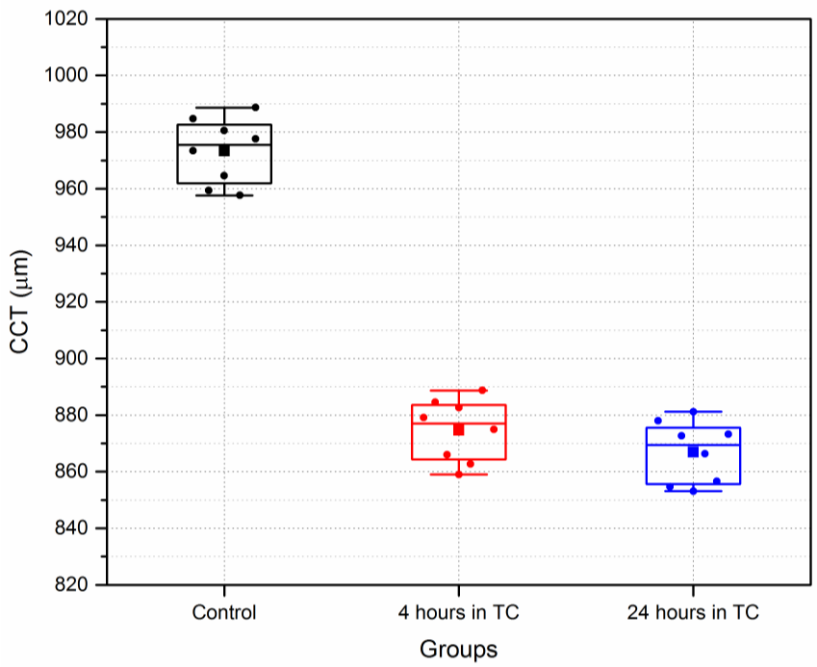

Figure A4.2: CCT of porcine corneas were incubated in tissue culture for 4 and 24 hours. Control group were tested without incubation in TC. Corneas were inflated at 15 mmHg. All data was represented as box plots and data overlaid with lower and upper borders of the box to represent the lower and upper quartiles, and the middle horizontal line to represent the median. The upper and lower whiskers represent 5th and 95th percentile of the data. The solid square in the box represents mean value of the data. n=8 porcine eyes/box.

4. Conclusions

Incubation of porcine corneas in TC for 24 hours does not affect G' and G", which make it a suitable solution for *in vitro* biomechanical investigations. However, TC significantly decreases CCT of porcine corneas.

Appendix V

Peak Force QNM calibration: AFM in air

To avoid accumulated errors that can cause errors in elastic modulus measurements, the relative calibration method was utilised using a reference sample (Vishay Photostress PS1 Polymer; Wendell, NC, USA) of known elastic modulus (2.7±0.1 GPa) prior to the Peak Force QNM mechanical measurement.

First of all, a probe was chosen that could produce sufficient sample deformation and still retain high force sensitivity. The following advisory Table A5.1 was provided from the manufacturer. The RTESPA-300 cantilever was used in this study.

Table A5.1: Bruker's recommendations for chossing the type of probe according to sample elastic modulus.

Sample modulus (E)	Probe tip	Nominal spring constant (k)
0.7 < E < 20 MPa	SNL-A / ScanAsyst-Air	0.5 / 0.4 N/m
5 MPa < E < 500 MPa	RTESPA-150	5 N/m
200 MPa < E < 2000 MPa	RTESPA-300	40 N/m
1 GPa < E < 20 GPa	RTESPA-525A	200 N/m
10 GPa < E < 100 GPa	DNISP-HS	350 N/m

Second, the laser beam was adjusted at the free end of the cantilever ensuring an adequate sum signal (force sensitivity) - typically want >1.5V.

Third, the deflection sensitivity was calibrated by ramping the Z piezo to acquire force curves. The probe was in contact with a clean sapphire (Sapphire-12M; Bruker Nano Inc., Nano Surfaces Division, CA, USA) surface. In the ramp mode, if the system scanning is stopped, the probe will return to the centre of the previous image. It was needed to enter some parameters such as the scan size to 0 nm, single ramp, and the engage setpoint to 0.05 Volts. After choosing "Ramp", the force-z position curve was obtained and the deflection sensitivity around the contact (steepest) portion of the approach was calculated.

Fourth, the spring constant of the probe was calibrated using thermal tuning method. The probe was adequately withdrawn from the sample surface to ensure the probe could not interact with the

sample during its self-excitation in the thermal tune. A frequency range that includes the resonant frequency of the cantilever and active the thermal tune option was chosen to acquire the Power-Frequency curve, by which the spring constant (K) of the cantilever can be calculated.

Finally, the reference sample (PS1) was then uploaded for mechanical measurement calibration in ambient condition. At the beginning of the scanning, the nominal tip radius was entered and conducted the mechanical measurement in small scan size (< 1 μm^2). The 'ScanAsyst Auto Control' was deactivated. The Peak Force setpoint was adjusted accordingly until the deformation (shown in deformation channel) was around 1-3 nm. The tip radius was adjusted to obtain DMT elastic modulus that should be consistent with the known elastic modulus of the reference sample. It was important to adjust the Peak Force setpoint to keep the deformation consistent with both reference and measured samples.

Appendix VI

Biomechanical properties following corneal cross-linking of enzymatic treated corneas

1. Introduction

Corneal cross-linking therapy includes the use of riboflavin (vitamin B_2) and ultraviolet-A (UVA) radiation system, which emits homogeneous UVA, to increase corneal stiffness and to arrest corneal ectatic disorders like keratoconus and ectasia after refractive laser surgery. CXL has been successfully introduced into clinical ophthalmology and the frequency of penetrating keratoplasties and keratoconus have been considerably reduced.

Enzymatic treated porcine corneas that obtained from incubation of samples with different concentrations of amylase and collagenase for varying periods have shown a significant reduction in shear storage modulus (G') and shear loss modulus (G'') (refer to Chapter 6). These treated corneas were proposed as a biomechanical animal model for keratoconus at different progression stages (in Chapter 8). The aim of this pilot study is to assess whether CXL will increase the shear moduli or not.

2. Method

In this pilot study, corneas were in three groups. Six corneas were served as control, collected fresh from a local slaughterhouse. Six enzymatic treated corneas were served as moderate keratoconus (moderate group). Other six enzymatic-treated corneas were served as sever keratoconus. The enzymatic treatment was based on Table 8.1, Chapter 8. Epithelium layer was removed from all corneas. The mechanical properties were measured by using oscillatory nanoindenter (explained in Chapter 3). XLink™ corneal cross-linking system (Opto, Mumbai, India) with 0.1% Riboflavin (B_2) (Sigma-Aldrich, Dorset, UK) were utilised to crosslink the corneas, see Figure A6.1. Corneas were inflated at 15 mmHg and riboflavin was applied abundantly on the anterior surface of corneas for 30 min. the CXL device was set on intensity of 6 mW/cm^2 of power 4.7 mW, autofocusing mode with spot diameter of 8 mm. The machine was automatically peep for applying Riboflavin every 4 min (Figure 1). All corneas were re-examined with the nanoindenter. Pair-samples t-test statistical was used (α=0.05).

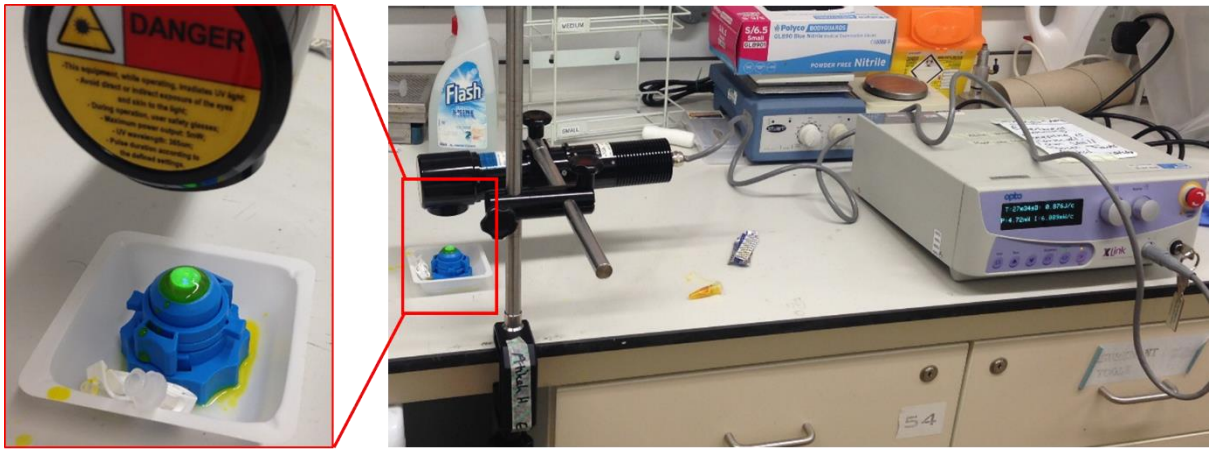

Figure A6.1: A photograph shows the setup of the corneal cross-linking experiment. The cornea was fixed in special holder and inflated at 15 mmHg.

3. Results

Figure A6.2 shows G' of corneas before and after CXL treatment. The results show that CXL has significantly increased G' ($p<0.05$). Figure A6.3 demonstrates G" of corneas before and after CXL treatment. G" has increased significantly following CXL treatment ($p<0.05$).

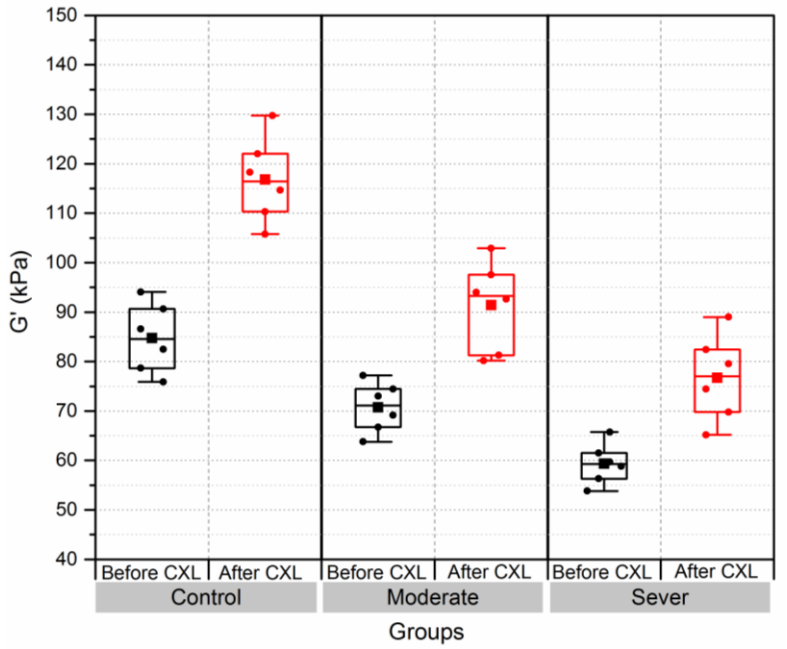

Figure A6.2: Shear storage modulus (G') of porcine corneas before (enzymatic treated corneas) and after corneal cross-linking (CXL) treatment. All data was represented as box plots and data overlaid with lower and upper borders of the box to represent the lower and upper quartiles, and the middle horizontal line to represent the median. The upper and lower whiskers represent 5th and 95th percentile of the data. n = 6 porcine corneas/box.

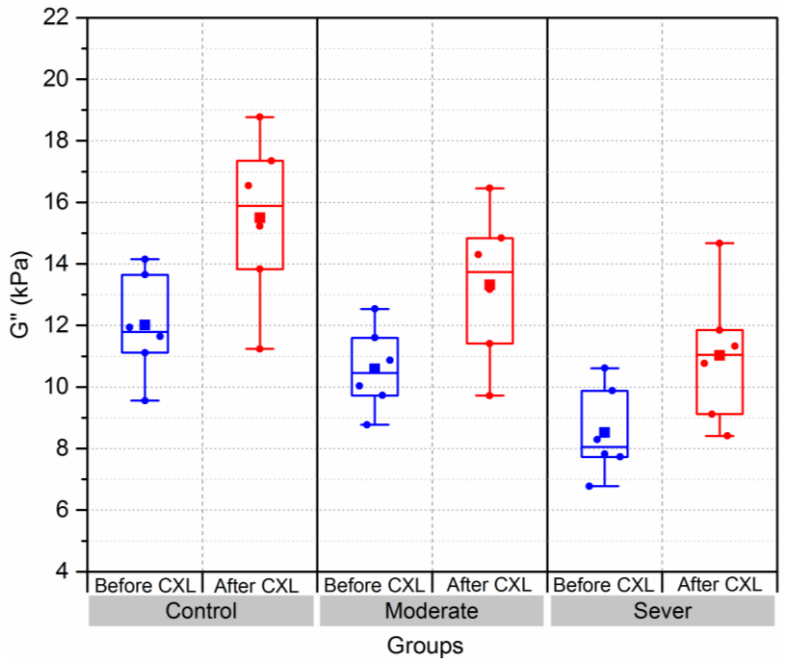

Figure A6.3: Shear loss modulus (G") of porcine corneas before (enzymatic treated corneas) and after corneal cross-linking (CXL) treatment. All data was represented as box plots and data overlaid with lower and upper borders of the box to represent the lower and upper quartiles, and the middle horizontal line to represent the median. The upper and lower whiskers represent 5th and 95th percentile of the data. n = 6 porcine corneas/box.

4. Conclusions

CXL treatment increases corneal stiffness, where G' and G" were significantly increased in all groups. This study suggests the usefulness of enzymatic treated corneas for CXL trials.

Appendix VII

Proteoglycans depletion with amylase: GAG assay

1. Introduction

Proteoglycans are an important marker in collagenous tissue such as corneal stroma. They serve important structural and biological functions such as bonding collagen fibrils that are responsible for tissue strength. The basic proteoglycan unit consists of a core protein with one or more covalently attached glycosaminoglycan (GAG). GAGs are long unbranched polysaccharides consisting of repeating disaccharide units. Depending on the disaccharide unit, GAGs can be organised into five groups: chondroitin sulfate, dermatan, heparan sulfate keratan sulfate and hyaluronic acid. A spectrophotometric assay is a valuable tool to measure the GAG content in biological fluids and tissue extracts, in which the day 1-9 dimethyl methylene blue (DMMB) is utilised. The DMMB is a thiazine chromatrope agent that presents a change in the absorption spectrum due to the induction of metachromasia when bond to sulfated GAGs enabling rapid detection/quantification of sulfated proteoglycans and GAGs in solution. Amylase has been reported to deplete proteoglycans of tendons. In this pilot study, amylase was used to deplete proteoglycans of corneal stroma.

2. Method

Eight fresh porcine corneas were collected from a local slaughterhouse. The epithelium of the corneas was removed. Four portions of 6.5 mg in weight were cut from the anterior central region of each cornea and organised into four groups: tissue culture (TC) group (n=8), control group (n=8) and amylase groups (n=16) that was divided into two subgroups. Each sample of the first amylase subgroup (n=8) were incubated with 1 ml of α-amylase (2 mg/ml) for 1 hour. Whereas, samples of the second amylase subgroup (n=8) were incubated with the same amount and concentration of the α-amylase for 2 hours. Control samples were incubated with 1 ml of PBS for 2 hours. Whereas, TC group samples were incubated with 1 ml of TC (CARRY-C, ALCHIMIA, Italy) for the same period. All samples were slightly shaken and incubated at 37.5°C. All the chemicals were provided from Sigma-Aldrich, Dorset, UK, unless stated otherwise. These treatment solutions were assessed by DMMB assay to quantify the depleted proteoglycans in the solutions.

The DMMB dye was performed by mixing 16 mg the dye, 2 g sodium formate and 2 ml formic acid in 1 litter of distilled water. The dye pH was maintained to be 3.5. A standard curve was prepared using 5 mg/ml chondroitin sulphate C as a stock solution (made up in PBS) from which to make the standards as in the following Table A7.1:

Table A7.1: Standard concentrations and stock volumes of chondroitin sulphate C for the experiment.

Standard Concentration (µg/ml)	Volume stock to add (µl)	Volume of PBS to add (µl)
0	0	1000
10	2	998
20	4	996
30	6	994
40	8	992
50	10	990
60	12	988
70	14	986

A transparent flat bottomed 96 well plate was used, where a 50 µl standard to appropriate wells was added in triplicate (3 wells filled with 50 µl each standard concentration). A 50 µl of each incubation solution was added to a well (preform in triplicate). A 250 µl of DMMD dye was added to each well. A plate reader was used to read the absorbance at 570 nm wavelength.

3. Results

Figure A7.1 shows standard curve, by which the quantity of the GAGs in the treatment solutions.

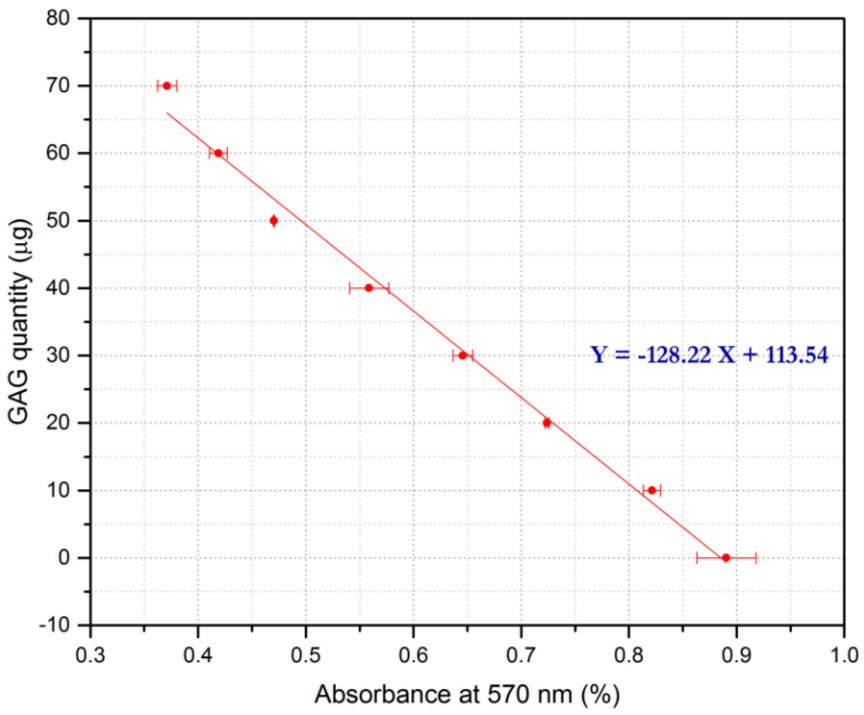

Figure A7.1: Standard curve for amylase treated stromal samples of porcine corneas. The equation represents a linear fit that was used to connect the points. Error bars are standard deviations.

Figure A7.2 shows the quantities of the GAGs in treatment solutions. The quantities of GAGs released in treatment solutions of amylase 1 hour and amylase 2 hours subgroups were 47.3±8.4 μg/ml and 73.3±7.5 μg/ml, respectively. GAG quantities released in treatment solutions of amylase group were much higher than in other groups (control and tissue culture groups). A small quantity of GAGs (14.2±3.1 μg/ml) was released in treatment solutions of PBS group. Approximately, no GAG was released in treatment solutions of TC group.

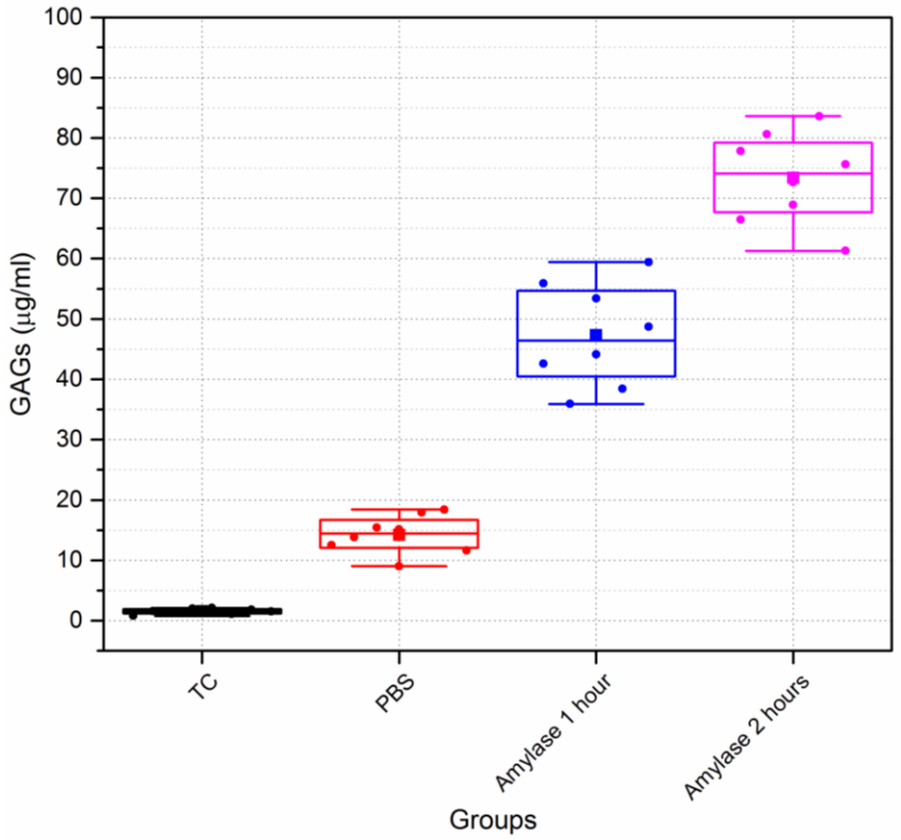

Figure A7.2: Depleted sulfated GAGs of porcine corneal samples following incubation with amylase.

4. Conclusions

GAGs were depleted from stromal samples of porcine corneas following incubation with α-amylase. The quantity of depleted GAGs from the samples seems to be a function of incubation time. A small quantity of GAGs was released after incubation with PBS, which could have occurred as a result of tissue swelling which may damage the tissue surface and thereby lead to GAG release.